Spring 2023

Seismic Soil-Structure Interaction and Foundation Rocking in Unsaturated Ground

Matthew Michael Turner
University of New Hampshire, Durham

Seismic Soil-Structure Interaction and Foundation Rocking in Unsaturated Ground

By

Matthew M. Turner

B.Sc. University of New Hampshire, 2018

M.Eng. University of New Hampshire, 2020

DISSERTATION

Submitted to the University of New Hampshire

in Partial Fulfillment of

the Requirements for the Degree of

Doctor of Philosophy

in

Civil and Environmental Engineering

May 2023

This dissertation was examined and approved in partial fulfillment of the requirements for the degree of Doctor of Philosophy in Civil and Environmental Engineering by:

Dissertation Director, Dr. Majid Ghayoomi, Associate Professor of Civil and Environmental Engineering at the University of New Hampshire.

Dr. Jean Benoît, Professor Emeritus of Civil and Environmental Engineering at the University of New Hampshire.

Dr. Yashar Eftekhar Azam, Assistant Professor of Civil and Environmental Engineering at the University of New Hampshire.

Dr. James Kaklamanos, Associate Professor of Civil Engineering at Merrimack College.

Dr. Ramin Motamed, Associate Professor of Civil and Environmental Engineering at the University of Nevada, Reno.

On Thursday, January 19, 2023

Approval signatures are on file with the University of New Hampshire Graduate School.

ACKNOWLEDGEMENTS

First and foremost, I am extremely grateful for the continuous support and wisdom provided by my advisor, Professor Majid Ghayoomi. His knowledge and experience provided me with the platform I needed to succeed. I would also like to thank my committee members Professor Jean Benoît, Professor Yashar Eftekhar Azam, Professor James Kaklamanos, and Professor Ramin Motamed for their support and advice and for making my dissertation defense a memorable occasion. I would like to thank Professor Ryosuke Uzuoka and Professor Kyohei Ueda of the Disaster Prevention Research Institute at Kyoto University for welcoming me to their university and allowing me to perform research in their laboratories for 16 months. I would like to acknowledge the extensive laboratory assistance provided by Ms. Ayako Namigishi, Ms. Nada Ayano, and Mr. Yasuto Tatsuyama of the Geotechnical Centrifuge Center at the Disaster Prevention Research Institute.

Finally, I would like to express my gratitude to my parents, family, and friends. I could not have completed this degree without their encouragement these past years.

This study was partly supported by the collaborative research program (2019W-03) of the Disaster Prevention Research Institute of Kyoto University. Additional partial funding was provided by the Institute of International Education Global E3 Program.

TABLE OF CONTENTS

LIST OF TABLES

LIST OF FIGURES

LIST OF SYMBOLS AND ACRONYMS

A = foundation area

A_c = critical contact area of a foundation required to cause bearing capacity failure

AEV = Air Entry Value

a = acceleration time history

a_f = curve fitting parameter

a_0 = dimensionless frequency

a_x = horizontal component of structural acceleration

a_y = vertical component of structural acceleration

a_{xy} = angular acceleration of the structure

B = foundation width

B_c = critical contact width of the foundation required to cause bearing capacity failure

BM = Bedrock Motion

C_c = coefficient of curvature

C_r = coefficient of uniformity

C_r = base shear coefficient of foundation

C_y = base shear coefficient of column

c' = effective cohesion

c_u = real foundation damping corresponding to translational deformation mode

c_θ = real foundation damping corresponding to rotational deformation mode

D = soil hysteretic damping ratio

D_f = foundation embedment depth

D_{min} = minimum soil hysteretic damping ratio

D_w = depth of water table below the soil surface

D_w = depth of the water table below the soil layer surface

D_{5-95} = earthquake significant duration

DPRI = Disaster Prevention Research Institute

d = effective foundation depth

e_{max} = maximum void ratio

e_{min} = minimum void ratio

ESB = Equivalent Shear Beam

F = foundation side frictional resistance

F_v = static vertical factor of safety against bearing capacity failure

FFM = Free-Field Motion

FM = Foundation Motion

FM_R = Foundation Rocking Motion

f_0 = fixed-base fundamental period of the structure

G = shear modulus

G_{max} = small-strain soil shear modulus

$G_{max,OC}$ = maximum overburden corrected shear modulus

G_r = strain-reduced soil shear modulus

G_s = specific gravity

g = acceleration due to gravity

H = total building height

h = effective height of the building above the foundation level

h_{cg} = height of a structures' center of gravity above the base of the foundation

$h_{cg,y}$ = height of structures' center of gravity above yield point of interest

I = mass moment of inertia of the structure about its center of gravity

I_a = Arias Intensity

I_f = foundation moment of inertia

i = hydraulic gradient

ICSS = Inelastic Column Structural System

K_{ini} = initial rotational stiffness of a surface foundation

$(K_{ini})_e$ = initial embedment corrected foundation rotational stiffness

K_u = translational static stiffness of a circular foundation on half-space

K_0 = at-rest coefficient of lateral earth pressure

K_θ = rotational static stiffness of a circular foundation on half-space

k = fixed-base stiffness of the structure

k_p = intrinsic soil permeability

k_s = saturated hydraulic conductivity

k_u = real stiffness of the foundation corresponding to translational deformation mode

k_θ = real stiffness of the foundation corresponding to rotational deformation mode

L = foundation length

M = seismically induced foundation overturning moment

$M_{c,foot}$ = theoretical ultimate moment capacity of a foundation

M_{max} = seismically induced maximum overturning moment experienced by the foundation

M_s = mass of the structure

M_w = moment magnitude

ML = USCS two-letter symbol for Silty Sand

N_c, N_q, N_γ = foundation bearing capacity factors

N = scale factor in centrifuge modeling corresponding to g-level

n = van Genuchten fitting parameter

P_P = passive pressure applied to the foundation

PPT = Pore-Pressure Transducer

PGA = Peak Ground Acceleration

Q = total vertical load applied to the foundation

q = foundation bearing pressure

q_o = overburden pressure at foundation depth

q_u = foundation ultimate bearing capacity

r_u = equivalent circular foundation radius corresponding to translation deformation mode

r_θ = equivalent circular foundation radius corresponding to rotational deformation mode

RFSS = Rocking Foundation Structural System

S = soil degree of saturation

S_a = spectral acceleration

S_{avg} = average degree of saturation

S_e = soil effective degree of saturation

S_r = soil residual degree of saturation

S_{xx} = smoothed power spectral density function of motion x

S_{xy} = smoothed cross-power spectral density function of motions x and y

SFSI = Soil-Foundation-Structure Interaction

SHM = Structure Horizontal Motion

SSI = Soil-Structure Interaction

SSBRF = Single-Span Bridge with Rocking Foundations

SWRC = Soil Water Retention Curve

T = fixed-base system period

T_m = mean period of earthquake motion

$\tilde{T}$ = flexible-base system period

$\tilde{T}_{an}$ = analytically derived flexible-base system period

$\tilde{T}_{ex}$ = experimentally derived flexible-base system period

TSBRF = Two-Span Bridge with Rocking Foundations

u_a = pore air pressure

u_w = pore water pressure

V_s = small-strain soil shear wave velocity

$V_{s,FF}$ = small strain shear wave velocity of the soil in the free field

$V_{s,r}$ = strain-reduced shear wave velocity of the foundation soil

$V_{s,OC}$ = overburden corrected small strain shear wave velocity

$\bar{V}_{s,OC}$ = average overburden-corrected small-strain shear wave velocity

$\bar{V}_{s,r,OC}$ = average overburden-corrected, strain-reduced, shear wave velocity.

v_w = velocity of fluid flow

z = depth below soil surface

z_e = effective profile depth of the soil layer

Δ_{FF} = seismically induced permanent free-field settlement

Δ_{SF} = seismically induced permanent foundation settlement

α = van Genuchten fitting parameter

α_{max} = maximum global rotation of bridge deck due to differential foundation settlement

α_{max} = residual global rotation of bridge deck due to differential foundation settlement

α_u, α_θ, β_u, and β_θ = dynamic coefficients accounting for frequency dependence of impedance terms

α_{res} = residual global rotation of bridge deck due to differential foundation settlement

β = fixed-base system damping ratio

$\tilde{\beta}$ = flexible-base system damping ratio

$\tilde{\beta}_0$ = foundation damping ratio

$\tilde{\beta}_{an}$ = analytically derived flexible-base system damping ratio

$\tilde{\beta}_{ex}$ = experimentally derived flexible-base system damping ratio

γ = total unit weight of the soil

γ' = effective unit weight of the soil

γ_{avg} = average unit weight of the soil

γ_m = structure-to-soil mass ratio

γ_r = reference strain

γ_s = shear strain

γ_t = total unit weight of soil

γ_w = unit weight of water

λ_{cs}, λ_{qs}, $\lambda_{\gamma s}$ = foundation shape factors

λ_{cd}, λ_{qd}, $\lambda_{\gamma d}$ = foundation depth factors

δ_{max} = maximum deck drift

δ_{res} = residual deck drift

δW = accumulated work done by foundation rocking

$\delta(\%)$ = percent difference

$\bar{\delta}$ = average percent difference

$\bar{\bar{\delta}}$ = difference in percent difference across SSBRF and TSBRF seismic response parameters

η = bearing capacity fitting parameter

θ_f = seismically induced foundation rotation

θ_P = seismically induced peak foundation rotation

θ_R = seismically induced residual foundation rotation

μ_w = kinematic viscosity of water

ν = Poisson's ratio of the soil

ρ = total density of the soil

σ = total normal stress

σ_h = total horizontal stress

σ_{ini} = initial total normal stress

σ_v = total vertical stress

σ' = effective normal stress

σ_s = structure-to-soil stiffness ratio

$\sigma_v{}'$ = effective vertical stress

ϕ' = effective friction angle of the soil

χ = Bishop's effective stress parameter

ψ_m = matric suction

$\psi_{m,avg}$ =average matric suction

ω = angular frequency

ABSTRACT

SESIMIC SOIL-STRUCTURE INTERACTION AND FOUNDATION ROCKING IN UNSATURATED GROUND

By

Matthew M. Turner

University of New Hampshire

Strong earthquake motions often cause severe damage to buildings and foundation systems, during which the interaction between the soil, foundation, and structure may dominate the seismic response. Most shallow foundations are located on, or embedded in, unsaturated and partially saturated soil deposits. Unsaturated soil layers are particularly common in zones above the water table where water can rise through different mechanisms like capillary action. Additionally, the degree of saturation throughout a soil deposit can vary both seasonally and yearly due to groundwater table fluctuation related to infiltration and evaporation. Properties of soil layers below foundations impact the seismic response of structural systems. Since soil moisture impacts soil properties, it is expected that changes in groundwater table depth would impact the seismic response of foundations and structures. However, the understanding of the mechanisms by which the degree of saturation and water table depth influences the foundation and structural response needs improvement. This dissertation aimed to evaluate the effect of the depth of the groundwater

table on the seismic response of soil-foundation-structure systems and to extend current seismic design guidelines leading to the implementation of rocking foundations in practice.

Three sets of dynamic centrifuge experiments were conducted on four physical models representing three prototype structures. The prototype structures included elastic and inelastic single-degree-of-freedom structures as well as single- and two-span bridge systems. The elastic single-degree-of-freedom structure and bridge systems were designed to incorporate rocking foundations, while the inelastic single-degree-of-freedom structure incorporated structural fuses designed to guide plastic deformations to above-ground structural locations. Physical models were slightly embedded in sandy silt layers with various groundwater table depths and subjected to a series of seismic motions. The experimental findings highlight the influence of the groundwater table depth on changes to the foundation and structural deformations and rotations, foundation-level overturning moments, period lengthening, and damping ratios. Furthermore, design procedures to predict several seismic response properties of a structure resting on unsaturated soil layers are derived in this research based on the fundamentals of unsaturated soil mechanics. These properties include the overturning moment capacity of the foundation, the initial rotational stiffness of the foundation, and the period lengthening and foundation damping ratio. Properties derived from these design guidelines are compared to the experimental results to judge the viability of implementation in practice or signify the need for further improvement.

CHAPTER 1

INTRODUCTION

1.1. RESEARCH MOTIVATION

Earthquakes pose a significant threat to communities throughout the world, where seismic waves propagate through soil layers and reach surface structures. When subjected to strong earthquake motions, soils may lose their strength, foundations may settle, structural members may yield, and, in extreme cases, buildings may collapse. Soil-Foundation-Structure Interaction (SFSI) evaluates the collective seismic response of a building system containing the superstructure, foundation, and surrounding soils given the earthquake motion at the ground surface. Thus, the properties of subsurface soils, especially their degree of saturation, influence the SFSI response. This becomes even more critical as seasonal fluctuation and climatic-driven changes in the groundwater table depth often result in drastic changes in the degree of saturation in soils and consequently the seismic response. The purpose of this research is to investigate the effects of groundwater table depth on the seismic response of soil-foundation-structure systems.

The dynamic response of unsaturated soil deviates from dry and saturated soil due to inter-particle suction stresses that alter the soil properties. For example, unsaturated soils have higher shear

stiffness and reduced damping compared with saturated and dry soil (Ghayoomi et al., 2017; Hoyos et al., 2015; Le & Ghayoomi, 2017; Vinale et al., 2001). The changes in soil properties related to inter-particle suction influence the motion propagation throughout the soil layer, seismically-induced settlements, and the seismic response of the foundation. Past studies such as Borghei et al. (2020) highlight the influence of soils' degree of saturation on the kinematic soil-foundation interaction. Kinematic interaction occurs due to the presence of stiff foundations resting on or embedded in the soil layer which alters the foundation motion compared to the motion occurring in the free-field, far from the structure. While Borghei et al. (2020) demonstrated the importance of considering the soil saturation condition on the foundation input motion, their study was limited by the properties of the tested physical model which were unable to capture the influence of the water table depth on inertial interaction. Stinson (2014) attempted to fill this research gap through forced vibration of a field-scale structure to evaluate the influence of the water table depth on changes to the natural period of the structure. However, further investigation into the water table effects is warranted due to the cyclic nature of the forced-vibration loading used by Stinson (2014). In addition, extensive testing and modeling are needed to evaluate the influence of the water table depth on additional SFSI parameters, like foundation and overall system damping, as well as foundation-level deformations such as settlements and rotations.

In this dissertation, centrifuge physical modeling is performed on soil-foundation-structure systems placed on soils with varying degrees of saturation. Experiments on unsaturated soils are conducted by generating the unsaturated zone through capillarity, altering the water level within the soil layer. Furthermore, four scaled foundation-structure systems are designed, fabricated, and tested while placed on soil layers with slight foundation embedment. These systems are modeled based on criteria to produce two rocking isolated systems and one system where nonlinear

deformation occurred at both the soil-foundation interface and in above-ground superstructure locations. The insight gained from this study sheds light on the collective impacts of SFSI, soil versus structure yielding, and the degree of water saturation on the seismic response of soil-foundation-structure systems. This new knowledge advances the state of the art in earthquake engineering by reducing seismic hazard destruction and enhancing the sustainability, safety, and cost-efficiency of building foundation systems.

1.2. RESEARCH OBJECTIVES

This PhD dissertation seeks to accomplish the following main objectives: (1) Study the effects of the depth of the groundwater table on SFSI and the seismic performance of rocking foundations; and (2) Develop and validate seismic design recommendations for SFSI and rocking foundations that consider and incorporate unsaturated soil mechanics and the depth of the groundwater table.

The secondary objectives of this research are to (1) Compare the effects of the depth of the groundwater table on the seismic response of different structures; and (2) Investigate the influence of the degree of soil saturation on the at-rest coefficient of lateral earth pressure, K_0.

1.3. RESEARCH SCOPE AND DISSERTATION STRUCTURE

This dissertation is presented in nine chapters. In addition to the introduction, background, experimental methods, and reference chapters, Chapters 4 through Chapter 7 discuss the research tasks performed to address the research objectives. Figure 1-1, shows how Chapters 4 through Chapter 7 relate to each other, while the following provides a brief description of the chapters.

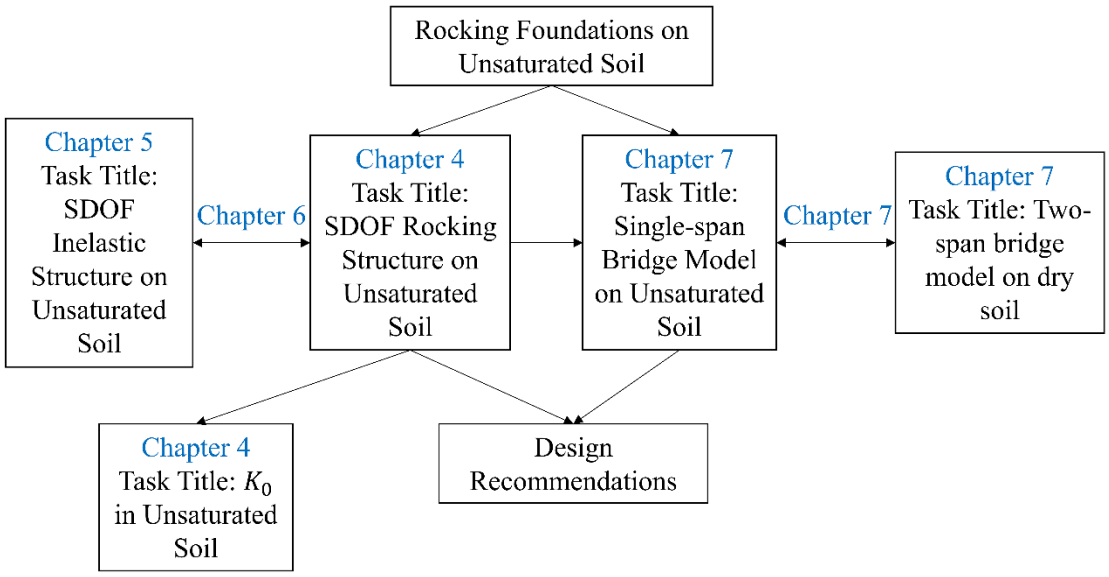

Figure 1-1. Flow chart of interrelationships between tasks and chapters of this dissertation.

Chapter 2 provides the scientific background necessary to understand the primary objectives and findings of this study. The chapter begins by introducing the concept and principles of soil-structure interaction. Design philosophies used in earthquake engineering are discussed, including the concept of rocking isolated design. Unsaturated soil mechanics concepts and methods for modeling unsaturated soils in seismic events are also presented.

Chapter 3 is intended to provide information about the experimental program, beginning with the centrifuge facility and equipment used in this study. Methods of specimen preparation and soil saturation are detailed, while the procedure used to control the water table depth in the soil layer throughout centrifugation is described. The chapter concludes with a discussion of the design of the physical models. These physical models were tested in this research.

Chapter 4 describes the results of a series of dynamic centrifuge experiments conducted to evaluate the performance of an elastic structure incorporating rocking foundations embedded in a

soil layer with varying water table depths. The performance is evaluated in terms of foundation-level deformations, accumulated work done by foundation rocking, maximum foundation overturning moments, and frequency-dependent motion amplifications. Additionally, design considerations are developed to predict the value of the moment capacity and the initial rotational stiffness of a foundation embedded in unsaturated soils. Predicted values are then compared with the experimental results to assess the quality of the proposed approaches. As a side-product of this research, the influence of the water table elevation on the at-rest coefficient of lateral earth pressure, K_0, is investigated. The results of this chapter were published in Géotechnique Journal (Turner et al., 2022a), the proceedings of the 20th International Conference on Soil Mechanics and Geotechnical Engineering (Turner et al., 2022b), and the proceedings of the 10th International Conference on Physical Modelling in Geotechnics (Turner et al., 2022c).

Chapter 5 involves a series of centrifuge dynamic experiments performed to evaluate the influence of variable groundwater table elevations on the seismic response of an inelastic building. Initially, an extension of an analytical procedure to predict flexible-base SFSI parameters, considering the influence of the water table elevation on the system response is developed. SFSI parameters, like flexible-base natural period and system damping, that are computed analytically are compared with those achieved experimentally to judge the accuracy of the proposed procedure for use in practice and signify the need for further improvements. Furthermore, the performance of the soil-foundation-structure system is evaluated through settlements, rotations, overturning moments, accelerations, drifts, and bending strains. The results of this chapter were published in the ASCE Journal of Geotechnical and Geoenvironmental Engineering (Turner et al., 2022d).

Chapter 6 compares the seismic response of the inelastic building from Chapter 5 to the response of the elastic building from Chapter 4. To promote cross-experimental comparisons, variations in

the experimental conditions, input seismic motions, and other physical model parameters (aside from superstructure flexibility), between the two experimental series are minor. The results of this chapter were published in the proceedings of ASCE Geo-Congress 2022 (Turner et al., 2022e).

Chapter 7 builds upon the results and conclusions of Chapter 4 through Chapter 6 and involves a series of centrifuge experiments performed on single- and two-span models of a prototype bridge system built to incorporate rocking foundations. Initially, a brief comparison is made between the seismic response of the single- and two-span bridge systems when placed on a dry soil layer. Then, a detailed analysis of the response of the single-span bridge model is presented to evaluate the influence of the water table condition on the seismic response of a bridge with rocking foundations. Furthermore, the procedure, developed in Chapter 4, to predict the ultimate moment capacity of the foundation as a function of the depth of the water table is further validated against the experimental results. Finally, analysis is performed to assess variations in the response of the elastic building from Chapter 4 and the single-span bridge model as a function of the water table depth. The outcomes of this chapter will be modified and submitted for possible publication in journals and conference proceedings.

Chapter 8 summarizes the conclusions of this research and provides recommendations for future research.

Chapter 9 lists the references cited throughout this dissertation.

CHAPTER 2

BACKGROUND

2.1. ABSTRACT

The goal of this chapter is to introduce the theoretical background and procedures which were used to perform and investigate the dynamic centrifuge experiments conducted in this research. Initially, the concept of soil-structure interaction is introduced, then analytical and experimental approaches for identifying soil-structure interaction are discussed. Design philosophies used in earthquake engineering are defined, including both conventional capacity and rocking isolated design. The chapter also discusses unsaturated soil mechanics and centrifuge modeling. Methods for modeling unsaturated soil layers and seismic events are described.

2.2. INTRODUCTION TO SOIL-STRUCTURE INTERACTION

Structural motion experienced during a seismic event is a function of four mechanisms including (1) earthquake source, (2) travel path of the motion, (3) site-response, and (4) soil-structure interaction (SSI). The motion experienced at the soil layer surface, far from the structure, is termed the “free-field” or “far-field” motion. The free-field motion is a product of the combined effects of the first three mechanisms. Meanwhile, SSI influences the response as the motion propagates

from the free-field to the structural system. SSI is the interaction between the ground (soil) and the structure, wherein the movement of the structure, soil, or both influences the stress distribution throughout the entire system. The study of SSI is especially applicable in areas of high seismic activity. Most civil engineering structures involve some support system that is in direct contact with the ground. When forces due to seismic events act on these systems, the displacements of the structure and soil are not independent of each other. The process in which the response of the soil influences the structure, and the response of the structure influences the soil is known as soil-structure interaction (SSI). The term SSI is used interchangeably with Soil-Foundation-Structure Interaction (SFSI) throughout this dissertation.

Figure 2-1 highlights key features in typical dynamic SFSI, where the dynamic response of a structure placed on rock is compared with that of the same structure embedded in soil. A hypothetical seismic motion occurs at the base (bedrock), at points A and D. Since the structures are located close to each other, it is reasonable to assume that the motions occurring at both A and D are identical. As the motion propagates vertically throughout the stiff rock site, the motion will reach points B and C. From a practical point of view, the motion at point B will be the same as that of point A. As the structure vibrates, overturning moments and base shear forces will be generated at the foundation level. However, the high stiffness of the rock will resist deformations at the foundation level. Therefore, the motion measured at point C will be identical to that of point A. In contrast, for the structure embedded in the soil, the motion at the foundation level, point F, will diverge from Motion D due to site and soil-structure interaction effects. First, due to site response, where geologic structures alter the seismic motion, the motion at point E will be different than that at point D. Second, embedment and base-slab averaging causes changes in the motion from E to F. Finally, the structure vibrates, and the inertial loads will generate base shear and

overturning moments at the foundation level. These forces and overturning moments lead to foundation-level deformations which further alter the motion at point F.

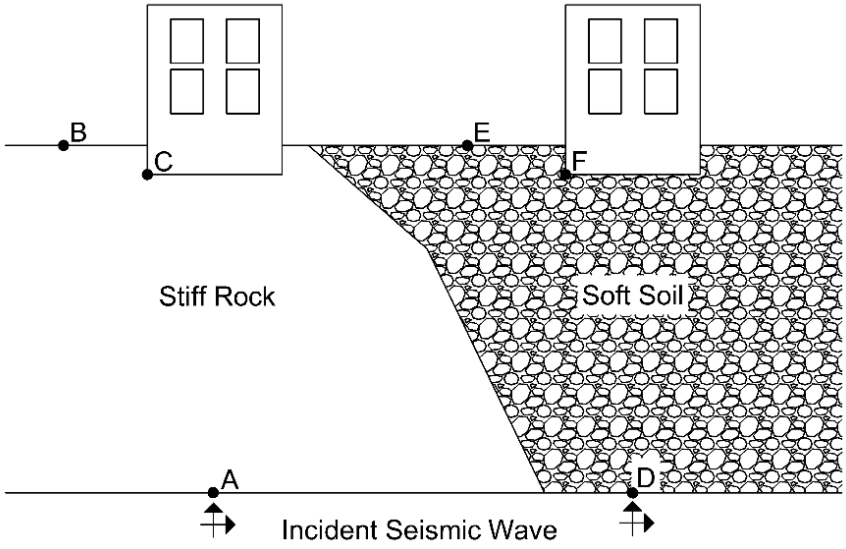

Figure 2-1. Two identical structures placed on stiff rock and soft soil, highlighting motion propagation and variations due to site-response and soil-structure interaction (after Wolf, 1985).

Soil-structure interaction is broken up into two main mechanisms between the structure, foundation, and soil which include kinematic and inertial interaction. Kinematic interaction arises due to stiff foundation elements resting on, or embedded in, soil, which cause the foundation motion to diverge from the free-field owing to ground motion incoherence, wave inclination, and/or embedment effects (Borghei & Ghayoomi, 2019; Kim & Stewart, 2003). Kinematic effects are described using a frequency-dependent transfer function that relates the free-field motion to the motion that would occur at the foundation if the foundation and structure were massless (Stewart et al., 1999a). The focus of this research is on inertial interaction effects which occur when inertia developed in a structure leads to base shear and overturning moments. Inertial interaction causes displacements of the foundation, including translation and settlement, relative

to the free-field. Frequency-dependent foundation impedance functions describe changes in the flexibility and damping associated with soil-foundation systems. Although inertial effects can be more important for structures without large, rigid slabs and deep embedment (Stewart et al., 1999a), it is important to note that kinematic and inertial interactions occur concurrently.

2.3. INERTIAL INTERACTION ANALYTICAL PROCEDURES

Veletsos & Meek (1974) determined that maximum seismically induced displacements, velocities, and accelerations experienced by a single-degree-of-freedom structural model, supported on compliant soil, can be computed using the flexible-base period, $\tilde{T}$, and damping ratio, $\tilde{\beta}$, of a system. Values of $\tilde{T}$ and $\tilde{\beta}$ characterize an oscillating system that can translate and rotate about its foundation. SFSI effects can be evaluated by comparing the response of the system supported in a fixed-base condition, with that of the system supported by a flexible foundation soil.

A simplified, idealized system, frequently used for the assessment of inertial interaction, is shown in Figure 2-2. This system consists of a linear single-degree-of-freedom oscillator (with a height h), resting on a flexible elastic foundation medium. When the system is excited in one lateral direction, two primary modes of foundation deformation are considered, translational and rotational. Each mode of deformation is characterized by springs and dashpots, signifying the stiffness and damping, respectively. The impedance function, shown in Equation 2-1, composed of complex variables can be used to express the associated stiffness and damping for these modes (Veletsos & Verbic, 1973).

$$\bar{k}_j = k_j(a_0, \nu) + i\omega c_j\left(a_{0,j}, \nu\right) \qquad 2\text{-}1$$

where k is the foundation stiffness, c is the foundation damping coefficient, ν is the Poisson's ratio of the soil, ω is the angular frequency, the subscript j denotes the mode of deformation, either

translational or rocking (denoted u and θ, respectively), and a_0 is a dimensionless frequency expressed by Equation 2-2.

$$a_{0,j} = \frac{\omega r_j}{V_{s,r}} \qquad 2\text{-}2$$

where r corresponds to the foundation radius, and $V_{s,r}$ corresponds to the strain-reduced shear wave velocity of the foundation soil. Impedance functions for foundations of arbitrary shapes are commonly analyzed as equivalent circular mats if the foundation aspect ratio is less than 4:1 (Roesset, 1980). According to Stewart et al. (1999a), the value of r should be computed separately depending on the mode of deformation, such that $r_u = \sqrt{A/\pi}$ and $r_\theta = \sqrt[4]{4I_f/\pi}$, where A and I_f are the area and moment of inertia of the foundation, respectively.

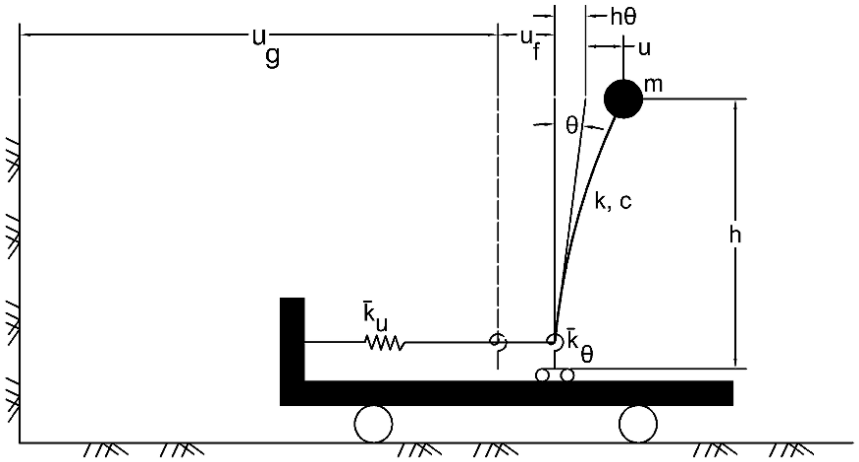

Figure 2-2. A simplified model for analysis of inertial interaction showing a lollipop model of a structural system with a column and lumped mass subjected to lateral ground deformation (after Stewart et al., 1999a).

The real stiffness and damping of the translational and rotational foundation springs and dashpots can be expressed by Equations 2-3 and 2-4 (Bielak, 1975).

$$k_u = \alpha_u K_u\,, \qquad k_\theta = \alpha_\theta K_\theta \tag{2-3}$$

$$c_u = \beta_u \frac{k_u r_u}{V_{s,r}}, \qquad c_\theta = \beta_\theta \frac{k_\theta r_\theta}{V_{s,r}} \tag{2-4}$$

where α_u, α_θ, β_u, and β_θ are dynamic coefficients accounting for the frequency dependence of the impedance terms, while K_u and K_θ are the static stiffnesses of a circular foundation on a half space expressed by Equations 2-5 and 2-6, respectively (Stewart et al., 1999a).

$$K_u = \frac{8}{2-\nu} G_r r_u \tag{2-5}$$

$$K_\theta = \frac{8}{3(1-\nu)} G_r r_\theta^3 \tag{2-6}$$

In the equations above, G_r is the strain-reduced soil shear modulus. The value of $\tilde{T}$ is evaluated from the period lengthening ratio, shown in Equation 2-7, while the value of $\tilde{\beta}$ is expressed by Equation 2-8 (Bielak, 1975; Veletsos & Nair, 1975).

$$\frac{\tilde{T}}{T} = \sqrt{1 + \frac{k}{k_u} + \frac{kh^2}{k_\theta}} \tag{2-7}$$

$$\tilde{\beta} = \tilde{\beta}_0 + \frac{\beta}{\left(\tilde{T}/_T\right)^3} \tag{2-8}$$

where T is the fixed-base period of the structure, k is the fixed-base stiffness of the structure, h is the effective height of the building above the foundation level, $\tilde{\beta}_0$ is the foundation damping ratio with contributions from both hysteretic and radiation damping, and β is the fixed-base damping ratio.

Roesset (1980) summarizes analytical procedures to evaluate impedance functions of rigid foundations. For this dissertation, the relatively rigorous analytical solutions proposed by Bielak (1975) were adopted, as they account for foundation embedment. The objectives of determining inertial interaction effects are to characterize the period-lengthening ratio, $\tilde{T}/_{T}$, and flexible-base damping ratio, $\tilde{\beta}$. These values can be used in conjunction with response-spectra methods to evaluate structural displacements, velocities, and accelerations during design.

According to the Bielak (1975) formulation, the relationship between the fixed and flexible-base parameters depends on the aspect ratio, h/r_θ, soil hysteretic damping ratio, D, and the following dimensionless parameters:

$$\sigma_s = h/V_{s,r}T \tag{2-9}$$

$$\gamma_m = \frac{M_s}{\rho\pi r_u^2 h} \tag{2-10}$$

where ρ is the density of the soil and M_s is the mass of the structure. Therefore, σ_s and γ_m reflect the ratio of the structure-to-soil stiffness and the structure-to-soil mass ratio, respectively. Avilés & Pérez-Rocha (1996) found that $\tilde{T}/_{T}$ and $\tilde{\beta}_0$ are sensitive to σ_s, while the sensitivity to γ_m is modest for $\tilde{T}/_{T}$ and low for $\tilde{\beta}$.

Parameters that are necessary for computing $\tilde{T}/_{T}$ and $\tilde{\beta}$ are summarized as follows:

- Soil Parameters: $V_{s,r}$ and D.
- Structural and Foundation Parameters: Embedment depth of the foundation, effective structural height (typically taken as $\sim 0.7 \times$ total building height), r_u, r_θ, and fixed-base parameters of T and β.

An equivalent half-space can be used to model soil profiles having a gradual increase in stiffness with depth, using an effective profile depth, z_e. The depth, z_e, extends to half the width of the foundation, as suggested by Roesset (1980) and Stewart et al. (2003). When evaluating the soil parameters within this depth, specifically the value of $V_{s,r}$, consideration should be placed on the underlying soil saturation condition, and the effect of the increased overburden pressure owing to the self-weight of the structure.

D is a strain-dependent soil property. Provided that the level of shear strain, γ_s, in the soil layer is known, values of D, for granular soils, can be estimated using the modification to material Masing behavior (Masing, 1926) suggested by Darendeli (2001).

According to the Stewart et al. (1999a) procedure (termed "modified Bielak" formulation) and using these parameters, the following steps are followed to determine $\tilde{T}$ and $\tilde{\beta}_0$:

1. Evaluate the impedance function at an assumed $\tilde{T}$. Dynamic coefficients α_u, α_θ, β_u, and β_θ are evaluated based on Bielak (1975).
2. Calculate dimensionless parameters of σ_s and γ_m.
3. Estimate $\tilde{T}/_T$ and $\tilde{\beta}$ using 2-7 and 2-8 and calculate a new estimate of $\tilde{T}$.
4. Repeat the above steps until α_u, α_θ, β_u, and β_θ are estimated at $\tilde{T}$.

Stemming from these analytical procedures, modern-day seismic design codes such as the linear elastic theory incorporated in ASCE 7 (2017) allow engineers to incorporate SSI impacts (namely period lengthening and foundation damping), into building designs that were traditionally designed assuming a completely fixed-base condition. However, under strong seismic motions, the soil-structure system may behave nonlinearly and inelastically, resulting in a response that may not be anticipated if linear elastic theories are used. Nonlinearity may stem from a combination of

deformations at the foundation level and in above-ground superstructure locations. Foundation-level deformations include rocking, sliding, and uplifting. Above-ground superstructure deformations include inelastic structural yielding and geometric nonlinearity such as force-displacement mechanisms. Due to the complex nature of nonlinear inelastic system responses, involving both soil and structural material behavior, seismic design codes and SSI analysis procedures incorporating these nonlinear inelastic impacts remain limited. One of the goals of this research is to further explore the effects of nonlinear inelastic SFSI impacts on the response of shallow foundations supporting structures.

2.4. SYSTEM IDENTIFICATION

Characterization of $\tilde{T}$ and $\tilde{\beta}$ can also be performed experimentally using system identification. This limited literature review introduces the concepts and well-established system identification procedures used throughout this dissertation. System identification is a means to evaluate the unknown properties of a system using known inputs and outputs to the system of interest. As shown in Figure 2-3, the unknown flexibility of a structure generates known differences between the input and output motion recordings. Stewart & Fenves (1998) derived input and output motion pairs required to evaluate the fixed-base and flexible-base conditions for a structure subjected to earthquake excitation, as shown in Table 2-1. Considering the fixed-base condition, parameters describing the system can be determined from input/output pairs that differ only by the acceleration of the structure, $\ddot{u}$. For the flexible-base condition, differences between the strong motion input and output pairs depend on foundation acceleration in translation, $\ddot{u}_f$, footing rotation, $\ddot{\theta}$, and $\ddot{u}$.

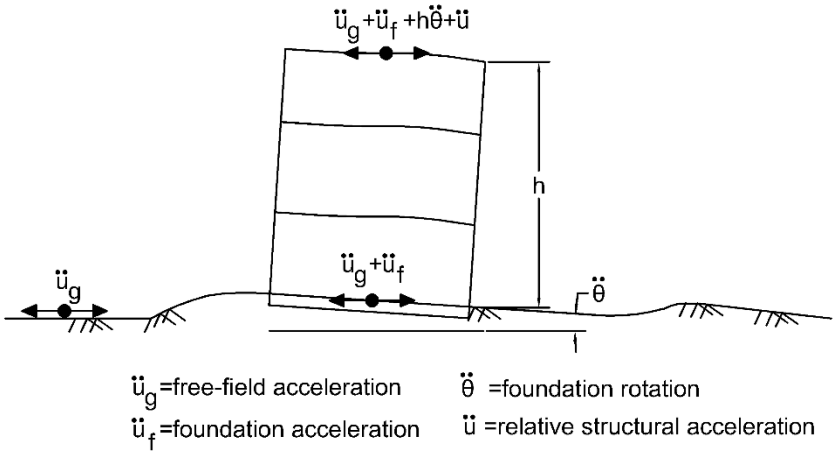

Figure 2-3. Recordings required for parametric system identification from earthquake excitation (after Stewart & Fenves, 1998).

Table 2-1. Input and output motion pairs required for parametric system identification.

	Input	**Output**
Flexible-base	$\ddot{u}_g$	$\ddot{u}_g + \ddot{u}_f + h\ddot{\theta} + \ddot{u}$
Fixed-base	$\ddot{u}_g + \ddot{u}_f + H\ddot{\theta}$	$\ddot{u}_g + \ddot{u}_f + h\ddot{\theta} + \ddot{u}$

There are two main system identification procedures in the literature: nonparametric and parametric procedures. Nonparametric procedures are used to evaluate transmissibility functions from the input and output recordings without fitting a mathematical model. Transmissibility functions evaluated from this procedure estimate the ratio of the input and output motions in the frequency domain using power and cross-power spectral density functions. Frequencies and damping ratios are estimated from the peak amplitudes of the transmissibility functions (Ljung, 1987; Pandit, 1991). However, because the shape of the transfer functions is heavily dependent on the number of points in the fast Fourier transform and windowing procedures used for smoothing, accurate determination of damping ratios from nonparametric procedures can be difficult (Pandit, 1991).

In contrast, during the parametric system identification procedure, a numerical model of the transfer function between the input and output motions is formed in the Laplace domain. Peaks in the transfer function surface are related to modal frequencies and damping ratios. Defining the numerical model of the transfer function is an iterative process, which requires two user inputs. The necessary inputs include the time delay between the input and output signals and the order of the model. Parameters describing the transfer function surface are determined by reducing the error stemming from the variation between the model and recorded output using the least squares technique. The transfer function surface is defined by modal frequencies and damping ratios, which are selected from the complex-valued pole locations. Because parametric procedures only rely on two user-defined parameters, parametric system identification provides a relatively better model of system response. Stewart & Fenves (1998) define a parametric system identification procedure by means of an autoregressive with an exogenous input model developed by Şafak (1991). This approach was implemented for SSI identification at 58 sites in California (Stewart et al., 1999a, 1999b). The system identification program written by Tileylioglu (2008) was adapted for use in this dissertation. This program is based on the Stewart & Fenves (1998) method, where its formulation is fully documented in the literature (Chen et al., 2013; Stewart et al., 1999a; Stewart & Fenves, 1998; Tileylioglu, 2008; Tileylioglu et al., 2011).

2.5. SEISMIC DESIGN OF STRUCTURAL SYSTEMS

As illustrated in Figure 2-4(a) in modern seismic design, termed *capacity design*, seismic damage is guided to above-ground superstructure locations such as the ends of beams or column base points. At these locations, the structural members are designed to mobilize strength and isolate plastic deformations during strong shaking. In contrast, the foundation is purposefully overdesigned, to avoid foundation settlement, uplift, and/or translation. The base shear coefficient

of a column, C_y, and foundation, C_r, can be used as threshold values to compare an over- versus under-designed foundation. C_y, and C_r are defined as the ratio of superstructure horizontal acceleration which is required to cause the column or foundation to yield, to the gravitational acceleration. C_y and C_r are related to the column and foundation moment capacities using the relationships shown in Equation 2-11 and Equation 2-12 as implemented in Chopra (1995) and Deng et al. (2012b).

$$C_y = \frac{M_{c,col}}{(Q/h_{cg,y})} \quad 2\text{-}11$$

$$C_r = \frac{M_{c,foot}}{(Q/h_{cg,y})} \quad 2\text{-}12$$

where Q is the vertical load applied to the yield point, $M_{c,col}$ is the moment capacity of the column, $M_{c,foot}$ is the moment capacity of the footing, and $h_{cg,y}$ is the height above the yield point to the center of gravity. If $C_y < C_r$ the strength of the column will be less than the strength of the rocking foundation and the column will be the principal yield component of the structure, while the soil-foundation interface will respond within its elastic regime. In contrast if $C_r < C_y$ the rocking foundation will be the principal yield component of the structure. In high seismic areas, special moment resisting frames (SMRF) are commonly used as the force-resisting system against intense ground motions. The design of SMRFs allows the frame to develop zones of plastic deformation in structural fuse locations, typically located at the ends of beams and column bases (NIST, 2016). According to ASCE 7 (2017), the use of an SMRF system is permitted for any seismic design category. Likewise, in states like California, traditional seismic bridge design is based on inelastic column behavior while the soil-foundation interface is treated with overstrength factors to behave elastically (Caltrans, 2010).

Although capacity design limits inelastic soil-foundation deformations, under large seismic excitations, mobilization of the foundation bearing capacity may be unavoidable, and even advantageous (Anastasopoulos et al., 2010; Gajan et al., 2005; Housner, 1963; Liu et al., 2013; Paolucci, 1997). For instance, the energy dissipated by the nonlinear response at the soil-foundation interface may limit the seismic demand transmitted to the superstructure. However, large seismic demands at the foundation level must be controlled to ensure stability against bearing failure and to minimize settlements and foundation rotations under such conditions. In an emerging, performance-based, seismic design scheme, termed *foundation rocking*, the energy dissipative characteristics of the soil-foundation system are considered, leading to a reduction in expected superstructure demands.

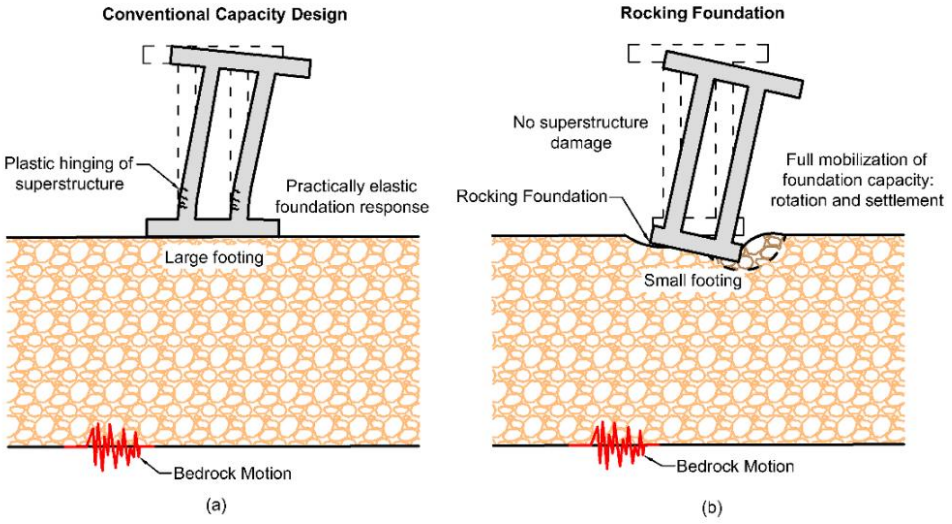

Figure 2-4. Comparison of seismic design characteristics showing (a) Conventional capacity design; and (b) Rocking foundation (after Tsatsis & Anastasopoulos, 2015).

Figure 2-4(b) describes the seismic response of a rocking foundation. In rocking foundation designs, the foundation is purposefully under-designed to promote rocking and limit the inertial

force transmitted to the superstructure. Foundation rocking occurs when an overturning moment is generated by seismic loading to the superstructure, which leads to foundation rotation. As the foundation rotates, the area of the foundation in contact with the soil (initially A), converges to a critical contact area, A_c, necessary to cause a localized bearing capacity failure at the leading edge of the foundation. When A converges to A_c, the overturning moment applied to the footing equals the ultimate moment capacity of the foundation, $M_{c,foot}$. Evidently, the moment capacity, energy dissipation, and settlement behavior of a rocking foundation are linked to A/A_c. Figure 2-5 shows a shallow foundation subject to an overturning moment, M. By using vertical and moment equilibrium about the base center point O, the formula for predicting $M_{c,foot}$ of a foundation embedded in the soil can be derived. This formula, proposed by Gajan & Kutter (2008), can be seen in Equation 2-13.

$$M_{c,foot} = \frac{QB}{2}\left(1 - \frac{A_c}{A}\right) + P_P\left(\frac{D_f}{3}\right) + F\left(\frac{B_c}{2}\right) \qquad 2\text{-}13$$

where B is the width of the foundation in the direction of shaking, Q is the total vertical load applied to the footing, P_P is the passive force applied to the edge of the foundation, D_f is the depth of embedment, and F is the side frictional resistance. The value of A/A_c is equal to the vertical bearing capacity factor of safety for static loading, F_v, if the ultimate bearing capacity is independent of the size and shape of the foundation. However, the shape factors (e.g., Vesic, 1973), depth factors (e.g., Hansen, 1970), and value of B used in conjunction with the general bearing capacity equation indicate that A/A_c is not equal to F_v, as the geometry of the footing changes throughout foundation rocking. For example, B converges to a critical width B_c, related to A_c.

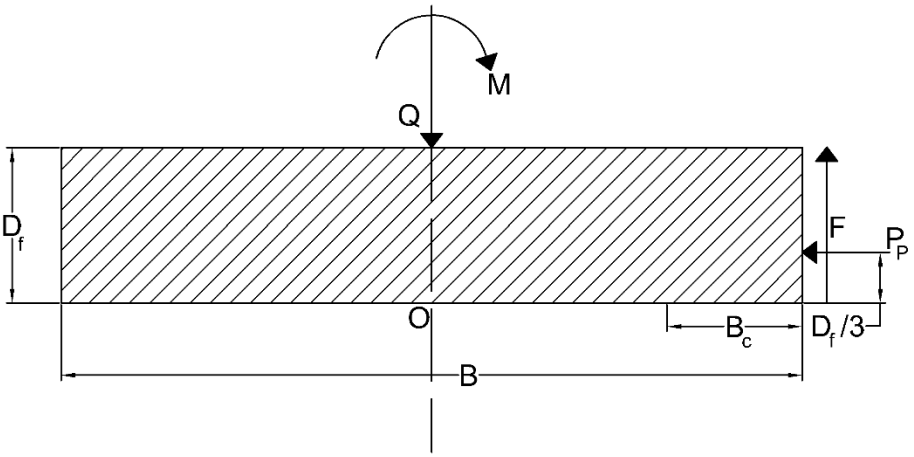

Figure 2-5. Forces and moments acting on a shallow foundation.

The effectiveness of foundation rocking has been explored analytically and experimentally for bridge piers and single-degree-of-freedom structures (Allmond & Kutter, 2014b; Anastasopoulos et al., 2012; Antonellis et al., 2015; Antonellis & Panagiotou, 2014; Deng & Kutter, 2012; Gajan et al., 2005; Gajan & Kutter, 2008). This reversal of capacity design, shifting the ductility demand away from the structure to the soil-foundation interface, may improve structural performance and increase safety throughout seismic events. On the other hand, rocking isolated based designs may come at the cost of increased settlements and rotations at the foundation level, especially for foundations with relatively small A/A_c ratios ($A/A_c < 15$) (Deng & Kutter, 2012). For foundations with $A/A_c > 15$ the seismic response of the foundation is uplift-dominated and excessive settlements and rotations are small. For foundations with low A/A_c values, the response of the foundation is settlement-dominated where excessive soil yielding beneath the foundation leads to the accumulation of significant settlements and foundation rotations. Ensuring an adequately large F_v to promote an uplift-dominated response depends on the exact soil properties

at the site. Past studies have shown that soil improvement through ground densification, installing concrete pads around footings, and the presence of underlying unattached piles and stone columns beneath the foundation can reduce the permanent settlement and residual rotations of the foundation caused by rocking (Allmond & Kutter, 2014b; Deng & Kutter, 2012; Kokkali et al., 2015; Liu & Hutchinson, 2018; Tsatsis & Anastasopoulos, 2015). Unsaturated soils, which are commonly found in the natural environment in zones above the water table, may also pose a viable solution to this problem.

2.6. INTRODUCTION TO UNSATURATED SOILS

Unsaturated soils are found in the vadose zone throughout the world. In such subsurface zones, the soil contains water under pressure less than that of the atmosphere. The depth of the vadose zone is limited by the ground surface and the upper zone of saturation of the water table. Thus, the vadose zone is maintained by capillary action, infiltration, and evaporation. These mechanisms act to add or remove water from the subsurface.

Unsaturated soils are generally described as three-phase materials composed of solids, water, and air. The solids, or the soil particles, consist of sand, silt, or clay. Soil grains are surrounded by air voids that may be either completely or partially filled with water. Fredlund & Morgenstern (1977) argued that unsaturated soils may be better described as a four-phase system with the introduction of the contractile skin, which is the same as the interface between the air and water. The water-air interface can be visualized as a thin membrane partitioning the air and water phases (Fredlund et al., 2012). Through surface tension, this membrane influences the mechanical behavior of the soil by pulling the soil particles together. However, because the air-water interface is a function of the air, water, and solid phases, the simplest representation of unsaturated soils is a three-phase system.

The effective stress variable is commonly used to describe the physical behavior of soils. The effective stress for saturated soil can be described using Equation 2-14 (Terzaghi, 1943).

$$\sigma' = \sigma - u_w \qquad 2\text{-}14$$

where σ and σ' are the total and effective normal stress, respectively and u_w is the pore-water pressure. From a physical point of view, effective stress defines the stress acting on the soil skeleton. Thus, changes in the effective stress of soil influence the volume change process and shear strength of the material.

The effective stress equation for saturated soil should be extended for unsaturated soils to consider the fact that the three-phase material is not 100% saturated due to the presence of both water and air within the voids. Two additional factors unique to unsaturated soils should be considered, which include the stress due to the pore air pressure and the difference between the pore air and pore water pressure, termed matric suction. Numerous attempts have been made to determine a single effective stress variable to define the stress state of unsaturated soil. The Bishop (1959) equation is the oldest and most widely used single-value effective stress equation for unsaturated soils:

$$\sigma' = (\sigma - \sigma_a) + \chi(u_a - u_w) \qquad 2\text{-}15$$

where σ_a is the pore air pressure, $(\sigma - \sigma_a)$ is referred to as net normal stress, while $(u_a - u_w)$ is referred to as matric suction (ψ_m). $\chi(u_a - u_w)$ is commonly referred to as suction stress. The net normal stress is related to the matric suction through a soil property, χ. The value of χ is generally considered to vary between 0 and 1 (Lu & Likos, 2004). For dry soil $\chi = 0$, while for a completely saturated soil $\chi = 1$. Thus, Equation 2-15 may reduce to Equation 2-14, correctly capturing the effective stress in a saturated soil.

The pore pressure and degree of saturation, S, profiles at equilibrium, without precipitation and/or evaporation, are shown in Figure 2-6. While pore pressures decrease linearly above the water table, the degree of saturation profiles follows a nonlinear trend. The soil-water characteristic curve, SWCC, describes the relationship between the amount of water occupying the voids and the matric suction, ψ_m, developed between the particles. This curve is sometimes denoted as the soil-water retention curve (SWRC). The relationship is commonly plotted as the variation of gravimetric volumetric water content, θ, or S, versus ψ_m.

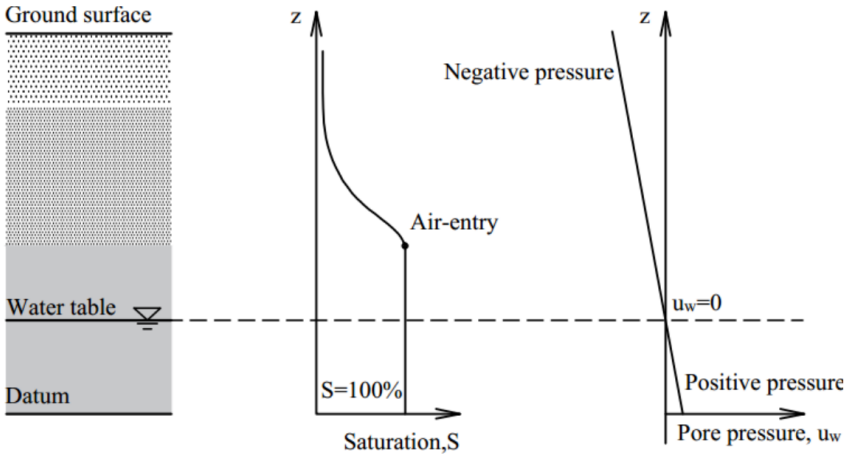

Figure 2-6. Pore pressure and degree of saturation profiles in equilibrium in the vadose zone (Lu & Likos, 2004).

Figure 2-7 shows a hypothetical SWCC. The figure indicates that a typical SWCC has three primary zones of desaturation including the saturated (boundary), transition, and residual zones. The SWCC curve becomes nonlinear in the transition zone, therefore mathematical formulations and curve-fitting procedures produce nonlinear models to best fit the data (e.g., Fredlund & Xing, 1994; van Genuchten, 1980). Two primary points describe the transition between the zones of desaturation. These points include the air entry value (AEV) and residual degree of saturation, S_r.

The AEV describes the matric suction value that must be exceeded before the air enters the voids of the soil. S_r is the residual degree of saturation at which an increase in matric suction produces no further change in the degree of saturation.

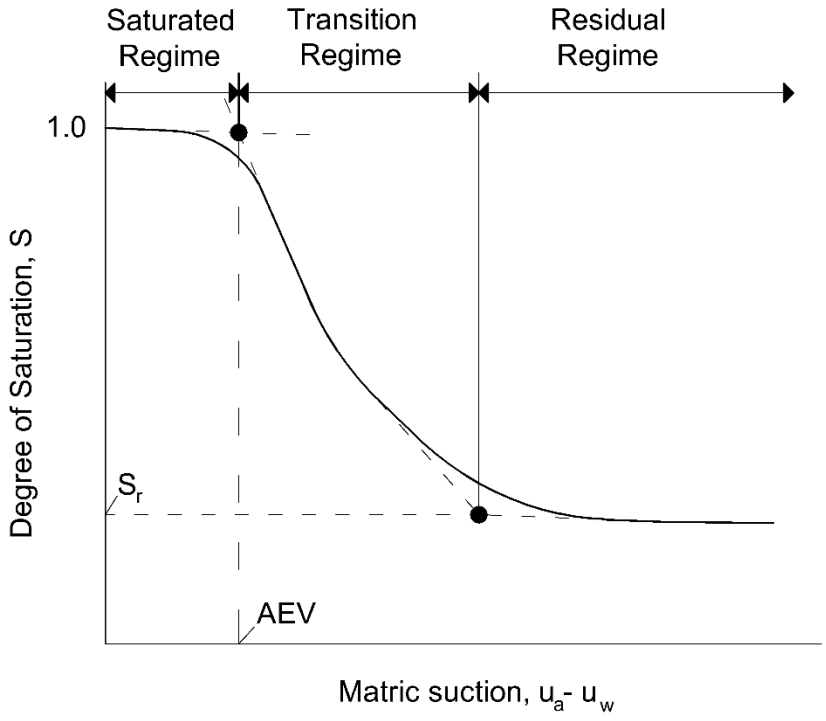

Figure 2-7. Typical soil-water retention curve (after Lu & Likos, 2004).

2.7. INFLUENCE OF DEGREE OF SATURATION ON DYNAMIC SOIL PROPERTIES

The dynamic response of soil is evaluated based on two principles: shear modulus, G, and damping ratio, D. The shear modulus relates the shear stress imposed on a soil layer to the corresponding shear strain, γ_s. The damping ratio provides a measure of energy dissipation during dynamic loading. The void ratio, mean effective confinement stress, stress history, and degree of saturation influence the shear modulus and damping ratio of soils (Ghayoomi et al., 2017; Hoyos et al., 2015;

Le & Ghayoomi, 2017; Oh & Vanapalli, 2014; Seed & Idriss, 1970). G and D are highly nonlinear and are controlled by the amount of shear strain introduced to the soil mass. As illustrated in Figure 2-8 and Figure 2-9, as shear strain increases, shear modulus decreases while damping follows the reverse trend (Hardin & Drnevich, 1972). Therefore, the maximum shear modulus, G_{max}, and minimum damping ratio, D_{min}, occur in the small strain region, typically $\gamma_s < 1 \times 10^{-6}$ (Kramer, 1996).

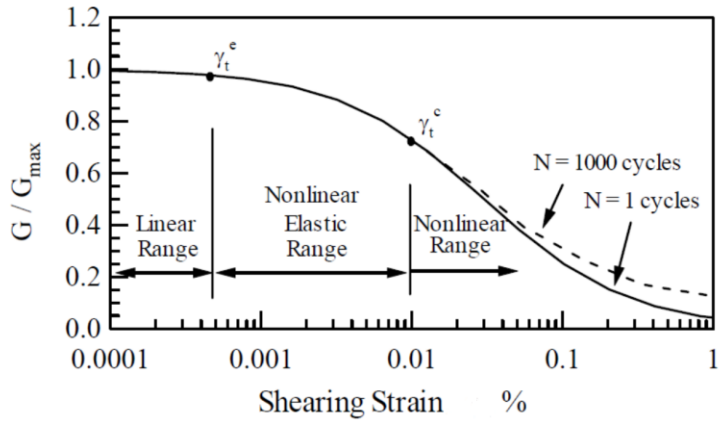

Figure 2-8. Typical shear modulus reduction curve (Menq, 2003).

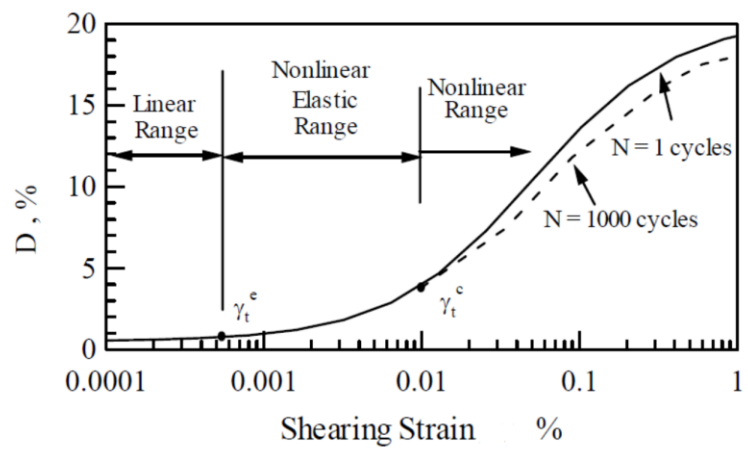

Figure 2-9. Typical damping increase curve (Menq, 2003).

Strain-dependent values of G and D are typically estimated as a function of G_{max} and D_{min}. After determining these small strain parameters, strain-dependent values can be determined using hyperbolic functions (Darendeli, 2001; Menq, 2003; Oztoprak & Bolton, 2013). The general form of the hyperbolic models for G and D are shown in Equation 2-15 and 2-16, respectively.

$$\frac{G}{G_{max}} = \frac{1}{1 + \frac{\gamma_s}{\gamma_r}} \quad 2\text{-}16$$

$$\frac{D}{D_{min}} = 1 - \frac{G}{G_{max}} \quad 2\text{-}17$$

where γ_r is a reference shear strain corresponding to $\frac{G}{G_{max}} = 0.5$. Thus, G_{max} and D_{min} play an important role in strain-dependent dynamic soil properties. In unsaturated soils, the increased effective stress leads to an increase in G_{max} and a reduction in D_{min} (Hoyos et al., 2015). Bender element experiments by Ghayoomi & McCartney (2011) indicated that G_{max} values can be 5-10% greater than those in the dry condition. In their results, the increase in G_{max} followed a nonlinear pattern, with maximum G_{max} values corresponding to mid-range degrees of saturation. Hoyos et al. (2015) conducted both resonant column and bender element tests on suction-controlled unsaturated silty sand to measure the variation of G_{max} and D_{min} with suction. Findings suggest that an increase in matric suction from 50 kPa to 400 kPa can result in a 200% increase in G_{max} for a silty sand. Meanwhile, for the same increase in matric suction, D_{min} reduces by a maximum of about 25%. Therefore, the impact of unsaturated soils may be greater on G_{max} than D_{min}.

Mousavi (2020) investigated the influence of degree of saturation on dynamic soil properties in the larger strain region ($0.025\% \leq \gamma_s \leq 0.4\%$) by performing undrained cyclic direct simple shear tests to impose dynamic loading on soils with different saturation levels. For lower degrees of saturation (i.e., $S < 0.8$), higher G values were observed in unsaturated specimens compared with

those of saturated or dry specimens across all reported shear strain values. Results suggest lower G values for fully saturated and nearly saturated samples (i.e., $S > 0.8$) compared to unsaturated and dry ones. The difference in G values between fully or nearly saturated and dry or unsaturated specimens was dependent on the shear strain amplitude. For example, the G value of saturated silty sand tested at $\gamma = 0.4\%$ was 40% lower than that of the dry one while the difference between their shear moduli was approximately 15% at $\gamma_s = 0.025\%$. This can be attributed to pore pressure induced effective stress reduction during undrained loading. Furthermore, Mousavi (2020) reported lower D values in unsaturated specimens compared with those of fully saturated specimens. Damping ratio values for samples with $S > 0.8$ were consistently greater than those in the dry condition. For specimens with higher degree of saturation, soil softening due to pore pressure generation led to elevated damping ratios. These findings are similar to those reported by Le & Ghayoomi (2017) during a similar experimental program.

2.8. INTRODUCTION TO CENTRIFUGE MODELING

Geotechnical centrifuge modeling is a technique used to conduct model-scale tests to replicate full-scale prototype geotechnical problems. Geotechnical centrifuges have been used to model, among other phenomena, foundations of bridges and buildings, settlement of embankments, stability of slopes, and earthquake-induced liquefaction. Most geotechnical systems have nonlinear mechanical behavior which depends on the confining stress and confinement history. By applying increased acceleration to physical models, identical self-weight stresses between models and prototype systems can be achieved. Compared to 1-g model tests, where small-scale models cannot correctly match full-scale prototype stresses, geotechnical centrifuge modeling enhances the similarity of models and makes it possible to obtain accurate data to solve complex problems. Figure 2-10 shows a three-dimensional schematic of a centrifuge model. This figure highlights

how a centrifuge arm rotates to produce an a g-field on the soil model. The soil model is mounted to the payload platform. This platform is hinged at the arm to allow the platform to rotate upwards during spinning. Therefore, the resultant centrifugal acceleration acts perpendicular to the base of the platform and “downwards” on the soil model.

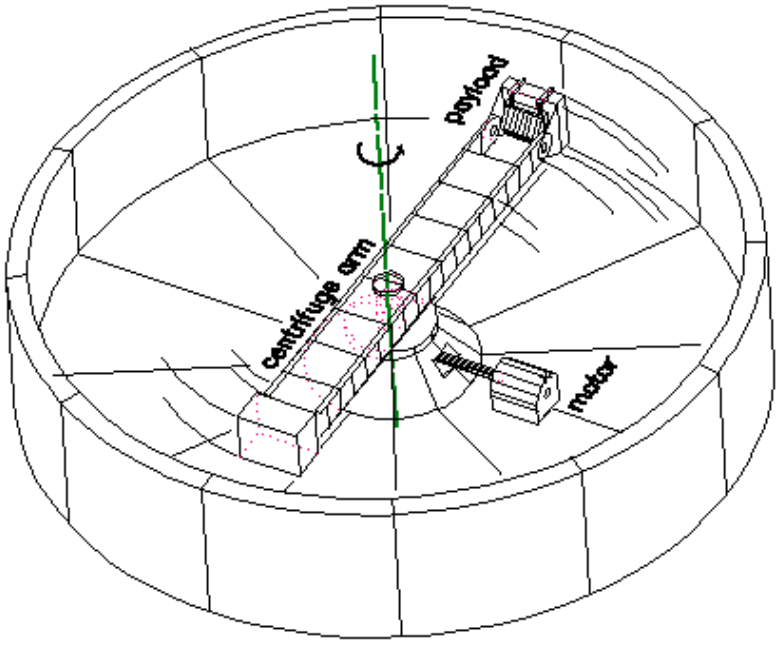

Figure 2-10. Three-dimensional schematic of a centrifuge in operation showing how the arm rotates to produce a g-field on the soil model (courtesy of UC Davis Center for Geotechnical Modeling).

The goal of centrifuge modeling is to produce identical self-weight stresses between the model and prototype. Mathematically, this goal can be stated as follows:

$$\frac{\sigma^*_{model}}{\sigma^*{}_{prototype}} = 1 \qquad 2\text{-}18$$

Where the asterisk on a quantity represents a scale factor for that quantity. σ can be any quantity with units of pressure. In centrifuge modeling the length, L, scales down by a factor of N, while acceleration, a, scales up the same factor. Therefore:

$$\frac{L^*_{model}}{L^*_{prototype}} = \frac{1}{N} \quad \text{2-19}$$

$$\frac{a^*_{model}}{a^*_{prototype}} = N \quad \text{2-20}$$

Meanwhile, the soil used in the model has the same density, ρ, as that of the prototype soil layer. Therefore:

$$\frac{\rho^*_{model}}{\rho^*_{prototype}} = 1 \quad \text{2-21}$$

Stress is related to the force applied to an object and the area of the distributed load. Therefore:

$$\sigma = \frac{F^*}{L^{*2}} = \frac{m^* a^*}{L^{*2}} = \frac{\rho^* \left(L^{*3}\right) a^*}{L^{*2}} = \rho^* L^* a^* \quad \text{2-22}$$

Substituting the relationships for L, a, and ρ, given in Equations 2-19, 2-20, and 2-21, respectively:

$$\frac{\sigma^*_{model}}{\sigma^*_{prototype}} = \frac{\rho^*_{model} L^*_{model} a^*_{model}}{\rho^*_{prototype} L^*_{prototype} a^*_{prototype}} = 1 \frac{1}{N} N = 1 \quad \text{2-23}$$

Thus, by building reduced scale physical models with lengths scaled down by N, subjecting the models to increased accelerations of N, and maintaining the same density of the materials, stresses between the model and prototype will be consistent. For example, consider a 0.5 m deep model container of soil, placed on the arm of a geotechnical centrifuge, and subjected to a gravitational acceleration of 50g. In this example, the pressures and stresses increase by a factor of 50. This means the vertical stress at the base of the soil profile is equal to the vertical stress 25 m below the surface of the ground. Therefore, the 0.5 m deep soil model effectively models the stress conditions

present in a 25 m deep prototype deposit. Table 2-2 summarizes additional scaling factors for other parameters derived from these relationships.

Table 2-2. Scaling factors used in centrifuge modeling (Ko, 1988).

Parameter	Prototype	Model
Length	1	$1/N$
Acceleration	1	N
Mass	1	$1/N^3$
Force	1	$1/N^2$
Stress	1	1
Frequency	1	N
Dynamic Time	1	$1/N$
Diffusion Time	1	$1/N^2$

2.9. CENTRIFUGE MODELING OF UNSATURATED SOILS

Centrifuge modeling has been used to study the behavior and application of unsaturation soils in geotechnical engineering. Previous studies included understanding the flow of pollutants in soils (Esposito, 2000; Knight & Mitchell, 1996), slope stability problems (Adapa et al., 2021; Deshpande & Muraleetharan, 1998), measurement of mechanical soil properties (Ghayoomi & McCartney, 2011), site-response analysis (Ghayoomi et al., 2011; Mirshekari & Ghayoomi, 2017), and soil-foundation interaction (Borghei et al., 2020; Ghayoomi et al., 2018; Stewart & McCartney, 2014). Among these experiments, the zone of unsaturated soils is controlled by three primary mechanisms: mixing soil to a certain degree of saturation, capillary rise from a known water table depth, and infiltration.

2.9.1. Mixing soil and water to generate unsaturated soils

Soil and water can be mixed to achieve unsaturated soil. This technique has been used to study the dynamic behavior of unsaturated soil embankments (Adapa et al., 2021; Deshpande & Muraleetharan, 1998). In these studies, soil and water were mixed to achieve a target degree of

saturation, then the moist soils were compacted to build small scale models of embankments. Difficulties of this approach include maintaining a constant degree of saturation in the soil profile throughout compaction and changes to the soil moisture content throughout testing.

2.9.2. Capillary rise to generate unsaturated zones

In the zone above the water table, soils are partially saturated with water. In this region, water rises in the soil due to different mechanisms such as capillarity, related to surface tension. Capillary fringe is the subsurface layer above the groundwater table where groundwater fills the pores. The height of the fully saturated soil in the capillary fringe region is less than the total height of the capillary action due to differences in pore sizes of the soil grains. Capillary action creates a vadose zone where the degree of saturation decreases with elevation above the water table. In soils with a wide range of particle sizes, the unsaturated soil layer can be thicker than the saturated zone formed by capillary fringe. The capillary fringe height is the height of the air entry matric suction, meanwhile, the height corresponding to the residual degree of saturation is termed capillary rise height (Lu & Likos, 2004).

Capillary rise has been used several times during centrifuge testing of unsaturated-saturated soils (Borghei et al., 2020; Depountis et al., 2001; Mirshekari et al., 2018). In this method, a fully saturated soil is spun-up in the centrifuge. After reaching the target acceleration the water table depth is gradually lowered in-flight until the target water table depth is reached. Solenoid valves are typically employed to remotely open and close valves attached to the base of the soil container. Drained water is stored in drainage tanks attached to the arm of the centrifuge.

2.9.3. Infiltration to generate unsaturated zones

Surface infiltration of water into soil layers has also been used to generate unsaturated soils during centrifuge testing. In these experiments, researchers prepare a soil specimen at 1g, then spin-up

the specimen to the target acceleration in the geotechnical centrifuge. At this point, valves supplying pressurized water are used to spray water on the surface of the soil while excess water is drained from the specimen. By changing the flow rate, different suction and degree of saturation profiles can be produced. This technique has been employed to simulate rainfall infiltration and subsequent seismic shaking of a slope (Xu et al., 2022), and steady-state infiltration of uniform unsaturated flow (Conca & Wright, 1990; Ghayoomi et al., 2011; Mirshekari et al., 2018; Mirshekari & Ghayoomi, 2017).

2.10. CENTRIFUGE MODELING OF SEISMIC EVENTS

Locations of seismic events are often difficult to predict, creating uncertainty in correctly choosing sites to install field instruments. This snowballs into a lack of data regarding the performance of infrastructure throughout strong shaking events. Centrifuge models can be heavily instrumented and subjected to strong ground motions in-flight. This makes centrifuge modeling an important source of data in earthquake engineering.

2.10.1. Dynamic load actuators

In recent years, numerous centrifuge shaking table facilities have been invented. Ko (1994) describes a majority of these facilities. In-flight shakers began with cocked springs and mass exciters (Ortiz et al., 1983), but these apparatuses were unable to produce sine waves with realistic frequency contents. During this time, the bumpy road apparatus was also being developed at Cambridge University (Schofield, 1980). The bumpy road apparatus uses a cam roller guided on a curved track along the wall of the centrifuge. The radial vibration of the cam is transmitted to the model. Changing the track influences the motion achieved by the model. However, altering the track requires substantial effort, therefore these systems have only been used to generate sinusoidal shaking without a broad range of frequencies.

Currently, one of the more sophisticated methods to generate powerful and realistic earthquakes in the centrifuge is the servo-hydraulic shaker, seen in Figure 2-11. Dynamic actuators installed in several geotechnical centrifuges such as the ones at the University of California Davis, University of Colorado Boulder, Rensselaer Technical Institute, University of New Hampshire, Hong Kong University of Science and Technology, and Kyoto University in Japan are some of the facilities leveraging in-flight servo-hydraulic shakers. Relying on stored energy in pressurized hydraulic oil, these actuators can shake a centrifuge model according to a calibrated earthquake motion (Kutter, 1995). Realistic earthquake motions are achieved by controlling the flow rate of oil through a servo-valve, according to the scaled earthquake time history. The servo-valve is an important component of this system, and they are specifically made to produce sufficient frequency contents, simulating realistic earthquake frequencies, under the additional acceleration of the centrifuge.

Figure 2-11. Servo-hydraulic actuator system at the University of New Hampshire.

2.10.2. Model soil containers

The model container is typically placed on the surface of the servo-hydraulic shaking table platform. This allows seismic motions to be applied to the base of the soil layer with motions propagating vertically to the soil layer surface. Soil layers in the field are often considered semi-infinite, extending laterally over great lengths. Centrifuge models of soil layers are finite, with lengths constrained by the dimensions of the model containers. To simulate field conditions, model containers should ideally allow lateral deformations to occur at the ends while allowing shear stresses to vertically propagate through the soil layer.

Rigid containers, with fixed side walls, restrict the lateral movement of soil layers. Laminar boxes (Hushmand et al., 1988; Law et al., 1991; Van Laak et al., 1994) and equivalent shear beam (ESB) containers (Ghayoomi et al., 2013; Zeng & Schofield, 1996) have been developed to overcome this problem. The boundaries of ESB containers are composed of vertically stacked rings. Rubber sheets placed between the rings influence the shear stiffness of the container. By changing the thickness and material of the rubber sheets, ESB containers can be designed to match the fundamental period of the soil layer. Although this approach has benefits, under nonlinear soil response, the container cannot capture the change in the fundamental period of the soil layer. To avoid this problem, a laminar container is used. Laminar containers ideally have zero lateral stiffness; thus, the deformation of the container is determined by the deformation of the soil layer. As schematically shown in Figure 2-12, Laminar containers are composed of vertically stacked rings that are separated by bearings. The bearings allow the rings to move independently of each other.

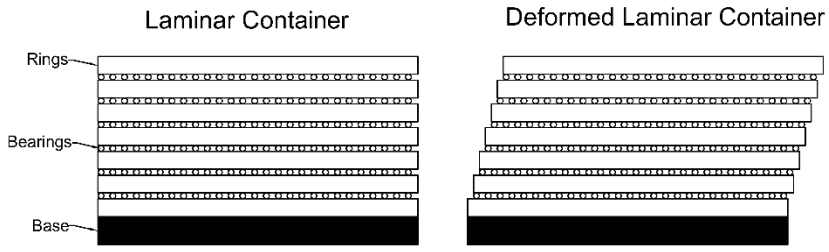

Figure 2-12. Schematic diagram of a laminar container.

2.11. GROUND MOTION PARAMETERS

Seismic motions can be characterized by numerous parameters. Although no single parameter can fully describe a seismic motion, holistic ground motion parameters and combinations of parameters describing the intensity, frequency content, and duration of a seismic motion correlate with seismic demand, site-response, and building settlement (Campbell & Bozorgnia, 2012; Dashti et al., 2010a; Ghayoomi & Dashti, 2015; Travasarou et al., 2003). To facilitate the interpretation of ground motions in this dissertation, earthquakes are characterized by peak ground acceleration (PGA), mean period (T_m), Arias Intensity (I_a), and significant duration (D_{5-95}). The PGA is the most widely used ground acceleration parameter in earthquake engineering. It is often used in building codes and incorporated in seismic hazard maps (e.g., ASCE 7, 2017). PGA is calculated as the maximum absolute value of acceleration occurring throughout the motion time duration. T_m, shown in Equation 2-24, utilizes a single representative number to describe the frequency content of the motion (Rathje et al., 2010).

$$T_m = \frac{\sum_j \frac{c_j^2}{f_j}}{\sum_j c_j^2} \text{ for } 0.25 \leq f_j \leq 20 \text{ Hz} \quad \text{2-24}$$

where c_j and f_j are the Fourier amplitude and the discrete Fourier transform frequencies, respectively. D_{5-95} describes the duration of an earthquake and is calculated as the change in time from 5% to 95% of the total I_a. I_a, as defined by Arias (1970), provides a means to measure the energy of an earthquake as a function of the acceleration and is calculated using Equation 2-25.

$$I_a = \frac{\pi}{2g} \int_0^{\infty} a^2(t) dt \quad \text{2-25}$$

where g, t, and $a(t)$ stand for the gravitational acceleration, time, and acceleration time history, respectively.

2.12. SUMMARY

This chapter provides a background of the theory used throughout the remainder of the dissertation. The chapter begins by introducing soil-structure interaction and provides definitions of the governing factors influencing this phenomenon. Analytical and experimental approaches for determining the extent of soil-structure interaction are defined. The seismic design of structural systems is introduced and is expanded to incorporate the influence of foundation rocking behavior. Discussion is provided on unsaturated soils and how changes in the degree of saturation influence the dynamic response of soil layers. Finally, the philosophy behind centrifuge modeling is discussed in detail, including ways to model both unsaturated soil layers and seismic events.

CHAPTER 3

EXPERIMENTAL METHODS

3.1. ABSTRACT

This chapter begins by introducing the centrifuge facility and equipment used in this research. Then, properties of the soil material and centrifuge model container are discussed. Descriptions of the instrumentation used to monitor the seismic response of the soil and structures throughout the experiments are provided. Next, methods of specimen preparation and saturation are summarized. Furthermore, the process of controlling the water table depth in the soil layer throughout centrifugation is described. The chapter concludes by discussing the design of the physical models tested throughout this research.

3.2. KYOTO UNIVERSITY GEOTECHNICAL CENTRIFUGE

Experiments in this research were performed at the Geotechnical Centrifuge Center located at the Disaster Prevention Research Institute (DPRI) of Kyoto University. This is a beam centrifuge with a radius of 2.5 m and a payload capacity of 24 g-ton. Figure 3-1(a) shows the Geotechnical Centrifuge Center at DPRI. This building houses the equipment necessary to perform a geotechnical centrifuge experiment. This equipment, shown in Figure 3-1(b) includes the

centrifuge chamber, located below ground, and the control room. A side view of the beam centrifuge is highlighted in Figure 3-1(c). The arm of the centrifuge has two sides: the shake table side and the counter-balance side. Equivalent loads must be applied to each side of the beam to avoid vibrations during testing. The geotechnical centrifuge is a Marui and Co., LDT device that was originally commissioned by Kyoto University in 1987. The centrifuge facility has been renovated three times since its initial operation in 1988. Additional specifications of this geotechnical centrifuge are shown in Table 3-1.

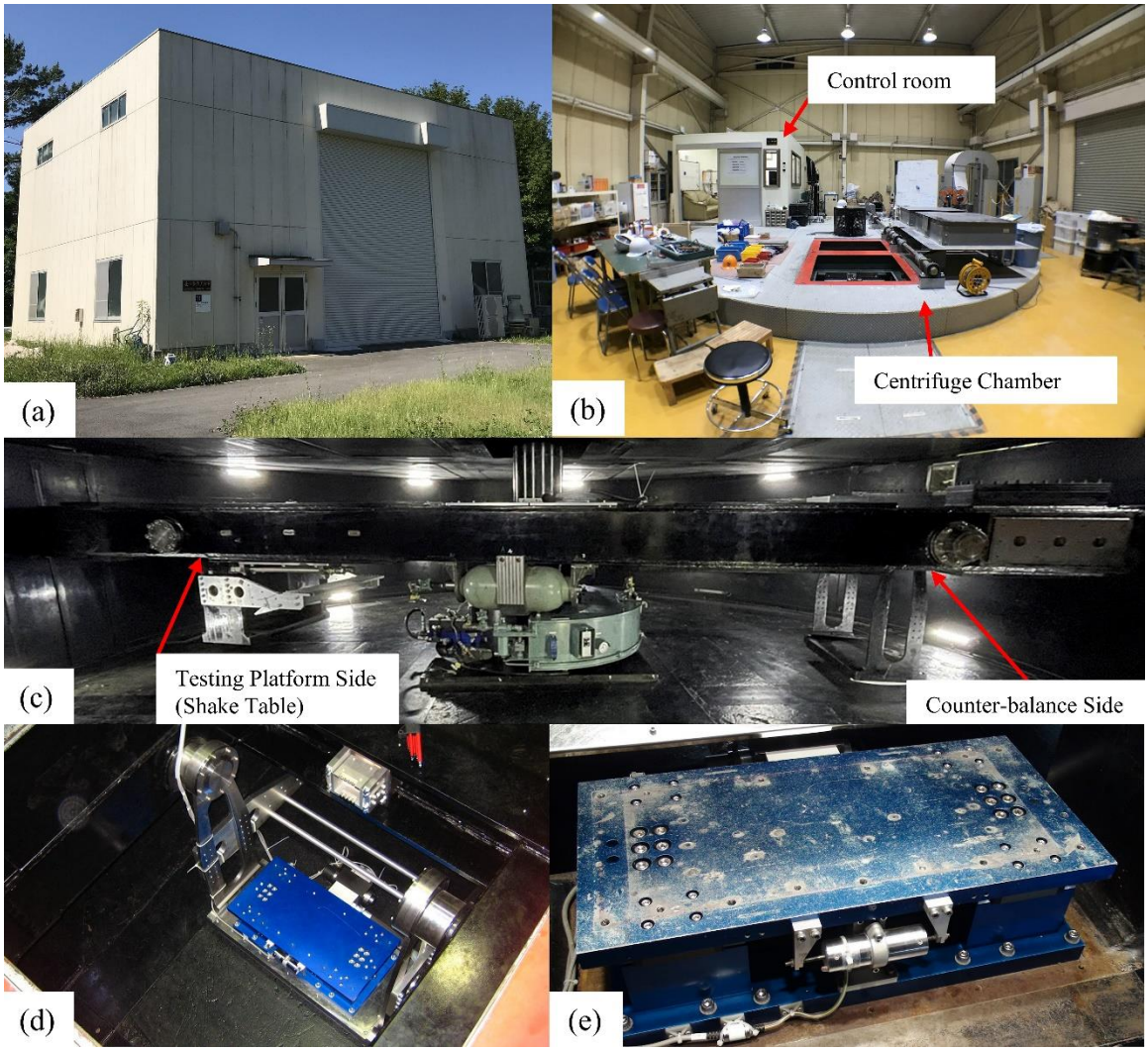

Figure 3-1. Geotechnical centrifuge facility at DPRI showing (a) building housing the centrifuge equipment; (b) view from inside the building; (c) view from inside the centrifuge; (d) top view of in-flight shake table; (e) side view of in-flight shake table.

Table 3-1. Technical specifications of the DPRI geotechnical centrifuge.

Parameter	**Value(s)**
Effective Radius (m)	2.5
Maximum size of model soil chamber (m)	Static: 0.80 (W) x 0.35 (D) x 0.80 (H) Dynamic: 0.61 (W) x 0.35 (D) x 0.62 (H)
Maximum payload ($g \times ton$)	24
Maximum centrifugal acceleration (g)	200
Maximum rotation velocity (rpm)	260
Maximum payload at 50g (kg)	Static: 245 Dynamic: 146

After preparing a soil sample for centrifuge testing, the container is placed on the shake table platform, shown in Figure 3-1(d) and (e). Then, weights are added to the counter-balance side to match the mass applied to the test platform side. During testing, an electronic motor is used to spin the centrifuge to the desired acceleration. After reaching the desired acceleration, a hydraulic pump is turned on to supply energy to shake the specimen and container using the in-flight servo-valve hydraulic shake table. The pump sends pressurized fluid to the hydraulic accumulators installed on the beam of the centrifuge through a slip ring. The hydraulic accumulators supply oil to the servo-valve. The servo-valve uses the pressurized oil to move an actuator and shake the table. The displacement of the shake table is monitored using a position sensor. The goal of the shake table is to shake the specimen according to a predefined earthquake signal. The input signal is provided to the shake table as a time series of displacements. As the shake table shakes the specimen, the displacement achieved by the shake table is monitored, compared, and adjusted based on the target input signal through a controlled feedback loop. Hence, calibration tests were carried out using an accelerometer installed on the shake table to produce achieved motions with the desired amplitudes and frequency contents.

3.3. LAMINAR CONTAINER

Soil specimens were prepared inside a laminar container that was bolted to the in-flight shake table during testing. Figure 3-2, shows a photograph of the laminar container, which is made of 20 vertically stacked aluminum rings. Seismic motions were applied through the base of the laminar container, which decreased the undesirable boundary effects and allowed one-dimensional (1-D) wave propagation from the base of the soil layer to the soil layer surface. The length, width, and depth of the laminar container are 500 mm, 200 mm, and 325 mm, respectively, while the four corners of the container are rounded with a radius of 40 mm.

A thin membrane, depicted in Figure 3-2(b), installed inside the laminar container was used to prevent soil and water from entering the small gaps between the aluminum rings during testing. The membrane was glued to the bottom plate of the laminar container using a waterproof silicone sealant. Furthermore, the bottom plate of the laminar container was modified to include a series of drainage holes. These drainage holes connect to the water drainage tank (Figure 3-2(a)) that was bolted to the bottom plate of the container. A 3 mm thick layer of fine gravel was placed on the bottom plate to allow uniform water drainage. Then, a thin filter paper, shown in Figure 3-2(b) was placed on the surface of the gravel layer and taped to the sides of the laminar container. This fabric filtered the water during the drainage process.

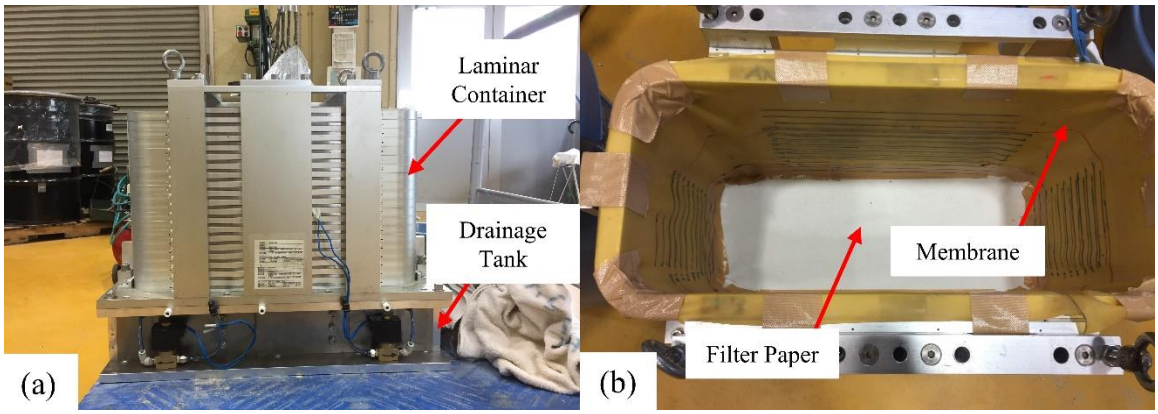

Figure 3-2. Photographs of the laminar container showing (a) side view of the laminar container; and (b) top view of the laminar container.

3.4. SOIL MATERIAL

A manufactured, cohesionless sandy silt, with a commercial name of Silica No. 9 sand, was used in this research. The grain size distribution of this soil, shown in Figure 3-3, indicates this soil has a D_{50} of about 0.066 mm, fines content of about 63.9%, and is classified as ML under the USCS classification system (ASTM D2487-11, 2011). The limiting minimum and maximum void ratios

were found to be 0.56 and 1.12, respectively, using the Japanese Geotechnical Society (JGS) 0161 (2015) test method. The drying path of the SWRC of this soil is shown in Figure 3-3(b). The methodology to determine the SWRC of this soil is discussed in Chapter 4, Section 4.5.

After determining the SWRC, the van Genuchten (1980) model, shown in Equation 3-1, was fit to the SWRC data points to facilitate interpretation.

$$S_e = \frac{S - S_r}{1 - S_r} = \left[\frac{1}{1 + (\alpha\psi_m)^n}\right]^{1-\frac{1}{n}} \quad 3\text{-}1$$

where S_e is the effective degree of saturation and α and n are fitting parameters obtained by fitting Equation 3-1 to the experimental data. According to Figure 3-3(b), the air entry matric suction and the fitted S_r of this soil are about 7.6 kPa and 19%, respectively. Other physical and hydraulic properties of this soil are listed in Table 3-2. This soil was chosen for its ability to generate greater matric suctions at higher degrees of saturation than other soils commonly used for centrifuge testing (e.g., sands to silty sands); thus, highlighting the influence of unsaturated soils on SFSI.

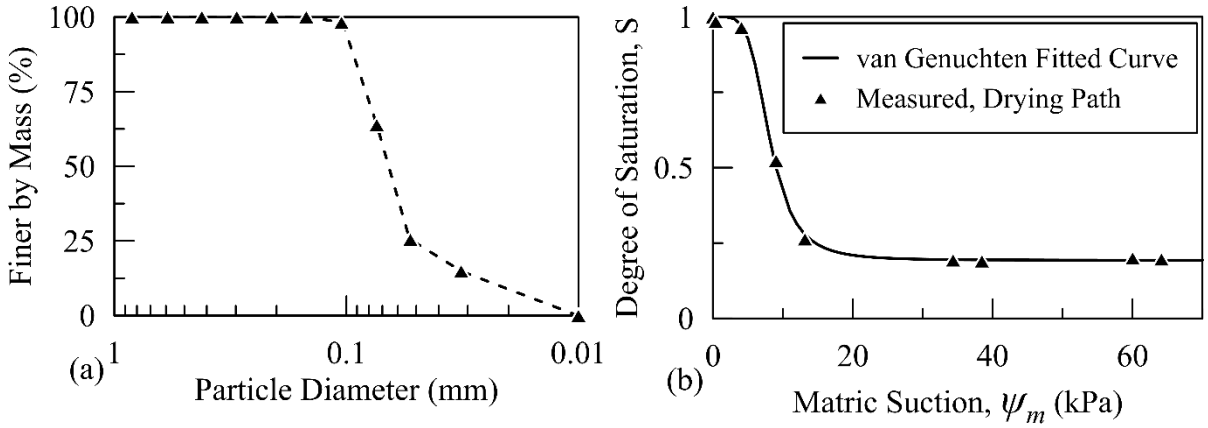

Figure 3-3. (a) Grain size distribution; and (b) Soil water retention curve drying path of the Silica No. 9 Sand fitted with the van Genuchten model.

Table 3-2. Physical and hydraulic properties of the Silica No. 9 sand.

Property	**Value**
Coefficient of uniformity, C_r	2.90
Coefficient of curvature, C_c	1.72
Specific gravity, G_s	2.72
Fines content (%)	63.9
Maximum void ratio, e_{max}	1.12
Minimum void ratio, e_{min}	0.56
van Genuchten α (kPa^{-1})	0.132
van Genuchten n	5
Residual degree of saturation, S_r (%)	19
USCS soil classification	ML
Saturated hydraulic conductivity, k_s (m/s)	1.8×10^{-6}

3.5. INSTRUMENTATION

Figure 3-4 shows photographs of the instruments used in this research. Instruments included accelerometers, pore pressure transducers, laser displacement sensors, dielectric sensors, earth pressure sensors, and strain gauges. These sensors measured accelerations, pore water pressures, displacements, volumetric water contents, total stresses, and strains, respectively. Table 3-3 describes the instruments used in this research including the measured parameter and the parent manufacturing company.

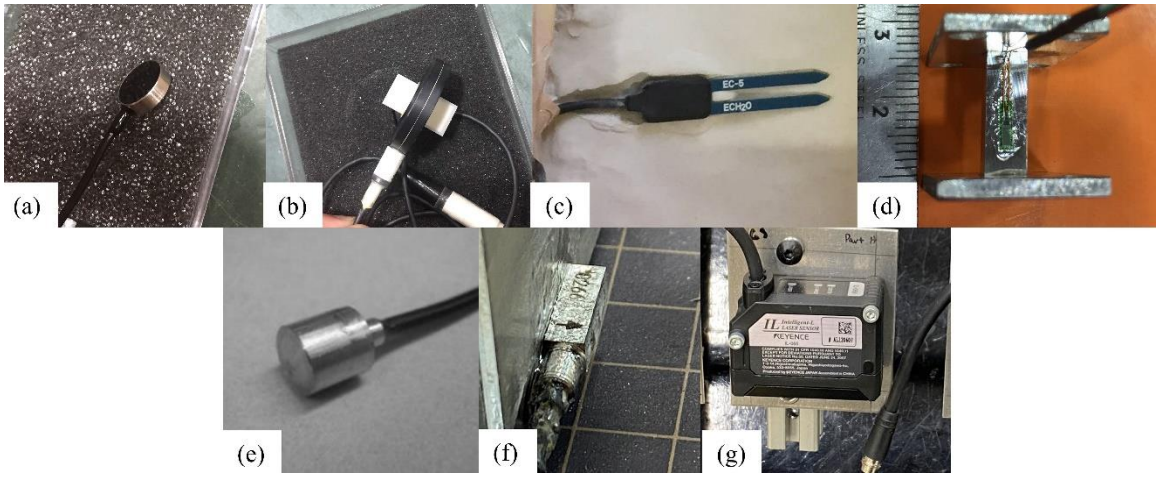

Figure 3-4. Photographs of instruments used in this research, including (a) earth pressure transducers; (b) bender elements; (c) dielectric sensors; (d) strain gauges; (e) pore pressure transducers; (f) accelerometers; and (g) laser displacement sensors.

Table 3-3. Description of the instruments used in the centrifuge experiments.

Sensor Type	**Measured Parameter**	**Parent Manufacturer**
Earth pressure transducer	Total earth pressure	SSK
Bender element	Shear wave velocity	Keysight
Strain gauge	Strain	Tokyo Measurement Instruments Lab
Dielectric sensor	Volumetric water content	Decagon Devices
Pore pressure transducer	Positive pore water pressure	SSK
Accelerometer	Acceleration	Fujicera
Laser displacement sensor	Displacement	Keyence

Figure 3-4(a) shows one of the earth pressure transducers. These relatively small (10 mm measuring diameter) sensors can be installed in the soil layer to measure total pressures in the horizontal or vertical directions. Pairs of bender elements were used to measure shear wave velocities in the soil layer. Bender elements generate small-magnitude shear waves using piezoelectric ceramics. A single bender element is shown in Figure 3-4(b). Dielectric sensors (Figure 3-4(c)) were used to measure volumetric water contents. Dielectric sensors produce a

magnetic field in the soil layers immediately around themselves and measure the dielectric constant of the media. A strain gauge, shown in Figure 3-4(d) measured strains at select structural locations during testing. These gauges measured strain over a length of 2 mm and were consistently arranged to form a half-bridge connection.

An example of a pore-pressure transducer is shown in Figure 3-4(e). These sensors were installed in the soil layer and were able to measure only positive pore water pressure, up to 200 kPa. An example of an accelerometer is shown in Figure 3-4(f). Accelerometers were installed both inside the soil layer and on the structure to measure accelerations. Finally, Figure 3-4(g) provides an example of the laser displacement sensors. Two types of laser sensors were used, distinguished solely based on their measuring range. Smaller range laser sensors were able to measure displacements from 55 to 105 mm, while larger range sensors had a measurement range of 70-130 mm. Laser sensors measured displacements of the soil layer surface, laminar container, and structures.

Except for the dielectric sensors, the calibration factors provided by the instrument manufacturers were used to convert measured signals into recorded parameters. According to Mirshekari et al. (2018), dielectric sensors should be calibrated for specific soil types to increase the accuracy of the measured volumetric water content. In this research, dielectric sensors were calibrated for the Silica No. 9 Sand according to the procedure outlined in Mirshekari et al. (2018).

3.6. SPECIMEN PREPARATION

Specimens were prepared at 1-g using dry pluviation, i.e., a crane and hopper system. Dry pluviation is a process where the soil is rained in the dry condition from a known drop height through an orifice of calibrated diameter. The procedure for calibration of the dry pluviation

technique is explained in Section 3.6.1. Because the soil material used in this research is fine-grained, small soil particles can be suspended in the air during the pluviation process. Suspended soil particles (like dust) create problems for the geotechnical centrifuge, laminar container, sensors, and centrifuge personnel. These problems include contamination of sensor connections and ports, reduced bearing life, and respiratory illness. Therefore, the samples were prepared inside a dust booth installed in the centrifuge facility. This dust booth, shown in Figure 3-5, provides ample space for the laminar container, sensors, and researcher. To further protect the laminar container from dust build-up, a thin dust protection plate (Figure 3-5) was attached to the top ring of the laminar container. The protection plate overhangs the side of the laminar and catches suspended soil particles that exceed the container boundaries.

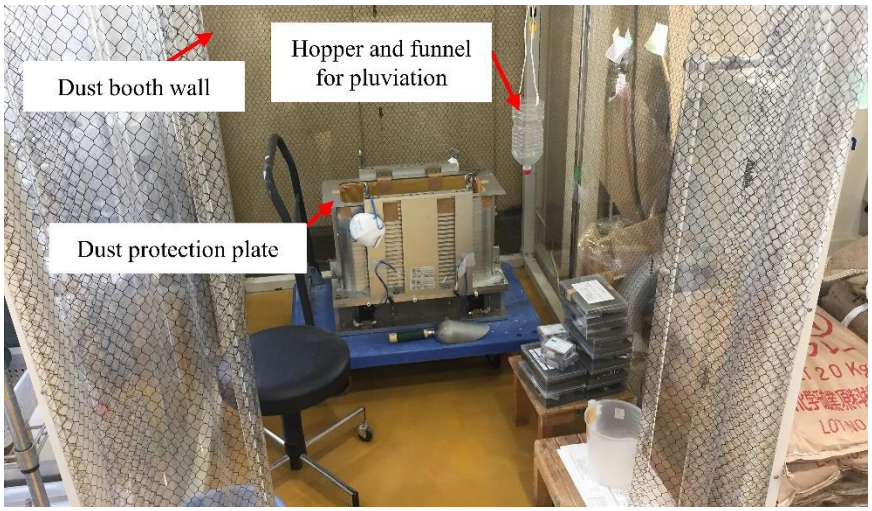

Figure 3-5. Photograph of a sample being prepared inside the dust booth.

Soil layers were pluviated in uniform lifts of about 2 cm, to achieve a uniform dry and relative density of about $1463\ kg/m^3$ and 55%, respectively, across all experiments. The pluviation was temporarily paused at select elevations to install instruments and to place physical models. Figure

3-6 highlights the placement of several of the sensors installed in the soil layer throughout the experiments. After pluviating to the desired total height of the soil layer, an additional lift of soil was pluviated. Then, a scraper was used to remove excess material and create a horizontal soil profile of the desired thickness. Sample preparation lasted about six hours for each experiment.

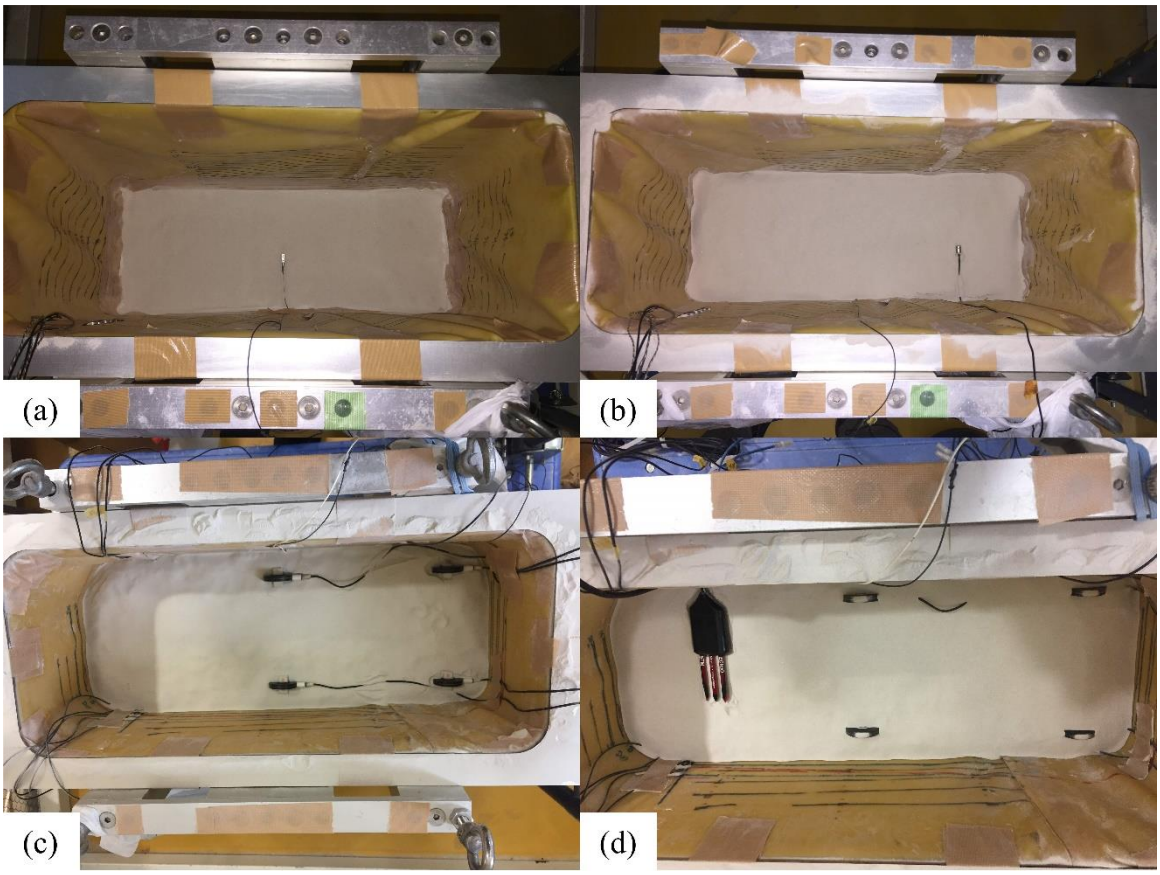

Figure 3-6. Examples of several sensors installed throughout the soil layer during sample preparation showing (a) accelerometer; (b) pore pressure transducer; (c) bender element; and (d) dielectric sensor.

3.6.1. Calibration of the dry pluviation technique

In this research, a medium-dense soil profile with a relative density of about 60%, corresponding to a dry density of 1481 kg/m^3, was desired. The dry pluviation technique was calibrated to

obtain an achieved relative density of 55% (corresponding to a dry density of $1463\ kg/m^3$) according to the following steps:

1. The hopper volume and orifice diameter were selected as 1 liter and 5 mm, respectively.
2. An initial drop height was assumed and measured using a plumb bob.
3. The soil was rained from the initial drop height into a small calibration container with a known volume ($100\ cm^3$) and height (4 cm).
4. The achieved dry density of the soil, inside the small calibration container, was compared to the target dry density of the soil.
5. The drop height was adjusted, and steps 3-4 were repeated until the achieved dry density somewhat converged with the target dry density.
6. Based on the chosen drop height from step 5, a large rigid container with length and width matching that of the laminar container was used to further confirm the achieved dry density of the soil. This container had a total volume of 0.01025 m^3. The soil was pluviated into the large rigid container in 2 cm lifts until the soil reached the surface of the container. The soil was then leveled, and the achieved dry density was calculated.

Figure 3-7 demonstrates the calibration results of the dry pluviation technique performed using the small mold. Results suggest that as the drop height increased, the dry density also increased. Based on this calibration procedure, the initial dry and relative density of the soil profiles prepared in this research was about 1463 kg/m^3 and 55%, respectively. These values are based on a calibrated drop height of 40.7 cm.

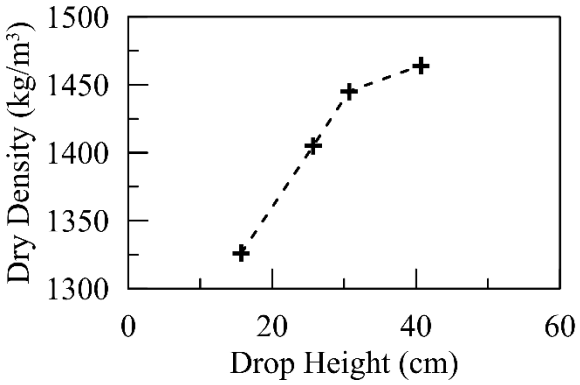

Figure 3-7. Calibration results for the dry pluviation technique determined using the small container.

3.7. SATURATION OF SPECIMENS

In this research, the tested specimens can be divided into three categories based on their soil saturation condition before the application of seismic motions: dry, saturated, and saturated-unsaturated with the zone of unsaturated soil located above the depth of the water table. For the saturated and saturated-unsaturated specimens, after achieving the target soil profile height through dry pluviation, the soil profiles were fully saturated with de-aired water according to Figure 3-8 and the following procedure:

1. All valves shown in Figure 3-8 were closed.
2. Valve 2 was opened, and the large de-air chamber was filled with water.
3. Valve 2 was closed and valve 1 was opened; the de-air pump was turned on and the water in the large chamber was de-aired for at least 2 hours and until no visual entrapped air bubbles remained.
4. Valve 1 was closed and valves 2, 3, and 4 were opened to allow water to flow from the large de-air chamber to the small de-air chamber.

5. The small de-air chamber was filled with water to an elevation less than the elevation necessary to cause a sand boiling condition.
6. Valve 3 was closed, and valve 5 was opened to allow water to flow from the small de-air chamber into the laminar container and soil layer.
7. The small de-air chamber was refilled periodically with water supplied from the large de-air chamber.
8. When the film of water on the surface of the soil layer reached a thickness of about 5 mm, valve 5 was closed. Then, the saturation lines inserted into the ports at the base of the laminar container were disconnected and the ports were plugged.
9. The combined mass of the saturated soil layer, laminar container, and instruments was measured, then the specimen was lifted via crane and placed and bolted to the shake table.

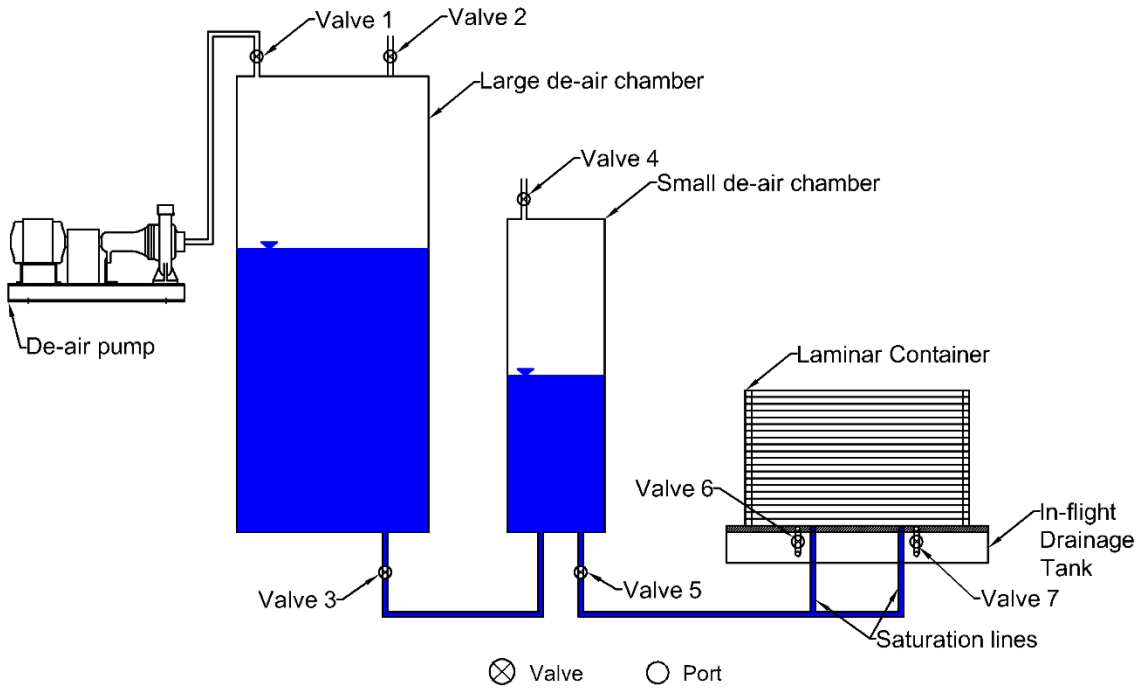

Figure 3-8. Schematic of the soil saturation procedure illustrating how de-aired water was used to saturate the soil layer in the centrifuge laminar container.

3.7.1. Experiment fluid selection

As shown in Table 2-2, in dynamic centrifuge modeling there exists a time scaling conflict in diffusion and dynamic problems. In diffusion events, time scales by $1/N^2$, between the model and prototype, while for dynamic events, time scales as $1/N$ (where N is the g-level). In seismic centrifuge experiments on saturated or partially-saturated soils, excess pore water pressures may be generated. The dissipation of this excess pore water pressure is a diffusion problem. However, because of the short duration of seismic simulation, dynamic and diffusion phenomena occur simultaneously.

Theoretically, the conflict between the dynamic and diffusion times can be resolved by slowing the time of the diffusion event. This can be accomplished using a more viscous pore fluid like

metolose solution (Dewoolkar et al., 1999). Darcy's law for the flow of water through soils is shown in Equation 3-2:

$$v_w = k_p \frac{\gamma_w}{\mu_w} i \qquad 3\text{-}2$$

where v_w is the velocity of the flow, k_p is the intrinsic permeability of the soil, γ_w and μ_w are the unit weight and kinematic viscosity of water, respectively, and i is the hydraulic gradient. By saturating the model with a pore fluid that is N times more viscous than water, Equation 3-2 shows that the flow velocity will be reduced by a factor of N (provided the unit weight of the substitute fluid is the same as water). Therefore, by using the higher viscosity pore fluid, the post-earthquake pore pressure dissipation time in the centrifuge model will increase by a factor of N, resolving the time scaling conflict between the diffusion and dynamic event.

In this research, we can divide the soil layers in the experiments based on the depth of their water table, with an unsaturated zone above and a saturated zone below this depth. Mirshekari et al. (2018) showed that soil-water retention would be scaled 1:1 between the model and prototype in the geotechnical centrifuge while the capillary height follows the length scaling law. This was achieved using several miniature tensiometers and moisture probes in soil layers that were subjected to in-flight wetting and drying. Further, very minimal, and often zero pore pressures are generated during dynamic loading of unsaturated soils, which would minimize the impacts of this scaling conflict. Also, using metolose solution in unsaturated soils would result in particle cellulose cementation, which would result in much stiffer soil at the surface, and lower overall settlement (Borghei, 2019).

Below the water table, in the saturated zone, the scaling issue becomes more relevant. Borghei (2019) investigated the effects of the viscosity of pore fluid on the seismic behavior of saturated

and unsaturated sandy soil. Experimental findings suggest that agreements in the response of the sandy soil saturated with metolose and water were noticed across the total seismic soil settlements, maximum lateral deformations, strain-dependent natural frequency of the soils, and seismic amplification factors for the range of excitation in this, and past research. The main contribution of the viscosity of pore fluid would be the transient rate of generation and dissipation of pore pressure.

Given the advantages and disadvantages of the use of substitute pore fluid, especially for unsaturated soils, and to have consistency across the range of degrees of saturation, de-aired water was chosen as the saturation fluid in this research.

3.8. CONTROLLING WATER TABLE DEPTH DURING CENTRIFUGE TESTING

The capillary rise technique, introduced in Chapter 2, Section 2.9.2 , was used to control the degree of saturation in the soil layers. The following procedure was used to lower the depth of the water table during centrifugation:

1. The laminar container was spun-up in the centrifuge to the target acceleration after being fully saturated.
2. Valves 6 and 7 (see Figure 3-8) were opened remotely to allow water to drain into the in-flight drainage tank (see Figure 3-2(a)) located between the laminar container and shake table.
3. The valves were closed after a calibrated time and the depth of the water table was estimated using an array of pore-pressure transducers.
4. Steps 2 and 3 were repeated until the water table reached the desired depth.

After achieving the desired water table condition, the specimen was subjected to a series of scaled, historic, seismic motions. Throughout testing, the water table depth may have changed, and the soil layer may have settled. Settlements and water table conditions were monitored and considered throughout the analysis.

3.9. DESIGN OF PHYSICAL MODELS

Four structures were modeled and designed. These structures are titled: (1) Rocking Foundation Structural System (RFSS); (2) Inelastic Column Structural System (ICSS); (3) Single-Span Bridge with Rocking Foundations (SSBRF); and (4) Two-Span Bridge with Rocking Foundations (TSBRF). These models were designed to reflect the response of realistic prototype structures when subjected to 46g acceleration inside the geotechnical centrifuge. The seismic response of RFSS and ICSS informed the design choice of models 3 and 4 (SSBRF and TSBRF).

3.9.1. RFSS versus ICSSS

Although RFSS and ICSS are both standalone SDOF structures, each model was designed to exhibit a unique response when subjected to seismic loading. RFSS was designed based on the rocking foundation concept introduced in Chapter 2, Section 2.5. Therefore, the superstructure of RFSS remained completely elastic under seismic loading. In contrast, during the design of ICSS, an inelastic superstructure response was elicited. However, to promote cross-experimental comparisons, several design parameters across RFSS and ICSS were chosen to be held approximately constant, regardless of the model structure. These parameters included the total height of the model (H), foundation width (B), foundation length (L), foundation embedment depth (D_f), foundation bearing pressure (q), and fixed-base modal parameters including T and system damping, β. Initially, a prototype mid-rise structure that could be scaled down to be represented by an equivalent SDOF model was selected from a database of full-scale moment-resisting frame

structures presented by Goel & Chopra (1997). Specifically, typical structural values of T, q, and H were selected from this database. Parameters of the prototype structure were then downscaled to be represented by a SDOF model when subjected to 46g centripetal acceleration at the surface of the soil, according to the generalized centrifuge scaling laws shown in Table 2-2. Then, structural design parameters were iteratively adjusted to elicit strong SSI effects and associated nonlinearity based on dimensionless parameters discussed by Veletsos & Nair (1975) and Bielak (1975) and shown in Equation 2-9 and Equation 2-10. Other constraints such as the size of the experimental container, centrifuge in-flight overhead clearance, and instrumentation requirements impacted the member size selection.

A photograph of the physical models designed for RFSS and ICSS is shown in Figure 3-9. The total height of the models in the prototype scale was 8.05 m, and each model had a square foundation of width and bearing pressure equal to 4.6 m and about 185 kPa, respectively. Table 3-4 summarizes the parameters of the physical models in the prototype scale.

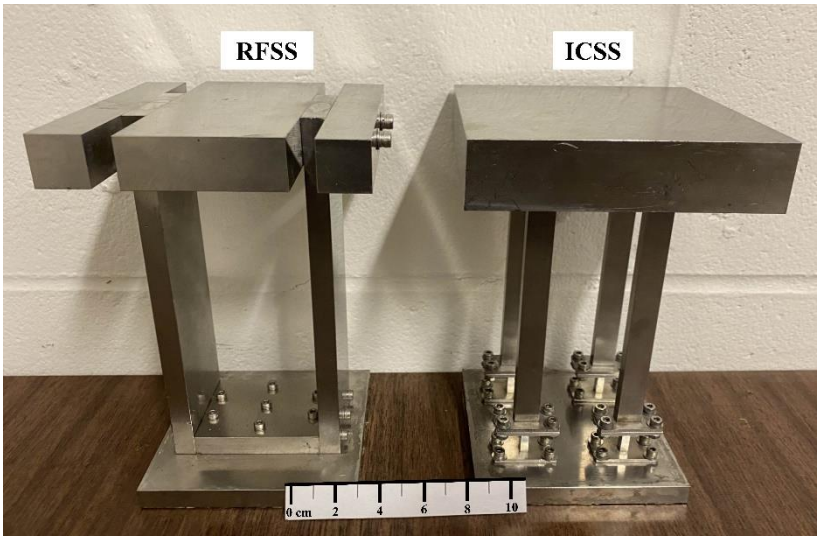

Figure 3-9. A photograph comparing the RFSS and ICSS models.

Table 3-4. Properties of the RFSS and ICSS models in the prototype scale.

	Physical Model	
Property	**RFSS**	**ICSS**
Height of structure, H (m)	8.05	8.05
Foundation width, B (m)	4.6	4.6
Embedment depth, D_f (m)	0.46	0.46
Bearing pressure, q (kPa)	188	185
Mass of structure, M_s (Mg)	406	398
Mass moment of inertia, I (M$g \cdot m^2$)	4226	3253
Translation mode foundation radius, r_u (m)	2.60	2.60
Rotational mode foundation radius, r_θ (m)	2.63	2.63
Fixed-base fundamental period T (s)	0.54	1.27
Fixed-base damping ratio, β (%)	2.68	2.15

Values of T and β were determined using a modal hammer analysis, with β determined using the logarithmic decrement method. During the modal hammer analysis, the physical models were instrumented with accelerometers that were installed to record foundation and superstructure motions in the horizontal directions. Models were fixed to the floor and excited with a modal hammer. Figure 3-10 shows the horizontal vibration of the superstructures. Throughout the vibration, the amplitude of the motion decayed due to the system damping. Acceleration time histories were converted from the time domain to the frequency domain to find the natural frequencies of the physical models, as shown in Figure 3-11. According to the figure, the fixed-base fundamental frequencies of the RFSS and ICSS models are 85 Hz and 36 Hz (in the model scale), respectively. When subjected to 46g acceleration in the geotechnical centrifuge, these frequencies result in a fixed-base fundamental period of 0.54 s and 1.27 s, respectively. The damping ratios were estimated using the logarithmic decrement method discussed by Chopra (1995). It should be noted that the modal hammer testing performed herein occurred in the small-strain region, thus the influence of inelastic deformations (especially for ICSS) is not considered in the reported values of T and β.

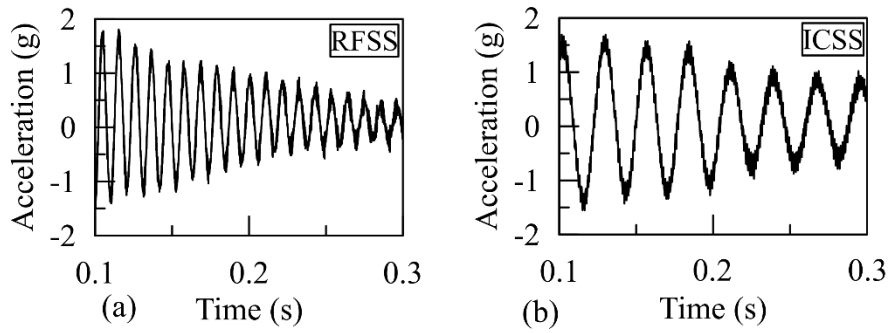

Figure 3-10. Horizontal vibration of the superstructure during modal hammer testing of (a) RFSS; and (b) ICSS.

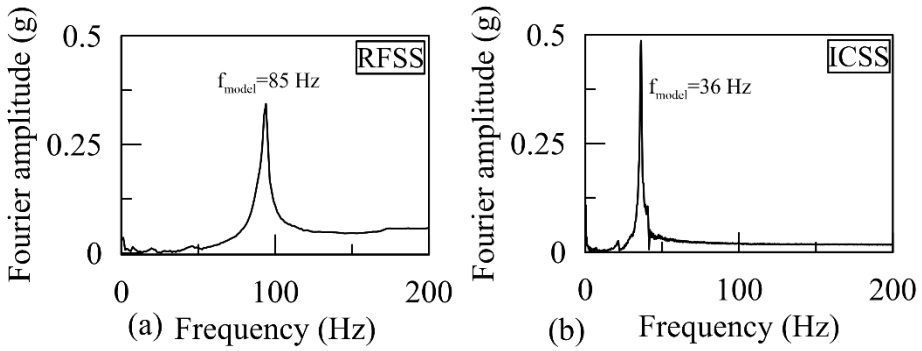

Figure 3-11. Fourier amplitude spectra of horizontal superstructure vibration during modal hammer testing of (a) RFSS; and (b) ICSS.

3.9.2. Design of RFSS

RFSS was made entirely of stainless steel. The following additional design criteria were considered during the design of RFSS: (1) the system consists of a moment-to-shear ratio greater than one and (2) the critical contact area ratio, A/A_c, of the foundation is less than fifteen regardless of the soil saturation condition, where A is the area of the foundation.

To promote a rocking response, rather than a translational one, it was important to design a system in which the moment-to-shear ratio was greater than one. Gajan & Kutter (2009) showed that when

this criterion is met the contribution of horizontal load on the bearing capacity is less than about 20%; therefore, the shear force may reduce the moment capacity of the foundation by less than 20% and can be neglected when evaluating the moment capacity. They also showed that the moment-to-shear ratio is equal to h_{cg}/B of the structure-foundation system, where h_{cg} is the height from the base of the foundation to the center of gravity of the structure, equal to 5.21 m in the prototype scale. The moment-to-shear ratio of RFSS was calculated as 1.13; therefore, the foundation-structure system herein is rocking dominant.

As a foundation rocks, the area of the foundation in contact with the soil (initially assumed to equal A) will converge to A_c, necessary to cause bearing capacity failure of the soil. Consequently, a plastic hinge at the edge of the foundation will form due to soil yielding. Deng & Kutter (2012) observed that for embedded shallow foundations on dry sand with A/A_c less than about fifteen, the structure settled rather than uplifted during foundation rocking. Thus, maintaining an $A/A_c < 15$ across all soil saturation conditions was an important factor to consider because settlement mitigation was a primary motivation of this research. Discussion of the methodology used to determine A/A_c ratios for each soil saturation condition is presented in Chapter 4, Section 4.7.1.

3.9.3. Design of ICSS

The design of ICSS was controlled by the desire to elicit a primarily inelastic response at select structural locations while having similar properties as RFSS. To localize inelastic behavior experienced by the structure, regions with the maximum moment and potential nonlinearity were designed to occur in reduced sections at the base of the columns at instrumented structural "fuse" locations. Fuses were designed and constructed out of a solid aluminum cross-section, simulating the approximate compressive yield strength of reinforced concrete. Since these elements deform primarily in flexure, the dimensions of the cross-section were governed by the slenderness and the

second moment of area. A design compressive stress due to bending under lateral load was calculated using an expected surface motion acceleration response spectrum. This lateral load was then used to ensure that the fuse would yield, rather than buckle, during seismic loading, based on an estimated aluminum yield strength of 70 MPa. To improve testing efficiency, the fuses, shown in Figure 3-12, were designed to be replaced and consisted of a 14 mm long I-shape with flat steel plates welded at both ends. These flat plates were bolted to matching plates on the column and foundation sections. Except for the structural fuses, ICSS was made entirely of stainless steel.

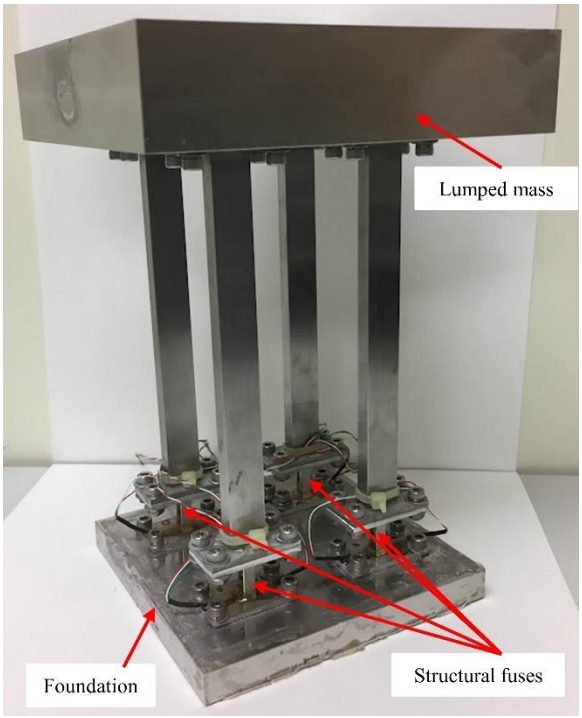

Figure 3-12. Diagram of ICSS highlighting the instrumented structural fuse locations.

3.9.4. Design of SSBRF and TSBRF

The seismic response of RFSS and ICSS informed the design of SSBRF and TSBRF. The purpose of SSBRF and TSBRF was to appropriately model the seismic behavior of a prototype bridge system built to incorporate rocking foundations. The prototype bridge configuration was selected

as a reinforced concrete single-lane bridge supported on two, two-column bents underlain by shallowly embedded square footings. The prototype bridge consisted of 8 m long spans. The bridge was assumed to be composed of a 0.05 m thick wearing coarse, underlain by a 0.2 m thick bridge deck, supported by two girders (running parallel to the bridge deck) and three diaphragms (running perpendicular to the bridge deck). To determine dead loads, member size selection was based on AASHTO 07 design examples (Purakaushal Projukti Limited, 2011), with structural components having an assumed unit weight of 24 kN/m^3 (typical of reinforced concrete). SSBRF represents one span of the prototype bridge, while TSBRF represents two spans of the prototype bridge. After determining the prototype bridge deck weight, the deck of the model bridge system was simulated by an appropriately sized aluminum plate, based on the centrifuge scaling laws presented in Table 2-2 and a target centripetal acceleration of 46g.

Figure 3-13 highlights the idealized deformation mechanisms of a bridge. A rigid connection between the column and bridge deck may create plastic hinges in these locations due to large bending moment demands as shown in Figure 3-13(a). Alternatively, plastic hinging at the deck-column connections can be mitigated by using a pin connection (Deng et al., 2012) as shown in Figure 3-13(b). Therefore, pin connections between the deck and columns were selected and modeled. The pins were constructed out of steel shoulder screws (McMaster-Carr part No. 92981A771) and orientated to allow the columns to rotate when subjected to horizontal loading in the longitudinal direction. A photograph of the fully constructed SSBRF and TSBRF physical models can be seen in Figure 3-14 and Figure 3-15 respectively. According to the figures, the bridge deck of the SSBRF is supported by two foundations, while the bridge deck of the TSBRF physical model is supported by three foundations. Across both SSBRF and TSBRF models,

foundations were sized uniformly and featured a model scale length, width, and height of 45, 45, and 10 mm, respectively.

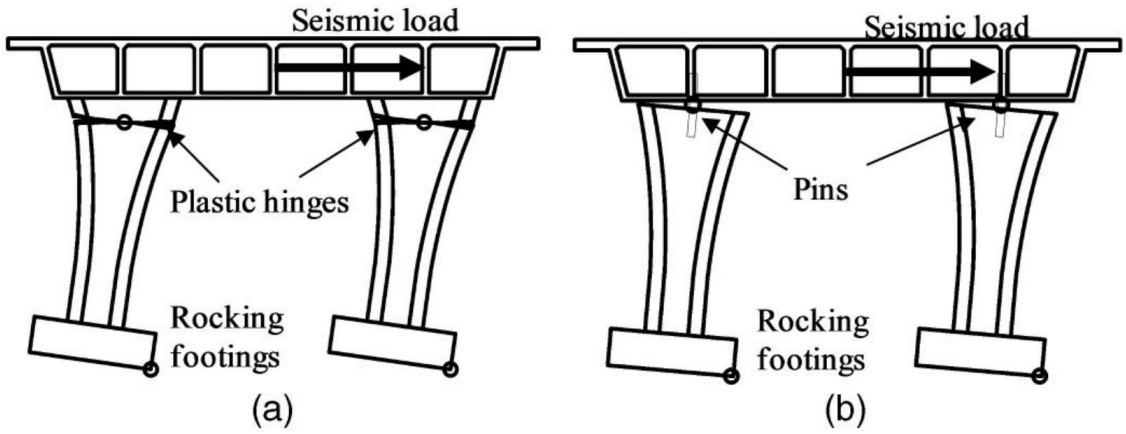

Figure 3-13. Idealized failure mechanisms of a bridge with (a) rocking foundation and column yielding at the top; and (b) rocking foundation and nonyielding column (Deng et al., 2012).

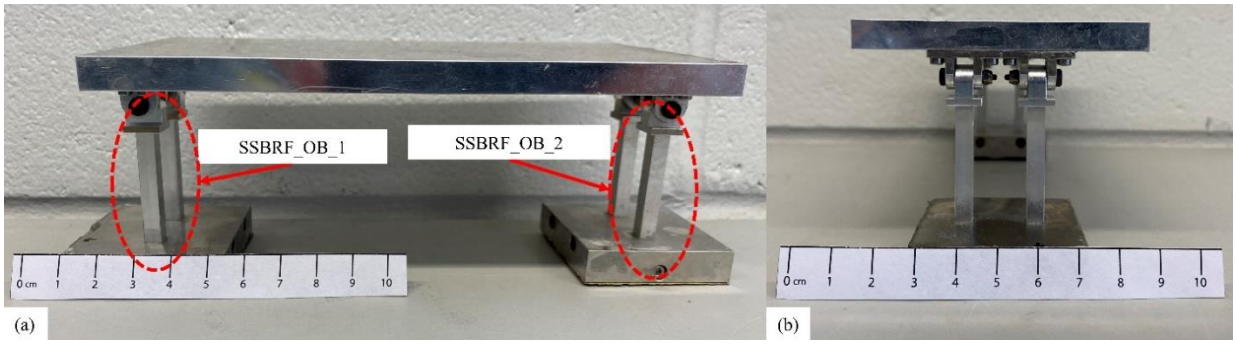

Figure 3-14. Photograph of SSBRF showing (a) front view; and (b) side view.

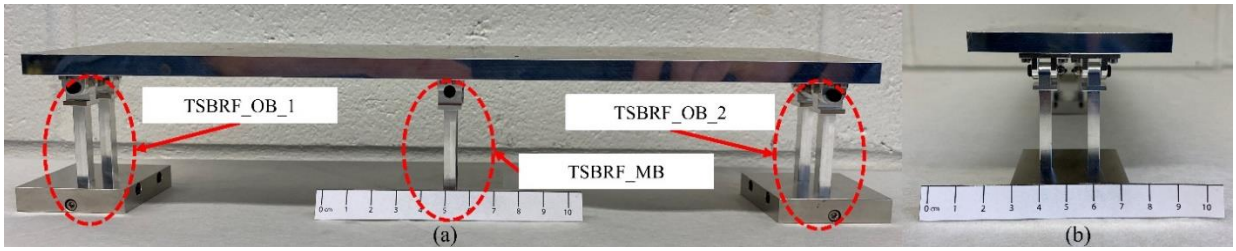

Figure 3-15. Photograph of TSBRF showing (a) front view; and (b) side view.

As the primary purpose of these model bridge systems is to simulate the behavior of a full-scale bridge supported by rocking foundations, several design criteria were implemented when designing the substructure. These criteria are similar to those implemented for the design of RFSS and include: (1) the ratio of h_{cg}/B must be greater than one to ensure a rocking dominant, rather than translation dominant, response (Gajan and Kutter 2009); (2) the moment capacity of the foundation must be less than the moment capacity of the columns; and (3) the A/A_c ratio of the foundation must be less than about fifteen to ensure a settlement dominant response, thus highlighting the influence of the soil saturation condition on foundation-level permanent deformations. When evaluating the criteria, a tributary area of the bridge deck was used to calculate the approximate vertical load applied to each bent. Bents are labeled in Figure 3-14 and Figure 3-15 according to their associated model and location. The location of the bents can be on the outer edges of the bridge deck, termed outer bent (OB) or in the middle of the bridge deck, termed middle bent (MB). Because the foundations and columns were sized uniformly and placed on a horizontal ground surface, the outer bents of the SSBRF structure (labeled SSBRF_OB_1 and SSBRF_OB_2 in Figure 3-14) were assumed to support 50% of the total bridge deck load. Meanwhile, for the TSBRF structure, the outer bents were assumed to each support 25% of the total bridge deck load, while the middle bent (labeled as TSBRF_MB in Figure 3-15) was assumed to support 50% of the

bridge deck load. After the footings were sized appropriately, several safety checks were made to ensure that the columns would behave elastically during loading which included factors of safety for column yielding and buckling. It was also necessary to limit the overall height of the system to within a reasonable range accounting for the overhead clearance available in the centrifuge. Table 3-5 highlights the main properties of the SSBRF and TSBRF physical models considered throughout the design and analysis. Except for the shoulder screws (constructed of stainless steel), the remainder of SSBRF and TSBRF was constructed of aluminum.

Table 3-5. Properties of the SSBRF and TSBRF models in the prototype scale.

	Physical Model	
Property	**SSBRF**	**TSBRF**
Height of structure, H (m)	3.04	3.04
Foundation width, B (m)	2.07	2.07
Embedment depth, D_f (m)	0.46	0.46
Bearing pressure, q (kPa)	77	77/108*
Total Mass of structure, $M_{s,t}$ (Mg)	67.8	115.1
Mass moment of inertia, I (M$g \cdot m^2$)	49.9	49.9/68.3*
Translation mode foundation radius, r_u (m)	1.17	1.17
Rotational mode foundation radius, r_θ (m)	1.18	1.18
Fixed-base fundamental period T (s)	0.26	0.26
Fixed-base damping ratio, β (%)	5.07	5.41

*Note: Mass moment of inertia and bearing pressure for TSBRF is given for both outer and middle bent locations in the form: outer/middle

3.10. SELECTION OF INPUT GROUND MOTIONS

Two naturally occurring ground motions were selected for use in this research. Selected motions were chosen from horizontal recordings of two well-known historical earthquakes to study the influence of input motions with different characteristics. These motions include the Northridge, 1994 moment magnitude (M_w) 6.7 earthquake, recorded at Newhal W Pico Canyon and the 1999 M_w7.6 Chi-Chi earthquake, recorded at TCU station. The 1994 Northridge earthquake occurred

on January 17, 1994, in the San Fernando Valley region of Los Angeles, California. This earthquake resulted in 57 fatalities, more than 9000 injuries, and property damage between $24-93 billion (2023 US dollars), making it one of the costliest natural disasters in the history of the United States (Bartholomew, 2014). The selected recording of the Northridge earthquake is denoted WPI throughout the remainder of this dissertation.

The 1999 Chi-Chi earthquake occurred on September 21, 1999, in Jiji, Nantou County, Taiwan. The highest peak ground acceleration recorded during this earthquake was 1.92 g. At one station, a peak ground velocity of 300 cm/s was recorded, this was the highest recorded velocity ever achieved by an earthquake. The 1999 Chi-Chi Taiwan earthquake resulted in 2489 fatalities, 11305 injuries, and $18 billion dollars in damage (2023 US dollars) (Shin & Teng, 2001; Tsai et al., 2001). The selected recording of the Chi-Chi earthquake is denoted TCU throughout the remainder of this dissertation.

The characteristics of the TCU and WPI ground motions are highlighted in Table 3-6. The table suggests that the ground motion parameters between the motions varied, especially in terms of PGA, mean period, and Arias intensity. Therefore, it is expected that a different seismic response will be observed when soils and structures are subjected to WPI and TCU motions.

Table 3-6. Comparison of the ground motion properties estimated from the recorded acceleration time histories of the Northridge 1994 and Chi-Chi 1999 earthquakes.

Target seismic Event	**Event ID**	**Year**	**PGA (g)**	**Mean Period, T_m (s)**	**Arias Intensity, I_a (m/s)**	**Significant Duration, D_{5-95} (s)**
Northridge	WPI	1994	0.26	0.79	2.32	26.1
Chi-Chi	TCU	1999	0.45	0.43	5.79	25.94

Throughout the design of the physical models, the response spectra of the TCU and WPI input motions were used to predict the seismic performance and demand of the structures. The 5% damped response spectra of the TCU and WPI motions are shown in Figure 3-16(a-d). Each subplot shows the response spectra of the input motions when scaled to different PGA values. For example, Figure 3-16(a) shows the response spectra when the motions are scaled to a PGA of 0.1g, while Figure 3-16(d) provides the response spectra when motions are scaled to 0.4g. The range of PGAs shown in this figure (0.1 to 0.4g) reflects the general range of the input motion amplitudes targeted throughout the experiments presented hereafter. The figure also highlights the fixed-base fundamental period of each structure (also provided in Table 3-4 and Table 3-5). This figure shows the influence of the motions on the peak response of the physical models, provided the motions are scaled to uniform PGAs. The figure suggests that the peak response of RFSS when subjected to WPI motion will be greater than the response observed when this physical model is subjected to TCU motion. In contrast, the peak response of SSBRF, TSBRF, and ICSS will be about the same across both motions. Furthermore, the figure suggests that SSBRF and TSBRF may experience resonance when subjected to both TCU and WPI input motions. In this research, input motions were scaled to different PGA values, thus this analysis provides a first-order approximation of the seismic response variation of the structural systems across the motions. It is important to note that this analysis neglects the variation in motion properties due to site-response, the performance of the hydraulic shake table, and the non-linear response of the soil-foundation and structural systems observed in this research.

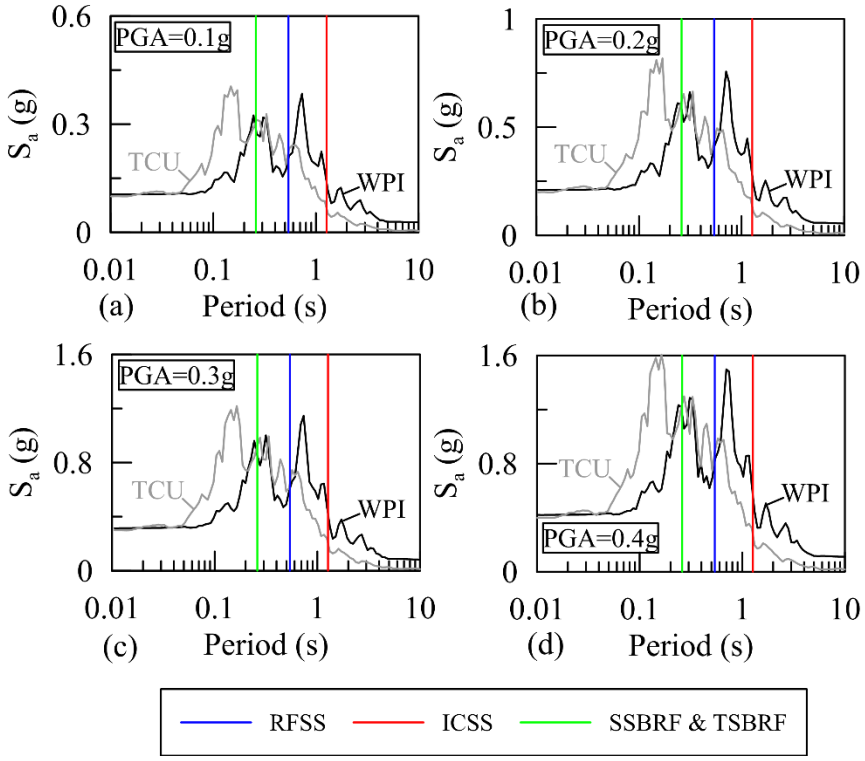

Figure 3-16. Comparison of the 5% damped spectral accelerations of the TCU and WPI input motions when acceleration time histories are scaled to several PGAs (a) scaled to PGA of 0.1g, (b) scaled to PGA of 0.2g, (c) scaled to PGA of 0.3g, and (d) scaled to PGA of 0.4g. Colored vertical lines indicate the fixed-base fundamental periods of each physical model.

3.11. SUMMARY

The geotechnical centrifuge system and equipment used to perform experiments in this research were introduced in this chapter. Furthermore, the soil material properties, specimen preparation techniques, and specimen saturation techniques used throughout the centrifuge experiments were presented. Finally, the design and construction of the physical models and the choice of input ground motions were explained.

CHAPTER 4

PERFORMANCE OF ROCKING FOUNDATIONS ON UNSATURATED SOIL LAYERS WITH VARIABLE GROUNDWATER LEVELS

4.1. ABSTRACT

An emerging foundation design scheme, termed rocking foundation, has the potential to limit loads transmitted to the superstructure, with the potential trade-off of increased settlements and rotations at the foundation level. These soil deformations can be significant for foundations with low vertical bearing capacity factors of safety. In this chapter, a set of dynamic centrifuge tests was performed to assess the response and to develop design considerations for a rocking foundation embedded in soil with varying degrees of saturation. Degree of saturation-dependent foundation design procedures are developed to predict moment capacities and initial rotational stiffness. Experimental data were used to validate the reliability of these procedures, regardless of the degree of saturation in the underlying soil. As the degree of saturation reduced, the moment capacity of the foundation increased, potentially increasing the load transmitted to the superstructure. Further,

foundation settlements and rotations in the saturated soils can be reduced by lowering the water table depth in the underlying soil layer, beneficial to the performance of rocking foundations. Consequently, the degree of saturation of the supporting soil should be considered in the foundation design to predict the foundation settlement-rotation response and to properly assess the superstructure ductility demands.

4.2. INTRODUCTION

Current building codes and design guidelines limit strength mobilization to above-ground structural members, while recommending a primarily elastic response for geotechnical components; thus, not taking full advantage of nonlinear soil-foundation-structure interaction (Stewart et al., 2003). In an emerging design strategy, termed *foundation rocking* or *rocking isolation*, the foundation is under-designed to promote soil yielding at the foundation-soil interface, shifting the ductility demand away from the superstructure (Anastasopoulos et al., 2010, 2014; Antonellis & Panagiotou, 2013; Figini & Paolucci, 2017; Gazetas, 2015; Hung et al., 2011; Kokkali et al., 2014; Loli et al., 2014). Although inelastic foundation response may improve structural performance during seismic loading (Bilotta et al., 2015; Heron et al., 2015; Housner, 1963), rocking isolation-based designs may come at the cost of increased settlements and rotations at the foundation level especially for foundations with relatively small vertical bearing capacity factors of safety ($F_v < 15$) (Deng & Kutter, 2012). Unsaturated soils (often referred to as partially saturated soils) present a unique condition in which inter-particle suction stresses may increase the stiffness of the soil underlying the foundation compared to that in dry and saturated conditions, thereby limiting unwanted foundation settlements and rotations. This chapter aims to evaluate the effect of unsaturated soils on the performance and design of a rocking foundation placed on soil

layers with different water levels, in terms of settlements, rotations, overturning moments, soil-structure interaction, and energy dissipation characteristics.

Recent studies on the response and implementation of rocking foundations have indicated that the foundation theoretical ultimate moment capacity, $M_{c,foot}$, is a main factor governing the energy dissipation at foundation level (Gajan et al., 2005; Gajan & Kutter, 2008; Kutter et al., 2016). The value of $M_{c,foot}$ is related to the contact area between the soil and foundation throughout the foundation rocking. For example, Gajan & Kutter (2008) evaluated the performance of rocking foundations using geotechnical centrifuge and found a correlation between the footing contact area required to support the vertical loads, known as the critical contact area (A_c), and the foundation moment capacity, energy dissipation, and permanent settlement. A_c in their formulation depends on the foundation factor of safety, F_v. When F_v is sufficiently large permanent foundation settlements are small; thus, settlements can be significant in lower F_v values. Past studies have shown that soil improvement through ground densification, installing concrete pads around footings, and utilizing foundation rocking in combination with underlying unattached piles can reduce the permanent settlement and residual rotations of the foundation caused by rocking (Allmond & Kutter, 2014b; Deng & Kutter, 2012; Kokkali et al., 2015; Tsatsis & Anastasopoulos, 2015).

Most previous experimental and numerical analyses on rocking isolated designs have focused on foundations placed on, or shallowly embedded in, dry and saturated sand and clay deposits. However, a growing body of research provides evidence that unsaturated soils may prove beneficial for implementation and consideration in rocking isolated designs (Antonellis et al., 2015). The behavior of unsaturated soils differs from both dry and saturated soils due to the presence of inter-particle suction stress, which increases the effective stress and changes the

dynamic properties of soils. For example, while unsaturated soils may have higher shear stiffness, they have lower damping when compared to dry and saturated soils (Biglari et al., 2011; Ghayoomi et al., 2017; Ghayoomi & McCartney, 2011; Hoyos et al., 2015; Le & Ghayoomi, 2017). Further, the degree of saturation and water table elevation in soil layers could impact the seismic site response (D'Onza et al., 2008; Mirshekari & Ghayoomi, 2017), seismic compression (Duku et al., 2008; Ghayoomi et al., 2011; Ghayoomi et al., 2013; Mousavi & Ghayoomi, 2021b; Stewart et al., 2004; Yee et al., 2014), seismic foundation response (Borghei et al., 2020; Ghayoomi et al., 2018), and liquefaction potential (Eseller-Bayat et al., 2013; Mousavi & Ghayoomi, 2021a; Okamura & Soga, 2006; Unno et al., 2008; Yegian et al., 2007; Yoshimi et al., 1989). Given the impact of the degree of saturation on the dynamic soil properties, water table fluctuation should be considered in evaluating the performance of the rocking isolated structures and the foundation design. Specially, the increased stiffness associated with unsaturated soils may mitigate the excessive settlements and rotations expected in rocking foundations.

Results from a series of dynamic centrifuge experiments are presented in this chapter to evaluate the performance of a rocking isolated design when embedded in a soil layer with varying water table depths. The results are presented in terms of residual free-field settlements (Δ_{FF}), residual foundation settlements (Δ_{SF}), peak (θ_P) and residual (θ_R) foundation rotations, accumulated work done by foundation rocking (δW), maximum foundation overturning moment (M_{max}), and frequency-dependent motion amplification. Additionally, procedures are developed to predict the value of $M_{c,foot}$ and the initial rotational stiffness of a foundation embedded in unsaturated soils. Predicted values are then compared with the experimental results to assess the quality of the proposed approaches. The goal of this study is to assess the effects of soils' degree of saturation

on the performance of a rocking foundation and to develop strategies for considering the mechanics of unsaturated soils in the design.

4.3. DESIGN OF MODEL STRUCTURE

A physical model, termed Rocking Foundation Structural System (RFSS), was designed and constructed to represent the target prototype structure in 46-g acceleration. The design and construction of the physical model are presented in Chapter 3, Section 3.9. The system is represented by a completely elastic, slender, single-degree-of-freedom physical model, shown in Figure 4-1, with properties tabulated in Table 3-4.

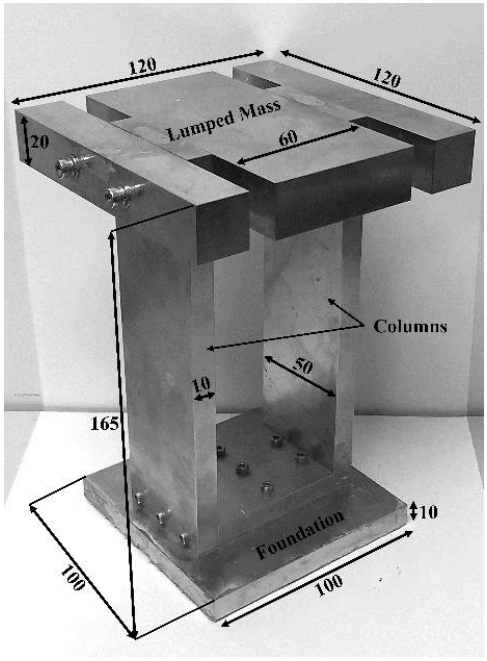

Figure 4-1. A photograph of the RFSS annotated with model scale dimensions, in mm.

4.4. GEOTECHNICAL CENTRIFUGE

The experiments were performed at the Geotechnical Centrifuge Center at the Disaster Prevention Research Institute, Kyoto University. The geotechnical centrifuge and laminar container used in this research are discussed in Chapter 3, Sections 3.2 and 3.3, respectively.

4.5. SOIL MATERIAL AND EXPERIMENTAL SETUP

Silica No. 9 sand, presented in Chapter 3, Section 3.4,was used in this research. The specimens were prepared using a dry pluviation technique at a void ratio of 0.81 and density of 1463 kg/m^3. When the height of the soil profile reached the depth of the foundation a physical model was placed on the surface of the soil layer, then the pluviation was continued until the desired soil profile height was reached. Front and side elevation views of the experimental setup can be seen in Figure 4-2(a) and (b) highlighting locations of the instrumentation arrays. A photograph of the fully assembled experimental setup can be seen in Figure 4-3.

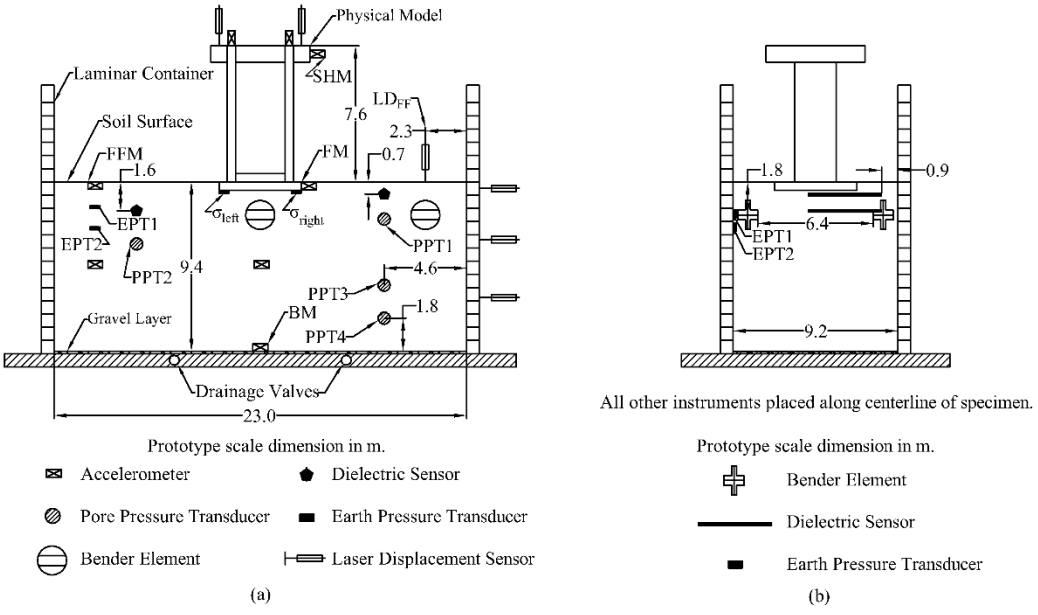

Figure 4-2. Schematic and instrumentation layout of a typical centrifuge experiment conducted in this chapter. (a) Front elevation view; (b) side elevation view.

Six profiles of degree of saturation in depth were investigated in this study by altering the water table level in the soil; i.e. a dry, a fully saturated, and four mixed unsaturated-saturated layers. Fully saturated and unsaturated soil layers were saturated according to Chapter 3, Section 3.7. Then, the laminar container was placed on the shake table and spun to the target centripetal acceleration of 46-g at the soil surface. The water table elevation was lowered in unsaturated soil layers, in flight, to the desired level using the method described in Chapter 3, Section 3.8. The depth of the water table was monitored using an array of pore pressure sensors located in the soil profile as shown in Figure 4-2(a). Table 4-1 describes the experiments' initial conditions, which slightly changed throughout testing due to soil densification. The target water table depths are presented as normalized depths using the D_w/B ratio, where D_w is the depth of the water table below the surface of the soil layer and B is the width of the foundation in the direction of shaking. The specimens are labeled as ML_D for dry experiments and ML_WL_#B for saturated or unsaturated experiments where # indicates D_w, as a function of B.

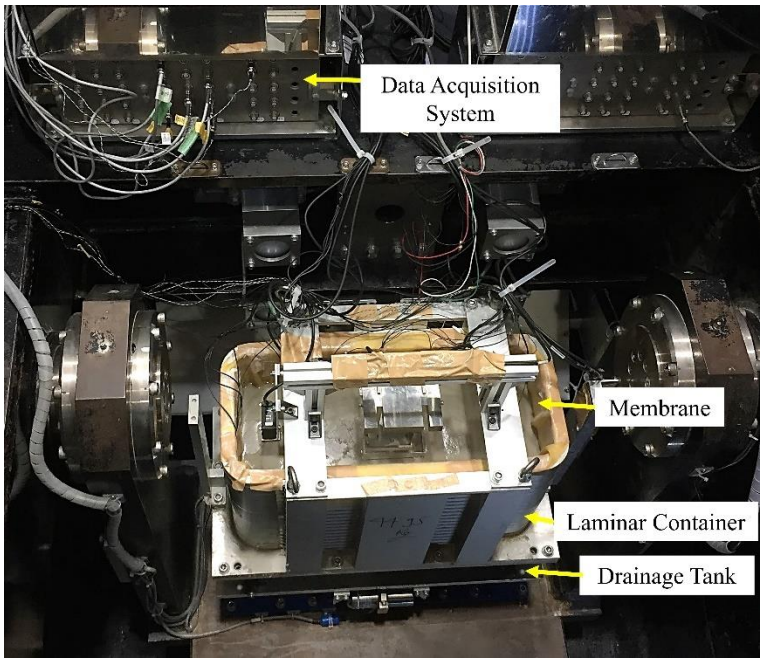

Figure 4-3. A photograph of the completely constructed experimental setup.

Table 4-1. Description of dynamic centrifuge experiments conducted in this chapter and specific parameters related to the specimen and foundation determined prior to WPI01 motion application.

Specimen Name	**Fluid**	D_w/B	A/A_c
ML_D	Dry	N/A	2.96
ML_WL_0.02B	Water	-0.02	2.31
ML_WL_0.24B	Water	0.24	2.66
ML_WL_0.44B	Water	0.44	3.15
ML_WL_1.00B	Water	1.00	4.00
ML_WL_1.52B	Water	1.52	4.34

Note: A positive D_w/B indicates that the groundwater table is below the soil surface, while a negative number shows that the groundwater table is above the soil surface.
The experiments were conducted at 46-g centripetal acceleration at the soil surface.

The capillary rise mechanism controlled the degree of saturation profile above the water table, where ψ_m and S correlate through the SWRC. The SWRC of the Silica No. 9 sand, shown in Figure 3-3(b), was determined using dielectric sensors placed at specific locations in unsaturated zones above the water table in the soil to measure the degrees of saturation, while the matric

suctions were estimated using the scaled height and assuming hydrostatic conditions (Mirshekari et al., 2018).

4.6. GROUND MOTION SEQUENCE

A series of scaled earthquake excitations were applied to the base of the laminar container using the one-dimensional shake table installed on the centrifuge platform. Selected motions were chosen from horizontal recordings of two historical earthquakes to study the effects of input motions with diverse characteristics (Ghayoomi & Dashti, 2015). Comparisons of the input motions and the order in which they were applied can be seen in Table 4-2. The M_w 6.7 Northridge, 1994 earthquake, recorded at Newhal W Pico Canyon, was used for the WPI input motions. The M_w 7.6 Chi-Chi, 1999 earthquake, recorded at TCU station was used for the TCU input motion. Although a total of five motions were applied, one was a control repeat test, and the results of only four motions are discussed herein, which include WPI01, TCU, WPI02, and WPI03; the WPI motions differ in intensity. Figure 4-4 compares the input PGA and input Arias Intensity (I_a) of the motions for ML_WL_0.02B and ML_D specimens, demonstrating that the shake table was able to produce similar seismic motions regardless of the mass of the specimen under different saturation scenarios. Acceleration time histories and 5% damped spectral accelerations (S_a) curves of the input motions achieved during experiment ML_D are shown in Figure 4-5 and Figure 4-6, respectively.

Table 4-2. Ground motion parameters as recorded at the base of the laminar container for ML_WL_0.02B specimen.

Order of Applied Motions	Target seismic Event	Event ID	PGA (g)	Mean Period (s)	Arias Intensity (m/s)	Significant Duration, D_{5-95} (s)
1	Northridge	WPI01	0.09	1.0	0.24	26.5
2	Chi-Chi	TCU	0.10	0.74	0.30	26.8
3	Northridge	WPI02	0.15	0.99	0.78	26.8
4	Northridge	WPI03	0.29	1.0	2.17	21.1
After each excitation, the specimens were excited with the next motion after at least 140 minutes in the prototype scale (≈3 minutes in the model scale), to let excess pore water pressure dissipate sufficiently.						

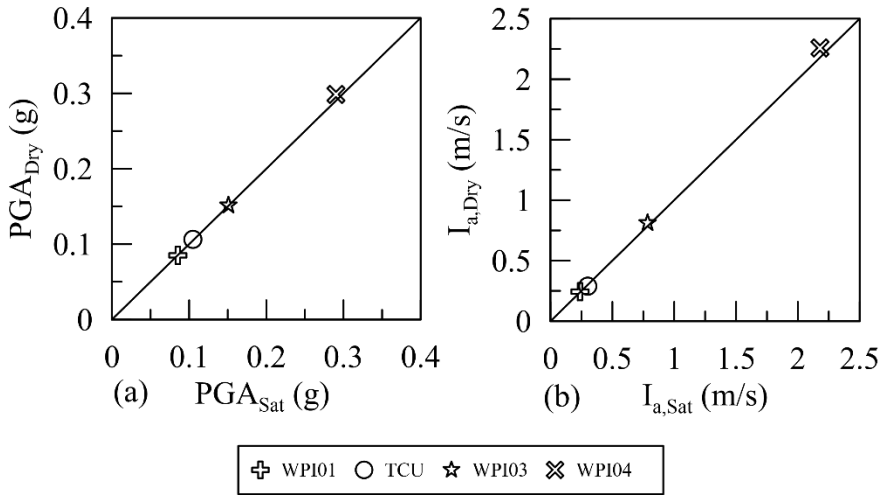

Figure 4-4. Comparison of input motion intensity parameters across specimen ML_WL_0.02B and ML_D with respect to (a) PGA and (b) maximum Arias Intensity.

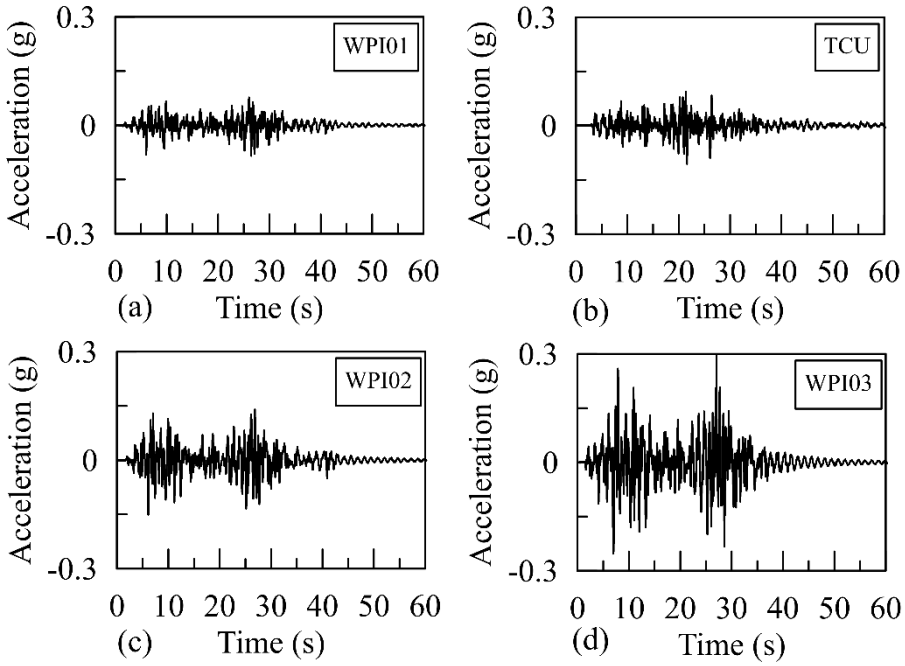

Figure 4-5. Comparison of the input motion acceleration time histories recorded during experiment ML_D. Each subplot corresponds to one input motion.

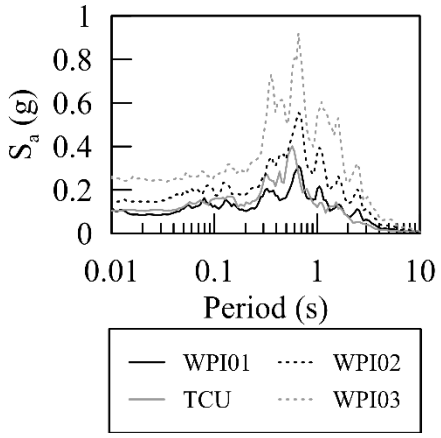

Figure 4-6. Response spectra of the recorded input motions during experiment ML_D (5% damped spectral accelerations versus period).

4.7. DEGREE OF SATURATION-DEPENDENT FOUNDATION DESIGN CONSIDERATIONS

Results of the experiments were analyzed to determine the effect of the groundwater table on the seismic response of the soil-foundation-structure system and to develop procedures for considering unsaturated soil effects in foundation design. The water table depth could slightly change after each motion due to soil densification, and this small change has been considered in the analysis. Parameters and results discussed throughout the remainder of this chapter are presented in prototype scale.

4.7.1. Theoretical ultimate moment capacities

When the overturning moment, M, experienced by a foundation converges to the ultimate moment capacity of the foundation, $M_{c,foot}$, soil yielding occurs under the leading edge of the foundation. Reliable estimation of $M_{c,foot}$ is necessary in the design of a rocking foundation. The formula, proposed by Gajan & Kutter (2008), for determining the ultimate moment capacity of a footing embedded in soil can be seen in Equation 2-13.

Deng & Kutter (2012) compared the experimental ultimate moment capacities of rocking foundations subjected to slow cyclic and dynamic loading and found reliable prediction accuracy of Equation 2-13 regardless of the loading condition. Owing to the change in unit weight and the presence of suction-induced apparent cohesion in unsaturated soils, the shear strength of an unsaturated soil differs from that of dry and saturated conditions. This section discusses a procedure which can be used to predict the value of $M_{c,foot}$ when a foundation is embedded in an unsaturated soil layer. The procedure is then verified against experimental results.

The value of A_c in Equation 2-13 is the contact area between the foundation and the soil, necessary to make $F_v = 1$. Therefore, the value of A_c is a function of the ultimate bearing capacity of the foundation, q_u. For saturated and dry soils, q_u was determined using the classical bearing capacity equation shown in Equation 4-1 with the corresponding factors for bearing capacity, depth (Hansen, 1970) and shape (Vesic, 1973).

$$q_u = c'\lambda_{cs}\lambda_{cd}N_c + q_o\lambda_{qs}\lambda_{qd}N_q + 0.5\lambda_{\gamma s}\lambda_{\gamma d}\gamma_{avg}BN_\gamma \qquad 4\text{-}1$$

where c' is the effective cohesion of the soil (equal to zero), q_o equals the overburden pressure at the depth of the foundation, λ_{cs}, λ_{qs}, $\lambda_{\gamma s}$ are shape factors, λ_{cd}, λ_{qd}, $\lambda_{\gamma d}$ are depth factors, and N_c, N_q, N_γ are bearing capacity factors. The unit weight of the soil at the depth of the foundation, γ, was modified to γ_{avg} to account for the depth of the water table according to the conditions given in Equation 4-2 (Das, 2010).

$$\gamma_{avg} = \begin{cases} \gamma' & for\ D_w \le D_f \\ \frac{1}{B}\left[\gamma(D_w - D_f) + \gamma'\left(B - (D_w - D_f)\right)\right] & for\ D_f < D_w \le B + D_f \\ \gamma & for\ D_w > B + D_f \end{cases} \qquad 4\text{-}2$$

where γ' is the effective unit weight of the soil and D_f is the foundation embedment depth that is equal to 0.46 m. Note for dry soil, $\gamma_{avg} = \gamma$.

Modifications to Equation 4-1 accounting for the increased shear strength generated by the matric suction in unsaturated soils have been proposed by several researchers (Fredlund & Rahardjo, 1993; Oloo et al., 1997; Vanapalli et al., 1996). For this study, the technique proposed by Vanapalli & Mohamed (2007) was employed to predict the contribution of matric suction on the bearing capacity of the unsaturated soils by modifying the first term in Equation 4-1 as shown in Equation 4-3.

$$c'\lambda_{cs}\lambda_{cd}N_c = \left[c' + \alpha\left(1 - {S_{avg}}^{\eta}\right)tan\phi' + \psi_{m,avg}{S_{avg}}^{\eta}tan\phi'\right]\lambda_{cs}\lambda_{cd}N_c \quad 4\text{-}3$$

where $\psi_{m,avg}$ and S_{avg} are the average values of ψ_m and S within the depth range of D_f and D_f+1.5B, η is a bearing capacity fitting parameter equal to 1 for non-plastic soils (Vanapalli & Mohamed, 2007), and ϕ' is the effective friction angle of the soil, equal to 38°. Vanapalli & Mohamed (2007) verified this formulation by subjecting model square footings to static vertical loads. Based on this formulation and given the foundation pressure, F_v values ranging from 2.25 to 4.32 were estimated, depending on the degree of saturation of the foundation soil.

An extension of the iterative procedure, employed by Deng & Kutter (2012), was used to find A_c for the foundation. The value of A_c was determined by iteratively adjusting the value of B to converge to the critical contact width of the foundation, B_c, required to make the F_v equal to 1. Iteration was necessary as the values of the shape, depth, and bearing capacity factors are all functions of B. It is worth noting that γ_{avg}, $\psi_{m,avg}$, and S_{avg} were assumed constant based on the total width of the foundation and not updated based on the value of B_c. Finally, the values of $M_{c,foot}$ were determined using Equation 2-13. Due to the shallow foundation embedment depth and the smooth sides of the foundation, the terms with P_P and F were approximately neglected as they only account for less than 1% of the moment capacity of the foundation regardless of water table condition. For the specimens in this research, the values of $M_{c,foot}$ determined prior to WPI01 motion are presented as a function of D_w/B in Figure 4-7. As the depth of the water table increases from zero in fully saturated condition, $M_{c,foot}$ increases due to the increased value of γ_{avg} and additional matric suction in the unsaturated soil. It should be noted that the value of ϕ' was determined by back calculating the experimental maximum overturning moment, M_{max} experienced by the foundation during WPI03 for specimen ML_D.

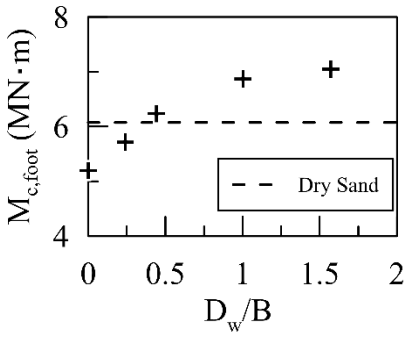

Figure 4-7. Comparison of the analytical ultimate moment capacity of the foundation as a function of the normalized depth of the groundwater table determined prior to applying WPI01 motion.

To evaluate the performance of the proposed methodology for estimating $M_{c,foot}$ in unsaturated soils, the values were compared with M_{max} values found throughout the loading. M_{max} values were determined by finding the maximum absolute value of the moment experienced at the base center point of the foundation, M, during each shaking event for all soil saturation conditions. M was determined using Equation 4-4, derived by Gajan & Kutter (2008), by simultaneous use of accelerometers and displacement sensors.

$$M = M_s a_x \cos\theta_f h_{cg} + M_s\left(g + a_y\right)\sin\theta_f\, h_{cg} + I a_{xy} \qquad 4\text{-}4$$

where M_s is the mass of the structure supported by the foundation, g is the acceleration due to gravity, a_x and a_y are the horizontal and vertical components of acceleration of the structure, a_{xy} is the angular acceleration of the structure, θ_f is the foundation rotation, and I is the mass moment of inertia of the structure about its center of gravity. The terms in this equation account for the vertical, lateral, and moment forces acting on the base center point of the foundation.

The relatively stronger intensity of WPI03 motion allowed the moment experienced by the foundation to converge to a maximum value where the foundation continued to rotate without a

change in the applied M. Figure 4-8 displays M_{max} values for WPI03 motion normalized by the theoretical $M_{c,foot}$ values, plotted with respect to the water table ratio. During WPI03 motion the structural mass rotated outside the range of the vertical laser displacement sensors for specimen ML_WL_0.02B, therefore, M_{max} are reported as maximum values prior to range exceedance. Considering the limitations of the testing conditions considered herein, the experimental results suggest that the moment capacity of a foundation embedded in unsaturated soil is reliably predictable. The percent errors between the theoretical ultimate moments and the analytical values were found to be up to about 10%, consistent with results presented by Gajan & Kutter (2009). It is believed that the abovementioned error may be associated with the assumptions used in predicting the $\psi_{m,avg}$ value below the footing and the omission of dynamic effects in the F_v calculation which have been shown to reduce soil bearing capacity (Kumar & Rao, 2002; Paolucci & Pecker, 1997; Richards et al., 1993). According to Equation 2-13, this bearing capacity reduction would lead to a corresponding reduction in $M_{c,foot}$, the quantification of which requires further research.

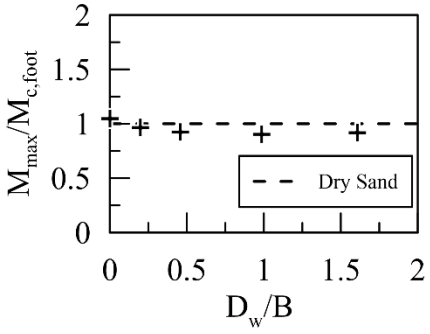

Figure 4-8. Normalized maximum overturning moment experienced by the foundation during WPI03 motion plotted as a function of the normalized depth of the groundwater table.

The water table elevation at a specific site fluctuates both seasonally and yearly. To evaluate the uncertainty of assuming a fully saturated soil layer when evaluating the $M_{c,foot}$ of a foundation embedded in an unsaturated soil the percent difference values, $\delta(\%)$, of the experimental M_{max}, found between the specimens having the groundwater table at the surface of the soil and the specimens having the groundwater table located below the soil surface, were calculated. These comparisons were made for the results of WPI03 motion and are displayed as a function of the water table depth ratio in Figure 4-9. As the depth of the groundwater table increased, percent difference values increased, almost linearly. These results suggest that designing a rocking foundation based on a saturated soil condition while the actual water table is located at a depth below the foundation may lead to an unanticipated underestimation of the strength or capacity at the soil-foundation level, imposing greater demand on the superstructure.

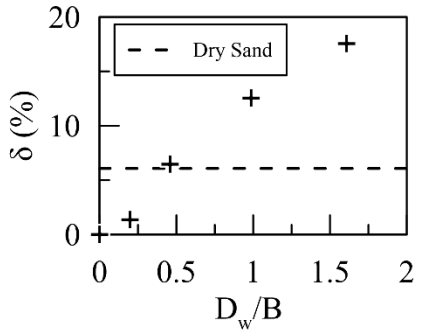

Figure 4-9. Percentage difference between experimental maximum overturning moments for the specimen having the groundwater table at the soil surface with those for the specimens having the groundwater table below the soil surface during WPI03 motion.

4.7.2. Initial rotational stiffness

The initial rotational stiffness of a surface foundation, K_{ini}, or an embedded foundation, $(K_{ini})_e$, is a design parameter related to energy dissipated by the underlying soil during foundation rocking (Deng et al., 2014; Kokkali et al., 2014). This section provides a method for considering the change

in small-strain shear wave velocity (V_s), caused by unsaturated soil conditions and foundation overburden pressure, for use when estimating the value of $(K_{ini})_e$.

Throughout the centrifuge tests, after achieving the desired water table depth, the values of V_s at a depth of $0.4B$ from the soil surface were measured using pairs of bender elements in the free-field ($V_{s,FF}$) and beneath the center of the foundation ($V_{s,OC}$). Bender elements generate small magnitude shear waves in the soil using piezoelectric ceramics. Locations and configurations of the bender elements are shown in Figure 4-2. Values of $V_{s,FF}$ and $V_{s,OC}$ were also estimated at the same locations in the soil profile using the following procedure. First, the small strain shear modulus of the soil at depth z, $G_{max}(z)$, was estimated using the equation proposed by Hardin (1978), with the Bishop (1959) effective stress in free-field at depth z, $\sigma_v'(z)$. Specifically, Equation 4-5 was used which accounts for the increased effective stress due to matric suction in unsaturated soils.

$$\sigma_v'(z) = \sigma - u_a + \chi\psi_m \cong \sigma - u_a + S_e\psi_m \quad \text{for } \psi_m \geq 0 \tag{4-5}$$

where χ is the effective stress parameter roughly equivalent to the effective degree of saturation, S_e, given by Equation 4-6 (Lu et al., 2010; Lu & Likos, 2004).

$$S_e = \frac{S - S_r}{1 - S_r} \tag{4-6}$$

Next, the shear wave velocity at depth z, $V_s(z)$, was computed from $V_s(z) = (G_{max}(z)/\rho)^{0.5}$, where ρ is the total density of the soil at that depth given the water table location. Finally, $V_{s,OC}$ at depth z was estimated by correcting for the induced vertical stress due to the weight of the physical model at depth z using Equation 4-7.

$$V_{s,OC}(z) \approx V_{s,FF}(z)\left(\frac{\sigma_v'(z) + \Delta\sigma_v'(z)}{\sigma_v'(z)}\right)^{\frac{1}{4}} \quad 4\text{-}7$$

where $\Delta\sigma_v'(z)$ was determined using the Poulos & Davis (1974) equation for predicting the value of induced vertical stress beneath the center of a square foundation. Figure 4-10 compares the estimated and recorded values of $V_{s,FF}$ and $V_{s,OC}$ plotted as a function of S_r at the bender element depths. The maximum percent error between the estimated and recorded values of $V_{s,OC}$ was 6.0% indicating reliability of the proposed methodology over a wide range of soil saturation conditions. However, the estimation can be even further improved by using shear modulus predictive models that directly incorporate both suction and degree of saturation (Dong et al., 2016; Oh & Vanapalli, 2014).

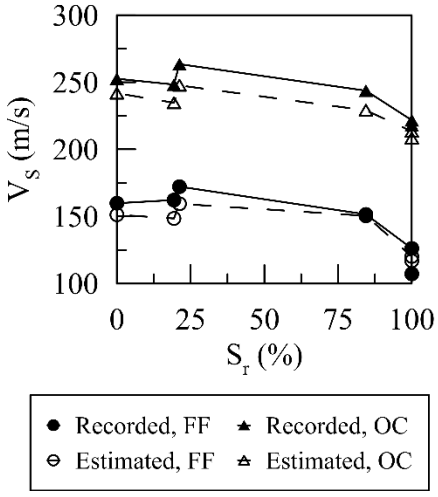

Figure 4-10. Shear wave velocities recorded and estimated in the free-field and beneath the foundation as a function of the degree of saturation of the soil.

The initial embedment-corrected rotational stiffness, $(K_{ini})_e$, of the foundation was determined using formulas adopted by ASCE 41-17 (2017) as shown in Equation 4-8 and Equation 4-9.

$$K_{ini} = \frac{G_{max,OC} B^3}{1-\nu}\left[0.4\left(\frac{L}{B}\right) + 0.1\right] \quad 4\text{-}8$$

$$(K_{ini})_e = K_{ini}\left[1 + 2.5\frac{d}{B}\left(1 + \frac{2d}{B}\left(\frac{d}{D_f}\right)^{-0.2}\sqrt{\frac{B}{L}}\right)\right] \quad 4\text{-}9$$

where $G_{max,OC}$ is the value of the overburden corrected shear modulus at the depth of the bender elements (determined from the measured $V_{s,OC}$ values), ν is the Poisson's ratio of the soil, d is the effective depth of the footing equal to D_f, and L is the length of the footing equal to B for a square foundation. Values of $(K_{ini})_e$ are presented as a function of D_w/B in Figure 4-11. $(K_{ini})_e$ increased as the depth of the water table increased until reaching a peak near $\frac{D_w}{B} \approx 0.5$ after which $(K_{ini})_e$ started to decrease. The peak value can be attributed to a combination of the slightly reduced ρ and the increased $V_{s,OC}$ of the soil when the water table was lowered to this depth. Considering a decomposed moment versus rotation diagram in foundation design, as discussed in Deng et al. (2014), the value of $(K_{ini})_e$ is vital in distinguishing between the elastic and plastic zones. The procedure described in this section provides a convenient method for considering the changes in the stiffness of an unsaturated soil layer when estimating the value of $(K_{ini})_e$.

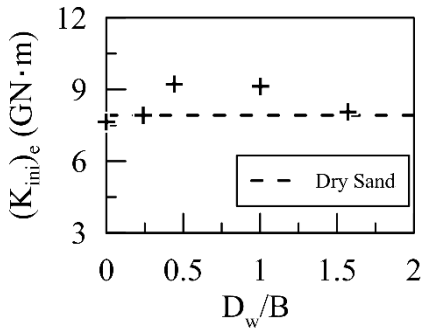

Figure 4-11. Comparison of the initial embedment-corrected rotational stiffness of the foundation as a function of the normalized depth of the groundwater table determined prior to applying WPI01 motion.

4.8. DEGREE OF SATURATION-DEPENDENT FOUNDATION SEISMIC RESPONSE

Figure 4-12 and Figure 4-13 display the overall foundation response in terms of moment-rotations, settlement-rotations, and normalized pressure-rotations for input motions WPI01 and WPI03, respectively. Foundation rotations, θ_f, and foundation settlements throughout the loading were determined using the two vertical laser displacement sensors targeting opposite sides of the lumped mass, with the foundation settlement taken as the average of the two readings. Two pressure sensors, labeled σ_{right} and σ_{left}, were placed beneath the foundation, on opposite sides, to observe the pressure variation during rocking. Pressure readings were then normalized by the initial pressure, σ_{ini}, recorded prior to WPI01 motion. The pressure sensors did not function properly during the tests on ML_WL_0.02B; therefore, results for this water table depth are omitted. Also, only the sensor labeled σ_{left} recorded the results during tests on ML_WL_1.00B.

As expected, as the water table depth increased, M values generally increased, while θ_f generally reduced. Comparisons of the two figures indicate that the moment-rotation response is nonlinear;

the foundation shows a stiffer response for the low-level input motion WPI01 while rotational stiffness degradation is apparent for input motion WPI03. This nonlinearity can be attributed to soil rounding beneath the foundation, decreasing the soil-footing contact area. For motion WPI03, S-shaped moment-rotation curves are visible, meaning that the foundation continued to rotate without a change in M. Therefore, ultimate foundation moments were mobilized during this input motion.

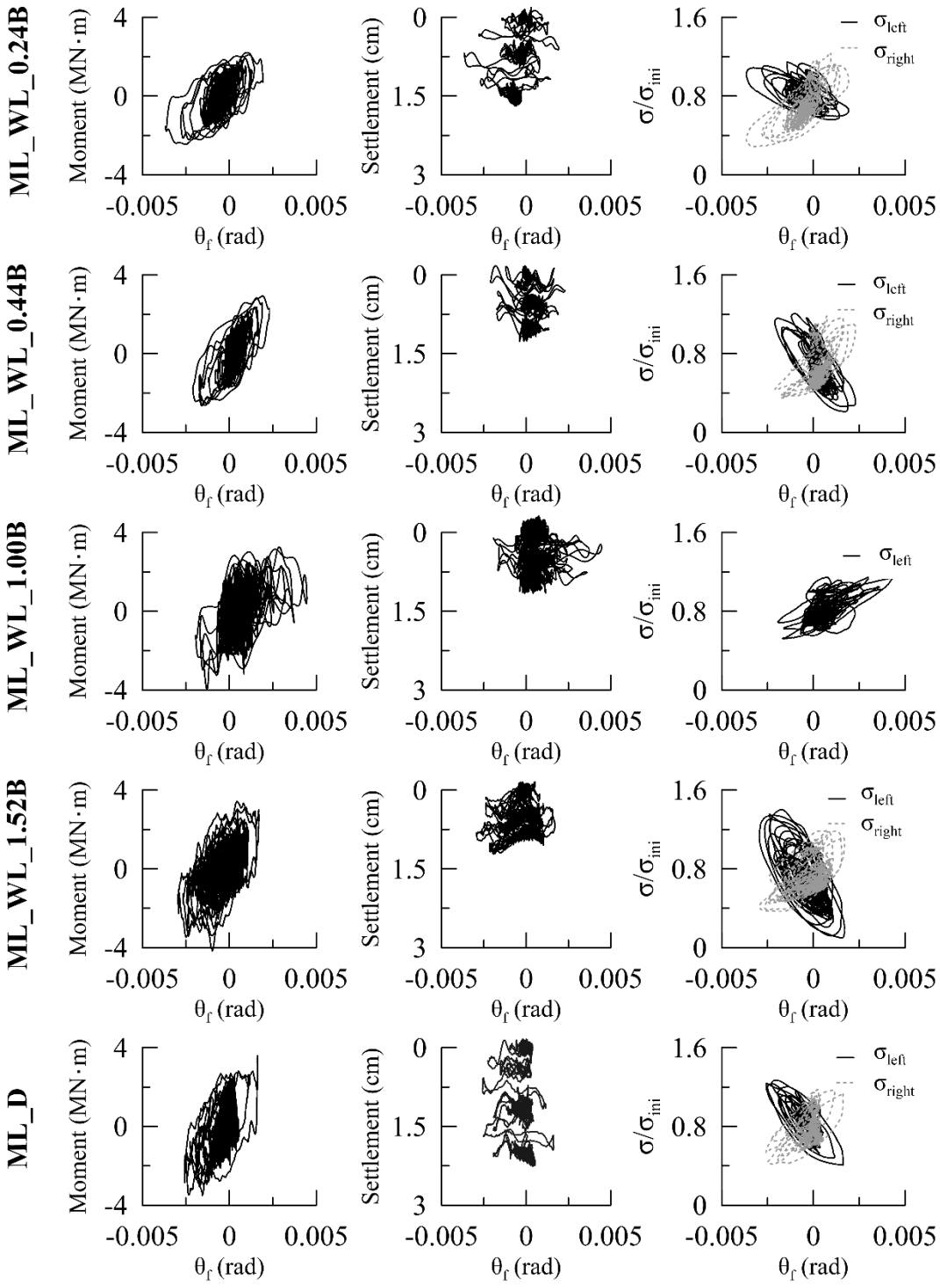

Figure 4-12. Comparison of moment, settlement, and foundation pressure as a function of foundation rotation across soil saturation conditions throughout WPI01 motion. Each row corresponds to one experiment.

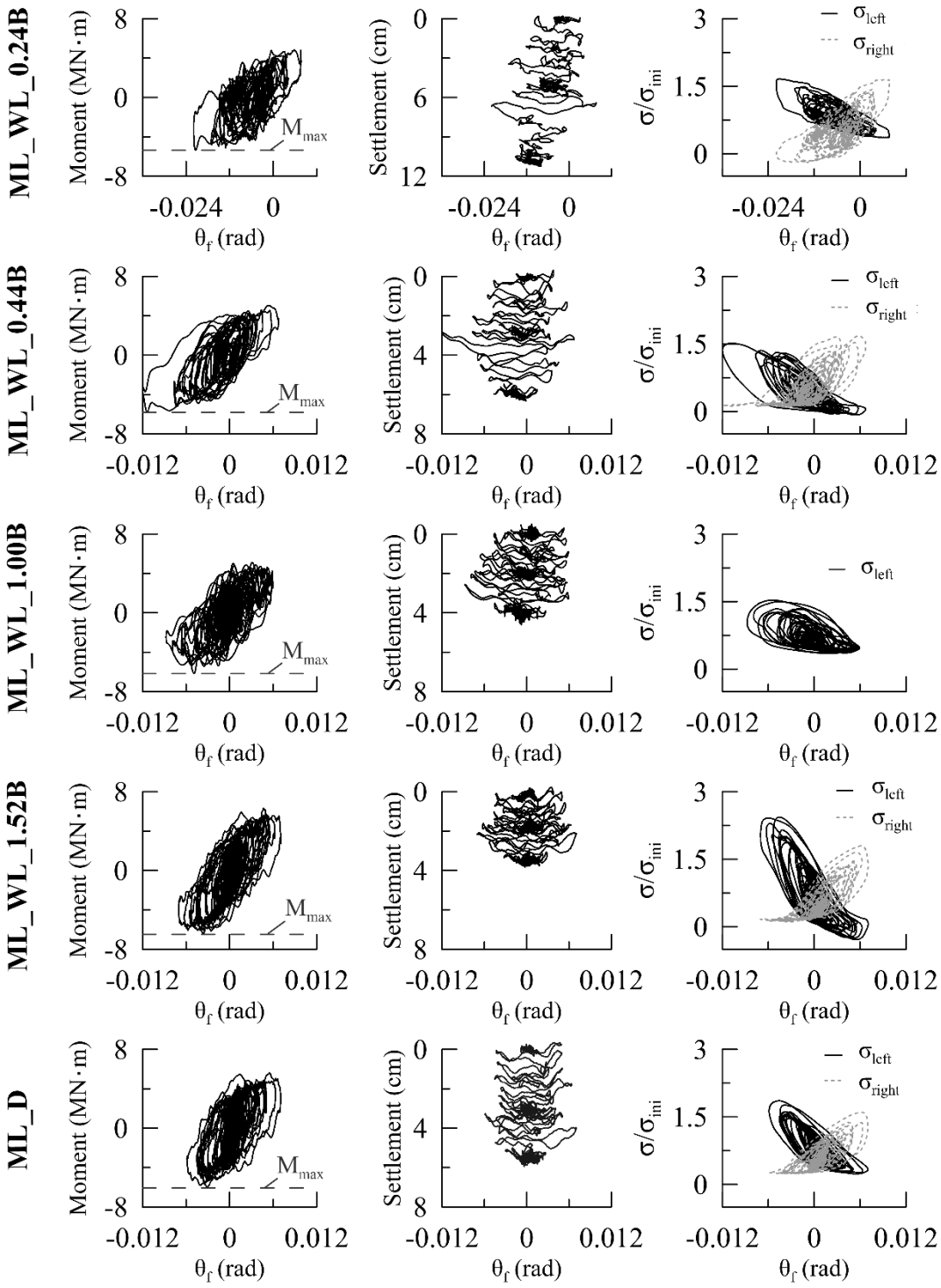

Figure 4-13. Comparison of moment, settlement, and foundation pressure as a function of foundation rotation across soil saturation conditions throughout WPI03 motion. Each row corresponds to one experiment.

Settlement-rotation plots indicate that the foundation accumulated permanent settlement throughout loading, along with some uplift as the foundation neared the peak rotations across all saturation conditions. Uplift generally increased as the depth of the water table increased, while permanent settlement followed the opposite trend. Therefore, the chance of soil yielding occurrence increased for the soil layers with shallower water table depths. Normalized pressure-rotation plots show that as the foundation rotates to a leading foundation side, the pressure on the leading-edge increases while the pressure on the opposite edge reduces; thus, foundation rocking was observed across all soil saturation conditions. As the depth of the water table increased, normalized pressure values are shown to generally increase, indicating that the leading foundation edge experiences greater soil contact, due to less soil yielding.

Absolute values of θ_R and θ_P determined for each motion can be seen in Figure 4-14. θ_P values were found by initializing the foundation rotation to zero at the start of each motion, then finding the absolute value of the maximum rotation experienced throughout the earthquake. During WPI03 motion, the structural mass rotated outside the range of the vertical laser sensors for specimen ML_WL_0.02B, therefore, θ_P are reported as maximum values prior to range exceedance. Fig. 14 indicates that lowering the water table from the fully saturated condition decreased the tendency for the foundation to experience residual rotation. Additionally, as the water table depth increased, θ_P generally reduced. The apparent cohesion of the unsaturated soil may limit the amount of soil sliding under the uplifted side of the foundation during rocking (Antonellis et al., 2015), which may have contributed to the reduced θ_R and θ_P values in the unsaturated soils compared to the saturated and, in some cases the dry. Allmond & Kutter (2014a) observed that foundations embedded in saturated soils experienced a relatively large drop in pore water pressure below the foundation during rocking. Such decrease in pore water pressure would lead to soil material being

sucked underneath the footing throughout the loading and a loss of re-centering ability. Excessive soil yielding, large decreases in pore water pressure, and low $(K_{ini})_e$ beneath the foundation in the specimen with the water table at the surface of the soil resulted in the largest θ_R and θ_P values across all motions.

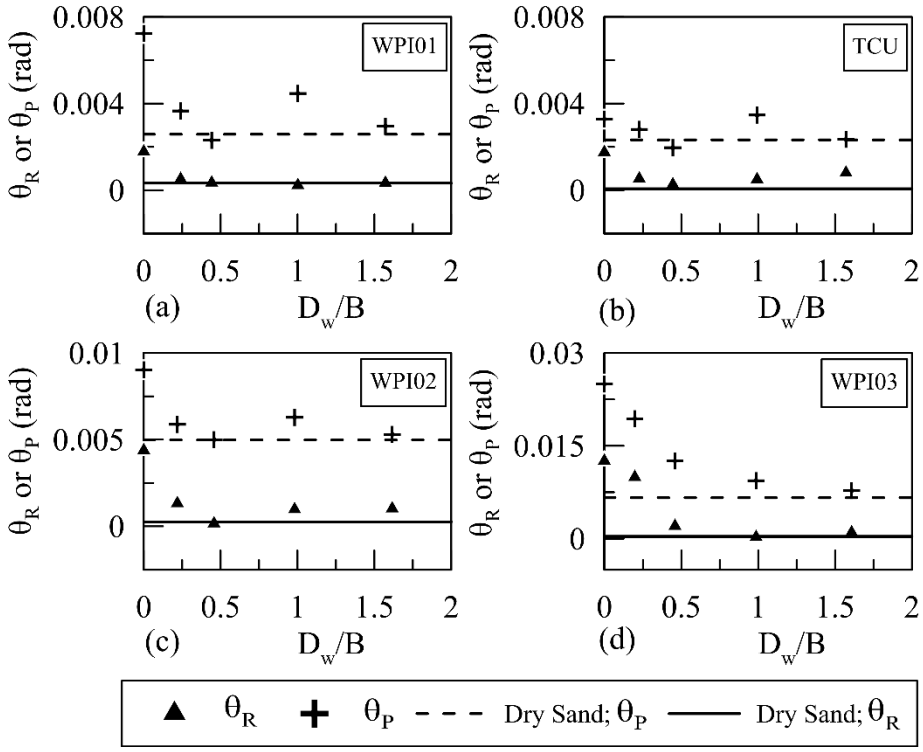

Figure 4-14. Peak and residual foundation rotations as a function of the normalized depth of the groundwater table. Each subplot shows the response during one input motion.

Δ_{FF} and Δ_{SF} values are summarized in Figure 4-15. As expected, as the water table depth increased, permanent settlements reduced, becoming less than those experienced by the dry soil layer when the normalized water table depth exceeded a value of about $0.5B$. Compared to saturated soil layers, unsaturated soils may have higher shear strength, higher shear stiffness, and experience a reduction in seismically induced pore-water pressures. In general, as the depth of the water table increased a greater percentage of the soil profile thickness was in a state of partial

saturation, while the percentage of the soil in the fully saturated condition reduced. Therefore, as the depths of the water table increased, the thickness of the saturated soil layer reduced while the unsaturated soil layer thickness increased, resulting in a reduction in seismically induced settlements. Results from these tests compare well with the results from previous research on the settlement of unsaturated soils considering a sand layer subjected to a steady-state infiltration of water (Ghayoomi et al., 2011; Mirshekari & Ghayoomi, 2017) and a sand layer with a foundation located on the soil surface, subjected to varying groundwater table depths (Borghei et al., 2020).

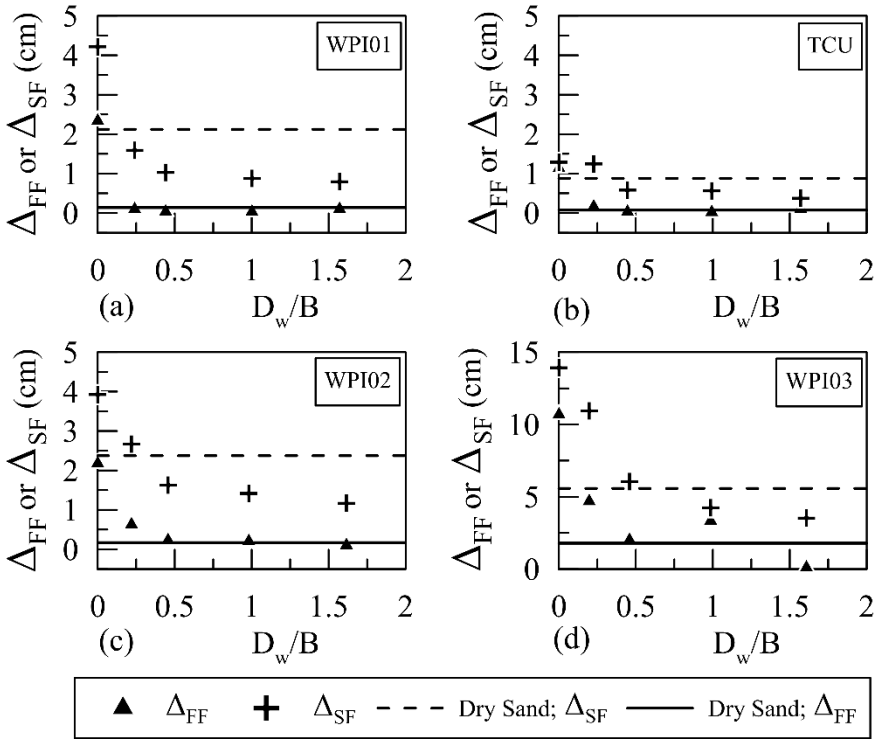

Figure 4-15. Permanently induced seismic soil settlements recorded in the free-field and beneath the foundation as a function of the normalized depth of the groundwater table. Each subplot shows the response during one input motion.

4.8.1. Foundation energy dissipation

The area contained in the $M - \theta_f$ hysteresis loops is known as kinetic rotational energy and is part of the foundation-structural system's total kinetic energy when loaded. The total kinetic energy of the system can be broken down into the sum of the kinetic rotational and kinetic translational energy. The kinetic translational energy is a function of the settlement experienced by the foundation throughout the loading. To further quantify the energy being dissipated, solely due to the foundation rocking, the accumulated work done by the foundation rocking, δW, for each motion was calculated using a modified form of the equation presented by Figueroa et al. (1994) shown in Equation 4-10.

$$\delta W = \sum_{i=1}^{n-1} \frac{1}{2}(M_i + M_{i+1})\left(\theta_{f,i+1} - \theta_{f,i}\right) \qquad 4\text{-}10$$

where n is the number of data points recorded throughout the motion duration. Figure 4-16 displays the δW values for each motion and each water table condition. Results for the tests on ML_WL_0.02B when subjected to WPI03 motion are not reported as the vertical displacement sensors exceeded their range. According to the figure, as the depth of the water level increased, the δW values generally increased, becoming even greater than the δW experienced by the dry soil for some water table elevations. Specimen ML_WL_0.24B sometimes exhibited higher δW values than ML_WL_0.44B. In comparison with specimen ML_WL_0.44B, specimen ML_WL_0.24B created a situation where the stiffness, damping, and strength characteristics of the soil below the foundation allowed for lower moment capacity and greater rotations to be generated. These conditions led to a significant accumulation of energy. Results from this section are in good agreement with Gajan & Kutter (2009) who showed that by increasing the vertical

factor of safety against bearing capacity failure, F_v, the energy dissipated by foundation rocking increases while the energy dissipated by translation in the vertical direction decreases.

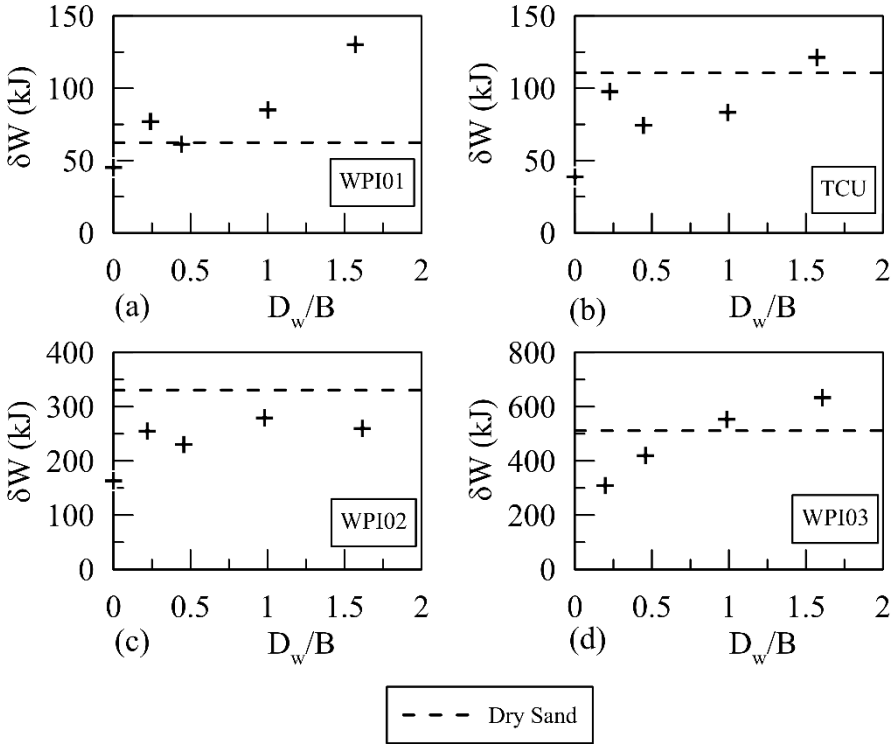

Figure 4-16. Accumulated work done by foundation rocking as a function of the normalized depth of the groundwater table. Each subplot shows the response during one input motion.

4.8.2. Non-parametric System identification frequency-dependent motion amplification

In this section, the nonparametric system identification procedure is used to evaluate changes in the structural response related to the input motions. A transfer function, $H(f)$, between an input motion, $x(t)$, and an output motion, $y(t)$, examines the amplification of the seismic motion across different frequencies. Transfer functions were computed using Equation 4-11, as implemented by Borghei et al. (2020); Ghayoomi & Dashti (2015); Kim & Stewart (2003).

$$H(f) = \frac{S_{xy}(f)}{S_{xx}(f)} \quad \text{4-11}$$

where S_{xx} represents the smoothed power spectral density function of $x(t)$, and S_{xy} represents the smoothed cross-power spectral density function of $x(t)$ and $y(t)$.

To evaluate the influence of the water table depth on soil-structure interaction introduced during shaking, Figure 4-17 shows the transmissibility functions relating rocking foundation motion (FM_R) to free-field (FF) horizontal accelerations across WPI01, TCU, and WPI03. The rocking response of the foundation was evaluated by computing the difference between the two vertical accelerometer recordings installed on the physical model, then dividing by the horizontal separation distance of the instruments. Consistent with Borghei et al. (2020), this acceleration time history was multiplied by the foundation half-width to obtain the rocking foundation motion, FM_R. Figure 4-17 indicates that foundation rocking was introduced to the system, regardless of the water table condition, a result of variations in the ground motion occurring along the foundation and inertia developed in the vibrating structure. As the depth of the water table increased, higher frequency components of rocking motions were introduced while lower frequency components were reduced.

Figure 4-18 shows the transmissibility functions of the recorded structure horizontal motion (SHM) and the foundation motion (FM) across several excitations. Figure 4-2 highlights the locations of the accelerometers installed to capture the SHM and FM. The fundamental natural frequencies (the frequency with the highest amplification) were observed at lower frequencies than the structures' fixed-based fundamental frequency, f_0, (or about 1.85 Hz), attributed to the nonlinear behavior of the soil-foundation system, associated softening, and the period lengthening (frequency shortening). In general, as the depth of the water table increased the peak motion

amplifications were observed at higher frequencies. The soil-foundation system behaved stiffer in the unsaturated soil layers and less total energy dissipation occurred at the foundation level. Therefore, while unsaturated soil has the potential to increase δW compared to the fully saturated and even dry soil conditions, the reduction in energy dissipation due to foundation translation in the vertical direction may lead to increased superstructure demands compared to the fully saturated condition and dry soil, as shown in Figure 4-16 through Figure 4-18. In addition, the motion with the highest intensity (i.e., WPI03) showed the lowest overall amplification, regardless of the water table depth, potentially due to the increased soil yielding and higher energy dissipation at the foundation level during stronger ground motions.

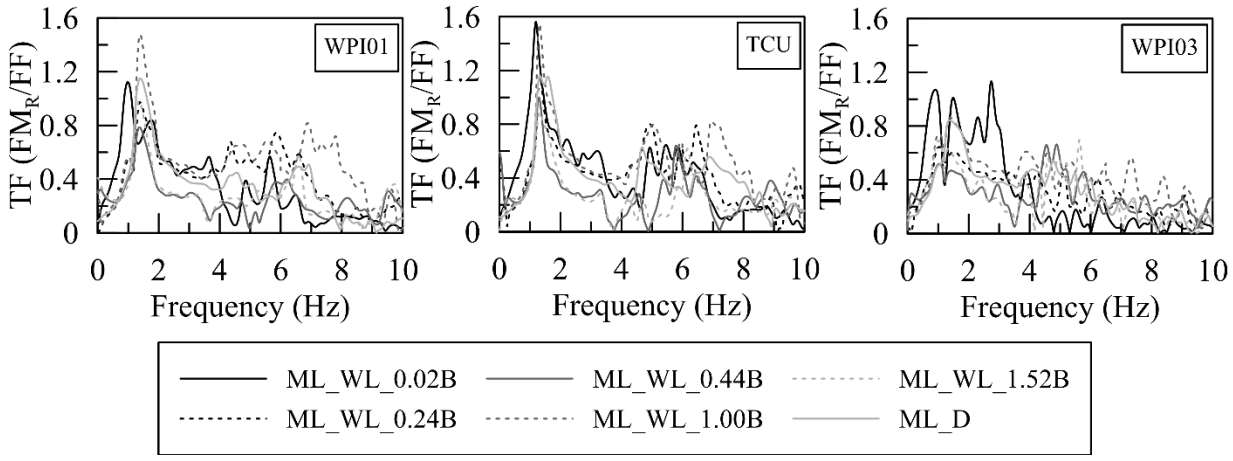

Figure 4-17. Rocking transmissibility functions (TF) between the computed foundation rocking motion and the horizontal free-field motion across different applied motions. Each subplot shows the response during one input motion.

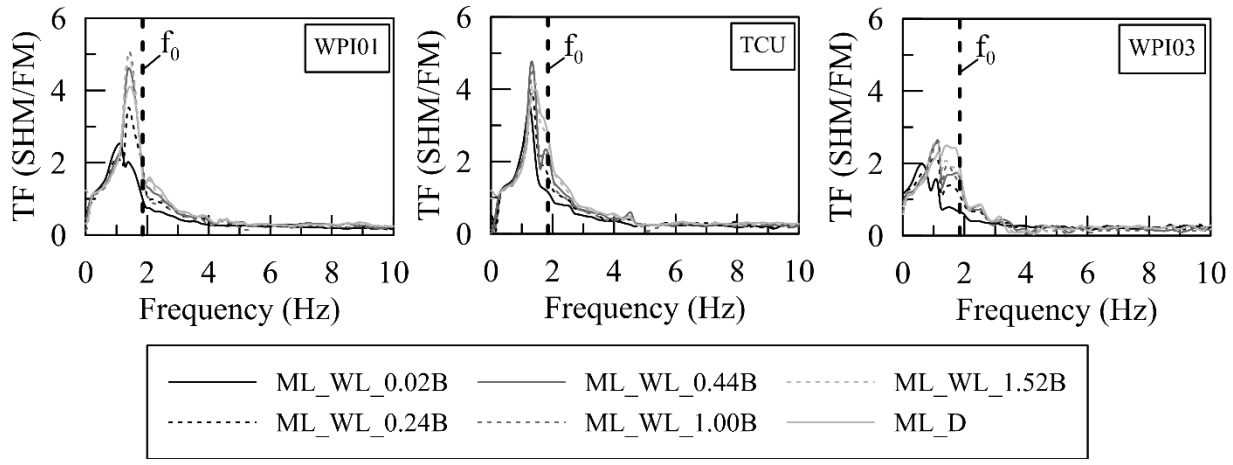

Figure 4-18. Translational acceleration transmissibility functions (TF) between the structure horizontal motion and the foundation horizontal motion across different applied motions. Each subplot shows the response during one input motion.

4.8.3. Parametric system identification to evaluate nonlinear SFSI

As discussed in Chapter 2, Section 2.4, determining damping ratios from nonparametric system identification can be difficult. Therefore, this section uses the parametric system identification procedure developed by Stewart & Fenves (1998) and described in Chapter 2, Section 2.4 to compute the period lengthening ratio, $\tilde{T}/T$, and flexible-base damping ratio, $\tilde{\beta}$. Values of $\tilde{T}$ and $\tilde{\beta}$ are compared with their fixed-base counterparts to evaluate the influence of the soil saturation condition on system nonlinearities stemming from SFSI.

An example application of the system identification procedure is provided to identify the flexible-base modal parameters during ML_D when subjected to WPI01 input motion. Input and output motions necessary to estimate the flexible-base modal parameters are given in Table 2-1 and include the horizontal motion in the free-field, far from the structure (FFM in Figure 4-2) and the SHM. Figure 4-19(a) and (b) show the deviation of the time delay and number of modes with respect to the error of the transfer function model in prototype scale. According to the figure, the

model error is minimized for a time delay of 0 seconds, while the model error does not change significantly above a model order of about 10. Therefore, the time delay and model order are selected as 0 and 10, respectively. Based on these chosen inputs, the surface of the transfer function is computed and shown in Figure 4-20. Flexible-base system frequencies, $\tilde{f}$, and damping ratios can be computed from the locations of the highs and lows in the transfer function surface. According to the figure, $\tilde{f}$ is equal to 1.49 Hz, while $\tilde{\beta}$ is equal to 12.6%. Note that $\tilde{T} = 1/\tilde{f} = 0.67\ s$.

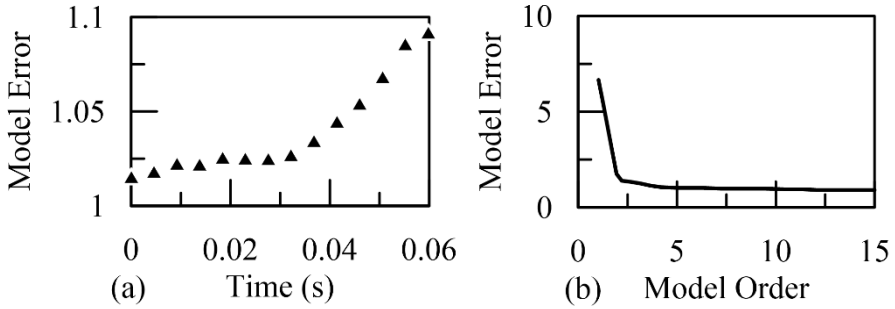

Figure 4-19. Variation of transfer function model error for ML_D when subjected to WPI01 input motion with respect to (a) prototype time; and (b) model order.

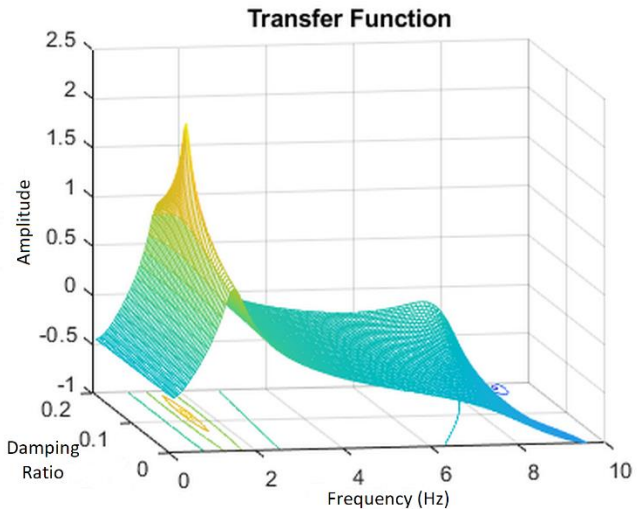

Figure 4-20. Flexible-base modal parameter transfer function surface and contour line determined for ML_D when subjected to WPI01 input motion.

Figure 4-21 shows the variation of $\tilde{T}/T$ with respect to the normalized depth of the water table, D_w/B, across all four input motions. Similarly, Figure 4-22 shows the variation of $\tilde{\beta}$ and $\tilde{\beta}_0$ (computed with Equation 2-8) with respect to D_w/B across all four input motions.

Results suggest that as the depth of the water table increased from the fully saturated condition, values of $\tilde{T}/T$, $\tilde{\beta}$ and $\tilde{\beta}_0$ reduced. Therefore, higher water table elevations correlate to increased system nonlinearities. The observed trend can be explained by the presence of matric suction in the zone above the water table, which is generated during the unsaturated experiments. Matric suction increases the effective stress in the unsaturated soil, leading to a stiffer seismic response compared with the fully saturated condition. As the water table elevation was lowered, the response of the system approached that of ML_Dry. As expected, results also indicate that the characteristics of the input motions influenced the amount of system nonlinearities. For the same soil saturation condition, relatively higher intensity input motions led to an increase in $\tilde{T}/T$, $\tilde{\beta}$ and $\tilde{\beta}_0$.

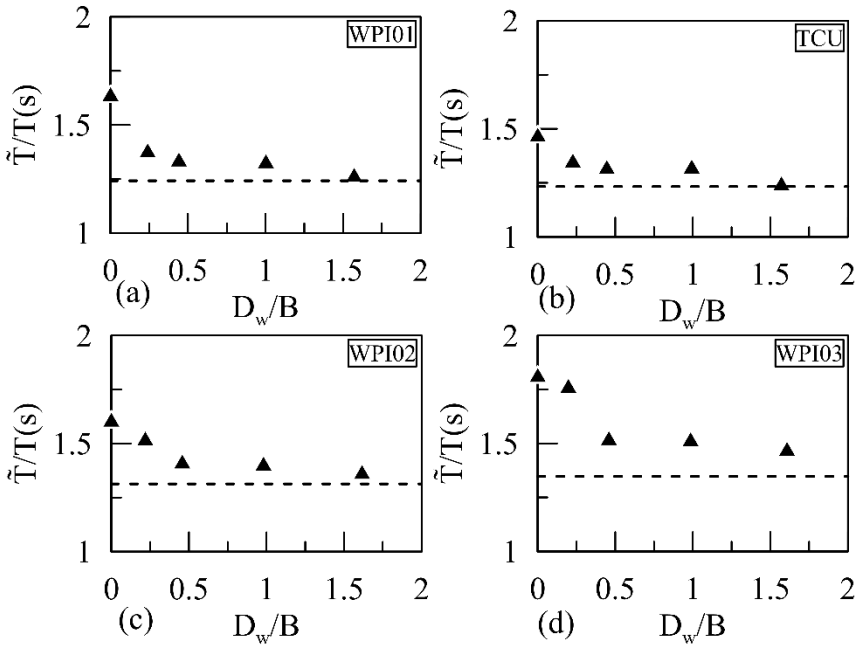

Figure 4-21. Variation of period lengthening ratio with respect to the normalized depth of the groundwater table across all four input motions. Each subplot shows the response during one input motion. Results from WL_D are indicated with the dashed line. Note: T=1.85 s.

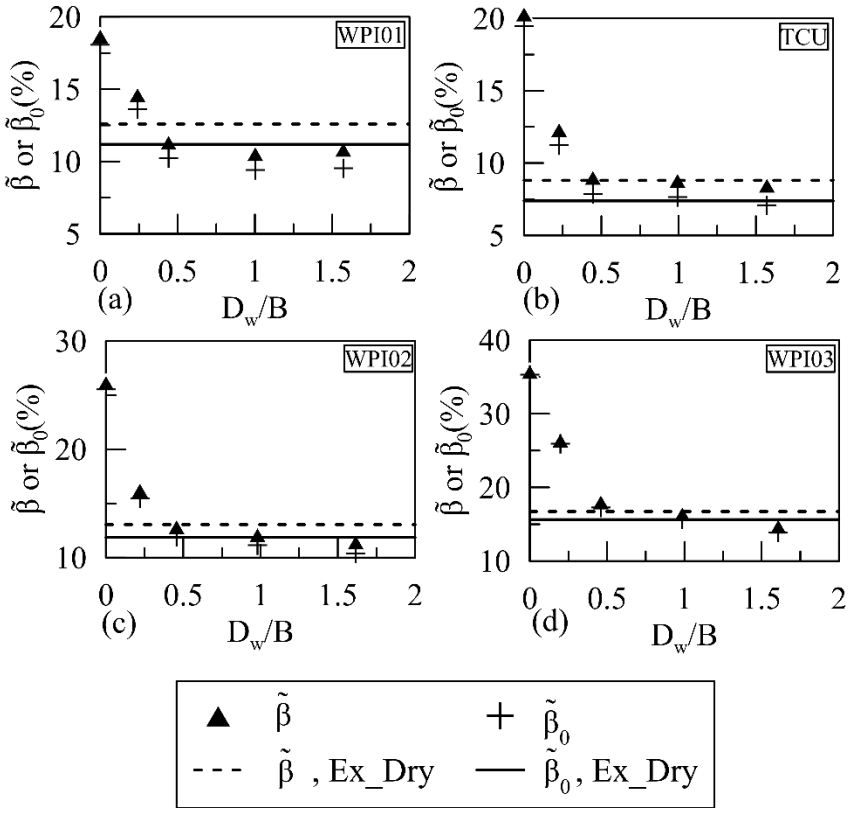

Figure 4-22. Variation of system and foundation damping with respect to the normalized depth of the groundwater table across all four input motions. Each subplot shows the response during one input motion.

4.9. INFLUENCE OF UNSATURATED SOILS ON K_0

For the design of many geotechnical structures, the state of stress in the soil is a primary analysis parameter. To design these structures, both vertical and horizontal (lateral) earth pressure must be estimated. Vertical earth pressure can be simply estimated based on the unit weight and depth of the soil. Meanwhile, the lateral earth pressure depends on several factors, including strain, shear strength, unit weight, and drainage conditions. When a mass of soil has experienced zero lateral strain, the soil is known to be in the at-rest condition. In this condition, the at-rest coefficient of earth pressure, K_0, is used to estimate the lateral earth pressure acting on a structure by a soil mass.

Estimation of K_0 has been the subject of much research over the years, often by using empirical correlations. Jaky (1944) proposed an estimation of K_0 for normally consolidated sands, as a function of effective friction angle. For clays, researchers have correlated K_0 with plasticity index (Alpan, 1967; Massarsch, 1979) or plasticity index and overconsolidation ratio (Brooker & Ireland, 1965). Most of these studies have focused on determining K_0 for soils in the dry or fully saturated states. However, many geotechnical structures are built on, or embedded in, unsaturated soils. Unsaturated soils are widespread in zones above the groundwater table where capillary rise leads to the introduction of a three-phase material (composed of solids, water, and air). In these regions, the unit weight of the soil is influenced by the degree of saturation, while the shear strength of the soil increases compared to the fully saturated condition due to the introduction of negative pore water pressure (matric suction) (Fredlund et al., 1996). Matric suction acts as an apparent cohesion and pulls the soil particles together.

In this section, a centrifuge test was performed to investigate the influence of the water table depth on K_0 in a sandy silt. K_0 for unsaturated soil is determined according to the definition by Lu & Likos (2004), shown in Equation 4-12 and for saturated soil according to Equation 4-13.

$$K_0 = \frac{\sigma_h - u_a}{\sigma_v - u_a} \quad for\ S < 1.0 \tag{4-12}$$

$$K_0 = \frac{\sigma_h - u_w}{\sigma_v - u_w} \quad for\ S = 1.0 \tag{4-13}$$

where σ_h and σ_v are the total stresses generated in the vertical and horizontal directions, respectively. S is the degree of saturation of the soil. While u_a and u_w are the pore air and water pressure, respectively. σ_h was measured directly during the experiments using miniature earth pressure transducers (EPTs) while σ_v was estimated based on the depth of the water table below

the soil surface and the corresponding influence of the degree of saturation on the unit weight. u_w was estimated based on the depth of the earth pressure transducer below the water table depth and u_a was assumed to be zero as the soil layer was open to the atmosphere throughout testing. Where necessary, Equation 4-14 (Jaky, 1944) is employed to estimate the value of K_0 for saturated soils based on the effective friction angle of the normally consolidated soil, ϕ'.

$$K_0 = 1 - sin\phi' \tag{4-14}$$

K_0 was also estimated for unsaturated soils based on Poisson's ratio, ν, as implemented by (Komolafe & Ghayoomi, 2021), and shown in Equation 4-15. The degree of saturation-dependent function for Poisson's ratio of unsaturated soils by (Thota et al., 2021) was used in this equation. K_0 values estimated using Equation 4-15 are compared to those determined experimentally, thus highlighting the potential use of Equation 4-15.

$$K_0 = \frac{\nu}{1 - \nu} \tag{4-15}$$

The centrifuge experiment for this analysis was a control repeat test of ML_WL_1.00B. The centrifuge test began with an initially fully saturated soil layer. Then, the water table depth was gradually lowered in-flight while the change in σ_h was recorded.

Figure 4-23 shows the pore pressure transducer (PPT) values measured as the water table was lowered, prior to application of the seismic motion, plotted with respect to time. Figure 4-2 shows the locations of the PPTs. Significant reductions in measured pore pressures correspond to reductions in the water table elevation in the soil profile. For this analysis, the data corresponding to ten distinct water table elevations were selected and analyzed. Time durations of pore pressure data used to determine the water table depths are highlighted in Figure 4-23 (pore pressure data

was averaged along these time spans). Estimated water table depths are given in Table 4-3, along with the names used to reference the water table depth. A negative water table elevation indicates the water level was above the surface of the soil layer and the soil was in the fully saturated condition.

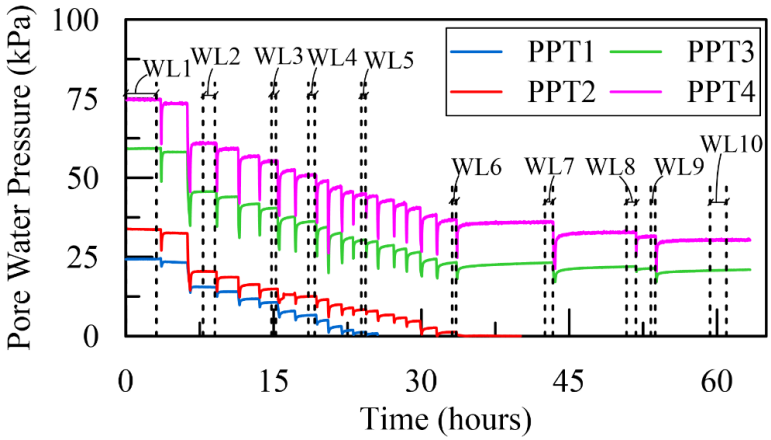

Figure 4-23. Measured pore water pressure throughout the control repeat experiment of ML_WL_1.00B along with the time durations used to estimate the water table depths.

Table 4-3. Water table depths throughout the control repeat experiment of ML_WL_1.00B and identifiers.

Water Table Name	**Water Table Depth Below Soil Surface (m)**	**Water Table Name**	**Water Table Depth Below Soil Surface (m)**
WL1	-0.365	WL6	2.813
WL2	0.918	WL7	2.965
WL3	1.463	WL8	3.323
WL4	1.632	WL9	3.434
WL5	2.041	WL10	3.638

Figure 4-24 highlights the EPT data plotted with respect to time. The locations of the EPTs are shown in Figure 4-2. σ_h were averaged along the same time intervals used to estimate the water table depths. The measured σ_h data for WL1 (fully saturated layer) can be used to validate the sensor measurements. σ_h data for WL1 can be compared to estimated σ_h calculated considering

the saturated unit weight of the soil, water table depth, sensor depth, and K_0 calculated using Equation 4-14 ($\phi' = 38°$). According to Figure 4-25, the measured values of σ_h closely match the estimated ones. Therefore, measured values were accepted as accurate and used throughout the analysis. It should be noted that, although minor, the differences between measured and estimated values are expected to be associated with the size of the PPT sensors (0.5 m diameter). Considering lateral earth pressure is influenced by depth, the size of the sensor may have influenced the results.

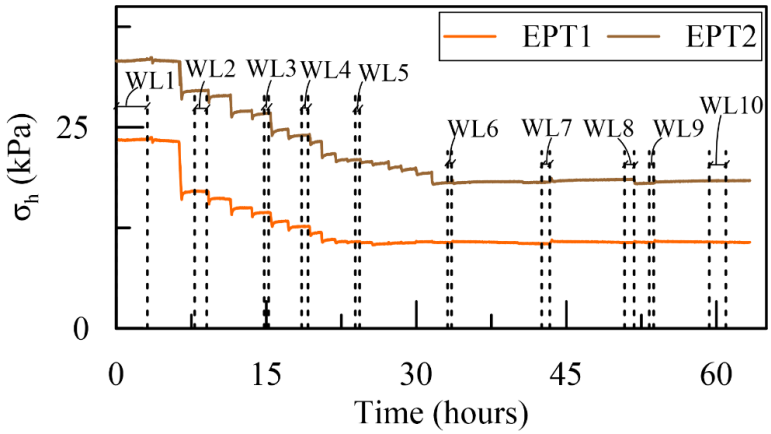

Figure 4-24. Measured horizontal stress during the control repeat experiment of ML_WL_1.00B along with time durations used to estimate the average earth pressures.

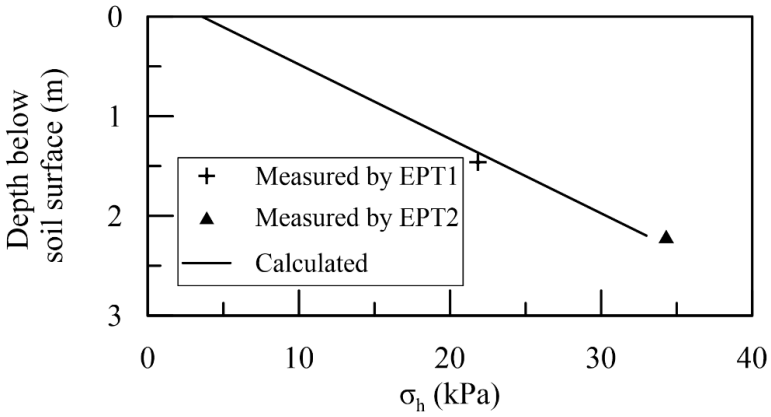

Figure 4-25. Comparison of measured values of horizontal stress to estimated values of horizontal stress for WL1 as a function of EPT depth below the soil surface.

The values of K_0 at the depths of the EPTs were calculated according to Equation 4-12 and Equation 4-13. To calculate K_0, the value of σ_v at the EPT depths were estimated from the total unit weight of the soil (γ_t) and depth below the soil surface. Above and below the water table elevation, the γ_t of the soil can be correlated to the degree of saturation of the soil through the SWRC shown in Figure 3-3(b), with matric suctions calculated assuming hydrostatic conditions. Figure 4-26 shows γ_t calculated at specific depths throughout the soil layer across each water table elevation. These curves were used to evaluate σ_v at the depth of the EPTs, and hence K_0.

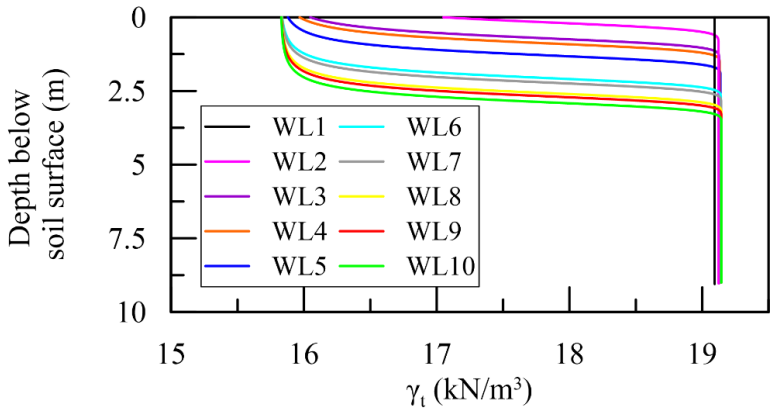

Figure 4-26. Variation of total unit weight with respect to soil depth below the soil layer surface during the control repeat test of ML_WL_1.00B.

Values of K_0 are displayed as a function of the degree of saturation of the soil at the depth of the corresponding EPT in Figure 4-27. K_0 values are shown only when unsaturated and saturated soils are present in the soil layer (i.e., results from WL1 are not shown). According to the figure, K_0 varies with S. K_0 reduces from a maximum value of about 0.61 at $S = 1.0$ to a minimum value of about 0.47 as the soil approaches S_r. The reduction of K_0 values with S can be explained due to a

reduction in γ_t throughout the soil profile. Finally, the values of K_0 obtained from Equation 4-15 are similar to those found experimentally.

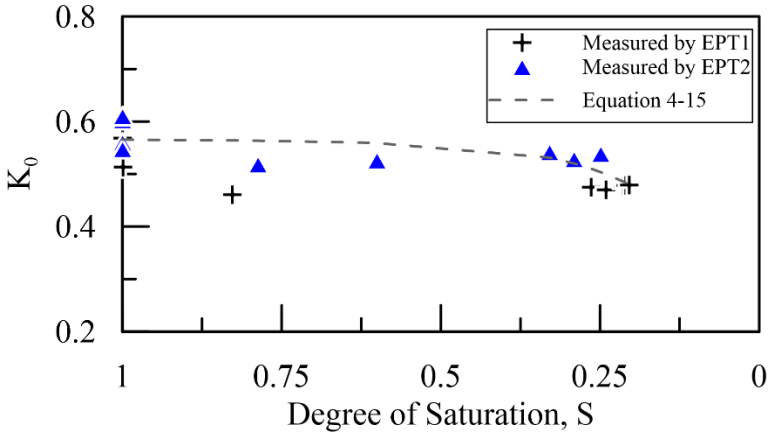

Figure 4-27. At-rest coefficient of lateral earth pressure versus degree of saturation when both saturated and unsaturated soil layers are present throughout the soil profile.

4.10. CONCLUSIONS

A series of dynamic centrifuge experiments was conducted on a rocking isolated foundation system when embedded in sandy silt layers with varying groundwater table elevations. Design criteria for the structural system was selected to generate a settlement dominated response throughout earthquake loading. The goals of the experimental campaign were to develop design considerations and assess the performance of a rocking foundation considering the degree of saturation of the underlying soil. Procedures were proposed to estimate the $M_{c,foot}$ and $(K_{ini})_e$ of foundations in unsaturated soils; both were verified with experimental data. Shear strength and wave velocities used in these formulations were determined in accordance with the fundamentals of unsaturated soil mechanics. Findings suggest that foundation moment capacities increased as the water table depth was lowered. The increased foundation moment capacity in unsaturated soil led to greater high frequency lateral motion amplifications between the foundation and the

superstructure, compared to the fully saturated soil conditions. Likewise, rocking motions were introduced to the system across all soil saturation conditions, with greater amplifications occurring at higher frequencies in the unsaturated compared to the saturated soil condition. Currently, a major limitation for the implementation of rocking foundations in practice is the potential for excessive foundation settlements and rotations. High settlements and rotations are expected for foundations with relatively low F_v values. The experimental result suggested that excessive foundation settlements in the fully saturated and dry soil layers can be mitigated by lowering the depth of the water table or decreasing the degree of saturation. The settlement of the foundation reached an optimal level for the water table depths of about $0.5B$ and greater. Further, peak and residual rotations were found to reduce with the increase in water table depth, while work done by foundation rocking was found to increase. In addition, as the degree of saturation in the soil layer decreased, K_0 was found to reduce. Overall, this study highlighted the potential use, performance, and predictability of rocking foundations when placed on unsaturated soils.

CHAPTER 5

SOIL-FOUNDATION-STRUCTURE INTERACTION OF INELASTIC STRUCTURAL SYSTEMS ON UNSATURATED SOIL LAYERS

5.1. ABSTRACT

Recently, progress has been made towards understanding the seismic response of structures placed on unsaturated soil layers. A missing link, however, involves the influence and assessment of the underlying soil saturation condition on the expected superstructure seismic demands. Simplified soil-structure interaction procedures which can be used to predict superstructure seismic demands have not been explicitly extended to incorporate the influence of unsaturated soil on the system response. In this chapter, results from a series of six centrifuge tests are compared. In each test, an inelastic single-degree-of-freedom physical model is shallowly embedded in a sandy silt with a distinct water table elevation or a completely dry soil condition. The soil-structure system is subjected to a series of earthquake motions. The response of the system is evaluated to assess the influence of the soil saturation condition on the seismic response. Specifically, a conventional

analytical procedure for predicting the influence of inertial interaction on the seismic response of the structure is extended to consider the water table elevation and underlying soil saturation condition and evaluated for its reliability. Analytical flexible-base modal parameters are compared with those determined from experimental results to judge the potential of the analytical procedure to be used in practice. Experimental results suggest that as the water table elevation is lowered from the fully saturated condition, both the flexible-base system period and damping ratio reduce. Therefore, the system behaves stiffer in the unsaturated soil compared to the dry and fully saturated conditions. The stiffer response reduces the seismically induced foundation settlements and rotations but amplifies superstructure seismic demands in the form of accelerations, flexural drifts, and bending strains.

5.2. INTRODUCTION

Modern seismic design, termed *capacity design*, aims at limiting seismic damage by guiding inelastic deformation to above-ground superstructure locations, preventing mobilization of the foundation bearing capacity, uplifting, sliding, or any relevant combination. For example, special moment resisting frames (SMRF) are commonly used as the seismic force-resisting system against intense ground motions. Structural design in such systems allows the frame to develop severe zones of plasticity, in structural fuse locations, typically located at the ends of beams and column bases. Column base points are critical elements of an SMRF system, where plastic hinging is likely to occur (NIST, 2016). The use of a SMRF is currently permitted, according to ASCE 7-16 (ASCE, 2017), for any seismic design category. Similarly, traditional seismic bridge design in states like California is established based on inelastic behavior of columns. Meanwhile the soil-foundation interface is treated using overstrength factors to behave within its elastic range (Caltrans, 2010).

Although capacity design limits inelastic soil-foundation deformations, under large seismic excitations, mobilization of the foundation bearing capacity may be unavoidable, and even advantageous. For instance, the energy dissipated by the nonlinear response at the soil-foundation interface may limit the seismic demand transmitted to the superstructure. However, large seismic demands at the foundation level must be controlled to ensure stability against bearing failure and to minimize settlements and foundation rotations under such conditions. In an emerging, performance-based, seismic design scheme, termed *foundation rocking*, the energy dissipative characteristics of the soil-foundation system are considered, leading to a reduction in expected superstructure demands.

Regardless of the seismic design approach (capacity or rocking foundation), the foundation soil plays a critical role, as it impacts both the site response and the motion transferred to the foundation through the soil-foundation interface, potentially changing the flexibility and natural frequency of the structural system (Kim & Stewart, 2003; Stewart et al., 1999a). Several analytical methods are available for determining the linear response of a system due to soil-foundation-structure interaction (SFSI) (Bielak, 1975; Veletsos & Nair, 1975). Past studies have also made progress to determine SFSI impacts using recorded data from field-scale seismic recordings (e.g., Chen et al., 2017; Stewart et al., 1999b; Stinson, 2014; Tileylioglu et al., 2011; Trifunac et al., 2001). Stemming from these analytical procedures and field-scale results, present-day seismic codes (ASCE, 2017) allow engineers to use linear elastic theory to incorporate SFSI impacts (namely changes in building natural period and foundation damping), into building designs that were previously designed with the assumption of a fixed-base condition. However, when subjected to strong seismic motions, non-linear SFSI may be introduced, which may not be adequately predicted by linear elastic theory. Nonlinearity may stem from foundation-level deformations such

as those encouraged in rocking foundation design and/or from deformations in above ground superstructure locations such as those encouraged in capacity design. Due to the complex nature of nonlinear system responses, SFSI analysis procedures incorporating these effects remain limited.

To add to SFSI analysis complexity, many code-based analysis procedures neglect the potential impacts of degree of soil saturation on the foundation response. However, a considerable portion of the built environment is built-on, or placed-in, unsaturated soils which are common in geoengineered structures involving compacted backfill and are present in natural soil deposits in zones above the water table. Partially saturated soils may even exist below the water table due to the formation of natural, injected, or biochemically generated occluded air bubbles (Mousavi et al., 2020; Mousavi & Ghayoomi, 2021a; Tsukamoto et al., 2002).

In recent years, progress has been made towards understanding the behavior and impacts of unsaturated soils on foundation design. The dynamic response of unsaturated soil is different from dry and saturated soil due to the existence of inter-particle suction stresses which changes the dynamic soil properties. For example, Biglari et al. (2012), Ghayoomi et al. (2017), Hoyos et al. (2015), Le & Ghayoomi (2017), Vinale et al. (2001) found that unsaturated soils have higher shear stiffness and reduced damping compared with saturated and dry soil. The changes in inter-particle suction linked to the degree of saturation influences the seismic site response (D'Onza et al., 2008; Mirshekari & Ghayoomi, 2017), seismic soil settlements (Duku et al., 2008; Ghayoomi et al., 2011; Ghayoomi, McCartney, et al., 2013; Mousavi & Ghayoomi, 2021b; Stewart et al., 2004; Yee et al., 2014), and the seismic foundation response (Borghei et al., 2020; Ghayoomi et al., 2018). Stinson (2014) used forced-vibration tests of a large-scale model structure to evaluate the changes in building's natural period due to the elevation of the water table below the soil surface. Results

show that as the water table elevation increased the building period also increased, which suggests that the system behaved stiffer when founded on soil with the water table nearer the soil surface. However, further investigation into these effects is warranted due to the cyclic nature of the forced-vibration loading used by Stinson (2014), and to evaluate the influence of the water table depth on additional SFSI parameters, like foundation, and overall system damping. As presented in Chapter 4, Turner et al. (2022a) modeled a completely elastic mid-rise building, shallowly embedded in soil, with varying water table elevations. The system was subjected to a series of scaled earthquake motions. Results suggest that the moment capacity of the foundation increased in the partly unsaturated soil layers compared to the saturated soil and, for some water table elevations, the dry soil condition. Greater foundation moment capacities limited settlements and residual foundation rotations but may have amplified superstructure demands.

Given the impact of unsaturated soils on SFSI, specifically related to changes in building and system properties, seismic amplifications, and superstructure demands, the water table elevation should be considered when evaluating the performance of structural systems designed to resist seismic loading. Shallow water table elevations may lead to greater deformations at the soil-foundation interface. Meanwhile, greater water table depths may lead to increased seismic demands and possible unanticipated plastic deformations in above-ground structural locations. Both soil-foundation and structural level deformations may contribute to changes in the fundamental period and system damping of a building (termed SFSI parameters). This issue becomes even more critical when considering structures founded on soil layers that experience seasonal changes in groundwater elevation due to hydrological processes such as infiltration and evaporation.

In this chapter, a series of centrifuge dynamic experiments conducted at the Disaster Prevention Research Institute, Kyoto University is presented to evaluate the influence of the water table elevation on the seismic performance of a potentially inelastic building model. The results highlight the effect of the water table depth on the SFSI parameters. The discussion begins with an overview of the model development criteria and the testing system. Then, the formulation of an analytical design procedure, incorporating unsaturated soil mechanics, is presented to estimate the change in SFSI parameters related to the depth of the water table below the foundation. Comparisons between the analytically estimated SFSI parameters and the centrifuge experimental observations are made to assess the potential of using the proposed analysis procedure in practice. The effects of the soil saturation condition on the response of the soil-foundation-structure system are also examined. The response is explored in terms of foundation deformations. Specifically, foundation rotations, overturning moments, and settlements are compared. Next, a detailed discussion is presented regarding superstructure seismic demands. Bending strain data from instrumented column locations along with calculated drift ratios and accelerations are used for this analysis. The aim of the presented results is to provide insight into the potential trade-offs of variable water table conditions in the context of building damage and performance.

5.3. STRUCTURAL DESIGN

5.3.1. Design requirements

As presented in Chapter 3, Section 3.9 a physical model, termed ICSS, was designed and constructed to represent the target prototype structure in 46-g acceleration. The system is represented by an inelastic single-degree-of-freedom physical model composed of a lumped mass supported by four columns and a shallowly embedded foundation. To localize inelastic behavior experienced by the structure, regions with the maximum moment and potential nonlinearity were

designed to occur in reduced sections at the base of the columns at instrumented structural "fuse" locations. A photograph of the fully constructed model can be seen in Figure 5-1(a), with properties tabulated in Table 3-4. Furthermore, the replaceable structural fuses are shown in Figure 5-1(b).

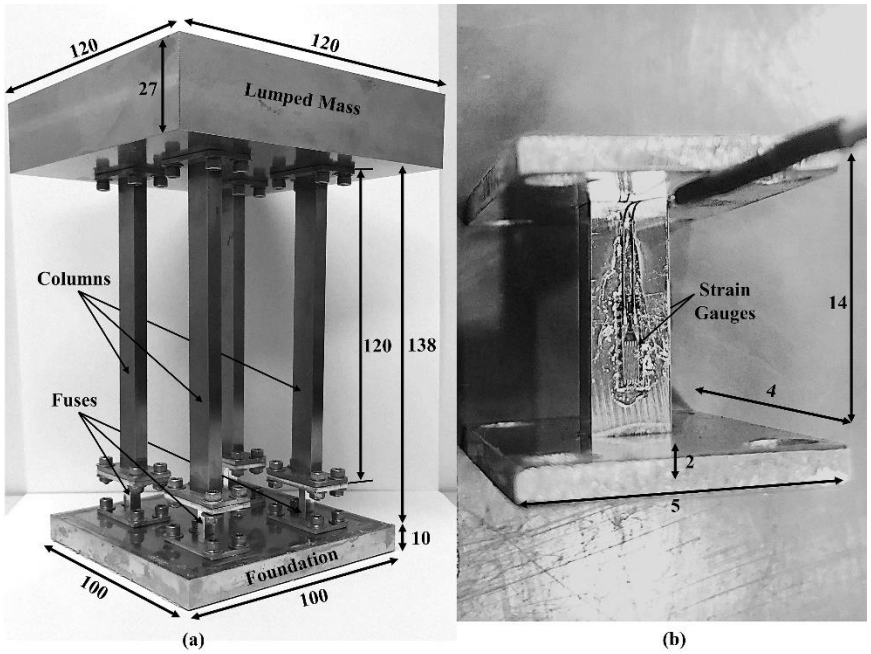

Figure 5-1. (a) ICSS model used in centrifuge; and (b) replaceable fuse at column ends. All dimensions listed are in model scale in mm.

5.4. CENTRIFUGE EXPERIMENTAL SETUP

Six dynamic centrifuge experiments were performed to evaluate the influence of the water table elevation on site response and behavior of a potentially inelastic SDOF structure. Tests consisted of saturated, dry, and four mixed unsaturated-saturated soil profiles, with the unsaturated zones located in the region between the water table and the surface of the soil layer. Test identification is based on the depth of the water table below the surface of the soil layer, D_w, as a function of the width of the foundation, B. For example, test WL_1.00B refers to the experiment performed on a soil layer with the water table 1.00B below the soil surface. Table 5-1 summarizes the initial

experimental conditions before the application of the first seismic motion along with the associated test identifiers. The geotechnical centrifuge and laminar container used in this chapter are discussed in Chapter 3, Sections 3.2 and 3.3. Several seismic motions (listed in Table 5-2) were sequentially applied to the base of the laminar container through the shake table, which allowed one-dimensional wave propagation to the surface of the soil. It should be noted that, due to soil densification after each seismic event, the water table elevation slightly changed, which has been considered in the analysis.

Table 5-1. Centrifuge testing program at the Disaster Prevention and Research Institute.

Test ID	Saturation Fluid	D_w/B
WL_Dry	Dry	N/A
WL_0.06B	Water	-0.06
WL_0.26B	Water	0.26
WL_0.54B	Water	0.54
WL_1.00B	Water	1.00
WL_1.39B	Water	1.39

Note: A negative D_w/B value indicates the water table was located above the surface of the soil layer.

Table 5-2. Ground motion properties of the bedrock motion (BM) as recorded during experiment WL_Dry.

Ground Motion No.	Event	Ground Motion ID	PGA (g)	Significant Duration, D_{5-95} (s)	Max. Arias Intensity (m/s)	Mean Period (s)
1	1994 Northridge	WPI01	0.25	30.33	2.80	0.98
2	1999 Chi-Chi	TCU01	0.20	29.18	1.60	0.72
3	1994 Northridge	WPI02	0.44	30.14	4.22	1.01
4	1999 Chi-Chi	TCU02	0.24	32.30	2.47	0.73

5.4.1. Sample preparation

The soil material used in this research is introduced in Chapter 3, Section 3.4. As discussed in Chapter 3, Section 3.6 the soil was prepared through dry pluviation, using a crane and hopper system, at a calibrated void ratio and density of 0.81 and 1463 kg/m^3, respectively. The corresponding initial relative density of the soil layer was 55%. The pluviation was temporarily paused at select elevations to install instruments and to place the SDOF structure. Locations of instrumentation and the layout of the centrifuge experiments performed in this research can be seen in Figure 5-2. For the saturated and unsaturated tests, after achieving the target soil profile height, the soil layer was saturated with de-aired water according to Chapter 3, Section 3.7. The reader is referred to Chapter 3, Section 3.7.1 for a detailed discussion of the pore fluid selection in this research, which addresses concerns related to the scaling conflict between dynamic time and pore pressure diffusion in a geotechnical centrifuge. After the water table elevation reached the surface of the soil, the valves were closed, the container was bolted to the in-flight shake table, and the centrifuge was spun to the target acceleration. Throughout specimen saturation and during testing, settlements experienced by the soil layer were monitored. The settlement and corresponding soil densification have been considered throughout the analysis. After achieving the correct acceleration, the water level was lowered to the target elevation according to Chapter 3, Section 3.8. The depth of the water table was monitored using the array of pore pressure transducer shown in Figure 5-2. It should be noted that pore pressure transducers referenced herein were able to measure only positive pore water pressure (up to 200 kPa), thus only those transducers installed below the water table were used to estimate the water table depth. Once the water table was at the target elevation, the specimen was subjected to a series of scaled, historic, seismic motions (shown in Table 5-2) and the response of the system was recorded.

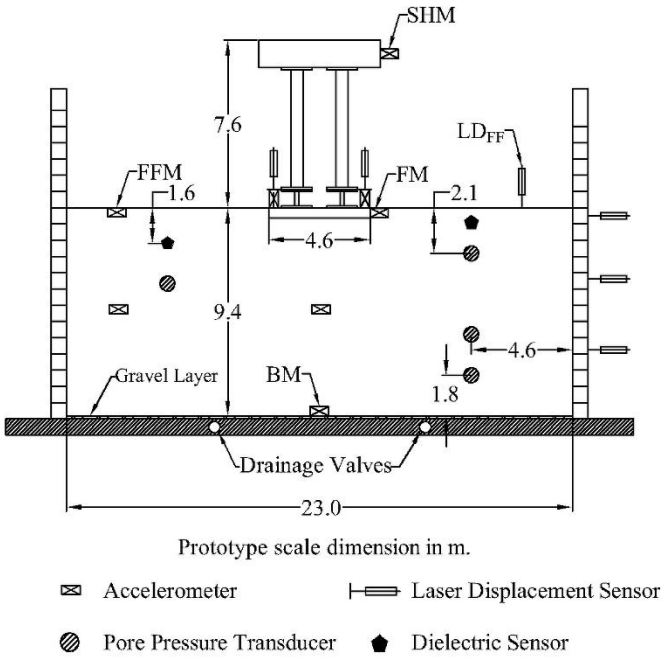

Figure 5-2. Schematic layout of a typical centrifuge test performed in this research.

5.4.2. Input ground motions

During each test a sequence of earthquake motions was applied to the base of the laminar container, in flight, using the servo-valve hydraulic shaking table. The motion recorded by the accelerometer at the base of the container is denoted as bedrock motion, BM. BMs were scaled horizontal components of two historic earthquakes which include the 1994 M_w 6.7 Northridge, California earthquake (WPI motion) and the 1999 M_w 7.6 Chi-Chi, Taiwan earthquake (TCU motion). Although a total of ten motions were applied, only results from the first four motions, referred to as WPI01, TCU01, WPI02, and TCU02 are presented. Table 5-2 lists the BMs, considered in this analysis, and the order in which they were applied in terms of several strong ground motion parameters, aiming to study a variety of motions in terms of accelerations, frequency contents, and durations to better understand SFSI (Ghayoomi & Dashti, 2015). The parameters in Table 5-2

include peak ground acceleration (PGA), maximum Arias Intensity (I_a) (Arias, 1970), mean period (T_m) (Rathje et al., 1998), and significant duration (D_{5-95}). Acceleration time histories, I_a time histories, and 5% damped response spectra of the BMs, as recorded in the centrifuge for Experiment WL_Dry, are shown in Figure 5-3 and Figure 5-4. Additionally, to allow excess pore water pressure to dissipate after each shake, input motions were separated by a period of at least 140 minutes in prototype scale. Mason et al. (2010) discussed the primary factors influencing the performance of, and motions achieved by a hydraulic shake table during centrifuge testing. Contributing factors include the dynamic characteristics of the servo-actuator, centrifuge reaction mass system, and test payload. In the experimental campaign considered herein, the servo-actuator and reaction mass system remained consistent between experiments, thus the test payload was the primary factor influencing the performance of the shake table. As the test payload during experiments WL_0.06B, WL_0.26B, WL_0.54B, WL_1.00B, and WL_1.39B were similar, BM parameters from a representative experiment (WL_0.26B) are compared with those of WL_Dry in Figure 5-5. The figure indicates that the achieved motions were similar across different test payloads and allowed for reliable comparison of the test results.

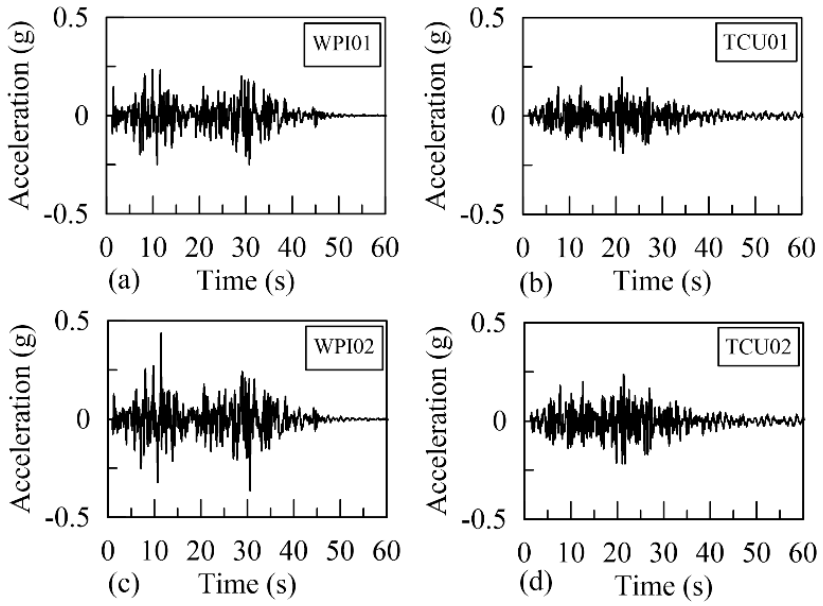

Figure 5-3. Acceleration time histories of the achieved bedrock motions (BMs) recorded during experiment WL_Dry. Each subplot corresponds to one input motion.

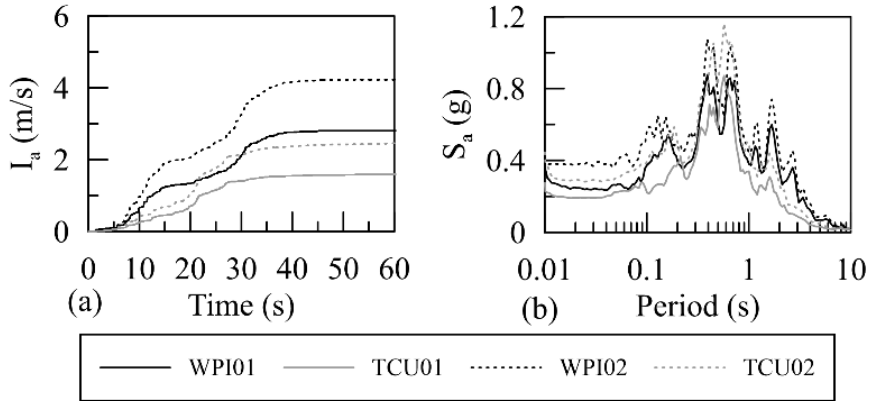

Figure 5-4. Comparison of the achieved bedrock motion (BM) recorded during Experiment WL_Dry showing (a) Arias intensity build-up; and (b) 5% damped acceleration response spectra.

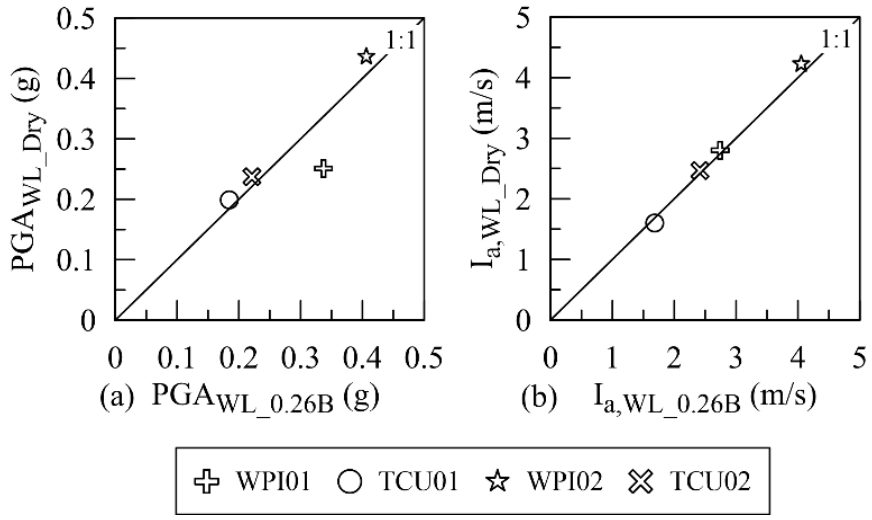

Figure 5-5. Comparison of bedrock motion (BM) intensity parameters across experiment WL_0.26B and WL_Dry with respect to (a) PGA; and (b) maximum Arias Intensity.

5.5. ESTIMATION OF SFSI PARAMETERS

5.5.1. Analytical methodology

The analytical method introduced in Chapter 2, Section 2.3 is used to estimate SFSI parameters of $\tilde{T}$ and $\tilde{\beta}$, denoted as $\tilde{T}_{an}$ and $\tilde{\beta}_{an}$. Parameters which are necessary for computing $\tilde{T}$ and $\tilde{\beta}$ are repeated here for reference as follows:

- Soil Parameters: $V_{s,r}$ and soil hysteretic damping ratio D.
- Structural and Foundation Parameters: Embedment depth of the foundation, effective structural height (typically taken as $\sim 0.7 \times$ total building height, H), r_u, r_θ, and fixed-base parameters of T and β, values of these parameters, determined for the physical model used in this experimental campaign, can be seen in Table 3-4, where T and β were evaluated from a modal hammer analysis.

An equivalent half-space can be used to model soil profiles having an increase in stiffness with depth, using an effective profile depth, z_e. The depth, z_e, extends to half the width of the foundation, as suggested by Stewart et al. (2003). When evaluating the soil parameters within this depth, specifically the value of $V_{s,r}$, consideration should be placed on the underlying soil saturation condition, and the effect of the increased overburden pressure owing to the self-weight of the structure. The following steps were carried out to evaluate an average value of $V_{s,r}$, within a depth below the foundation of z_e.

1. The small strain shear modulus, G_{max}, was evaluated along the profile depth using the Hardin (1978) equation, considering the value of effective vertical stress at depth z defined by Bishop (1959), shown in Equation 4-5, with S_e calculated according to Equation 4-6. It is worth noting that the use of the Bishop (1959) effective stress equation represents a reasonable shear modulus approximation, as evidenced by Ghayoomi & McCartney (2011). However, recent studies like Dong et al. (2016) showed that the accuracy of shear modulus predictive equations can be improved by additional direct incorporation of matric suction.
2. The small strain shear wave velocity along the profile depth was evaluated from $V_s(z) = \sqrt{G_{max}/\rho}$, where ρ is the total density of the soil at the depth of interest considering the water table elevation. The use of the Bishop (1959) effective stress equation in combination with the Hardin (1978) equation to predict V_s has been experimentally verified by Turner et al. (2022a) (also repeated in Chapter 4) where the authors compared predicted values to those interpreted from bender element test results.
3. The value of the shear wave velocity was corrected to account for the increased vertical stress due to the self-weight of the foundation-structural system using Equation 4-7.

4. A harmonic average equation was implemented to determine a representative, average, overburden-corrected small-strain shear wave velocity, $\bar{V}_{s,OC}$, beneath the foundation to a depth of z_e according to $\bar{V}_{s,OC} = z_e / \left[\int_0^{z_e} dz / V_{s,OC}(z)\right]$.

5. The value of $\bar{V}_{s,OC}$ was reduced based on the shear strain, γ_s, experienced throughout each seismic motion. An effective shear strain time history was computed by dividing the relative lateral displacement (measured using horizontal laser displacement sensors targeting the side of the laminar container) experienced at the soil surface and 2.9 m below the surface by the vertical separation distance between the two measuring instruments. The value of γ_s was evaluated as the maximum shear strain experienced throughout the time history. Using the value of γ_s, the value of $\bar{V}_{s,OC}$ was reduced to $\bar{V}_{s,r,OC}$ according to the modified hyperbolic shear modulus reduction model, defined by Darendeli (2001), and shown in Equation 5-1.

$$\frac{\bar{V}_{s,r,OC}{}^2 \rho}{\bar{V}_{s,OC}{}^2 \rho} = \frac{G_r}{G_{max}} = \frac{1}{1 + \left(\frac{\gamma_s}{\gamma_r}\right)^{a_f}} \qquad 5\text{-}1$$

where γ_r is a reference strain and a_f is a curve fitting parameter. Values of γ_r and a_f were estimated using empirically based equations proposed by Menq (2003) as 0.088% and 0.89, respectively.

Values of D were also determined based on the computed γ_s using the modification to material Masing behavior (Masing, 1926), suggested by Darendeli (2001) for granular soils. After identifying the abovementioned soil, foundation, and structural parameters, the iterative approach, defined by Stewart et al. (1999a), termed "modified Bielak" formulation, and shown in Chapter 2.3 was adopted to determine $\tilde{T}_{an}$ and $\tilde{\beta}_{an}$. These analytical values were compared to

experimentally achieved values in a proceeding section, to evaluate the accuracy of the proposed methodology over the range of soil saturation conditions.

5.5.2. Experimental methodology

The parametric system identification procedure discussed by Stewart & Fenves (1998) and introduced in Chapter 2, Section 2.4 was used to characterize flexible-base SFSI parameters of $\tilde{T}$ and $\tilde{\beta}$ achieved during experimentation, denoted as $\tilde{T}_{ex}$ and $\tilde{\beta}_{ex}$, respectively. For identification of flexible-base boundary condition parameters, considering both foundation translation and rotation, the input and output motions are the free-field (FFM) and structure horizontal (SHM) motion, respectively. The response of the soil layer far from the structure and container boundaries is referred to as the free-field response. Locations of horizontal accelerometers installed to record the SHM and FFM are shown in Figure 5-2.

5.6. EXPERIMENTAL RESULTS AND DISCUSSION

The dynamic centrifuge experiments were analyzed to evaluate the effect of the soil saturation condition on the seismic response of the soil, foundation, and structural systems. Specific comparisons are drawn between flexible-base SFSI parameters determined from experimental data to those computed using analytical methods. Then, a discussion is provided on the nonlinearities observed throughout each system. To avoid damage to instrumentation, experiment WL_0.06 was terminated after applying TCU01 input motion, during which excessive structural deformations and foundation rotations were observed. The following results are presented in prototype scale.

5.6.1. Comparison of analytical SFSI parameters with those achieved experimentally

In this section, analytical values of $\tilde{T}$ and $\tilde{\beta}$ are compared with those achieved during the centrifuge experiments. Then, $\tilde{T}_{ex}$ and $\tilde{\beta}_{ex}$ values are used to predict the spectral accelerations on the

superstructure; these demands are then compared with peak superstructure accelerations recorded during the tests.

Figure 5-6 and Figure 5-7 compare analytically and experimentally achieved values of $\tilde{T}$ and $\tilde{\beta}$, determined across each input motion, plotted as a function of the water table elevation. Values of $\tilde{T}_{ex}$ and $\tilde{\beta}_{ex}$ for WL_0.06B during the WPI01 motion are not shown due to significant ground settlements which impacted the reliability of the recorded FFM and SHM. Findings suggest that the accuracy of the proposed analytical procedure for predicting flexible-base parameters was highly dependent on the characteristics of the input motion. For example, during the relatively lower intensity input motions of TCU01 and TCU02, the analytical procedure overestimated the extent of period lengthening, when compared with the experimental results, across the full range of soil saturation conditions and input motions. The maximum percent error between the analytical and experimental values of $\tilde{T}$ was found to be about 11.9%, which occurred during WL_1.00B throughout TCU02 seismic motion. Discrepancies between analytical and experimental values are expected to be primarily associated with empirical methodology employed to predict the strain-dependent soil shear moduli and hysteretic damping ratios along with the simple formulation employed to predict values of G_{max} without directly incorporating suction. Furthermore, analytical values of $\tilde{\beta}$ were found to be well below those achieved experimentally, regardless of the soil saturation condition or the characteristics of the input motion. As discussed in proceeding sections, the structure and soil were observed to behave inelastically. As the analytical estimation employed in this study assumes an elastic soil-foundation interface response (a fundamental assumption of the "modified Bielak" formulation), and the small-strain fixed-base damping of the structure was used in Equation 2-8, the increased system damping generated by the structure and underlying soil layer during dynamic excitation could be the primary reason for this underprediction.

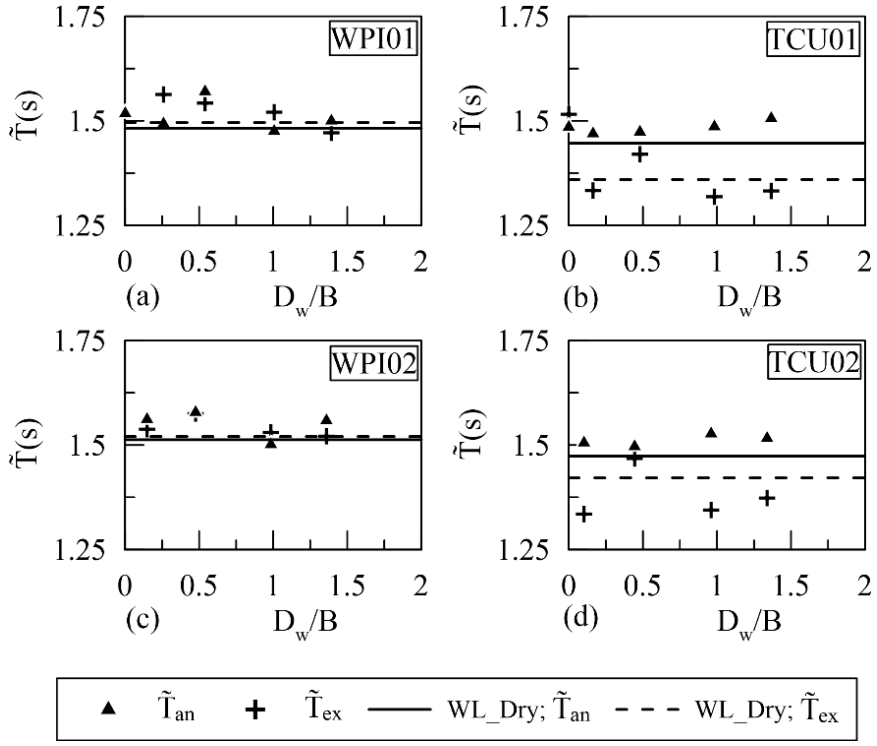

Figure 5-6. Variation of analytically and experimentally determined flexible-base fundamental period of the physical model as a function of the normalized depth of the groundwater table. Note that the fixed-base fundamental period equals 1.27 s. Each subplot shows the response during one input motion.

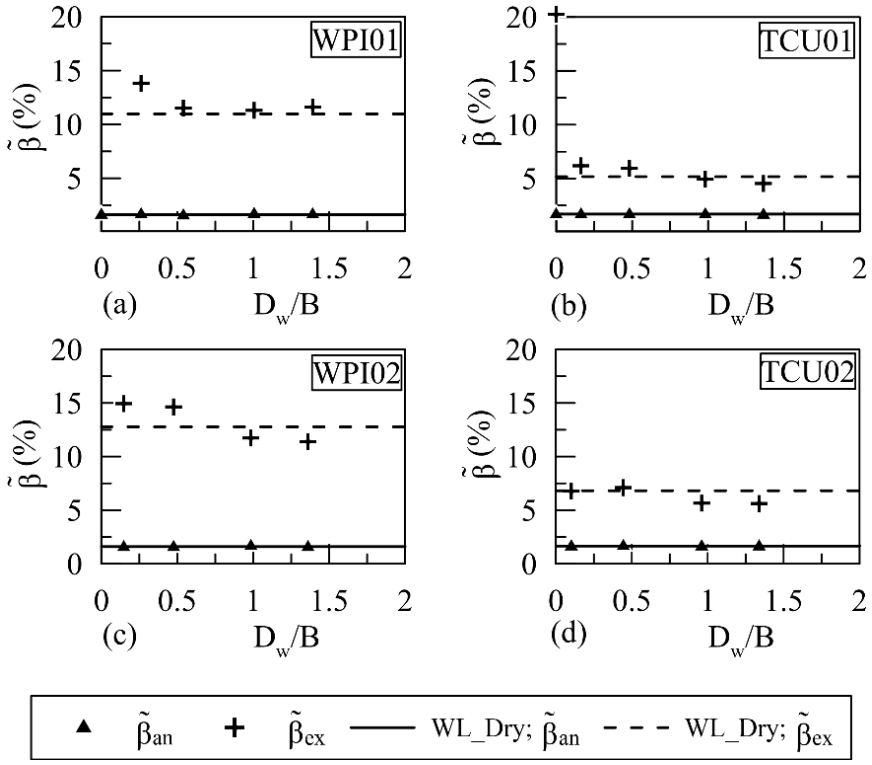

Figure 5-7. Variation of analytically and experimentally determined flexible-base system damping ratio of the physical model as a function of the normalized depth of the groundwater table. Each subplot shows the response during one input motion.

Experimentally identified modal parameters facilitate both cross-experimental and motion-to-motion comparison, enabling discussion regarding variation in the stiffness and damping of the system related to the soil saturation condition and input motion characteristics. In general, the variation of $\tilde{T}_{ex}$ with water table depth depends on the specific input motion considered. For example, during WPI01 motion, values of $\tilde{T}_{ex}$ tended to reduce with increasing water table depth while for other motions there was evidently more scatter in the data. For example, during the later motions of TCU01, WPI02, and TCU02, maximum $\tilde{T}_{ex}$ values corresponded to the shallow water table depths in the WL_0.54B experiment. Meanwhile, the values of $\tilde{\beta}_{ex}$ reduced with changes in water table elevation. When the water table was lowered from near-surface elevations (such as

WL_0.06B and WL_0.26B) to mid-range elevations (such as WL_0.54B) a significant reduction in $\tilde{\beta}_{ex}$ was achieved. Then, as the water table depth was lowered to deeper elevations (such as WL_1.00B and WL_1.39B), little variations in values of $\tilde{\beta}_{ex}$ were observed. The nonlinear trend of $\tilde{\beta}_{ex}$ as a function of D_w/B can be explained in terms of two distinct damping mechanisms contributing to the overall damping of the system. These two damping mechanisms are summarized in Equation 2-8 and are related to the energy dissipation generated by deformations at the soil-foundation interface and the energy dissipation generated by damping in above-ground superstructure locations. The depth of the water table, below the foundation, has a direct impact on the contributions of these two damping mechanisms and, consequently, the overall damping of the system. When the structure was placed on the soil, with shallow water table elevations, system damping was likely governed by the settlement-rotation tendencies at the soil-foundation interface. For example, as discussed in Sections 5.6.2 and 5.6.3, for near-surface water table elevations, foundation settlements and rotations were amplified compared with those experienced when the foundation was placed on the soil with deeper water table depths. This observation can be explained by the increased stiffness generated by the presence of matric suction in the unsaturated soil, which increases the soil shear strength, leading to a reduction in foundation deformations and foundation level damping. Furthermore, reductions in pore pressure generation in the unsaturated soil may have further reduced foundation deformations. Meanwhile, when the structure was placed on the soil with mid-range water table depths, superstructure demands and deformations were amplified, while foundation deformations were limited. Increased superstructure demands can be attributed to a stiffer soil-foundation interface when the foundation was embedded in the unsaturated soil layers. These two damping mechanisms (soil-foundation and structural) controlled

the amount of nonlinearity in the system and hence the corresponding changes in the overall system damping related to the soil saturation condition.

As the primary purpose of computing $\tilde{T}$ and $\tilde{\beta}$ is to predict structural demands, values of $\tilde{T}_{ex}$ and $\tilde{\beta}_{ex}$ were used to predict superstructure spectral accelerations, denoted $S_a(\tilde{T}_{ex}, \tilde{\beta}_{ex})$. Values of $S_a(\tilde{T}_{ex}, \tilde{\beta}_{ex})$ were calculated based on elastic response spectra developed from the FFM records and the motion specific modal parameters of $\tilde{T}_{ex}$ and $\tilde{\beta}_{ex}$ (i.e., the response spectrum of the FFM was computed using $\tilde{\beta}_{ex}$, then the value of $S_a(\tilde{T}_{ex}, \tilde{\beta}_{ex})$ was determined based on the corresponding $\tilde{T}_{ex}$ of the system). Figure 5-8 compares $S_a(\tilde{T}_{ex}, \tilde{\beta}_{ex})$ with the experimentally achieved peak superstructure accelerations, determined from SHM records (see Figure 5-2 for SHM accelerometer installation locations). Results suggest that across nearly all motions and soil saturation conditions, peak superstructure accelerations were less than those predicted by the elastic response spectra. The observed trend is due to increased motion damping stemming from a combination of inelastic foundation behavior and superstructure yielding. As expected, during the stronger WPI input motions, the discrepancies stemming from these damping factors were amplified, compared with the results from the relatively lower intensity TCU input motions. The results in Figure 5-8 highlight the shortcomings of using elastic spectrum results for predicting the response of inelastic buildings. However, for a conservative design scenario, where overpredictions are encouraged, using elastic response spectra results for predicting peak superstructure accelerations on inelastic buildings may prove beneficial. Results are generally consistent with those presented by Trombetta et al. (2013), where elastic response spectra overpredicted seismic demands on an inelastic building structure when founded on a dry soil.

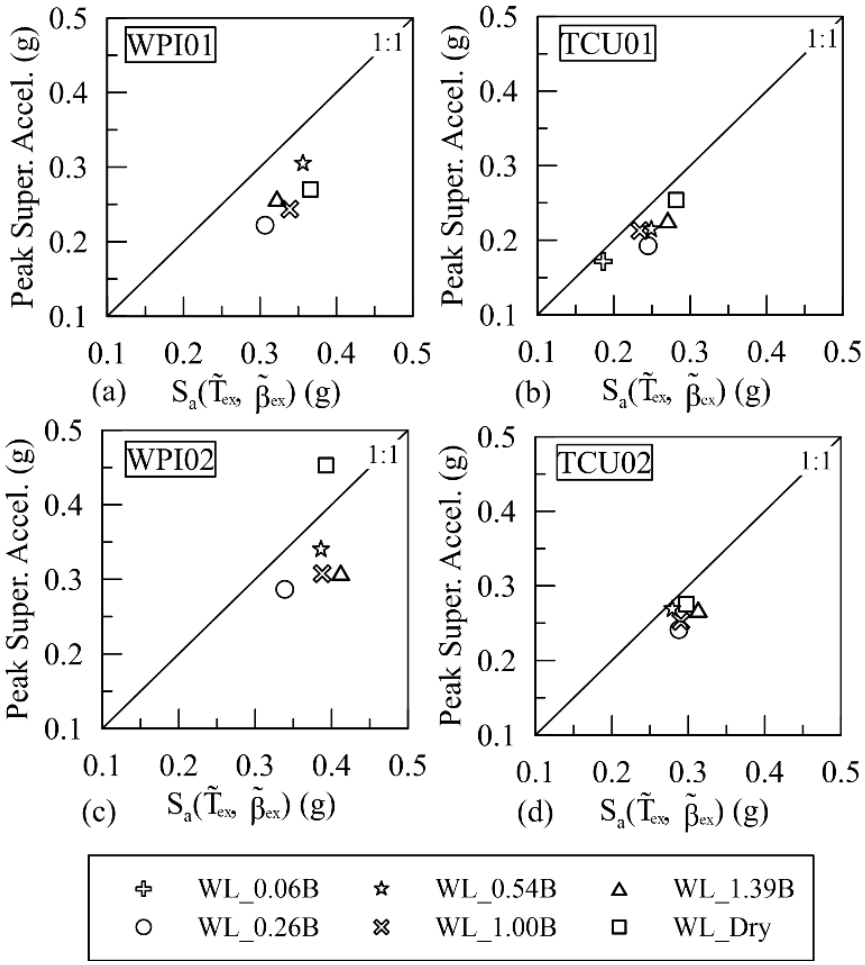

Figure 5-8. Peak superstructure accelerations versus estimated superstructure spectral accelerations. Estimations were determined using experimentally derived flexible-base modal parameters and free-field recorded motions. Each subplot shows the response during one input motion. A 1:1 reference line is provided.

The influence of the soil saturation condition is also highlighted in Figure 5-8, where peak superstructure accelerations were amplified in the unsaturated soil, compared to the fully saturated and near-saturated (WL_0.26B) soil conditions. Several factors play a role in this observation. In the free-field, far from the structure, Borghei et al. (2020) found that the depth of the water table influences the observed site-response due to changes in the dynamic soil properties related to the

degree of saturation. Primarily, deeper water table elevations lead to increased free-field motions compared with the fully saturated soil condition. Borghei et al. (2020) also found that as the depth of the water table was lowered from the fully saturated condition, greater lateral motion was introduced, as the ground motion propagated from the free-field to the foundation, due to kinematic interaction. Furthermore, as highlighted in Figure 5-6 and Figure 5-7, the soil-structural system behaved stiffer when placed on the unsaturated soil, which limited the amount of damping. Reductions of system damping led to further amplification as the motion propagated to the superstructure. Compared to the other BMs, the amplification of superstructure accelerations as the water table was lowered from the fully saturated condition was most pronounced during TCU01 motion, where peak superstructure motions were found to increase with an increase in water table depth. As highlighted in Table 5-2, TCU01 had the lowest mean period, PGA, and I_a of all BMs which may be the reason for this observation.

5.6.2. Soil and foundation response in the near-field

Figure 5-9 compares the settlement and rotation time histories of the building foundation during WPI01 and TCU01 motions, which relied on data recorded using the two vertical laser displacement sensors targeting opposite sides of the foundation. Foundation settlements were obtained by averaging the displacement recordings, while rotations were computed as the difference in the displacement time histories divided by the horizontal separation distance between the two instruments. Time histories of recorded BMs during experiment WL_Dry are also presented to facilitate interpretation. The structure was observed to immediately settle after the motions were applied and settlements became negligible after earthquake loading ceased. Foundation settlement was greatest for the fully saturated condition, with experiments showing cumulative settlement reductions as the groundwater table was lowered. The largest reduction in

seismically induced foundation settlements, about 41 cm, can be seen between experiments WL_0.06B and WL_0.26B during WPI01 motion. This observation can be explained by a reduction in excess pore water pressure in the soil, below the foundation in the experiments with saturated-unsaturated soil layers. For example, the maximum excess pore pressure ratios, r_u, during WPI01, at a depth below the soil surface of about 2.1 m, in WL_0.06B and WL_0.26B were determined as 0.86 and 0.23, respectively (where r_u is the ratio of excess pore water pressure during seismic motion to initial effective vertical stress). Because excess pore water pressure directly impacts soil shear strength and reconsolidation, these findings suggest the benefits of unsaturated soil layers below shallow foundations, which may lead to increased matric suction below the foundation and reduced excess pore pressures below the water table thereby generating lower seismically induced volumetric strains. It should be noted that the abovementioned excess pore pressure ratios were determined at a horizontal offset distance of about 4.6 m from the edge of the foundation. Pore pressure ratios directly below the foundation are expected to be lower due to the increased confinement generated by the structure.

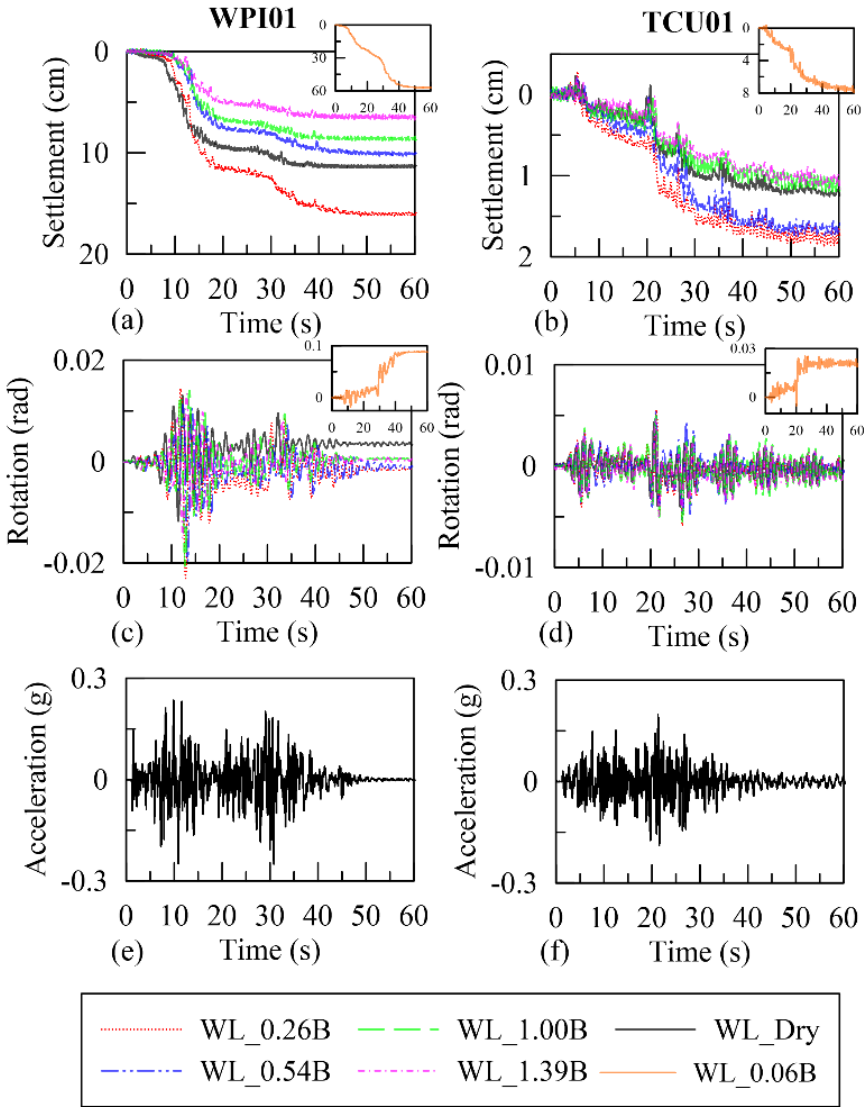

Figure 5-9. Time histories of foundation settlements (a, b) and rotations (c, d) during WPI01 and TCU01 input motions, in addition to the accelerations recorded at bedrock (e, f).

Figure 5-10 presents the variations in permanent seismically induced foundation and free-field settlements, termed Δ_{SF} and Δ_{FF}, respectively, as a function of D_w/B across each input motion. The laser displacement sensor which recorded the free-field vertical displacement is labeled LD_{FF} in Figure 5-2. Comparing Δ_{SF} and Δ_{FF} suggests that the foundation settled more than the free-field for the same applied motion and soil saturation condition. Theoretically, the primary deviatoric

settlement mechanisms dominating this increase in settlement are discussed by Dashti et al. (2010b) as: (1) the foundation soil experiences a partial bearing capacity loss under the static load of the structure, a result of soil softening; and (2) SFSI induced building ratcheting occurs. During an earthquake, foundation soil is subjected to repeated cyclic loading. When the soil is loaded, it's shear stiffness reduces, and it may experience inelastic and plastic deformations. When the loading is removed, the soil recovers a fraction of its pre-loading shear stiffness. In the case of SFSI induced building ratcheting, the shear stiffness of the soil is not fully recovered after each loading cycle, and a permanent deformation of the soil occurs. Experimentally, it is difficult to separate the mechanisms given by Dashti et al. (2010b), however, it is expected that a combination of both mechanisms created increased shear-type deformations in the foundation soil, as evidenced by the increased foundation settlements compared with those observed in the free-field.

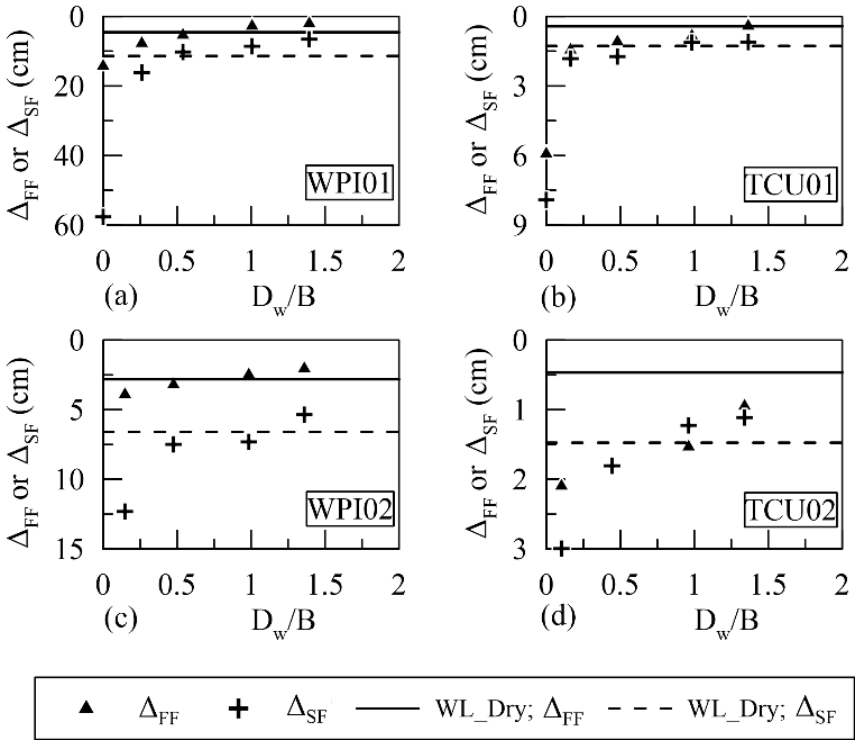

Figure 5-10. Variation of the permanent seismically induced free-field and foundation settlements as a function of the normalized depth of the groundwater table. Each subplot shows the response during one input motion.

The cumulative permanent rotation and settlement response of the structure across each experiment is shown in Figure 5-11.

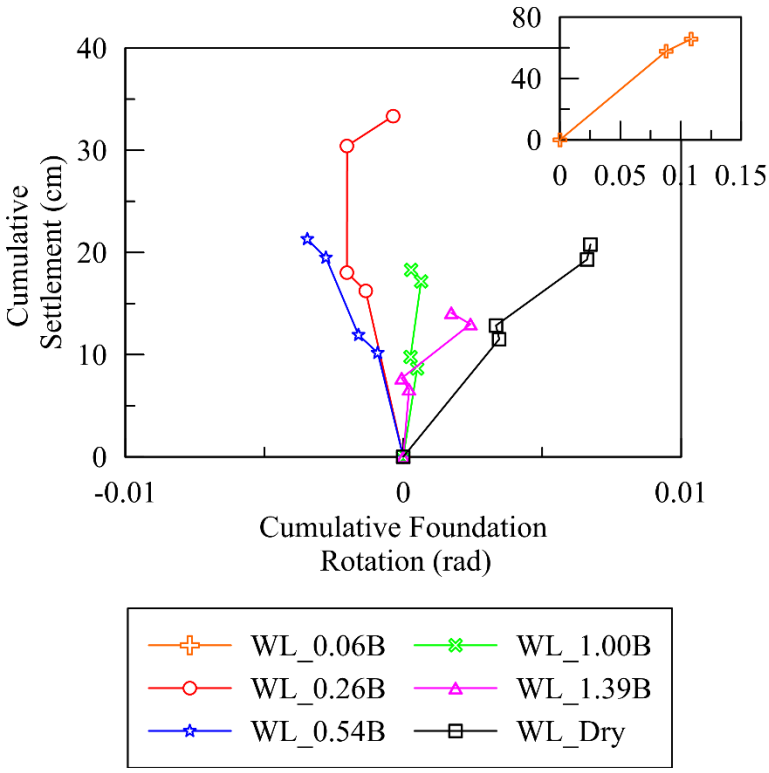

Figure 5-11. Variation of the permanent seismically induced foundation settlements and rotations across each experiment. Each data point corresponds to one input motion.

Cumulative foundation rotations in the unsaturated soil were reduced compared with the dry soil condition. Furthermore, compared with the fully saturated condition, the cumulative foundation rotations in the unsaturated tests were orders of magnitude lower. For example, the total cumulative foundation rotation, experienced during experiment WL_0.06B and WL_1.00B, were 0.0108 and 0.00029 rad, respectively. This observation can be explained by the increased stiffness generated by the presence of matric suction in the unsaturated soil, which increases the soil shear strength, leading to a reduction of foundation deformations. Furthermore, the limited pore pressure generation in the unsaturated soil may have further reduced the foundation deformations. Hence the effects of partial bearing capacity loss, which tend to control the permanent rotation of the foundation, were minimized in the unsaturated soil, compared with the fully saturated condition.

Figure 5-12 compares the foundation overturning moment versus foundation rotation for each experiment.

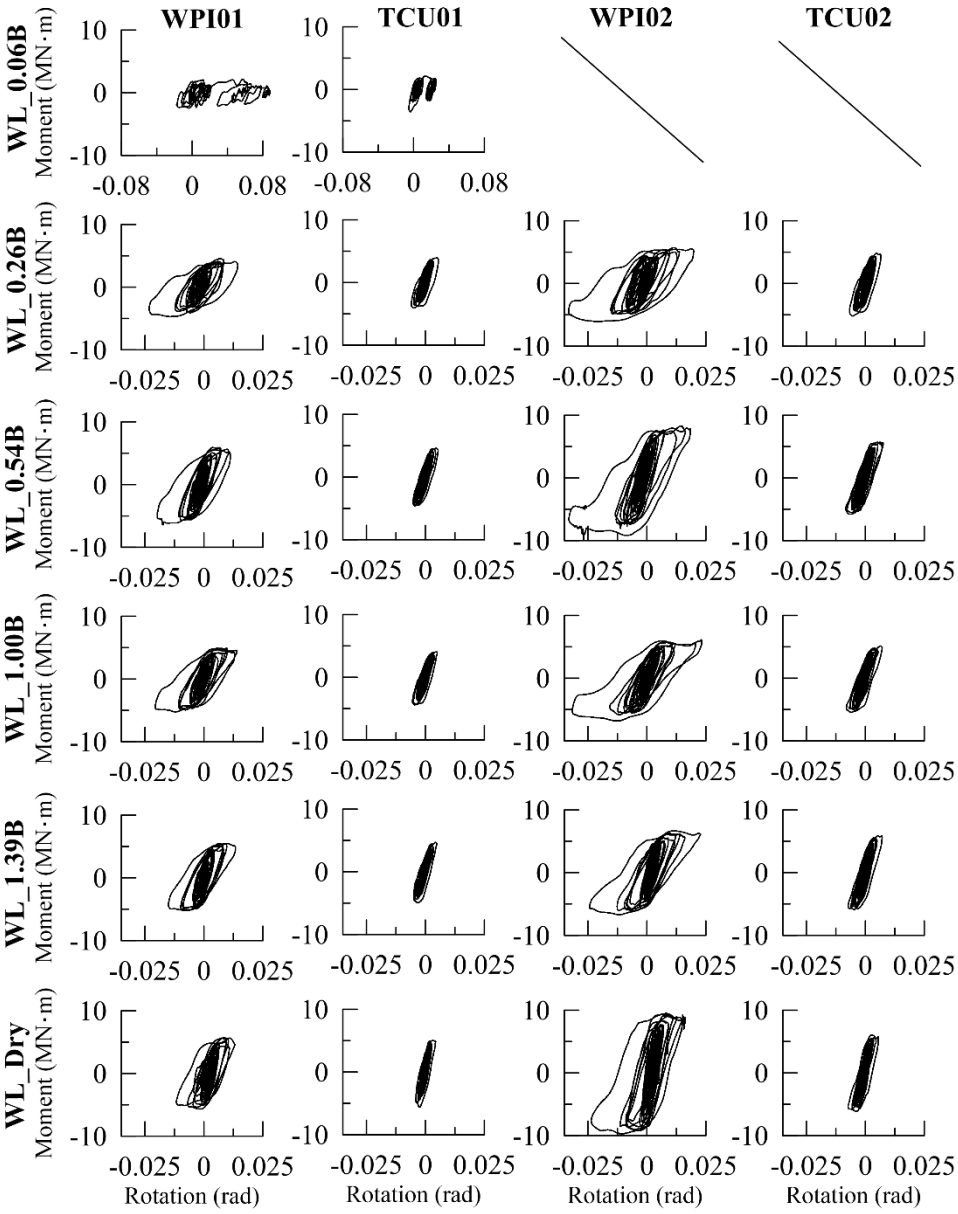

Figure 5-12. Foundation transient overturning moment versus rotation across all input motions. Each row corresponds to one input motion while each column corresponds to a single experiment. Experiment WL_0.06B was terminated after the application of the TCU01 input motion. Each column corresponds to one input motion while each row corresponds to one experiment.

WPI motions generated larger moment-rotation hysteresis loops than TCU motions. Markedly, during WPI01 and WPI02, the foundation was observed to reach its ultimate moment capacity, across all soil saturation conditions, by continuing to rotate without a clear change in the applied moment. The variation of the ultimate moment capacities, observed between WPI01 and WPI02, is the result of ground densification throughout testing. Ground densification increased the resistance of the foundation to bearing capacity failure and consequently increased the foundation moment capacity. When the structure was subjected to the more intense motions of WPI01 and WPI02, changes in the water table elevation had a clear influence on the shape and size of the hysteresis loops. Unsaturated soil below the foundation increased overturning moments compared with the fully saturated condition, due to increased soil stiffness at the soil-foundation interface which limited the extent of soil softening. The hysteresis loops tended to increase in size as the water level was lowered to WL_1.00B, thereafter showing a slight reduction. These observations point to the benefits of foundations resting on unsaturated soils, where rotational energy dissipation may be increased and settlements and rotations reduced, compared with the fully saturated and dry soil conditions. These findings are consistent with results reported in Chapter 4 (Turner et al., 2022a) for a completely elastic structure on unsaturated sandy silt. It should be noted that although the rotational energy dissipation may be greater in the unsaturated soil, settlement reductions in these conditions may result in lower overall energy dissipation at the foundation level. Energy dissipation at the foundation level comes from two primary mechanisms known as kinetic rotational and kinetic translational (Gajan & Kutter, 2009). The settlement reductions in the unsaturated experiments are linked to a decrease in the translational energy dissipation generated by vertical deformations. This decrease may result in lower overall energy dissipation at the foundation level, even though the energy dissipated by the rotational mechanism has increased.

5.6.3. Response of the superstructure

The response of the superstructure was experimentally assessed using transient drifts, superstructure accelerations, and bending strains at the column fuse locations. The calculation of total drift ratios was performed using accelerometer records from instruments mounted horizontally on the foundation and superstructure (labeled FM and SHM in Figure 5-2). Acceleration time histories were double integrated to produce records of transient horizontal displacements. Then, the total drift ratios were computed as the relative displacement between the superstructure and foundation, normalized by the height of the structure. The calculation of rocking drift ratios was performed using the vertical accelerometers mounted on opposite sides of the foundation (see Figure 5-2). Meanwhile, flexural drift ratios, were computed according to Karimi & Dashti (2016) as the difference between the total and rocking drift ratios.

Using the time histories of the transient drifts; the maximum absolute values of the total, rocking, and flexural drift ratios were computed for each experiment, and are presented in Figure 5-13 as a function of the normalized depth of the water table. In most cases, as the depth of the water table increased from the fully saturated condition, total and flexural drift ratios were amplified, while rocking drift ratios were reduced. Peak amplifications corresponded to mid-range water table depths between WL_0.54B and WL_1.00B. At water table depths greater than WL_1.00B, total and flexural drift ratios were observed to decrease. The reduction in total and rocking drift ratios between WL_1.00B and WL_1.39B can be attributed to the slightly reduced total density and degree of saturation in the underlying soil between the two experimental conditions. These two factors directly influence the shear stiffness and corresponding foundation level deformations. These findings are consistent with the results from Figure 5-7, where values of $\tilde{\beta}_{ex}$ were generally the lowest for these same water table elevations (WL_0.54B and WL_1.00B). Meanwhile, in a

related observation, the reduction in rocking drift ratios in the unsaturated and dry soil decreased the foundation deformations and damping. The reduction in $\tilde{\beta}_{ex}$ and foundation damping for the mid-range water table depths amplified seismic demand in the form of flexural drifts. In design, flexural drifts are typically limited to 2% (ASCE, 2017), or about $\pm$0.02 rad. Larger flexural drifts give rise to structural instability and nonstructural damage. Therefore, although the performance of the system when placed on unsaturated soil was improved (considering overall settlements and rotations), compared with the fully saturated condition, this improvement came at the cost of noticeable amplification in terms of seismic demand on the superstructure.

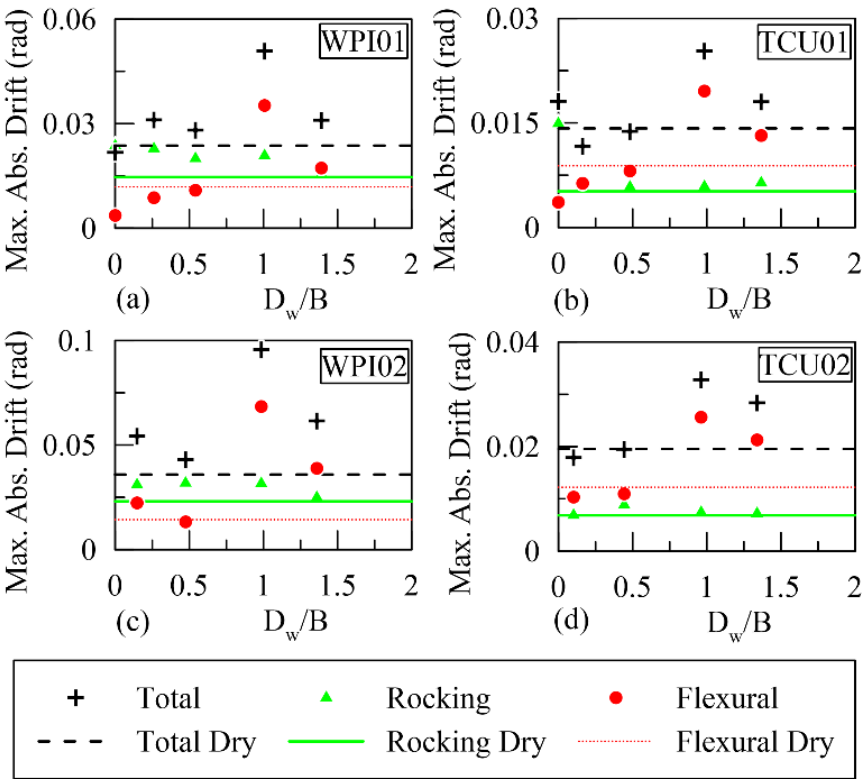

Figure 5-13. The maximum absolute values of the transient total, rocking, and flexural roof drift ratios across all input motions as a function of the normalized depth of the groundwater table. Each subplot shows the response during one input motion.

Amplification of seismic demand is further ameliorated in Figure 5-14 where comparisons are drawn between the peak bending strains recorded at the column fuse locations and the normalized depth of the water table. Peak bending strains were determined across all four structural fuses and are displayed as maximum, minimum, and residual values. Positive strains denote a clockwise bending moment, corresponding to the orientation of the structure shown in Figure 5-2. Results indicate that the fuses reached their yield strength and experienced inelastic, permanent, strains. The greatest maximum and minimum strains were observed to occur during WPI02, which was also the strongest ground motion. Notably, during this motion, WL_0.54B experienced the greatest bending strains observed across any experiment, with maximum and minimum values between 0.16 and -0.22 %, respectively. Although there is some scatter in the data presented in Figure 5-14, peak absolute bending strains were generally observed to increase as the water table depth was lowered.

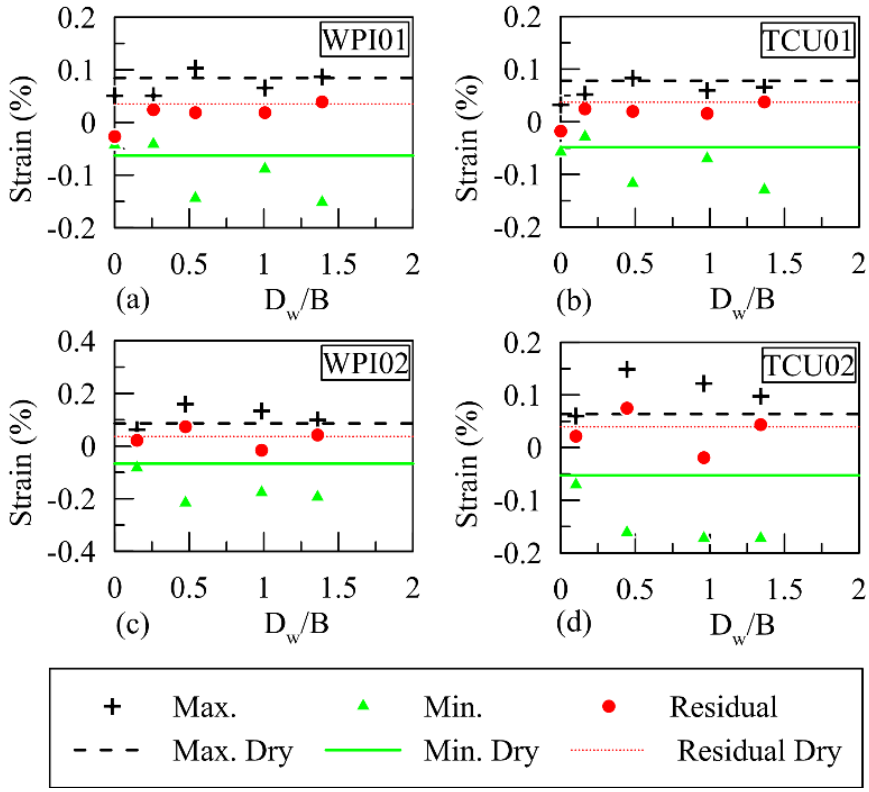

Figure 5-14. Maximum, minimum, and residual bending strains recorded at the column fuses across all input motions as a function of the normalized depth of the groundwater table. Each subplot shows the response during one input motion.

Consistent with the results presented in Figure 5-13, the highest bending strains generally corresponded to mid-range water table depths between WL_0.54B and WL_1.00B. Therefore, the reduction in energy damping at the soil-foundation interface in the unsaturated soil directly impacted the seismic demand on the superstructure. Increased seismic demands gave rise to greater flexural drifts and bending strains, compared with the fully saturated soil condition. It should be noted that although extensive efforts were made to ensure consistency between experiments, scatter in the presented data may be attributed to variations in the input motion characteristics between the experiments, strain gauge installation locations, and fuse strength properties.

5.7. CONCLUSIONS

This chapter described a centrifuge experimental campaign performed to evaluate the influence of variable groundwater table elevations on the seismic response of an inelastic building with a shallow foundation. The building was designed to amplify soil-structure interaction tendencies and to elicit nonlinear behavior at select instrumented locations, such as the base of the columns and the soil-foundation interface. Initially, an extension of an analytical procedure to predict flexible-base SFSI parameters, considering the influence of the water table elevation on the system response, was presented. The SFSI parameters computed analytically were compared with those achieved experimentally to judge the accuracy of the proposed procedure for use in practice and signify the need for further improvements. Results suggest that the analytical procedure significantly underestimated the values of $\tilde{\beta}$, while the prediction accuracy for the values of $\tilde{T}$ was dependent on the characteristics of the input motion. It is expected that the accuracy of the proposed procedure could be improved using analytical methods which capture inelastic and plastic soil and structural response. Furthermore increasing the number of modes of vibration considered in the analytical analysis could lead to a more accurate representation of the structural response to seismic loading, especially under higher seismic intensities. Additionally, the experimentally derived SFSI parameters of $\tilde{T}$ and $\tilde{\beta}$ were found to overpredict superstructure spectral accelerations using elastic response spectra computed from free-field motions. Therefore, using elastic free-field response spectra to predict seismic demands on an inelastic structure may lead to a conservative design scenario.

Furthermore, the performance of the soil-foundation-structure system was evaluated through settlements, rotations, overturning moments, accelerations, drifts, and bending strains. Results suggested that the response of the system was impacted by the depth of the water table and the

characteristics of the input seismic motions. Deeper water table depths increased the stiffness and reduced the damping of the underlying soil, which reduced foundation settlements and rotations, but led to amplifications, in terms of foundation overturning demands, compared with the fully saturated and dry soil conditions. Although greater overturning moments may have resulted in higher rotational energy dissipation, the overall energy dissipation at the soil-foundation interface was hypothesized to reduce in unsaturated soil, a consequence of the observed reduction in settlement. Stiffer soil in mid-range water table depths amplified the accelerations and forces transmitted to the superstructure, resulting in greater flexural drifts compared with the fully saturated and dry soil conditions. Greater flexural drifts often resulted in higher recorded bending strains at the base of the columns in the instrumented structural fuse locations. This study highlights the potential trade-offs of founding a structure on soil with variable water table depths. Shallow water table elevations give rise to greater deformations, in terms of settlements and rotations, and associated nonlinearity at the soil-foundation interface. Meanwhile, greater water table depths lead to greater deformations, in terms of flexural drifts and bending strains, and associated nonlinearity in above-ground superstructure locations.

CHAPTER 6

CROSS-EXPERIMENTAL COMPARISON OF RFSS AND ICSS SEISMIC RESPONSE

6.1. ABSTRACT

The Rocking Foundation Structural System (RFSS) and Inelastic Column Structural System (ICSS) models were designed to exhibit unique responses when subjected to dynamic loading in the geotechnical centrifuge. RFSS was designed to exhibit a completely elastic structural response. In contrast, ICSS was designed to exhibit an inelastic structural response. However, both models were tested under similar experimental conditions, allowing for cross-experimental comparisons to be made. In this chapter, the influence of the water table depth on the behavior of RFSS is compared to ICSS during a representative input motion, which was applied to both model structures. Results show that the depth of the water table has a greater influence on the dynamic response of the RFSS model, thus the water table elevation should be considered in the design and analysis of rocking foundations. The findings from this chapter inform the seismic design concept incorporated in the SSBRF and TSBRF physical models, tested in Chapter 7.

6.2. INTRODUCTION

As discussed in Chapter 2, Section 2.2, soil-structure interaction characterizes the physical interaction which occurs between the foundation of a structural system and the supporting, compliant, soil layer during seismic excitation. Compared with a structure, supported in a fixed-base condition, SSI typical results in lengthening of the building's fundamental period, $\tilde{T}/T$ and the generation of foundation damping, $\tilde{\beta}_0$. Both the period lengthening and the introduction of $\tilde{\beta}_0$ influence the overall damping of the soil-structure system, $\tilde{\beta}$, as characterized by Equation 2-8.

In this chapter, results from the two series of dynamic centrifuge experiments presented in Chapter 4 and Chapter 5, termed RFSS and ICSS experiments, respectively, are compared. In each series of experiments, a SDOF structural system is shallowly embedded in sandy silt, and several experiments are performed. In each experiment, the water table is located at a distinct depth below the surface of the soil layer with capillary rise controlling the degree of saturation above the water table depth. In the first series of experiments, outlined in Chapter 4 and performed on RFSS, the response of a building model, designed to exhibit a completely elastic structural response is explored. In the second series of experiments, outlined in Chapter 5 and performed on ICSS, the response of a building model, designed to exhibit an inelastic structural response (at select instrumented locations) is explored. Regardless of the experimental series, results are presented which compare seismically induced nonlinear SSI parameters to the depth of the water table below the surface of the soil. Namely, the response is explored in terms of $\tilde{T}$, $\tilde{T}/T$, and $\tilde{\beta}$. The goal of this chapter is to highlight and compare the influence of the water table elevation on the nonlinear response of the soil-structure systems. Conclusions from this chapter are used to inform the structural design of the SSBRF and TSBRF physical models.

6.3. DESIGN OF PHYSICAL MODELS

The design of the RFSS and ICSS physical models is discussed in Chapter 3, Section 3.9. To promote cross-experimental comparisons between the two models, several design parameters were chosen to be held approximately constant, regardless of the model structure. These parameters include the total height of the model (H), foundation width (B), foundation length (L), foundation embedment depth (D_f), foundation bearing pressure (q), and fixed-base modal parameters including T and system damping, β. Table 3-4 summarizes and compares the parameters of the physical models in the prototype scale.

6.4. CENTRIFUGE EXPERIMENTS AND INPUT MOTION

A total of six centrifuge experiments were conducted on each physical model. Table 6-1 summarizes experimental identifiers and compares the initial depths of the water table below the surface of the soil layer as a function of B. The table suggests that the achieved water table depths were similar across both experimental campaigns. For detailed descriptions of the experiments performed on RFSS and ICSS, the reader is referred to Chapter 4 and Chapter 5, respectively.

Table 6-1. Description and comparison of the experiments performed on the RFSS and ICSS physical models prior to seismic motion application.

RFSS Model		**ICSS Model**	
Specimen Name	D_w/B	**Specimen Name**	D_w/B
ML_D	N/A	WL_Dry	N/A
ML_WL_0.02B	-0.02	WL_0.06B	-0.06
ML_WL_0.24B	0.24	WL_0.26B	0.26
ML_WL_0.44B	0.44	WL_0.54B	0.54
ML_WL_1.00B	1.00	WL_1.00B	1.00
ML_WL_1.52B	1.52	WL_1.39B	1.39

The influence of the water table depth on the behavior of the physical model built for RFSS can be compared to that of ICSS during a representative input motion, which was applied across both test series. This representative motion was the first applied motion in Chapter 5 (WPI01 in Table 5-2), while it was the fourth motion in Chapter 4 (WPI03 in Table 4-2). Changes in the specimen density due to the preceding input motions during the experiments performed on RFSS are expected to have a relatively minor, though non-zero impact on the presented results. Figure 6-1 compares the achieved WPI01 input motion response spectrum recorded during ML_WL_0.24B with the WPI03 input motion response spectrum recorded during WL_1.00B. The figure suggests, for periods greater than about 0.3 s, the spectral accelerations across the motions were similar. Between a period of 0.1 to 0.3 s, spectral accelerations of the WPI03 motion during the WL_1.00B were greater than those of WPI01 during ML_WL_0.24B. Because the fixed-base fundamental periods of both structures were greater than 0.5 s, the observed difference in short-period spectral accelerations (from 0.1 to 0.3 s) is not expected to generate seismic response variations between the experiments. Therefore, the input motions were similar across the two experimental conditions, especially considering the periods of interest, and allows for a reliable comparison of the system responses.

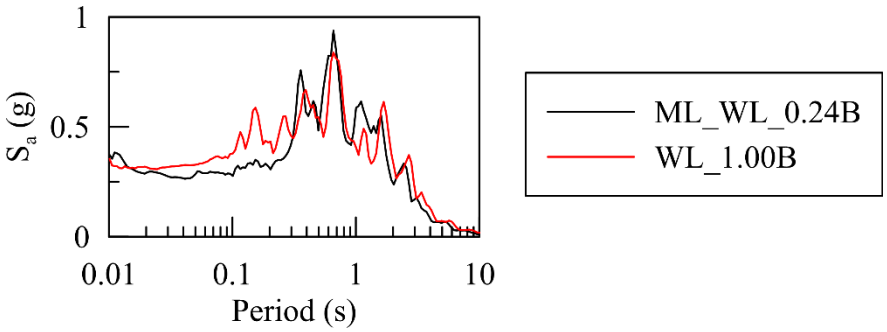

Figure 6-1. Comparison of recorded input motion acceleration response spectra (5% damped) showing WPI01 during ML_WL_0.24B and WPI03 during WL_1.00B.

6.5. CROSS-EXPERIMENTAL RESULTS AND DISCUSSION

Figure 6-2 shows the deviation of $\tilde{T}$, $\tilde{T}/T$, and $\tilde{\beta}$, determined across RFSS and ICSS, with respect to the normalized depth of the water table. This figure shows that as the depth of the water table increased, values of $\tilde{T}$, $\tilde{T}/T$, and $\tilde{\beta}$ decreased. Therefore, the soil, with the deeper water table depths, behaved stiffer, leading to less flexibility at the soil-foundation interface. Furthermore, as the depth of the water table increased, the seismically induced pore water pressure generation reduced in the unsaturated zones below the foundation. These factors led to an overall stiffer seismic soil response and a corresponding reduction in damping, for the soil with the deeper water table depths. These findings are consistent with Stinson (2014), where deeper water table depths led to decreased values of $\tilde{T}/T$ for a field-scale model structure subject to cyclic loading.

Results also suggest that changes in $\tilde{T}$, $\tilde{T}/T$, and $\tilde{\beta}$ with respect to the depth of the water table were a function of the flexibility of the superstructure. For example, increasing the depth of the water table during experiments on RFSS had a major impact on the flexible-base SSI parameters. Meanwhile, increasing the depth of the water table during experiments performed on ICSS had a relatively minor impact on these parameters.

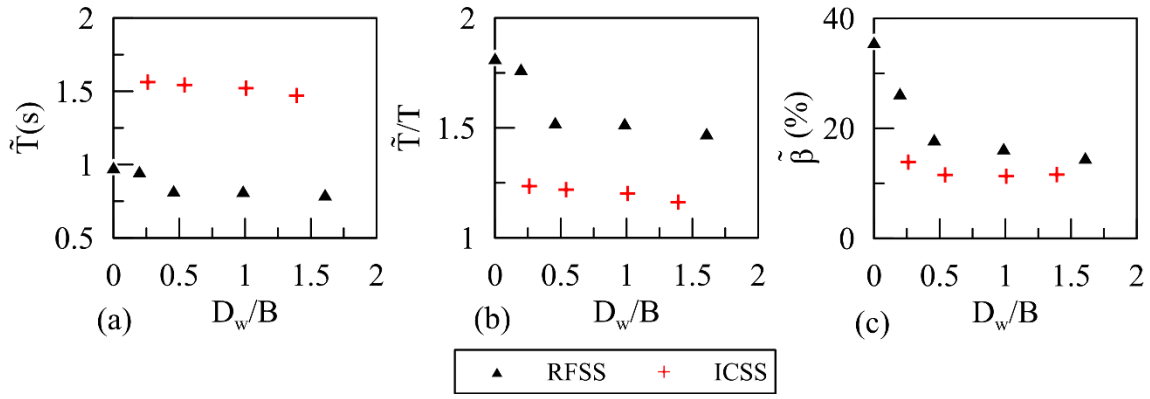

Figure 6-2. Variation of the flexible-base parameters determined across RFSS and ICSS with respect to the normalized depth of the water table showing (a) flexible-base fundamental periods; (b) period-lengthening ratios; and (c) flexible-base system damping ratios.

Equation 2-8 can be used to explain the factors contributing to this phenomenon, where $\tilde{\beta}$ is a function of two damping sources that include $\tilde{\beta}_0$ and β. The physical model built for RFSS was observed to behave within its elastic range during testing, therefore the fixed-base modal parameters of β and T remained uniform during dynamic loading. Meanwhile, the physical model built for RFSS was observed to behave inelastically, resulting in increased fixed-base modal parameters during dynamic loading. Therefore, flexible-base SSI parameters during the RFSS experiments were governed by deformations at the soil-foundation interface. In contrast, during ICSS experiments, the amount of system nonlinearity was governed by deformations at both the soil-foundation interface and in above-ground superstructure locations (changing β and T). Regardless of the test series, increasing the water table depth led to a stiffer soil-foundation interface response. During the RFSS experiments, the stiffer soil-foundation interface caused a corresponding reduction in $\tilde{T}$, $\tilde{T}/T$, and $\tilde{\beta}$ as the water table was lowered. Meanwhile, during experiments performed on RFSS experiments, reductions in nonlinearity at the soil-foundation interface, due to deeper water table depths, were offset by the introduction of deformations and

associated nonlinearity in above-ground superstructure locations. Therefore, increasing the water table depth during the experiments performed on ICSS had a lower overall impact on the flexible-base SSI parameters, compared with the response observed during the experiments performed on RFSS.

6.6. CONCLUSIONS

In Chapter 4 and Chapter 5, two series of dynamic centrifuge experiments were performed to evaluate the influence of the water table depth on the dynamic response of a building, shallowly embedded in sandy silt. In one series of tests, the building was designed to remain completely elastic during dynamic loading, in the other, the building was designed to behave inelastically at select structural locations. To promote cross-experimental comparisons, variations in the experimental conditions, input seismic motions, and other physical model parameters (aside from superstructure flexibility), between the two experimental series were minor. Results suggest that the depth of the water table, below the soil surface, had a clear influence on the SSI induced parameters of period lengthening and system damping. As the water table depth increased, period lengthening and system damping were found to reduce, suggesting the soil behaved stiffer due to increased matric suction generated in the soil, above the water table elevation. Furthermore, the response of the structural system also influenced the SSI induced parameters. As the water table elevation was lowered during the experiments performed on the elastic structural model, greater changes in SSI parameters were observed compared to when the water table was lowered during the experiments performed on the inelastic building.

CHAPTER 7

SEISMIC PERFORMANCE OF BRIDGE SYSTEMS INCORPORATING ROCKING FOUNDATIONS ON UNSATURATED SOIL

7.1. ABSTRACT

Rocking shallow foundations have seismic performance advantages over conventional fixed-base foundations; they can limit the inertial load transmitted to the structure as a function of the capacity of the foundation. Although previous experimental campaigns have highlighted the effectiveness of rocking foundations in practice, these have tended to focus on standalone simplified single-degree-of-freedom systems. Structures incorporating rocking foundations, such as bridges, are more complex than these simplified designs. In addition, limited experimental work has been performed to assess the influence of the soil's degree of saturation on the seismic performance of rocking foundations, with most studies focusing on soil layers in dry or fully saturated conditions. The purpose of this chapter is to appropriately model and assess the behavior of a prototype bridge system, built to incorporate rocking foundations, and placed on unsaturated sandy silt layers. A

series of dynamic centrifuge tests were performed on single- and two-span models of the prototype bridge. The soil and structure were subjected to a suite of seismic motions in the transverse direction. The experimental program consisted of tests on dry, saturated, and four mixed saturated-unsaturated soil layers where the water table depth was lowered to a certain depth below the soil surface. Initially, a brief comparison is made between the response of the Single-Span Bridge with Rocking Foundations (SSBRF) and Two-Span Bridge with Rocking Foundations (TSBRF) models when embedded in a dry soil layer. Then, a detailed analysis of the response of the SSBRF physical model is presented to evaluate the influence of the water table condition on the seismic response. Finally, comparative analyses are performed to assess variations in the response of the SDOF Rocking Foundation Structural System (RFSS) and SSBRF as a function of the water table depth. The results show that as the depth of the water table increased, the foundation settlements, foundation rotations, bridge deck drifts, and overall bridge deck rotations decreased, while the overturning moment applied to the foundations increased. Furthermore, the procedure, developed in Chapter 4, Section 4.7.1, to predict the ultimate moment capacity of the foundation as a function of the depth of the water table is further validated against the M_{max} values achieved across the SSBRF experimental response.

7.2. INTRODUCTION

Researchers have been working towards implementing rocking foundations into the design methodologies for ordinary bridges considering drift, settlement, and overturning moment demand. Previous experimental work on rocking foundations has shown that the nonlinear behavior of foundations can dissipate seismic energy while protecting the columns if the moment capacity of the footing is lower than the moment capacity of the column (Anastasopoulos et al., 2010; Deng & Kutter, 2012; Loli et al., 2014). Similar to the structures designed for Chapter 4 and

Chapter 5, termed Rocking Foundation Structural System (RFSS) and Inelastic Column Structural System (ICSS), most previous experimental work has relied on simplified SDOF systems composed of a lumped mass, supported by columns and a foundation (i.e., Antonellis et al., 2015; Gajan & Kutter, 2008, 2009; Kokkali et al., 2015; Tsatsis & Anastasopoulos, 2015; Turner et al., 2022a, 2022b). In practice, structures incorporating rocking foundations, such as bridges, are more complex than these simplified designs. Little attention has been given to the behavior of rocking foundations integrated into full-scale design and modeling of bridge behavior. A typical mid-span of a bridge is composed of a bridge deck supported on both sides by a column-foundation system. The dynamic behavior of a "realistic bridge" may be different than that of a SDOF system due to the interconnectedness of the substructure and superstructure systems.

Deng & Kutter (2012) modeled the seismic response of bridge systems incorporating rocking foundations, but only considered the performance of rocking foundations placed on dry soil. Modeling soil layers as completely dry may not fully reflect the in-situ conditions for most natural ground layers. For example, in regions with a shallow water table, surficial soil layers, above the groundwater table, are mostly classified as unsaturated. Due to variations in precipitation levels throughout the year, the water table and vadose zone, vary seasonally. When the water table is lower than the depth of the soil layer surface, water ascends due to capillarity and generates a zone of unsaturated soil.

This chapter characterizes the dynamic response of a bridge system built to incorporate rocking foundations when placed on soils with variable saturation conditions. The physical model is subjected to seismic loading in the longitudinal direction and the response of the system is recorded. Initially, a brief comparison is made between the response of the Single-Span Bridge with Rocking Foundations (SSBRF) and Two-span bridge with Rocking Foundations (TSBRF)

models when embedded in a dry soil layer. Then, a detailed analysis of the response of the SSBRF physical model is presented to evaluate the influence of the water table condition on foundation-level settlements, foundation rotations, maximum foundation overturning moments, bridge deck drifts, global bridge deck rotations, and changes in the damping ratios and fundamental period of the system. Furthermore, the procedure, developed in Chapter 4, Section 4.7.1, to predict the ultimate moment capacity of the foundation as a function of the depth of the water table is further validated against the M_{max} values achieved across the SSBRF experimental response. Finally, analysis is performed to assess variations in the response of RFSS and SSBRF as a function of the groundwater table depth.

7.3. DESIGN OF PHYSICAL MODELS

The influence of the water table depth on the performance of simplified SDOF systems is studied in Chapter 4 and Chapter 5. Chapter 6 compared the seismic response of these systems. Results show that the water table depth has a greater influence on the seismic response of the RFSS model compared to the ICSS model, suggesting that the influence of the water table should be considered in the design and analysis of rocking foundations.

The purpose of the SSBRF and TSBRF physical models is to appropriately model the behavior of a prototype bridge system, built to incorporate rocking foundations using a geotechnical centrifuge. SSBRF models a single span of the prototype bridge, while TSBRF models two spans of the prototype bridge. Therefore, SSBRF incorporates two bents supporting the superstructure and TSBRF incorporates three bents. In both SSBRF and TSBRF models, foundations were sized uniformly and featured a model scale length, width, and height of 45, 45, and 10 mm, respectively. Chapter 3, Section 3.9 provides a detailed discussion regarding the seismic design of the SSBRF and TSBRF physical models. Figure 3-15 displays a photograph of the SSBRF and TSBRF

physical models while the main properties of these models are highlighted in Table 3-5. Properties, including foundation bearing pressure and mass moment of inertia, are based on the tributary mass estimated to be applied to each bent location. Bridge bents are labeled in Figure 7-1 and Figure 7-2.

7.4. EXPERIMENTAL PROCEDURES

In this chapter, seven geotechnical centrifuge experiments were conducted. One of the experiments was performed on the TSBRF model in the dry condition. Meanwhile, six experiments were performed on the SSBRF physical model, with each experiment having a unique soil saturation condition. The experimental layout for the dry test on the TSBRF model is shown in Figure 7-1, while Figure 7-2 shows a typical experimental layout for the experiments performed on the SSBRF physical model. Due to instrumentation constraints, only two foundations of the TSBRF model were instrumented with accelerometers and laser displacement sensors. These foundations are shown in Figure 7-1, and include the foundations associated with TSBRF_OB_1 and TSBRF_MB.

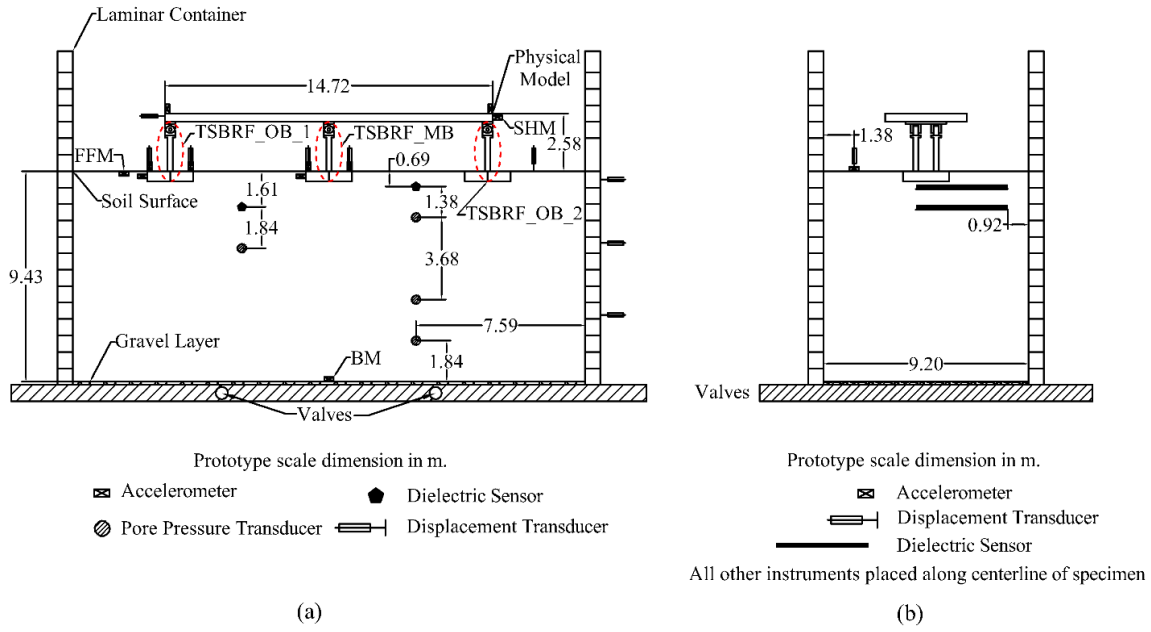

Figure 7-1. Schematic instrumentation layout of the centrifuge experiment performed on the TSBRF physical model showing (a) front view and (b) side view.

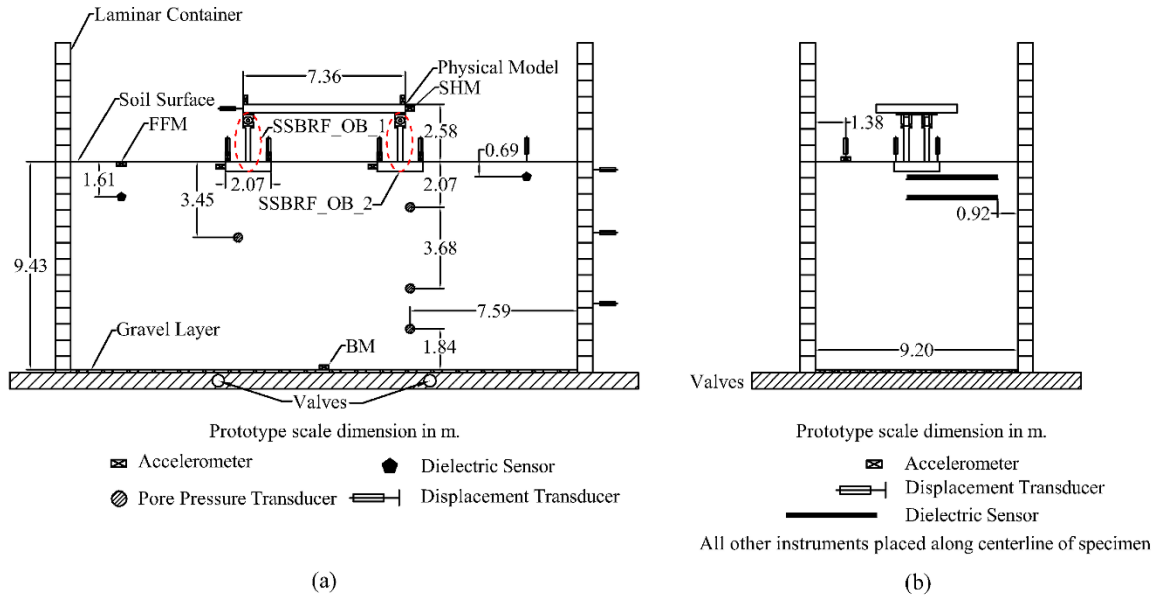

Figure 7-2. Schematic instrumentation layout of a typical centrifuge experiment performed on the SSBRF physical model showing (a) front view and (b) side view.

Soil profiles were prepared in the laminar container according to Chapter 3, Section 3.6, then the soil layer was either saturated or left in a dry state depending on the desired saturation condition. After the sample was prepared, the laminar container was transferred to the shake table platform and spun up to 46-g centripetal acceleration. After reaching the target centripetal acceleration, the water level was lowered, in-flight, to the desired depth according to Chapter 3, Section 3.8. Table 7-1 describes the experimental conditions and provides experimental identifiers related to the depth of the water table. Reference names are provided in the following example form: SSBRF_WL_XXB, where XX is the initial depth of the water table (before application of the first seismic motion) below the soil layer surface as a function of the width of the foundation, B.

Table 7-1. Description of dynamic centrifuge experiments conducted in this chapter and specific parameters related to the specimen and foundation determined prior to WPI01 motion application.

Specimen Name	Structure	Fluid	Initial D_w/B^*	Initial $A/A_c{}^{**}$
TSBRF_WL_Dry	TSBRF	Dry	N/A	2.59/3.09
SSBRF_WL_Dry	SSBRF	Dry	N/A	3.09
SSBRF_WL_0.00B	SSBRF	Water	-0.17	2.41
SSBRF_WL_0.57B	SSBRF	Water	0.57	5.05
SSBRF_WL_1.07B	SSBRF	Water	1.07	7.96
SSBRF_WL_1.49B	SSBRF	Water	1.49	8.63
SSBRF_WL_1.97B	SSBRF	Water	1.97	9.41

*A positive D_w/B indicates that the groundwater table is below the soil surface, while a negative number shows that the groundwater table is above the soil surface.

** Initial A/A_c values are provided for both outer (TSBRF_OB_1 and TSBRF_OB_2) and middle (TSBRF_MB) bent locations in the form: outer/middle

After the desired water table depth was achieved, each experiment was subjected to a series of four seismic motions. The motion recorded by the accelerometer at the base of the container is denoted as bedrock motion, BM. Input motions were scaled horizontal components of two historic earthquakes, which include the 1994 M_w 6.7 Northridge, California earthquake (WPI motion) and the 1999 M_w 7.6 Chi-Chi, Taiwan earthquake (TCU motion). These motions were separated by a

period of about three minutes in the model scale to allow for pore-water pressure dissipation to occur. Table 7-2 lists the input motions and the order in which they were applied. Furthermore, ground motion parameters, determined based on the BM recorded during SSBRF_WL_Dry, are listed in Table 7-2. Figure 7-3 and Figure 7-4 show the acceleration time histories, I_a time histories, and 5% damped response spectra of the recorded BMs during SSBRF_WL_Dry. To ensure achieved motions were similar across different test payloads, Figure 7-5 compares BM parameters from SSBRF_WL_1.97B with those of SSBRF_WL_Dry. The figure indicates that the motions were similar, therefore the seismic response of the structure(s) can be compared as a function of the underlying soil saturation condition.

Table 7-2. Characteristics of the input motions and the order in which they were applied.

Ground Motion No.	**Event**	**Ground Motion ID**	**PGA (g)**	**Significant Duration, D_{5-95} (s)**	**Max. Arias Intensity (m/s)**	**Mean Period (s)**
1	1994 Northridge	WPI01	0.09	21.3	0.22	1.04
2	1999 Chi-Chi	TCU01	0.12	17.65	0.29	0.74
3	1994 Northridge	WPI02	0.27	21.12	2.00	1.03
4	1999 Chi-Chi	TCU02	0.20	20.32	1.16	0.77

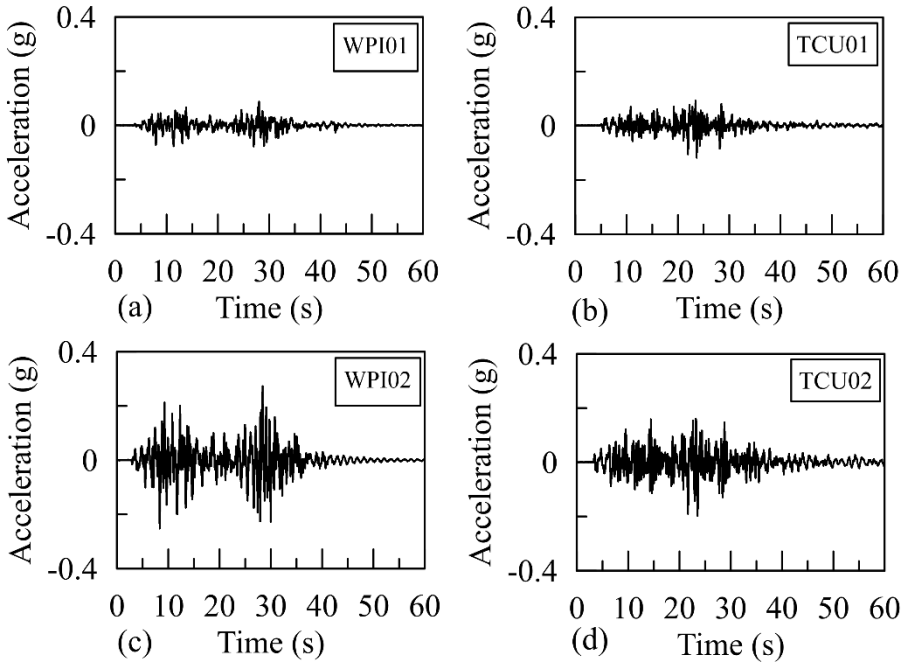

Figure 7-3. Acceleration time histories of the recorded BMs during SSBRF_WL_Dry. Each subplot corresponds to one input motion.

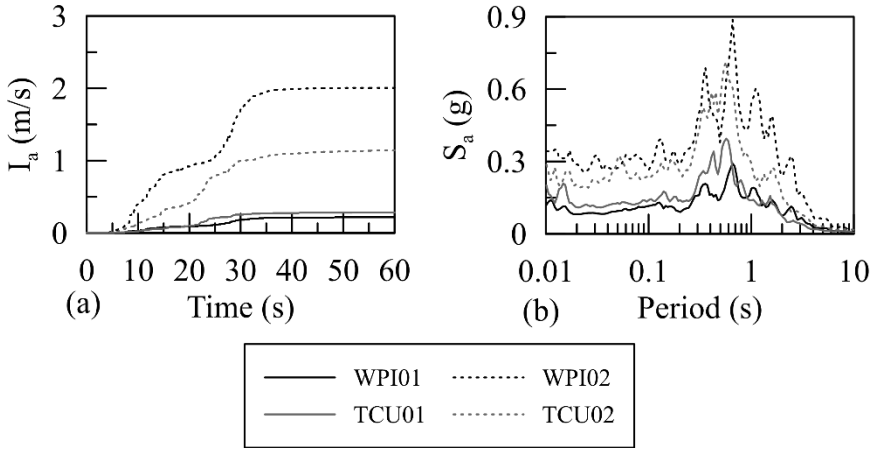

Figure 7-4. (a) Arias intensity time histories and (b) response spectra of the recorded BMs during SSBRF_WL_Dry.

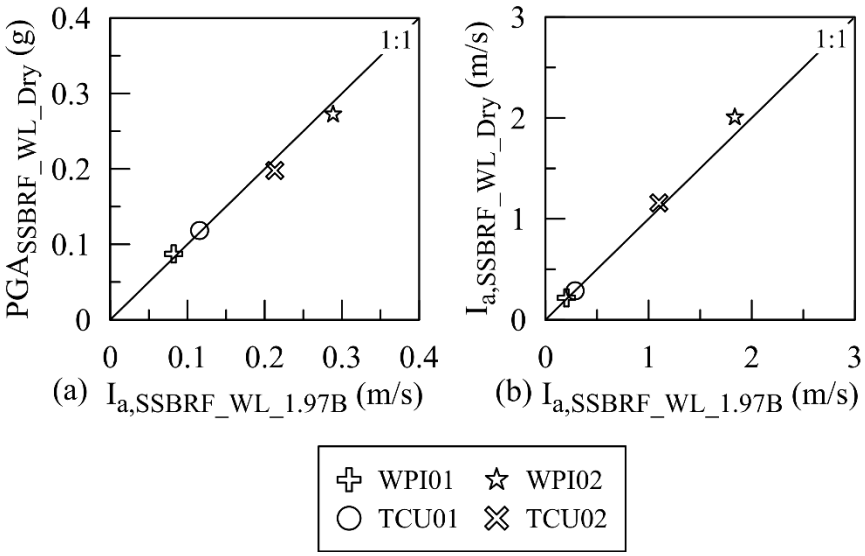

Figure 7-5. Comparison of input motion parameters between SSBRF_WL_Dry and SSBRF_WL_1.97B showing (a) PGA; and (b) maximum Arias intensity.

7.5. RESULTS AND DISCUSSION

The dynamic centrifuge experiments were analyzed to evaluate the effect of the soil saturation condition on the seismic response of the soil, foundation, and structural systems. The following results are presented in the prototype scale.

7.5.1. Comparison of the seismic response of SSBRF and TSBRF

SSBRF and TSBRF represent single and two-span models of the prototype bridge structure described in Chapter 3, Section 3.9. This section compares the results of experiment SSBRF_WL_Dry to experiment TSBRF_WL_Dry. Emphasis is placed on comparisons between the foundation and bridge deck response.

Figure 7-6 displays the overall response of the foundations in terms of settlement-rotations across the input motions. Each foundation was monitored by a pair of vertical laser displacement sensors targeting opposite sides of the foundation, as shown in Figure 7-1 and Figure 7-2. Displacement

recordings were initialized to zero at the start of each motion, then foundation settlements were obtained by averaging the initialized displacement recordings, while rotations were computed as the difference in the displacement time histories divided by the horizontal separation distance between the instruments.

The gradient of the settlement-rotation curves indicates whether the foundation midpoint loses contact with the supporting soil as the foundation rotates, providing evidence of foundation uplift that takes place throughout the experiment and input motions. Settlement-rotation plots show that the foundations accumulated permanent settlement throughout loading. Based on the understanding of the rocking mechanism, the foundation should experience residual settlement, as opposed to residual uplift, if the A/A_c ratio is small (e.g., <15). Table 7-1 specifies that the initial A/A_c ratios of the foundations varied from 2.59 to 3.09, depending on the structure and bent location. Findings from Figure 7-6 further confirm the notion that for foundations with $A/A_c < 15$, residual foundation settlements should be expected. It should be noted that TSBRF_MB experienced minor transient foundation uplift during the beginning of WPI01, while TSBRF_OB_1 experienced transient settlement. If the outer footing of the bridge settled more than the middle footing, the vertical load applied to the supporting soil beneath the middle footing may be influenced, which could have led to the minor transient uplifts observed during the beginning of WPI01 motion for TSBRF_MB.

Figure 7-6 also indicates that the foundation response is a function of the intensity of the input motion. For example, during the low-level input motions of WPI01 and TCU01, the foundations behaved stiffer and experienced reduced settlements and rotations compared to the response when subjected to the higher-intensity input motions of WPI02 and TCU02.

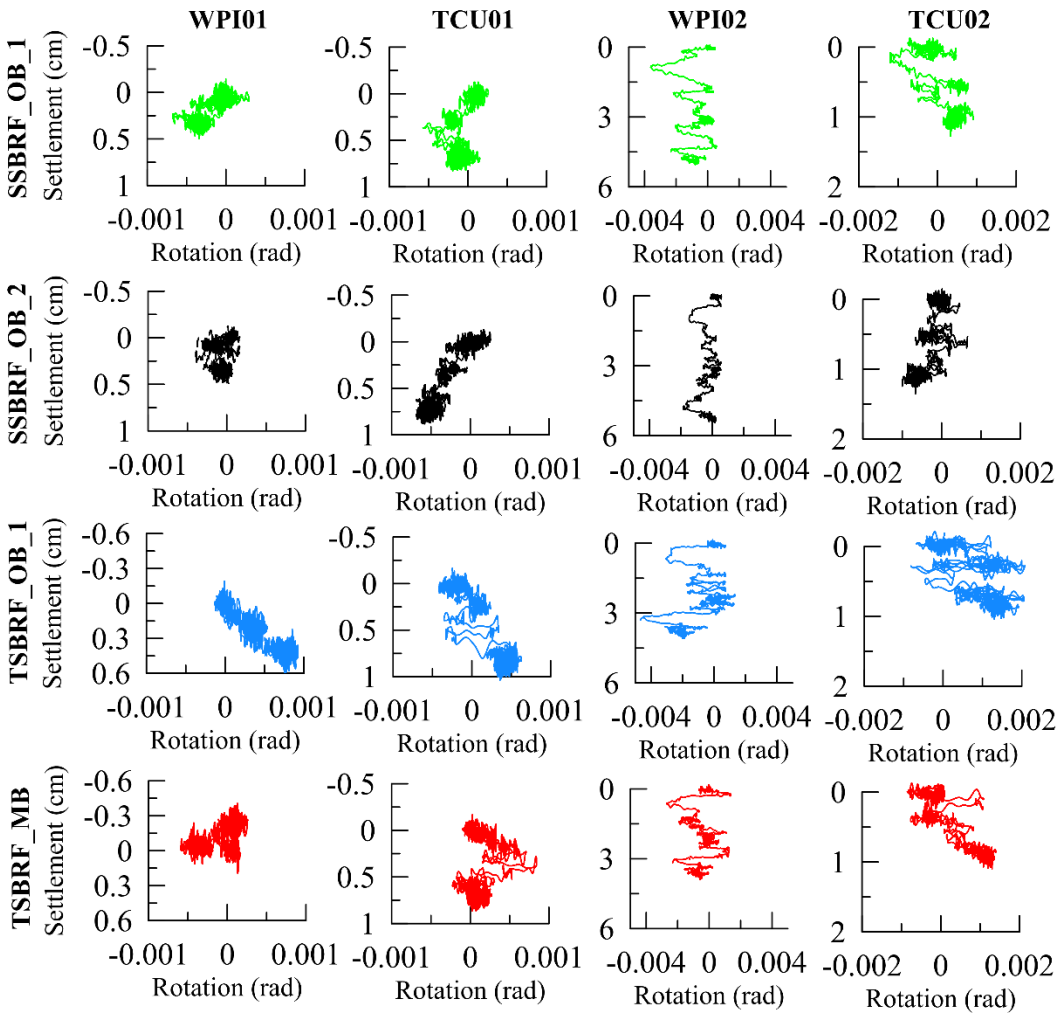

Figure 7-6. SSBRF and TSBRF foundation settlement-rotation plots across the input motions when placed on the dry soil layer. Each column corresponds to one input motion while each row shows the foundation response at one bent location.

The settlement-rotation response across the foundations is further synthesized in Figure 7-7 and Figure 7-8. Figure 7-7 displays the peak, θ_P, and residual, θ_R, foundation rotations determined for each foundation across each motion. θ_R values were found by initializing the foundation rotation to zero at the start of each motion, then finding the residual rotation at the end of the motion. θ_P values were determined from the initialized rotation-time histories and were taken as the absolute

value of the maximum rotation experienced throughout the applied motion. Figure 7-8 displays the residual foundation settlements, Δ_{SF}, after the application of the motion.

As highlighted in Figure 7-7 and Figure 7-8, due to the relatively low levels of seismic excitation generated by WPI01 and TCU01, the seismic response variations between the foundations and across both structures were minor. In general, TSBRF_OB_1 experienced the largest peak and residual rotations among the four foundations. During motion WPI02, TSBRF_OB_1 experienced a maximum of about 0.0047 radians of rotation, which was the largest observed rotation among the foundations across all input motions. Furthermore, during the higher intensity ground motion of WPI02, the foundations of SSBRF settled an average of 1.3 cm greater than the foundations of TSBRF. The presence of three bents supporting the bridge deck in TSBRF may have influenced the stability of the system, resulting in a slight reduction in foundation-level settlements, compared to SSBRF when subjected to the WPI02 motion. Soil layer densification due to WPI02 motion limited the amount of residual settlement generated during TCU02. It is worth mentioning that residual foundation level settlements due to WPI02 motion (across both TSBRF and SSBRF) were limited to 1.8-2.6% of the total foundation width (2.07 m). Thus, variations in settlements between the foundations and structures were relatively insignificant.

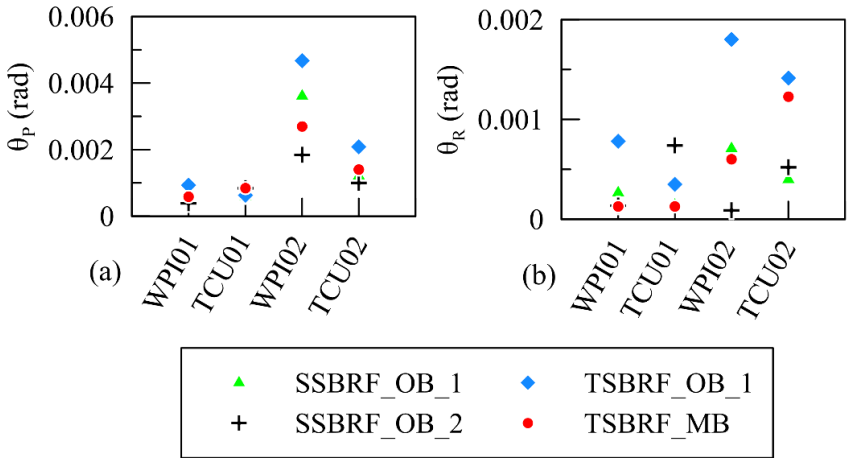

Figure 7-7. Foundation rotations across the input motions recorded during the dry experiments performed on TSBRF and SSBRF showing (a) peak rotations and (b) residual rotations.

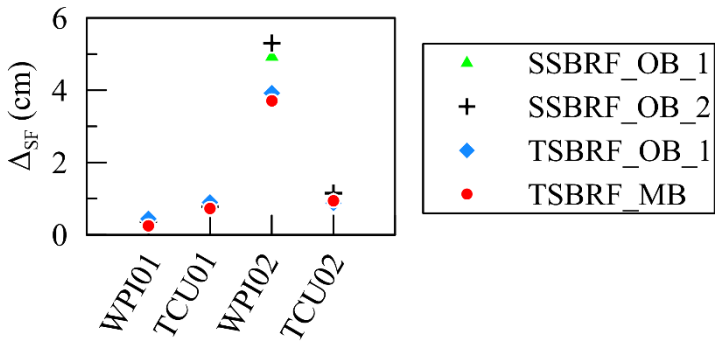

Figure 7-8. Residual foundation settlements across the input motions recorded during the dry experiments performed on TSBRF and SSBRF.

Finally, Figure 7-9 displays the absolute values of the maximum, δ_{max} , and residual, δ_{res}, deck drift across each structure and input motion. Deck drift is an important performance criterion for a bridge system because it determines the vulnerability to collapse. The deck drift ratio was determined by initializing the lateral displacement to zero at the start of each input motion and then dividing the lateral displacement of the bridge deck by the deck elevation relative to the base of the footing. SSBRF and TSBRF decks had almost the same performance across the first three

input motions. During TCU02 motion relatively minor, though nonzero differences between the two bridge deck responses were observed. The greatest deck drift was observed during WPI02 motion, where SSBRF and TSBRF decks were observed to drift by 0.008 and 0.0074 radians, respectively. Maximum deck drifts were well below the allowable story drift limit of about 0.02 radians given by ASCE 7-16 (ASCE, 2017). Furthermore, after the structures were subjected to WPI02 motion, the δ_{res} of the two structures was the same at about 0.0043 radians. δ_{res} observed throughout other motions were limited to below 0.001 radians.

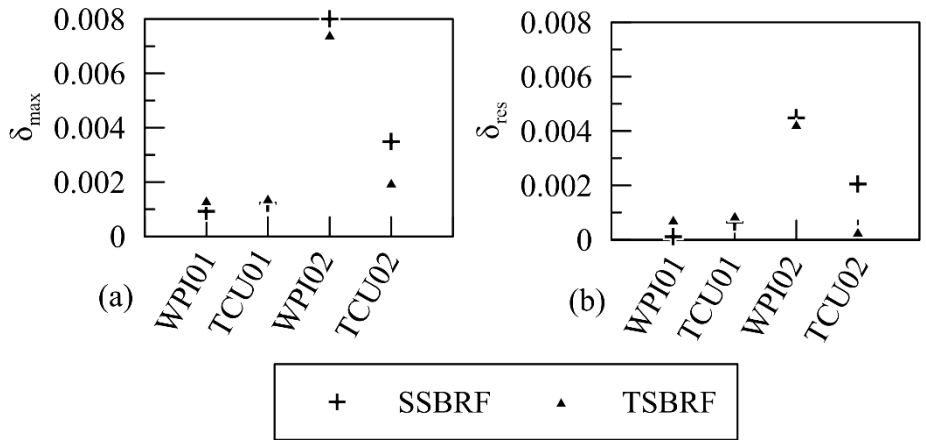

Figure 7-9. Deck drift variation across the input motions recorded during the dry experiments performed on TSBRF and SSBRF, showing (a) maximum deck drifts and (b) residual deck drifts.

According to the above discussions and the experimental results, both structures experienced a settlement-dominated response, as anticipated, considering the design of the physical models. Additionally, relatively insignificant differences were observed between the response of the systems in terms of foundation-level settlements, rotations, and deck drifts. Thus, the bent location (middle or outer), number of bents, and number of spans did not play an important role in generating seismic response variations between the two structures. Deck drifts were minor, well below those necessary to cause structural instability. Both structures survived toppling collapse

and experienced small residual settlements and rotations, even when subjected to an intense sequence of seismic events.

7.5.2. Influence of water table depth on the seismic response of SSBRF

Based on the findings in Section 7.5.1, SSBRF was tested under extended soil saturation conditions to identify the role of the water table elevation on the seismic response of a bridge system built to incorporate rocking foundations. The laser displacement sensor targeting SSBRF_OB_1 did not function properly during SSBRF_WL_1.49B; therefore, where appropriate, results leveraging this dataset are omitted.

Figure 7-10 displays the overall response of the foundations in terms of overturning moment-rotations across the input motions and water table conditions. Also indicated in the figures are the theoretical values of $M_{c,foot}$ (dashed horizontal lines). The theoretical values of $M_{c,foot}$ are calculated based on the depth of the water table below the soil layer surface, before the application of the seismic motion, and the procedure developed in Chapter 4, Section 4.7.1. During the first two input motions (WPI01 and TCU01) the overturning moment applied to the footing did not reach the theoretical values of $M_{c,foot}$. However, when the higher intensity input motions of WPI02 and TCU02 were applied, the maximum overturning moments, M_{max}, converged to, and occasionally exceeded, the theoretical ultimate moment capacity of the footings.

Notably, during WPI02 and TCU02 motion, the $M_{c,foot}$ values sometimes slightly underpredicted the observed ultimate overturning moments. The percent errors between the theoretical ultimate moments and the experimental values were found to be up to about 35% during TCU02 motion. As subsequently explained, this underprediction (and potential overstrength) is presumed to be the result of localized soil densification beneath the footings, due to the settlements from both the

applied and preceding input motions. Intuitively, local densification of the bearing layer would increase bearing capacity and, correspondingly, ultimate moment capacity as suggested by Equation 2-13.

For a bridge system built with a rocking foundation, the yield mechanism of the bridge is characterized by the moment capacity of the column, $M_{c,col}$, and the moment capacity of the foundation, $M_{c,foot}$. The base shear coefficient of a column, C_y, and foundation, C_r, are defined as the ratio of superstructure horizontal acceleration which is required to cause the column or foundation to yield, to the gravitational acceleration. C_y and C_r are related to the column and foundation moment capacities using the relationships shown in Equation 2-11 and Equation 2-12 as implemented in Chopra (1995) and Deng et al. (2012b). If $C_y < C_r$, the strength of the column will be less than the strength of the rocking foundation. In contrast if $C_r < C_y$, the rocking foundation will be the principal yield component of the bridge. Therefore, when the overturning moment experienced by a foundation during an earthquake exceeds $M_{c,foot}$, the foundation experiences an overstrength which may not be anticipated during the foundation design. This foundation overstrength could shift the ductility demand back to the column. Furthermore, exceeding $M_{c,foot}$ during an earthquake increases the C_r, which leads to a proportional increase in the superstructure horizontal acceleration required to yield the foundation.

WPI02 was the first applied motion where M_{max} values converged to $M_{c,foot}$, hence the influence of soil densification on M_{max} values are less pronounced than observed during TCU02. The percent errors between the theoretical ultimate moments and the experimental values were found to be up to about 30% during WPI02 motion. Percent errors are consistent with the ranges presented by Drosos et al. (2012) for a shallow foundation on dry soil. While this percent error

needs to be considered by an appropriate factor of safety during design, specially considering the abovementioned influence of foundation overstrength on bridge yield mechanisms and accelerations, results from Figure 7-10 help further validate the design procedure to predict the theoretical values of $M_{c,foot}$ developed in Chapter 4, Section 4.7.1. This procedure has been extended to consider the interconnectedness of realistic bridge components, built to incorporate rocking foundations.

Figure 7-10 also indicates that the moment capacity of the foundations showed no degradation, even after being subjected to a sequence of seismic events. As the depth of the water table increased, maximum moments increased while maximum rotations generally followed the opposite trend. Therefore, the depth of the water table below the soil layer surface plays a dominant role when foundation moment capacities are considered.

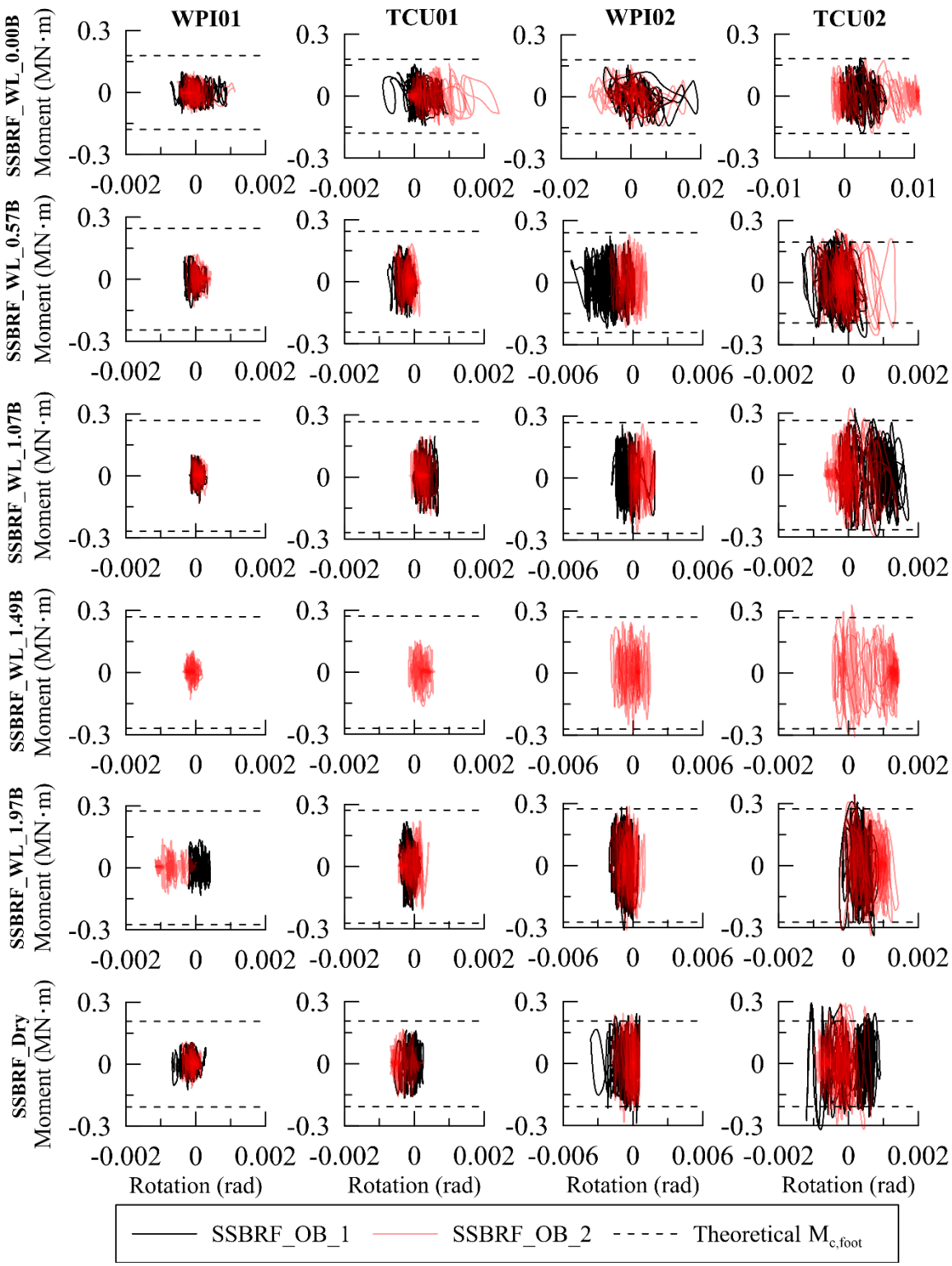

Figure 7-10. Foundation overturning moment versus rotation across all input motions and experiments performed on the SSBRF model. Each column corresponds to one input motion while each row corresponds to one experiment.

The rocking mode of foundation deformation involves the uplifting of the foundation on one side with soil yielding on the other, resulting in the accumulation of permanent settlements and rotations. This behavior is reflected in the settlement-rotation loops of Figure 7-11. Figure 7-11 displays the movement of the foundation midpoint as a function of the footing rotation across all input motions and soil saturation conditions. The figure suggests that the foundations tended to rock in-phase with each other. In general, as the depth of the water table increased from the fully saturated condition, foundation level settlements were found to reduce, becoming less than those experienced when the structure was placed on the dry soil layer. For example, during experiment SSBRF_WL_0.00B, when subjected to WPI02 input motion, the foundations experienced the greatest seismically induced settlement, about 35 cm. Then, when the water table was lowered to about 0.57B in experiment SSBRF_WL_0.57B, foundations level settlements were reduced to about 9 cm during WPI02. Finally, when the water table was lowered to about 2B (SSBRF_WL_1.97B) the observed foundation settlements were limited to about 3 cm (during WPI02). This settlement was even less than that experienced by the foundations when placed on the dry soil layer (about 5.3 cm). These findings point to the benefits of placing rocking foundations on unsaturated soil layers, which may significantly reduce foundation-level settlements compared to the fully saturated, and even the dry soil condition. Furthermore, almost no uplift occurred throughout the experiments regardless of the water table condition. In fact, the settlement-dominated response throughout these experiments is believed to be a reason for the observed foundation overstrength.

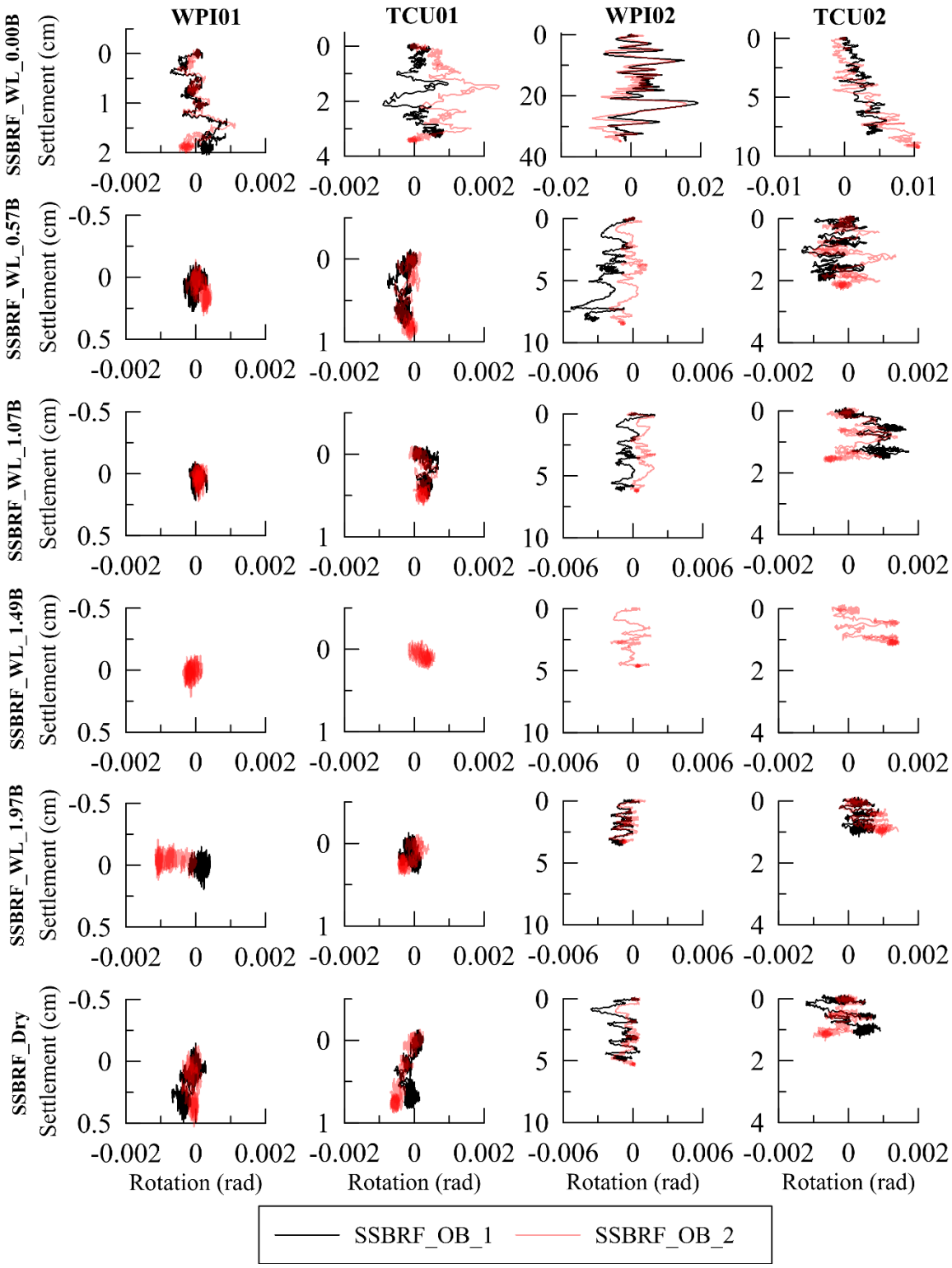

Figure 7-11. Foundation settlements versus rotation across all input motions and experiments performed on the SSBRF model. Each row corresponds to one input motion while each column corresponds to one experiment.

The settlement-rotation response across the foundations is further synthesized in Figure 7-12, Figure 7-13, and Figure 7-14. Figure 7-12 and Figure 7-13 display the peak, θ_P, and residual, θ_R, foundation rotations determined for each foundation across each motion and soil saturation condition. Similarly, Figure 7-14 displays the residual foundation settlement. The data in these plots are based on displacement time histories of the foundation that were initialized to zero at the start of the applied motion. Figure 7-12 through Figure 7-14 suggest that as the depth of the water table increased, peak foundation rotations, residual foundation rotations, and foundation settlements significantly reduced.

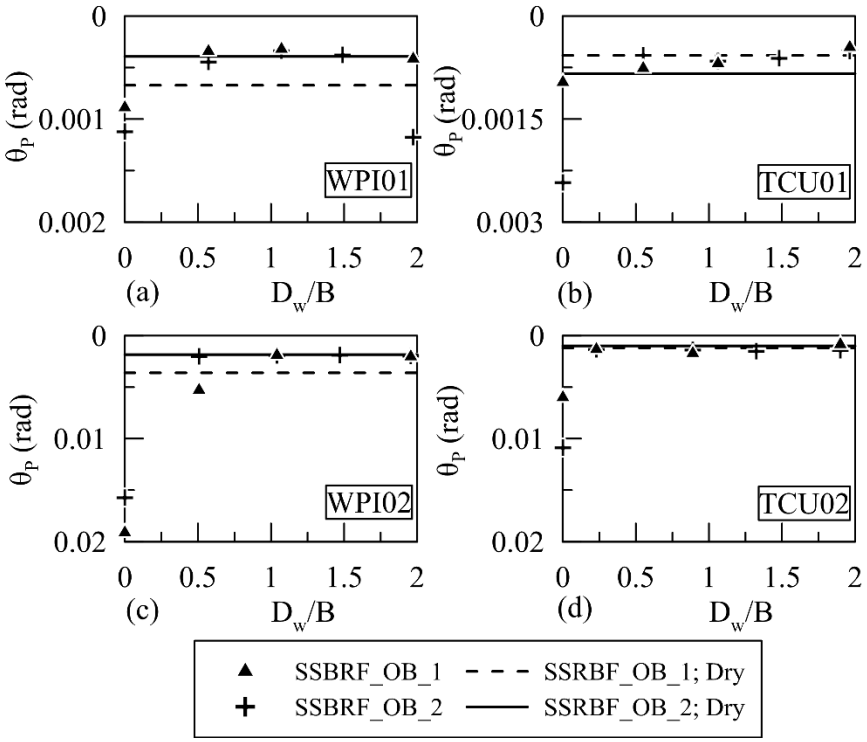

Figure 7-12. The absolute values of the maximum foundation rotations across all input motions as a function of the normalized depth of the groundwater table during the experiments performed on the SSBRF. Each subplot shows the response during one input motion.

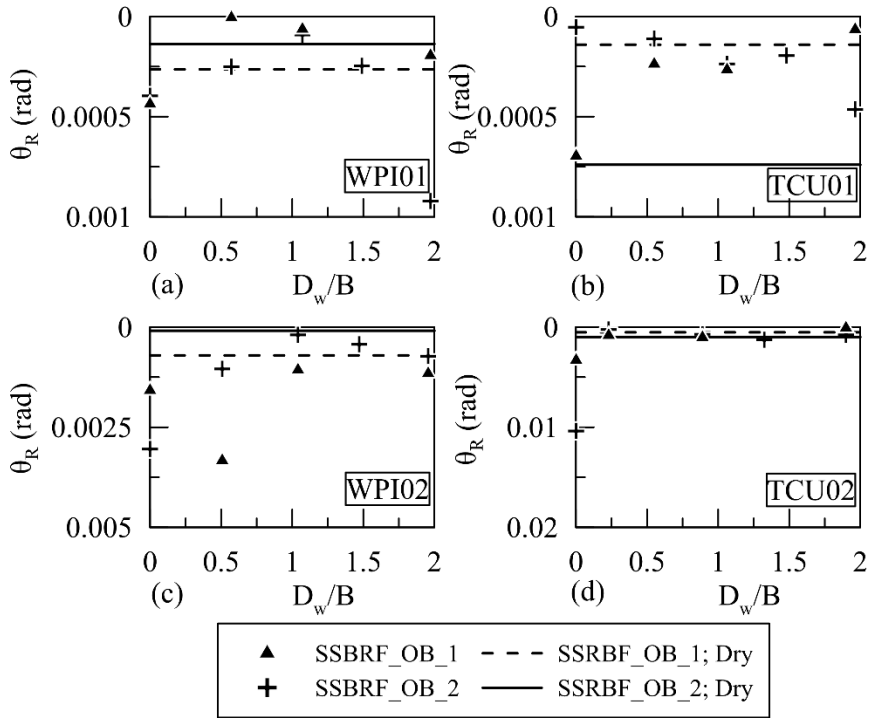

Figure 7-13. The absolute values of the residual foundation rotations across all input motions as a function of the normalized depth of the groundwater table during the experiments performed on the SSBRF. Each subplot shows the response during one input motion.

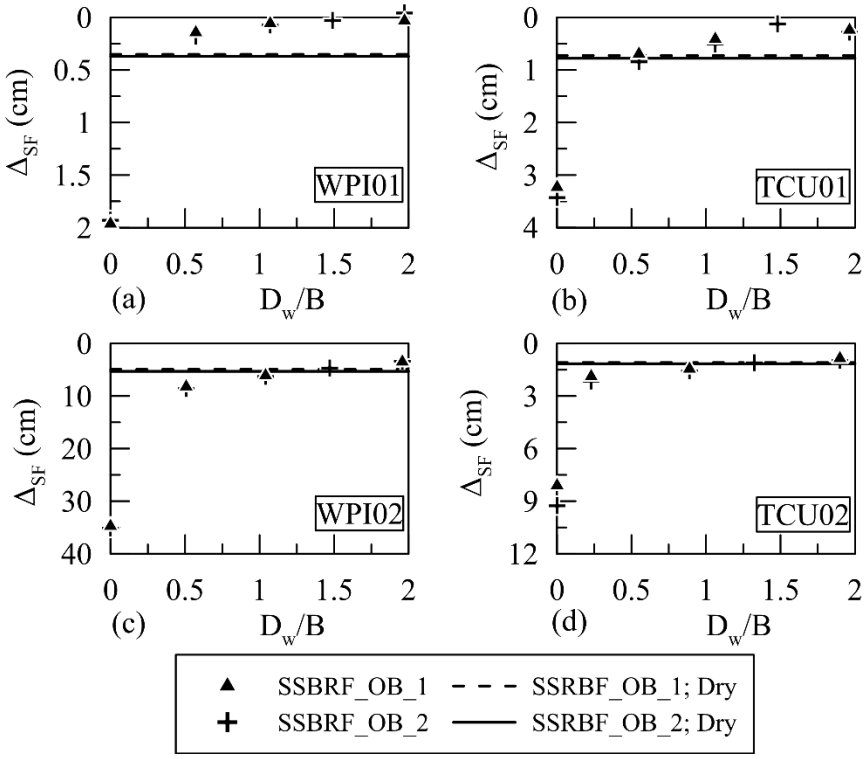

Figure 7-14. The residual foundation-level settlements across all input motions as a function of the normalized depth of the groundwater table during the experiments performed on the SSBRF. Each subplot shows the response during one input motion.

Figure 7-15 and Figure 7-16 display absolute values of the maximum (δ_{max}) and residual (δ_{res}) lateral deck drift across each foundation, input motion, and soil saturation condition. As the depth of the water table increased, δ_{max} and δ_{res} generally reduced. The greatest deck drift was observed during WPI02 motion, where the deck in experiment SSBRF_WL_0.00B was observed to drift up to 0.036 radians. This deck drift is greater than the allowable story drift limit of about 0.02 radians given in ASCE 7-16 (ASCE, 2017). Drifts greater than the allowable story drift limit have the potential to generate inelastic deformations in ductile members, generate displacements that compromise the structural stability of the structure, and damage nonstructural components which could pose a life-threatening hazard (ASCE, 2017). Lowering the water table to about 0.5B in

SSBRF_WL_0.57B limited the maximum drift to 0.01 radians, well below the code-based value. This finding further highlights the benefits of unsaturated soil in the context of seismically induced building deformations.

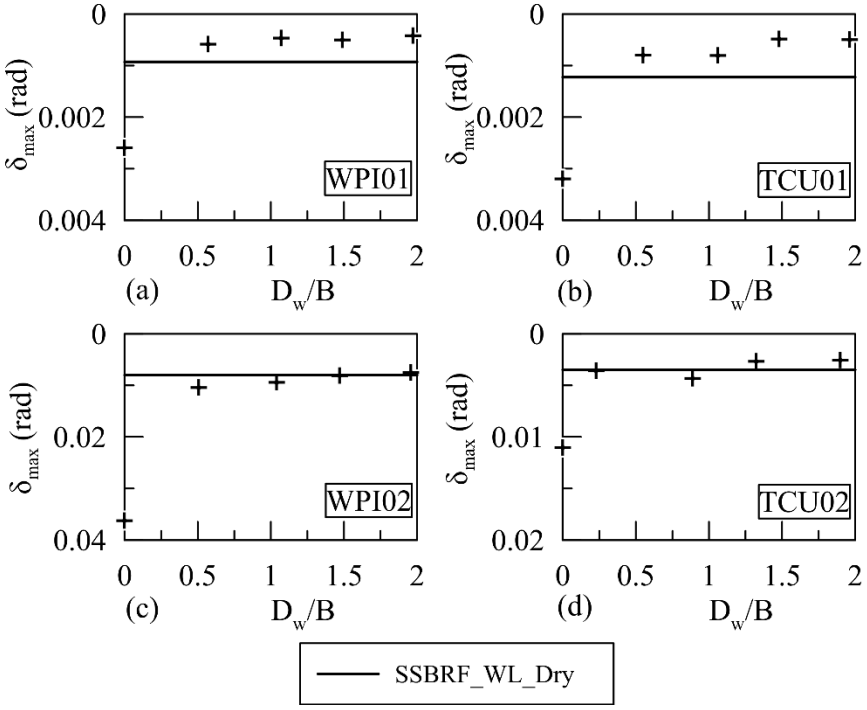

Figure 7-15. The absolute values of the maximum deck drift across all input motions as a function of the normalized depth of the groundwater table during the experiments performed on the SSBRF. Each subplot shows the response during one input motion.

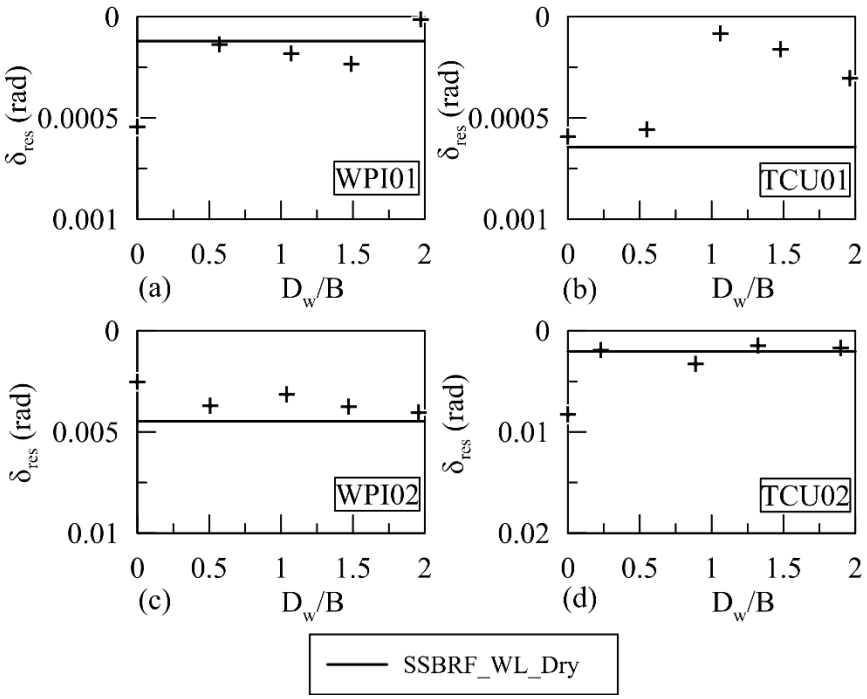

Figure 7-16. The absolute values of the residual deck drift across all input motions as a function of the normalized depth of the groundwater table during the experiments performed on the SSBRF. Each subplot shows the response during one input motion.

Global rotation of a bridge deck is another important performance criterion during seismic events, especially from the public perception of safety. In this study, global bridge deck rotation is defined as the difference in the settlement between the two foundations, divided by the horizontal distance between the foundation centers. Figure 7-17 and Figure 7-18 display the absolute values of maximum, α_{max}, and residual, α_{res}, global rotation of the bridge deck across each soil saturation condition and input motion. Data in this figure are based on foundation settlement time histories initialized to zero at the start of the motion application. As the depth of the water table increased from zero at the surface, differential settlements between the foundations reduced, leading to a reduction in global bridge deck rotations. The greatest α_{max} of 0.0017 radians was observed in SSBRF_WL_0.00B when subjected to TCU02 input motion.

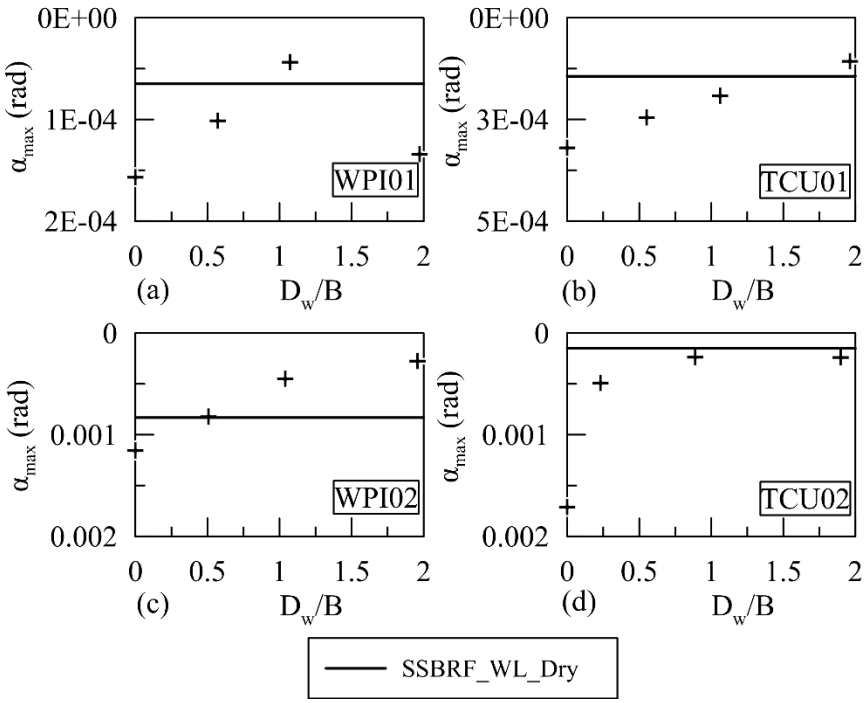

Figure 7-17. The absolute values of the maximum deck global rotations across all input motions as a function of the normalized depth of the groundwater table during the experiments performed on the SSBRF. Each subplot shows the response during one input motion.

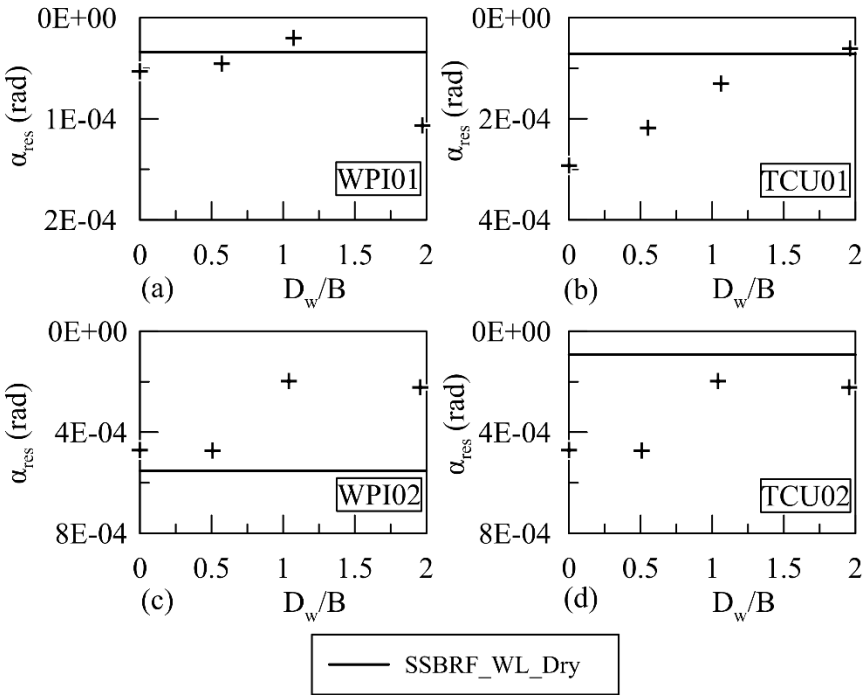

Figure 7-18. The absolute values of the residual deck global rotations across all input motions as a function of the normalized depth of the groundwater table during the experiments performed on the SSBRF. Each subplot shows the response during one input motion.

The response of the structure and foundation can also be explored in terms of accumulated residual deformations and rotations after being subjected to the entire sequence of seismic motions. For this analysis, displacement-time histories were initialized to zero at the start of WPI01 motion, and analysis was performed to determine residual deformations and rotations after the experiments were subjected to all four input motions. Figure 7-19(a) and (b) present the accumulated residual drift and global rotation of the bridge deck, respectively, as a function of the normalized depth of the water table. Figure 7-20(a) and (b) display the accumulated residual settlement and rotation of the foundations, respectively as a function of the normalized depth of the water table.

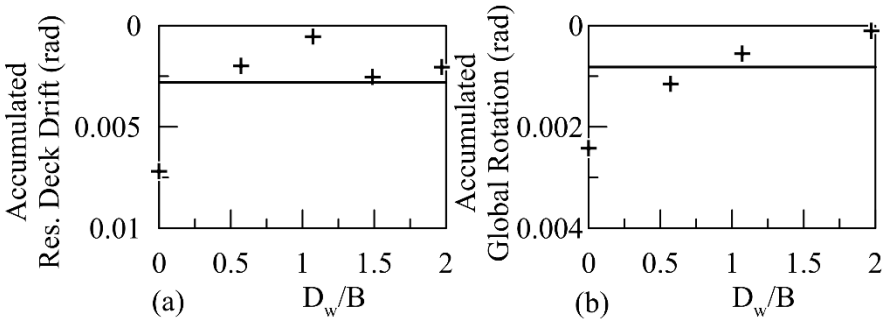

Figure 7-19. The accumulated residual rotations of the SSBRF structure after being subjected to all input motions as a function of the normalized depth of the groundwater table showing (a) residual deck drifts; and (b) residual global rotation.

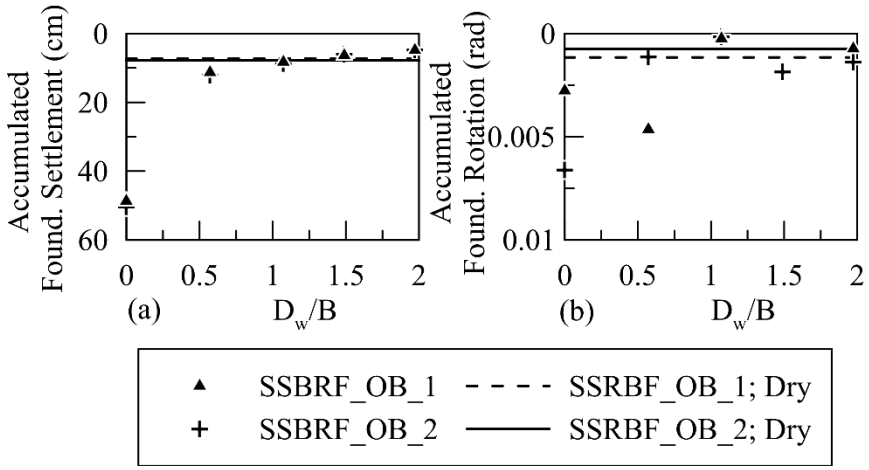

Figure 7-20. The accumulated residual rotations and settlements of the SSBRF foundations after being subjected to all input motions as a function of the normalized depth of the groundwater table showing (a) foundation settlement; and (b) foundation rotation.

The variation of $\tilde{T}/T$ with respect to the normalized depth of the water table, D_w/B, across all four input motions, is shown in Figure 7-21. Similarly, Figure 7-22 shows the variation of $\tilde{\beta}$ and $\tilde{\beta}_0$ with respect to D_w/B. Figure 7-21 and Figure 7-22 suggest that as the water table depth increased from the fully saturated condition, the system behaved stiffer, and values of $\tilde{T}/T$, $\tilde{\beta}$, and $\tilde{\beta}_0$ reduced. Results further highlight the influence of the input motion on changes to system

nonlinearities. For the same water table depth, higher-intensity input motions correlate to increased values of $\tilde{T}/T$, $\tilde{\beta}$, $\tilde{\beta}_0$.

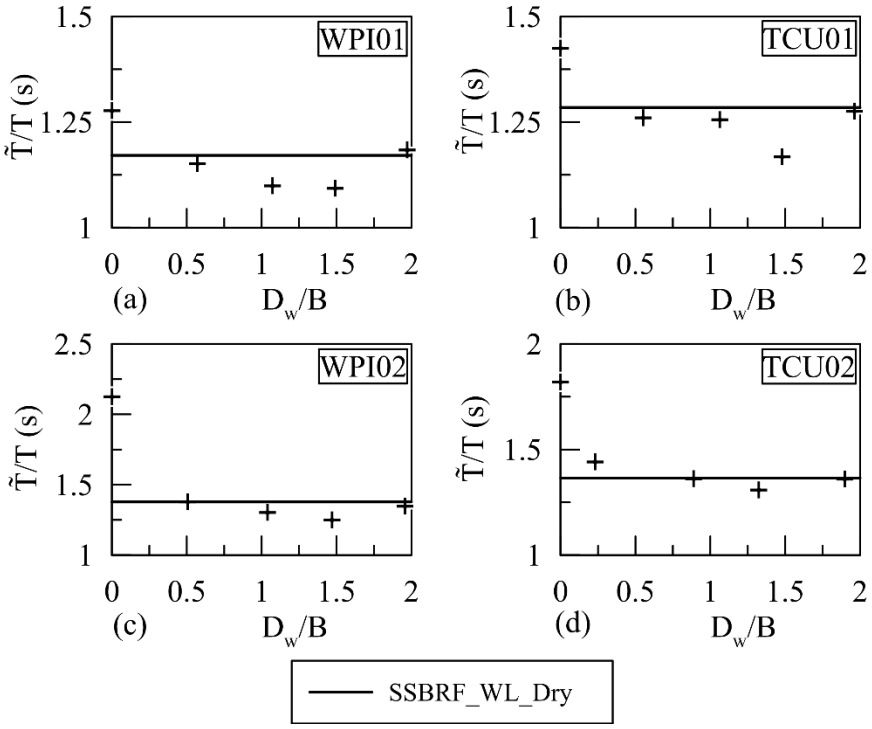

Figure 7-21. Variation of the period lengthening ratio across all input motions as a function of the normalized depth of the groundwater table during the experiments performed on SSBRF. Each subplot shows the response during one input motion.

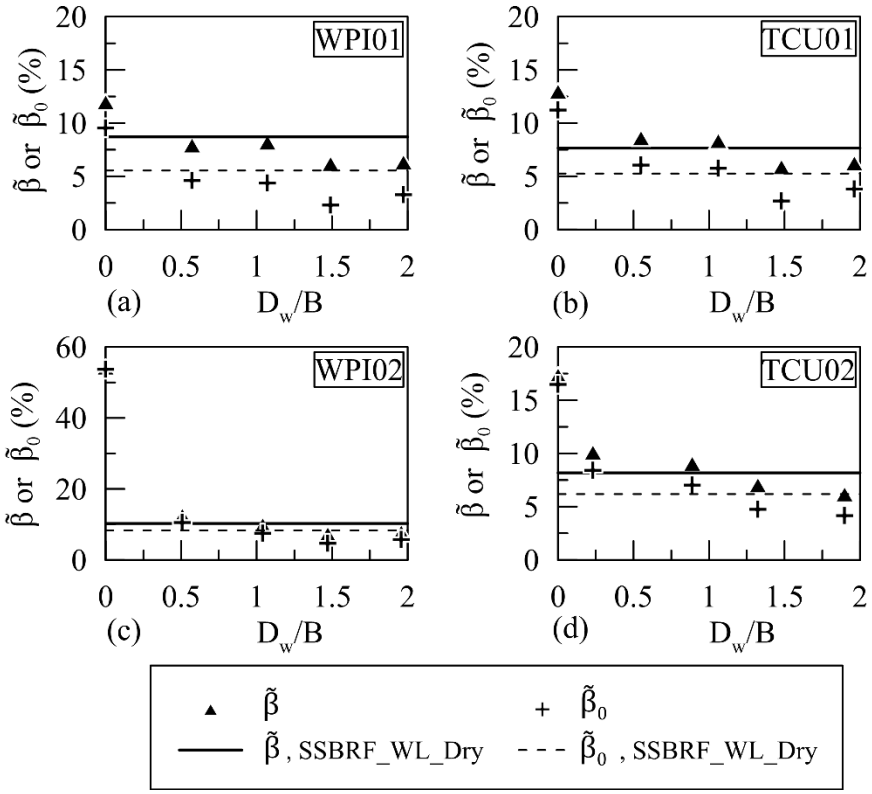

Figure 7-22. Variation of the system and foundation damping ratios across all input motions as a function of the normalized depth of the groundwater table during the experiments performed on SSBRF. Each subplot shows the response during one input motion.

7.5.3. Comparison of the seismic response of SSBRF and RFSS due to variations in groundwater table depth

Owing to variations in precipitation and evaporation intensities throughout the year, the water table and vadose zone, vary seasonally. As a result, the water table depth at the time of an earthquake may be different than the water table depth recorded during the preconstruction site investigation. Furthermore, the response of a realistic bridge, such as SSBRF, may be different from the response of a simplified SDOF structure, such as RFSS. Differences in the behavior between a realistic bridge and a simplified SDOF structure could influence the anticipated effect of the depth of the groundwater table on the seismic response of a system. In this section, first, the influence of the

water table depth on the behavior of RFSS is compared to that of SSBRF during a representative input motion that was applied to both structures. The results are presented by comparing seismically induced nonlinear SSI parameters to the depth of the water table below the soil surface. Namely, the response is explored in terms of the dimensionless parameters of $\tilde{T}/T$, $\tilde{\beta}$, and $\tilde{\beta}_0$. Then, statistical analysis is performed to quantify the influence of the groundwater table and structural system on changes to the seismic response parameters of maximum foundation overturning moment, residual foundation settlement, peak and residual foundation rotation, overall damping, and period lengthening. Although the properties of the RFSS and SSBRF models vary, especially in terms of fixed-base fundamental frequencies, damping ratios, bearing pressures, and overall masses, this analysis provides a first-order approximation of the benefits and drawbacks of using a simplified SDOF system to model the behavior of a structure implementing rocking foundations.

The influence of the water table depth on the behavior of the physical model built for RFSS can be compared to SSBRF during seismic motions that were applied to both structures. These motions were the first, second, and fourth applied motions in Chapter 4 (WPI01, TCU02, and WPI03, respectively in Table 4-2), and the first, second, and third applied motions in Chapter 7 (WPI01, TCU02, and WPI02, respectively in Table 7-2). The fourth motion in Chapter 4 and the third motion in Chapter 7 were similar, and the highest intensity motions applied to the structures. Results from this representative input motion were used to compare the nonlinear SSI parameters to the depth of the water table below the soil layer surface across both structures.

Figure 7-23(a-c) show the deviation of $\tilde{T}/T$, $\tilde{\beta}$, and $\tilde{\beta}_0$, determined in RFSS and SSBRF, with respect to the normalized depth of the water table during the representative input motion. This figure shows that the depth of the water table governed the influence of SSI, and the associated

effects that were introduced into the seismic response of the systems. For example, when the water table was nearer to the soil surface, SSBRF experienced greater $\tilde{T}/T$, $\tilde{\beta}$, and $\tilde{\beta}_0$ values than RFSS. Then, as the depth of the water table increased, RFSS experienced greater $\tilde{T}/T$, $\tilde{\beta}$, and $\tilde{\beta}_0$ values than SSBRF.

The structure-to-soil stiffness ratio, σ_s, presented in Equation 2-9 ($\sigma_s = h/V_{s,r}T$) can be leveraged to help interpret the trends observed in Figure 7-23(a-c). Avilés & Pérez-Rocha (1996) found that $\tilde{T}/_T$ and $\tilde{\beta}_0$ are sensitive to the structure-to-soil stiffness ratio; with all other contributing factors remaining equal, as the structure-to-soil stiffness ratio increases, $\tilde{T}/_T$ and $\tilde{\beta}_0$ increase. The structure-to-soil stiffness ratios for the experiments performed on SSBRF and RFSS when subjected to the representative seismic motion were computed, with $V_{s,r}$ values determined according to Chapter 5, Section 5.5.1. Figure 7-23(d) presents the variation of σ, determined for experiments performed on SSBRF and RFSS, with respect to the normalized depth of the groundwater table. The trends of Figure 7-23(d) correlate with the trends of the SSI parameters observed in Figure 7-23(a-c). Although the values of h and T in Equation 2-9 remain constant with changing water table depths, $V_{s,r}$ varies and is influenced by the degree of saturation in the underlying soil layer. Due to the higher confining stress imposed by RFSS on the supporting soil, values of $V_{s,r}$ during the experiments performed on RFSS were consistently greater than those of SSBRF. Meanwhile, h/T for RFSS ($= 10.4$) was slightly larger than h/T for the SSBRF structure ($= 8.2$). Thus, the variation of $V_{s,r}$ due to the foundation-induced confinement and degree of saturation controlled the change in σ with respect to the depth of the water table. When the water table was nearer the soil surface, the increased values of $V_{s,r}$, due to the higher confining stress imposed by RFSS, led to a reduction in σ_s, compared to the values of σ_s computed for the

experiments performed on SSBRF. Then, as the depth of the water table increased, the increased value of h/T present for RFSS, offset the influence of the higher confining stress on the $V_{s,r}$ values and led to slightly greater σ values compared to SSBRF. Therefore, σ_s was a factor influencing the trends in the SSI parameters of $\tilde{T}/T$, $\tilde{\beta}$, and $\tilde{\beta}_0$, observed between the structures with increasing water table depth in Figure 7-23(a-c). On the other hand, although the trends in these parameters across the structures with water table depth may be correlated with σ_s, the actual differences between these values, especially considering the shallow water table depth regime, may be better correlated with other seismically-induced parameters, such as pore-pressure ratios (also related to the confining stresses imposed by the foundation). The impact of these parameters on changes in $\tilde{T}/T$, $\tilde{\beta}$, and $\tilde{\beta}_0$ requires further scrutiny.

The simplified SDOF model may appropriately capture the seismically induced SSI parameters of a realistic bridge, provided that the structural parameters of foundation bearing pressure, structural height, fixed-base natural period, and damping ratio are modeled appropriately.

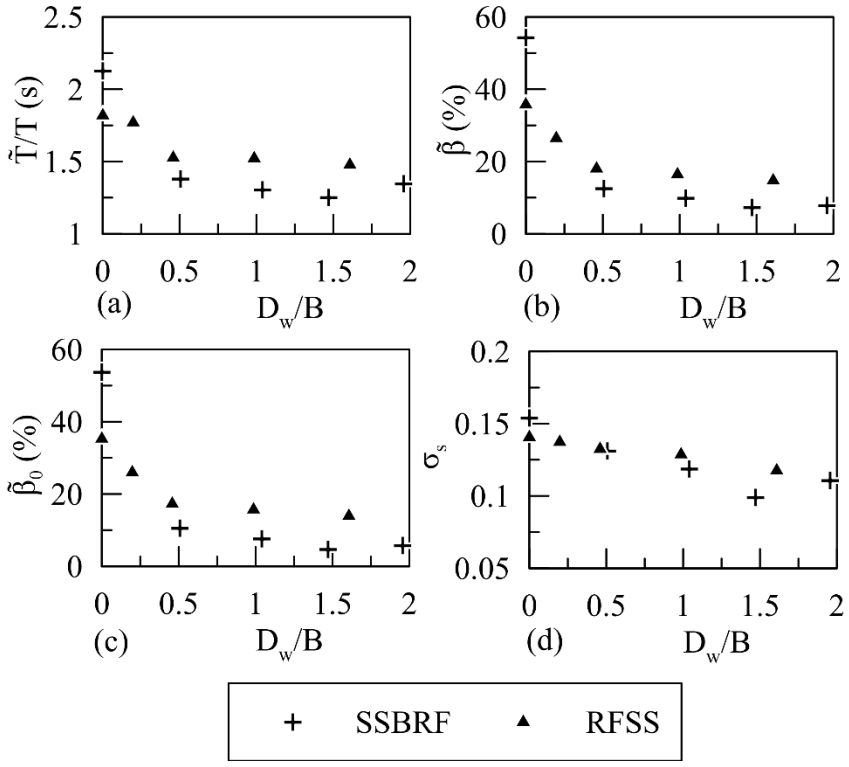

Figure 7-23. Variation of the SSI parameters during the representative input motion determined across SSBRF and RFSS with respect to the normalized depth of the water table showing (a) period-lengthening; (b) system damping; (c) foundation damping; and (d) structure-to-soil stiffness ratio.

Statistical analysis was also performed to quantify the influence of the groundwater table and structural system on changes to several additional seismic response parameters including those associated with foundation-level deformations and rotations.

For each set of experimental results, the following statistical analysis was performed:

1. Percent difference values, δ, between the seismic response parameters of the saturated soil and the soil layers with the groundwater table below the soil surface were calculated for each seismic motion. If the seismic response parameter was recorded for both SSBRF

foundations during an input motion (i.e., Δ_{sf}, θ_R, and θ_P), the average value of the response parameter was calculated for each water table depth.

2. The arithmetic mean, δ, across the suite of seismic motions was calculated for each seismic parameter.
3. Figure 7-24 was created, showing arithmetic means of the key response parameters between the saturated soil and the soil specimens with the groundwater table below the soil surface. Curves are drawn by connecting the arithmetic mean data points for each parameter.
4. The average percent difference, $\bar{\delta}$, for each parameter was calculated by dividing the area beneath the curves by the range of D_w/B values. A negative percent difference value indicates the parameter in the unsaturated soil is less than that of the saturated soil, while a positive value indicates the reverse trend. $\bar{\delta}$ are labeled according to their associated physical model, for example $\bar{\delta}_{SSBRF}$ is the average percent difference for a parameter of the SSBRF physical model.

Finally, for each parameter, the absolute value of $\bar{\delta}$ of SSBRF was subtracted from the absolute value of $\bar{\delta}$ of RFSS to generate $\bar{\bar{\delta}}$. A positive $\bar{\bar{\delta}}$ indicates the depth of the water table had a greater influence on the parameter of the SSBRF model while a negative $\bar{\bar{\delta}}$ indicates the reverse trend.

Figure 7-24 shows that in comparison with the response of the soil specimens having the water table below the soil surface, the saturated soil led to greater seismically induced peak foundation rotations ($\bar{\delta}_{SSBRF} = -92\%$; $\bar{\delta}_{RFSS} = -52\%$), seismically induced residual foundation rotations ($\bar{\delta}_{SSBRF} = -62$; $\bar{\delta}_{RFSS} = -123\%$), seismically induced foundation settlements ($\bar{\delta}_{SSBRF} = -137\%$; $\bar{\delta}_{RFSS} = -88\%$), system damping ratios ($\bar{\delta}_{SSBRF} = -69\%$; $\bar{\delta}_{RFSS} = -59\%$), and period

lengthening ratios ($\bar{\delta}_{SSBRF} = -21\%$; $\bar{\delta}_{RFSS} = -15\%$). Meanwhile, the saturated soil resulted in reduced maximum foundation overturning moments ($\bar{\delta}_{SSBRF} = 29\%$; $\bar{\delta}_{RFSS} = 24\%$), compared to the soil specimens having the water table below the soil surface. The statistical analysis performed herein highlights the influence of the water table on the seismic response of the soil-foundation-structure systems. This analysis shows that ignoring the uncertainty of the depth of the water table on the seismic response of the system can significantly impact the expected seismic response of rocking foundations and the overall structure. The extent of this impact depends on both the target motion characteristics and the seismic response parameter under consideration.

Compared to the response of RFSS, increased water table depths had a greater influence on SSBRF in terms of maximum foundation overturning moments ($\bar{\bar{\delta}} = 5\%$), seismically induced peak foundation rotations ($\bar{\bar{\delta}} = 40\%$), seismically induced foundation settlements ($\bar{\bar{\delta}} = 49\%$), system damping ratios ($\bar{\bar{\delta}} = 10\%$), and period-lengthening ratios ($\bar{\bar{\delta}} = 6\%$). Meanwhile, compared to the response of RFSS, increased water table had a reduced influence on SSBRF in terms of seismically induced residual foundation rotations ($\bar{\bar{\delta}} = -61\%$). This analysis further confirms the notion that a simplified SDOF model may appropriately capture the change in seismic response of a bridge system due to changes in groundwater table depth in terms of foundation overturning moments, system damping ratios, and period lengthening ratios. However, in terms of seismically induced settlements and rotations, additional consideration is necessary. For example, the large $\bar{\bar{\delta}}$ values determined for residual foundation rotations may be influenced by the interconnectedness and behavior of the bents, altering the self-centering capability of the foundation during and after the seismic event. Furthermore, it is hypothesized that the large $\bar{\bar{\delta}}$ determined for seismically induced settlements may be reduced by using physical models composed of foundations with similar bearing pressures and dimensions. Bearing pressure is a primary factor governing the generation

of seismically induced settlements, while the dimensions of the footing influence the mode of shear failure. When a foundation is subjected to concentric vertical loads, the mode of shear failure is a function of the foundation embedment depth, D_f, and the foundation width, B (Vesic, 1973). Changes in the depth of embedment throughout seismic loading influence the ratio of D_f/B, which may influence the mode of shear failure. Changes in the load eccentricity, related to foundation rotations, may further influence the mode of shear failure at the foundation level. Therefore, the behavior of a prototype bridge, in terms of seismically induced settlements and rotations may be better reflected by a more realistic model with appropriate bent locations, foundation bearing pressures, and foundation dimensions. This analysis highlights the benefits and drawbacks of using SDOF systems to model the behavior of more complex structures implementing rocking foundations resting on unsaturated soil layers.

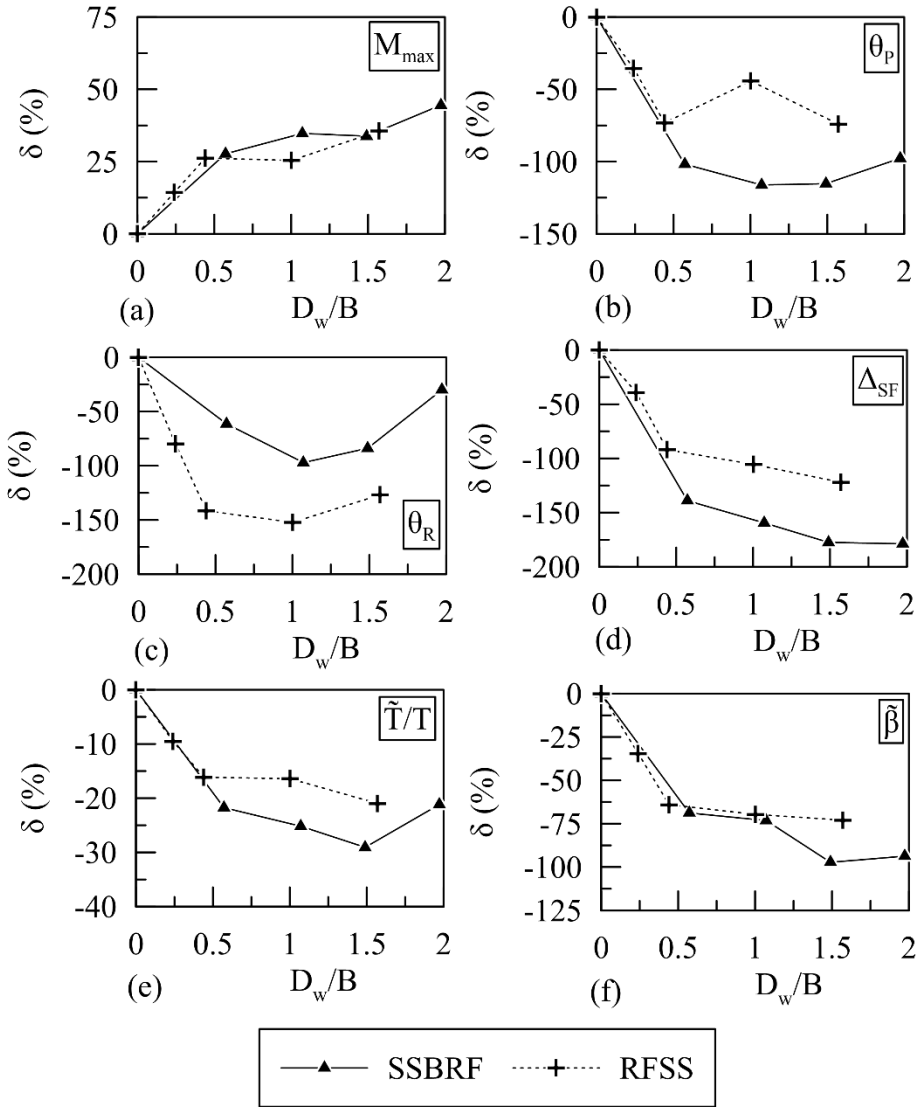

Figure 7-24. Percentage difference between the seismic parameters for the specimen having the groundwater table at the soil layer surface and those for specimens having the groundwater table below the surface of the soil layer across SSBRF and RFSS physical models.

7.6. CONCLUSIONS

Centrifuge model tests on a prototype bridge system, built to incorporate rocking foundations, were performed. Each experiment was subjected to a series of scaled seismic motions while the response of the soil and structure was recorded. One test on a two-span configuration of the

prototype bridge placed in dry soil was compared to a similar test performed on a single-span configuration of the bridge. Relatively insignificant differences were observed between the response of the single- and two-span systems in terms of foundation-level settlements, rotations, and deck drifts. Thus, the bent location (middle or outer), number of bents, and number of spans did not play an important role in generating seismic response variations between the two structures.

Five additional tests were performed on the single-span configuration of the bridge, with each test having a unique water table condition, including a fully saturated and four mixed saturated-unsaturated soil layers. Analysis was performed to highlight the influence of the water table depth on foundation and structural deformations and rotations as well as seismically-induced SSI parameters. Finally, the influence of the water table depth on the seismic response of the SSBRF model was compared to that of the RFSS model. Based on the experimental results, the following conclusions can be drawn:

1. The rocking moment capacity of a foundation resting on unsaturated, saturated, and dry soil layers is well-defined and non-degrading.
2. The rocking moment capacity of a foundation is a function of the depth of the water table below the soil layer surface. When subjected to the same seismic motion, as the depth of the water table increases from the fully saturated condition, maximum foundation overturning moments increase.
3. As the depth of the water table increases from the fully saturated condition, foundation level settlements, foundation level rotations, bridge deck drifts, bridge deck global rotations, system damping, foundation damping, and period lengthening ratios reduce.
4. The foundations of the SSBRF and TSBRF models experienced residual settlements after being subjected to seismic excitation. These foundations had A/A_c ratios ranging from 2.59

to 9.41. This finding further confirms the notion that for foundations with A/A_c ratios less than about 15, residual settlements, rather than residual uplifts are expected.

5. A simplified SDOF model may appropriately capture the change in seismic response of a bridge system due to changes in groundwater table depth in terms of foundation overturning moments, system damping ratios, foundation damping ratios, and period lengthening ratios.
6. The influence of the water table depth on the behavior of a prototype bridge, in terms of seismically induced settlements and rotations, may be better reflected by a more realistic model, as opposed to a simplified SDOF system. The more realistic model should feature appropriate bent locations, foundation-bearing pressures, and foundation dimensions.
7. Incorporating a hinge connection at the top of columns guides plastic deformation to the soil-foundation interface and limits column damage.

CHAPTER 8

SUMMARY, CONCLUSIONS, AND FUTURE WORK

8.1. ABSTRACT

This chapter provides a conclusion and summary of the work presented throughout this dissertation. Initially, the objectives of the dissertation are stated, then the techniques implemented to address these objectives are discussed. Findings and conclusions supporting the objectives are presented. Recommendations for future work and research related to the dissertation topic are presented. Finally, the intellectual merit behind this dissertation is summarized.

8.2. SUMMARY AND CONCLUSIONS

8.2.1. Objectives

The primary objectives of this dissertation are to:

1. Study the effects of the depth of the groundwater table on SFSI and the seismic performance of rocking foundations.

2. Develop and validate seismic design recommendations for SFSI and rocking foundations that consider, and incorporate, unsaturated soil mechanics and the depth of the groundwater table.

The secondary objectives of this research are to:

3. Compare the effects of the depth of the groundwater table on the seismic response of different structures.
4. Investigate the influence of the degree of soil saturation on the at-rest coefficient of lateral earth pressure.

These objectives were addressed through the following steps, summarized below:

- Initially, two SDOF physical models were designed. These physical models exhibit unique responses to seismic loading. One physical model was designed based on the rocking foundation concept and featured a completely elastic superstructure, while the other was designed to incorporate structural fuses, guiding the locations of inelastic structural deformations.
- Dynamic centrifuge tests were performed on the two physical models. The groundwater table was varied between experiments to create dry, saturated, and unsaturated sandy silt layers.
- The influence of the water table depth on the seismic response of the rocking foundation physical model was compared to that of the inelastic structure.
- Based on the response comparison, two additional physical models were designed and fabricated based on a prototype bridge structure built to incorporate rocking foundations. One physical model represented a single span of the prototype bridge, while the other

represented two spans of the prototype bridge. Several dynamic experiments were performed on the physical models, with each experiment having a unique water table condition or a completely dry soil layer.

A summary of the research conclusions is listed below. Conclusions are labeled based on the research objective they answer. An asterisk at the start of a conclusion reflects a key takeaway from this research. In the author's opinion, key takeaways may have the most significant impact on the field.

1-1. Several series of dynamic centrifuge experiments were conducted across different structures resting on sandy silt with varying water table depths. These structures include the SDOF elastic structure with a rocking foundation, termed RFSS, the SDOF inelastic structure, ICSS, and the single-span bridge incorporating rocking foundations, SSBRF. In these experiments, as the depth of the groundwater table increased, foundation overturning moment demands increased, while foundation settlements and rotations typically reduced.

1-2. *For the models built with rocking foundations and elastic superstructures (RFSS and SSBRF), as the depth of the water table increased, structural deformations and rotations typically reduced.

1-3. For the inelastic structure built with structural fuses (ICSS), as the depth of the water table increased, structural deformations and rotations typically increased.

1-4. *For the models built with the rocking foundations and elastic superstructures (RFSS and SSBRF), as the depth of the water table increased, period lengthening, system damping ratios, and foundation damping ratios reduced.

1-5. As the depth of the water table increased during the experiments performed on the ICSS physical model, foundation and system damping ratios reduced, while variations in period lengthening depended on the specific seismic motion being considered.

1-6. *Experimental findings highlight the potential trade-offs of founding a structure, built with rocking foundations, on soil with variable water table depths. Shallow water table elevations give rise to greater deformations, in terms of settlements and rotations, and associated nonlinearity at the soil-foundation interface. Meanwhile, deeper water table depths lead to increased superstructure seismic demands that generate greater foundation-level overturning moments.

2-1. *Procedures are proposed to estimate the ultimate moment capacity and initial rotational stiffness of rocking foundations in unsaturated soils; both were validated with experimental data. Shear strength and wave velocities used in these formulations were determined in accordance with the fundamentals of unsaturated soil mechanics.

2-2. *The water table depth should be considered during the design and analysis of rocking foundations. Potential foundation overstrength related to the depth of the water table influences the moment capacity of the foundation, which could shift ductility demand back to above-ground superstructure locations.

2-3. *Linear elastic SFSI analysis is the current method employed by ASCE 7-16 (ASCE, 2017). An extension of the linear elastic analytical procedure, to predict flexible-base SFSI parameters, considering the influence of the water table elevation on the system response, is presented. Although this analytical procedure may provide satisfactory results for soil-foundation-structure interaction in the linear elastic regime, the soil layers in the experiments performed in this research experienced plastic deformation. Thus, results

suggest that the analytical procedure significantly underestimated the values of $\tilde{\beta}$, while the prediction accuracy for values of $\tilde{T}$ was dependent on the characteristics of the input motion. This highlights the shortcomings of current analysis procedures used in design verification, suggesting the need for further improvement.

2-4. Experimentally derived SFSI parameters of $\tilde{T}$ and $\tilde{\beta}$ were found to overpredict superstructure spectral accelerations using elastic response spectra computed from free-field motions. Therefore, using elastic free-field response spectra to predict seismic demands on an inelastic structure may lead to a conservative design scenario.

3-1. The influence of the groundwater table depth on the seismic response of the RFSS and ICSS physical models was compared. Findings suggest that the response of the structural system influenced the SFSI parameters of period lengthening and system damping.

3-2. As the water table elevation was lowered during the experiments performed on the RFSS model, greater changes in SFSI parameters were observed compared to when the water table was lowered during the experiments performed on the ICSS model.

3-3. The influence of the groundwater table depth on the seismic response of RFSS and SSBRF physical models was compared. Findings show that a simplified SDOF model may appropriately capture the change in seismic response of a bridge system due to changes in groundwater table depth in terms of foundation overturning moments, system damping ratios, and period lengthening ratios.

3-4. The influence of the water table depth on the behavior of a prototype bridge, in terms of seismically induced settlements and rotations, may be better reflected by a more realistic

model, as opposed to a simplified SDOF system. The more realistic model should feature appropriate bent locations, foundation-bearing pressures, and foundation dimensions.

4-1. *For soil with unsaturated layers present, findings suggest K_0 decreases with a reduction in the degree of saturation.

8.3. RECOMMENDATIONS FOR FUTURE WORK

While this dissertation provides insights into the mechanisms with which groundwater table fluctuation influences the seismic response of different types of structures and foundations, this work can be expanded in several ways. The following recommendations aims to guide the future work to improve the knowledge of the seismic response of structures resting on unsaturated soil layers.

- This study was limited to a certain type of soil, tested at a specific initial relative density. Observations and equations can be validated against other soils tested under different initial conditions. For example, similar experiments can be performed on natural silt or clay.
- In the centrifuge experiments presented herein, the zone of unsaturated soil was controlled by the capillary rise technique. Observations and recommendations can be further validated and extended against tests performed on soil layers with zones of unsaturated soil generated by alternative mechanisms such as wet compaction and infiltration.
- This study investigates the response of soils and structures tested under scaled historic seismic motions. Centrifuge experiments performed on similar structures and soils under cyclic and monotonic loading would complement the results presented in this study.

- Numerical modeling can be used to expand the results of this study for other structures tested under extended boundary conditions. The calibration of these numerical models can be performed using the results presented in this dissertation.
- Analytical methods, which capture inelastic and plastic soil and structural response and consider increased modes of vibration, could be validated against the results of the experiments presented herein.
- The design procedures for rocking foundations in unsaturated soil layers presented in this dissertation can be further validated against the response of instrumented field-scale structures. The SFSI test structure located in Garner Valley, California could provide viable data for this purpose. This facility is owned by the University of California Santa Barbara and funded by the Network for Earthquake Engineering Simulation.

8.4. DISSERTATION INTELLECTUAL MERIT

This research tackles the outstanding problem of ignoring the influence of unsaturated soil uncertainties on the response of structures when subjected to seismic loading. Climate change is expected to lead to an increase in the frequency and intensity of extreme precipitation events, which in turn may affect the saturation levels of soil, making this research especially relevant. Particularly, this research experimentally evaluates and compares the response of elastic and inelastic structural systems when founded on dry, saturated, and unsaturated soil layers. Compared to the response of structures founded on saturated or dry soil, unsaturated soil may lead to increased superstructure demands, while reducing the deformations experienced at the foundation level. State-of-the-art centrifuge testing facilities are leveraged to produce small-scale models that replicate the behavior of full-scale soil-structure systems. The research also complements and extends current design guidelines leading to the implementation of rocking foundations in practice.

Design recommendations incorporating the fundamentals of unsaturated soil mechanics are derived and presented in this research. These recommendations can be used to predict the response of rocking foundations resting on soil layers with variable water table conditions. Dynamic centrifuge tests are also performed on single- and two-span bridge systems incorporating rocking foundations. Design procedures used for standalone rocking foundations are validated and extended to consider the interconnectedness of realistic bridges. The outcomes can be used to consider the influence of unsaturated soils during seismic design and help facilitate the implementation of rocking isolated structures in practice.

Table 8-1 summarizes publications resulting from this dissertation. Furthermore, the table summarizes journal articles currently in preparation at the time of submission of this dissertation, that will be subsequently submitted for publication.

Table 8-1. Summary of conference papers and journal articles published, or in preparation, at the time of submission this dissertation.

Journal Article	
No.	Citation
4	Turner, M. M., Ghayoomi, M.., Ueda, K., & Uzuoka, R. (2022). Seismic Performance of Single and Two-Span Bridges built using Rocking Foundations on Dry Soil. Undecided Journal, In preparation.
3	Turner, M. M., Ghayoomi, M.., Ueda, K., & Uzuoka, R. (2022). Seismic Performance of a Single-Span Bridge System Incorporating Rocking Foundations on Unsaturated Soil Layers. Undecided Journal, In Preparation.
2	Turner, M. M., Ghayoomi, M., Ueda, K., & Uzuoka, R. (2022). Soil-Foundation-Structure Interaction of Inelastic Structural Systems on Unsaturated Soil Layers. ASCE Journal of Geotechnical and Geoenvironmental Engineering 148(7):04022049.
1	Turner, M. M., Ghayoomi, M., Ueda, K., & Uzuoka, R. (2021). Performance of rocking foundations on unsaturated soil layers with variable groundwater levels. Géotechnique, 72(11): 984-997.
Conference Paper	
No.	Citation
3	Turner, M. M., Komolafe, K., Ghayoomi, M., Ueda, K., and Uzuoka, R. Centrifuge test to assess K_0 in unsaturated soil layers with varying groundwater table levels. *10^{th} International Conference on Physical Modelling in Geotechnics (ICPMGE)*, 1-4.
2	Turner, M. M., Ghayoomi, M., Ueda, K., and Uzuoka, R. (2022), Centrifuge modeling of a rocking shallow foundation on variably saturated ground, *20th International Conference on Soil Mechanics and Geotechnical Engineering (ICSMGE) 2022*, 1-6.
1	Turner, M. M., Ghayoomi, M., Ueda, K., & Uzuoka, R. (2022). Centrifuge Modeling to Evaluate the Seismic Response of Elastic and Inelastic Structures Embedded in Unsaturated Soil. In *Geo-Congress 2022*, 1-8.

CHAPTER 9

REFERENCES

Adapa, G., Ueda, K., & Uzuoka, R. (2021). Seismic stability of embankments with different densities and upstream conditions related to the water level. *Soils and Foundations*, *61*(1), 185–197. https://doi.org/10.1016/j.sandf.2020.11.007

Allmond, J. D., & Kutter, B. (2014a). *Fluid Effects on Rocking Foundations in Difficult Soil*. NCEE 2014 - 10th U.S. National Conference on Earthquake Engineering: Frontiers of Earthquake Engineering.

Allmond, J. D., & Kutter, B. L. (2014b). Design Considerations for Rocking Foundations on Unattached Piles. *Journal of Geotechnical and Geoenvironmental Engineering*, *140*(10), 04014058. https://doi.org/10.1061/(ASCE)GT.1943-5606.0001162

Alpan, I. (1967). The Empirical Evaluation of the Coefficient K0 and K0R. *Soils and Foundations*, *7*(1), 31–40. https://doi.org/10.3208/sandf1960.7.31

Anastasopoulos, I., Gazetas, G., Loli, M., Apostolou, M., & Gerolymos, N. (2010). Soil failure can be used for seismic protection of structures. *Bulletin of Earthquake Engineering*, *8*(2), 309–326. https://doi.org/10.1007/s10518-009-9145-2

Anastasopoulos, I., Gelagoti, F., Spyridaki, A., Sideri, J., & Gazetas, G. (2014). Seismic Rocking Isolation of an Asymmetric Frame on Spread Footings. *Journal of Geotechnical and Geoenvironmental Engineering*, *140*(1), 133–151. https://doi.org/10.1061/(ASCE)GT.1943-5606.0001012

Anastasopoulos, I., Kourkoulis, R., Gelagoti, F., & Papadopoulos, E. (2012). Rocking response of SDOF systems on shallow improved sand: An experimental study. *Soil Dynamics and Earthquake Engineering*, *40*, 15–33. https://doi.org/10.1016/j.soildyn.2012.04.006

Antonellis, G., Gavras, A. G., Panagiotou, M., Kutter, B. L., Guerrini, G., Sander, A. C., & Fox, P. J. (2015). Shake Table Test of Large-Scale Bridge Columns Supported on Rocking Shallow Foundations. *Journal of Geotechnical and Geoenvironmental Engineering*, *141*(5), 04015009. https://doi.org/10.1061/(ASCE)GT.1943-5606.0001284

Antonellis, G., & Panagiotou, M. (2013). *Seismic design and performance of bridges with columns on rocking foundations* (PEER Report No. 2013/21). Pacific Earthquake Engineering Research Center.

Antonellis, G., & Panagiotou, M. (2014). Seismic Response of Bridges with Rocking Foundations Compared to Fixed-Base Bridges at a Near-Fault Site. *Journal of Bridge Engineering*, *19*(5), 04014007. https://doi.org/10.1061/(ASCE)BE.1943-5592.0000570

Arias, A. (1970). A measure of earthquake intensity. *Seismic Design for Nuclear Power Plants (R. J. Hansen Ed.)*, 438–483.

ASCE. (2017). *Minimum design loads and associated criteria for buildings and other structures*. American Society of Civil Engineers.

ASCE 41-17. (2017). *Seismic Evaluation and Retrofit of Existing Buildings*. American Society of Civil Engineers.

ASTM D2487-11. (2011). *Standard Practice for Classification of Soils for Engineering Purposes (Unified Soil Classification System)*. American Society for Testing and Materials.

Avilés, J., & Pérez-Rocha, L. E. (1996). Evaluation of interaction effects on the system period and the system damping due to foundation embedment and layer depth. *Soil Dynamics and Earthquake Engineering*, *15*(1), 11–27. https://doi.org/10.1016/0267-7261(95)00035-6

Bartholomew, D. (2014). Northridge Earthquake: 1994 quake still fresh in Los Angeles minds after 20 years. *Daily News*. https://www.dailynews.com/general-news/20140111/northridge-earthquake-1994-disaster-still-fresh-in-los-angeles-minds-after-20-years

Bielak, J. (1975). Dynamic behaviour of structures with embedded foundations. *Earthquake Engineering & Structural Dynamics*, *3*(3), 259–274. https://doi.org/10.1002/eqe.4290030305

Biglari, M., d'Onofrio, A., Mancuso, C., Jafari, M. K., Shafiee, A., & Ashayeri, I. (2012). Small-strain stiffness of Zenoz kaolin in unsaturated conditions. *Canadian Geotechnical Journal*, *49*(3), 311–322. https://doi.org/10.1139/t11-105

Biglari, M., Jafari, M. K., Shafiee, A., Mancuso, C., & d'ONOFRIO, A. (2011). Shear Modulus and Damping Ratio of Unsaturated Kaolin Measured by New Suction-Controlled Cyclic Triaxial Device. *Geotechnical Testing Journal*, *34*, 103635. https://doi.org/10.1520/GTJ103635

Bilotta, E., Sanctis, L. D., Di Laora, R., D'Onofrio, A., & Silvestri, F. (2015). Importance of seismic site response and soil–structure interaction in dynamic behaviour of a tall building. *Géotechnique*, *65*(5), 391–400. https://doi.org/10.1680/geot.SIP.15.P.016

Bishop, A. W. (1959). The principle of effective stress. *Teknisk Ukeblad*, *106*(39), 859–863.

Borghei, A., & Ghayoomi, M. (2019). The role of kinematic interaction on measured seismic response of soil-foundation-structure systems. *Soil Dynamics and Earthquake Engineering*, *125*, 105674. https://doi.org/10.1016/j.soildyn.2019.05.013

Borghei, A., Ghayoomi, M., & Turner, M. (2020). Effects of Groundwater Level on Seismic Response of Soil–Foundation Systems. *Journal of Geotechnical and Geoenvironmental Engineering*, *146*(10), 04020110. https://doi.org/10.1061/(ASCE)GT.1943-5606.0002359

Borghei, S. A. (2019). *Seismic response of soil-foundation systems on unsaturated ground* [University of New Hampshire, Durham]. https://scholars.unh.edu/dissertation/2469

Brooker, E. W., & Ireland, H. O. (1965). Earth Pressures at Rest Related to Stress History. *Canadian Geotechnical Journal*, *2*, 1–15.

Caltrans. (2010). *Seismic Design Criteria version 1.6*. California Department of Transportation.

Campbell, K. W., & Bozorgnia, Y. (2012). Use of Cumulative Absolute Velocity (CAV) in Damage Assessment. *Proceedings of the 15th World Conference in Earthquake Engineering*, 1–10.

Chen, M. C., Astroza, R., Restrepo, J. I., Conte, J. P., Hutchinson, T., & Bock, Y. (2017). Predominant period and equivalent viscous damping ratio identification for a full-scale building shake table test. *Earthquake Engineering & Structural Dynamics*, *46*(14), 2459–2477. https://doi.org/10.1002/eqe.2913

Chen, Z., Trombetta, N. W., Hutchinson, T. C., Mason, H. B., Bray, J. D., & Kutter, B. L. (2013). Seismic System Identification Using Centrifuge-based Soil-Structure Interaction Test Data. *Journal of Earthquake Engineering*, *17*(4), 469–496. https://doi.org/10.1080/13632469.2012.762956

Chopra, A. K. (1995). *Dynamics of structures: Theory and applications to earthquake engineering*. Pretence Hall, Inc.

Conca, J. L., & Wright, J. (1990). Diffusion coefficients in gravel under unsaturated conditions. *Water Resources Research*, *26*(5), 1055–1066. https://doi.org/10.1029/WR026i005p01055

Darendeli, M. B. (2001). *Development of a new family of normalized modulus reduction and material damping curves* [Ph.D. Thesis, University of Texas at Austin]. https://repositories.lib.utexas.edu/handle/2152/10396

Das, B. M. (2010). *Principles of Foundation Engineering, SI Edition* (7th ed.). Cengage Learning. https://books.google.com/books?id=8bYPXVi6iLwC

Dashti, S., Bray, J. D., Pestana, J. M., Riemer, M., & Wilson, D. (2010a). Centrifuge Testing to Evaluate and Mitigate Liquefaction-Induced Building Settlement Mechanisms. *Journal of Geotechnical and Geoenvironmental Engineering*, *136*(7), 918–929. https://doi.org/10.1061/(ASCE)GT.1943-5606.0000306

Dashti, S., Bray, J. D., Pestana, J. M., Riemer, M., & Wilson, D. (2010b). Mechanisms of Seismically Induced Settlement of Buildings with Shallow Foundations on Liquefiable Soil. *Journal of Geotechnical and Geoenvironmental Engineering*, *136*(1), 151–164. https://doi.org/10.1061/(ASCE)GT.1943-5606.0000179

Deng, L., & Kutter, B. L. (2012). Characterization of rocking shallow foundations using centrifuge model tests. *Earthquake Engineering & Structural Dynamics*, *41*(5), 1043–1060. https://doi.org/10.1002/eqe.1181

Deng, L., Kutter, B. L., & Kunnath, S. K. (2012a). Centrifuge Modeling of Bridge Systems Designed for Rocking Foundations. *Journal of Geotechnical and Geoenvironmental Engineering*, *138*(3), 335–344. https://doi.org/10.1061/(ASCE)GT.1943-5606.0000605

Deng, L., Kutter, B. L., & Kunnath, S. K. (2012b). Probabilistic Seismic Performance of Rocking-Foundation and Hinging-Column Bridges. *Earthquake Spectra*, *28*(4), 1423–1446. https://doi.org/10.1193/1.4000093

Deng, L., Kutter, B. L., & Kunnath, S. K. (2014). Seismic Design of Rocking Shallow Foundations: Displacement-Based Methodology. *Journal of Bridge Engineering*, *19*(11), 04014043. https://doi.org/10.1061/(ASCE)BE.1943-5592.0000616

Depountis, N., Harris, C., & Davies, M. C. R. (2001). An assessment of miniaturised electrical imaging equipment to monitor pollution plume evolution in scaled centrifuge modelling. *Geoenvironmental Engineering*, *60*(1), 83–94. https://doi.org/10.1016/S0013-7952(00)00091-0

Deshpande, S., & Muraleetharan, K. K. (1998). Dynamic behavior of unsaturated soil embankments. *Geotechnical Earthquake Engineering and Soil Dynamics III*, 890–901.

Dewoolkar, M., Ko, H., Stadler, A., & Astaneh, S. (1999). A Substitute Pore Fluid for Seismic Centrifuge Modeling. *Geotechnical Testing Journal*, *22*(3), 196–210. https://doi.org/10.1520/GTJ11111J

Dong, Y., Lu, N., & McCartney, J. S. (2016). Unified Model for Small-Strain Shear Modulus of Variably Saturated Soil. *Journal of Geotechnical and Geoenvironmental Engineering*, *142*(9), 04016039. https://doi.org/10.1061/(ASCE)GT.1943-5606.0001506

D'Onza, F., D'Onofrio, A., & Mancuso, C. (2008). Effects of unsaturated soil state on the local seismic response of soil deposits. *1st European Conference on Unsaturated Soils*, 531–536.

Drosos, V., Georgarakos, T., Loli, M., Anastasopoulos, I., Zarzouras, O., & Gazetas, G. (2012). Soil-Foundation-Structure Interaction with Mobilization of Bearing Capacity:

Experimental Study on Sand. *Journal of Geotechnical and Geoenvironmental Engineering*, *138*(11), 1369–1386. https://doi.org/10.1061/(ASCE)GT.1943-5606.0000705

Duku, P. M., Stewart, J. P., Whang, D. H., & Yee, E. (2008). Volumetric Strains of Clean Sands Subject to Cyclic Loads. *Journal of Geotechnical and Geoenvironmental Engineering*, *134*(8), 1073–1085. https://doi.org/10.1061/(ASCE)1090-0241(2008)134:8(1073)

Eseller-Bayat, E., Yegian, M. K., Alshawabkeh, A., & Gokyer, S. (2013). Liquefaction Response of Partially Saturated Sands. I: Experimental Results. *Journal of Geotechnical and Geoenvironmental Engineering*, *139*(6), 863–871. https://doi.org/10.1061/(ASCE)GT.1943-5606.0000815

Esposito, G. (2000). Centrifuge simulation of light hydrocarbon spill in partially saturated Dutch Dune Sand. *Bulletin of Engineering Geology and the Environment*, *58*(2), 89–93. https://doi.org/10.1007/s100640050001

Figini, R., & Paolucci, R. (2017). Integrated foundation–structure seismic assessment through non-linear dynamic analyses. *Earthquake Engineering & Structural Dynamics*, *46*(3), 349–367. https://doi.org/10.1002/eqe.2790

Figueroa, J. D., Saada, A. S., Liang, L., & Dahisaria, N. M. (1994). Evaluation of Soil Liquefaction by Energy Principles. *Journal of Geotechnical Engineering*, *120*(9), 1554–1569. https://doi.org/10.1061/(ASCE)0733-9410(1994)120:9(1554)

Fredlund, D. G., & Morgenstern, N. R. (1977). Stress State Variables for Unsaturated Soils. *Journal of the Geotechnical Engineering Division*, *103*(5), 447–466. https://doi.org/10.1061/AJGEB6.0000423

Fredlund, D. G., & Rahardjo, H. (1993). *Soil Mechanics for Unsaturated Soils* (1st ed.). Wiley.

Fredlund, D. G., Rahardjo, H., & Fredlund, M. D. (2012). *Unsaturated Soil Mechanics in Engineering Practice*. John Wiley & Sons, Inc.

Fredlund, D. G., & Xing, A. (1994). Equations for the soil-water characteristic curve. *Canadian Geotechnical Journal*, *31*(4), 521–532. https://doi.org/10.1139/t94-061

Fredlund, D. G., Xing, A., Fredlund, M. D., & Barbour, S. L. (1996). The relationship of the unsaturated soil shear strength to the soil-water characteristic curve. *Canadian Geotechnical Journal*, *33*(3), 440–448. https://doi.org/10.1139/t96-065

Gajan, S., & Kutter, B. L. (2008). Capacity, Settlement, and Energy Dissipation of Shallow Footings Subjected to Rocking. *Journal of Geotechnical and Geoenvironmental Engineering*, *134*(8), 1129–1141. https://doi.org/10.1061/(ASCE)1090-0241(2008)134:8(1129)

Gajan, S., & Kutter, B. L. (2009). Effects of Moment-to-Shear Ratio on Combined Cyclic Load-Displacement Behavior of Shallow Foundations from Centrifuge Experiments. *Journal of Geotechnical and Geoenvironmental Engineering*, *135*(8), 1044–1055. https://doi.org/10.1061/(ASCE)GT.1943-5606.0000034

Gajan, S., Kutter, B. L., Phalen, J. D., Hutchinson, T. C., & Martin, G. R. (2005). Centrifuge modeling of load-deformation behavior of rocking shallow foundations. *Soil Dynamics and Earthquake Engineering*, *25*(7), 773–783. https://doi.org/10.1016/j.soildyn.2004.11.019

Gazetas, G. (2015). 4th Ishihara lecture: Soil–foundation–structure systems beyond conventional seismic failure thresholds. *Soil Dynamics and Earthquake Engineering*, *68*, 23–39. https://doi.org/10.1016/j.soildyn.2014.09.012

Ghayoomi, M., & Dashti, S. (2015). Effect of Ground Motion Characteristics on Seismic Soil-Foundation-Structure Interaction. *Earthquake Spectra*, *31*(3), 1789–1812. https://doi.org/10.1193/040413EQS089M

Ghayoomi, M., Dashti, S., & McCartney, J. S. (2013). Performance of a transparent Flexible Shear Beam container for geotechnical centrifuge modeling of dynamic problems. *Soil Dynamics and Earthquake Engineering*, *53*, 230–239. https://doi.org/10.1016/j.soildyn.2013.07.007

Ghayoomi, M., Ghadirianniari, S., Khosravi, A., & Mirshekari, M. (2018). Seismic behavior of pile-supported systems in unsaturated sand. *Soil Dynamics and Earthquake Engineering*, *112*, 162–173. https://doi.org/10.1016/j.soildyn.2018.05.014

Ghayoomi, M., & McCartney, J. (2011). Measurement of Small-Strain Shear Moduli of Partially Saturated Sand During Infiltration in a Geotechnical Centrifuge. *Geotechnical Testing Journal*, *34*(5), 503–513. https://doi.org/10.1520/GTJ103608

Ghayoomi, M., McCartney, J., & Ko, H. (2011). Centrifuge Test to Assess the Seismic Compression of Partially Saturated Sand Layers. *Geotechnical Testing Journal*, *34*(4), 321–331. https://doi.org/10.1520/GTJ103355

Ghayoomi, M., McCartney, J. S., & Ko, H.-Y. (2013). Empirical Methodology to Estimate Seismically Induced Settlement of Partially Saturated Sand. *Journal of Geotechnical and Geoenvironmental Engineering*, *139*(3), 367–376. https://doi.org/10.1061/(ASCE)GT.1943-5606.0000774

Ghayoomi, M., Suprunenko, G., & Mirshekari, M. (2017). Cyclic Triaxial Test to Measure Strain-Dependent Shear Modulus of Unsaturated Sand. *International Journal of Geomechanics*, *17*(9), 04017043. https://doi.org/10.1061/(ASCE)GM.1943-5622.0000917

Goel, R. K., & Chopra, A. K. (1997). Period Formulas for Moment-Resisting Frame Buildings. *Journal of Structural Engineering*, *123*(11), 1454–1461. https://doi.org/10.1061/(ASCE)0733-9445(1997)123:11(1454)

Hansen, J. B. (1970). A revised and extended formula for bearing capacity. *Danish Geotechnical Institution Bulletin*, *28*, 5–11.

Hardin, B., & Drnevich, V. (1972). Shear Modulus and Damping in Soils: Design Equations and Curves. *J. Soil Mech. Found. Div.*, *98*. https://doi.org/10.1061/JSFEAQ.0001760

Hardin, B. O. (1978). THE NATURE OF STRESS-STRAIN BEHAVIOR FOR SOILS. *Proceedings of the ASCE Geotechnical Engineering Division Specialty Conference*, Article Proceeding.

Heron, C. M., Haigh, S. K., & Madabhushi, S. P. G. (2015). A new macro-element model encapsulating the dynamic moment–rotation behaviour of raft foundations. *Géotechnique*, *65*(5), 442–451. https://doi.org/10.1680/geot.SIP.15.P.020

Housner, G. W. (1963). The behavior of inverted pendulum structures during earthquakes. *Bulletin of the Seismological Society of America*, *53*(2), 403–417.

Hoyos, L. R., Suescún-Florez, E. A., & Puppala, A. J. (2015). Stiffness of intermediate unsaturated soil from simultaneous suction-controlled resonant column and bender element testing. *Engineering Geology*, *188*, 10–28. https://doi.org/10.1016/j.enggeo.2015.01.014

Hung, H.-H., Liu, K.-Y., Ho, T.-H., & Chang, K.-C. (2011). An experimental study on the rocking response of bridge piers with spread footing foundations. *Earthquake Engineering & Structural Dynamics*, *40*(7), 749–769. https://doi.org/10.1002/eqe.1057

Hushmand, B., Scott, R. F., & Crouse, C. B. (1988). Centrifuge liquefaction tests in a laminar box. *Géotechnique*, *38*(2), 253–262. https://doi.org/10.1680/geot.1988.38.2.253

Jaky, J. (1944). The coefficient of earth pressure at rest. *Journal of the Hungarian Society of Architects and Engineers, 25*, 355–358.

JGS 0161. (2015). *Test Method for the Minimum and Maximum Densities of Sands* (Japanese Geotechnical Society of Standards: Laboratory Testing Standards of Geomaterials). The Japanese Geotechnical Society (JGS).

Karimi, Z., & Dashti, S. (2016). Numerical and Centrifuge Modeling of Seismic Soil–Foundation–Structure Interaction on Liquefiable Ground. *Journal of Geotechnical and Geoenvironmental Engineering*, *142*(1), 04015061. https://doi.org/10.1061/(ASCE)GT.1943-5606.0001346

Kim, S., & Stewart, J. P. (2003). Kinematic Soil-Structure Interaction from Strong Motion Recordings. *Journal of Geotechnical and Geoenvironmental Engineering*, *129*(4), 323–335. https://doi.org/10.1061/(ASCE)1090-0241(2003)129:4(323)

Knight, M. A., & Mitchell, R. J. (1996). Modelling of light nonaqueous phase liquid (LNAPL) releases into unsaturated sand. *Canadian Geotechnical Journal*, *33*(6), 913–925. https://doi.org/10.1139/t96-121

Ko, H. Y. (1988). *Summary of the state-of-art in centrifuge model testing: Vol. Centrifuges in Soil Mechanics*. Craig and Schofield.

Ko, H. Y. (1994). Modeling Seismic Problems in Centrifuges. *Centrifuge 94, Leung, Lee and Tan (Eds.)*, 3–12.

Kokkali, P., Abdoun, T., & Anastasopoulos, I. (2015). Centrifuge Modeling of Rocking Foundations on Improved Soil. *Journal of Geotechnical and Geoenvironmental Engineering*, *141*(10), 04015041. https://doi.org/10.1061/(ASCE)GT.1943-5606.0001315

Kokkali, P., Anastasopoulos, I., Abdoun, T., & Gazetas, G. (2014). Static and cyclic rocking on sand: Centrifuge versus reduced-scale 1g experiments. *Géotechnique*, *64*(11), 865–880. https://doi.org/10.1680/geot.14.P.064

Komolafe, O., & Ghayoomi, M. (2021). *Theoretical Ultimate Lateral Resistance Near the Soil Surface in Unsaturated Cohesionless Soils*. 178–187.

Kramer, S. L. (1996). *Geotechnical earthquake engineering*. Pretence Hall, Inc.

Kumar, J., & Rao, V. B. K. (2002). Seismic bearing capacity factors for spread foundations. *Géotechnique*, *52*(2), 79–88. https://doi.org/10.1680/geot.2002.52.2.79

Kutter, B. L. (1995). *Recent Advances in Centrifuge Modeling of Seismic Shaking*. International Conferences on Recent Advances in Geotechnical Earthquake Engineering and Soil Dynamics.

Kutter, B. L., Moore, M., Hakhamaneshi, M., & Champion, C. (2016). Rationale for Shallow Foundation Rocking Provisions in ASCE 41-13. *Earthquake Spectra*, *32*(2), 1097–1119. https://doi.org/10.1193/121914eqs215m

Law, H., Ko, H. Y., Sture, S., & Pak, R. (1991). Development and Performance of a Laminar Container for Earthquake Liquefaction Studies. *Centrifuge 91, Ko and McLean (Eds.)*, 369–376.

Le, K. N., & Ghayoomi, M. (2017). Cyclic Direct Simple Shear Test to Measure Strain-Dependent Dynamic Properties of Unsaturated Sand. *Geotechnical Testing Journal*, *40*(3), 20160128. https://doi.org/10.1520/GTJ20160128

Liu, W., & Hutchinson, T. C. (2018). Numerical investigation of stone columns as a method for improving the performance of rocking foundation systems. *Soil Dynamics and Earthquake Engineering*, *106*, 60–69. https://doi.org/10.1016/j.soildyn.2017.10.015

Liu, W., Hutchinson, T. C., Kutter, B. L., Hakhamaneshi, M., Aschheim, M. A., & Kunnath, S. K. (2013). Demonstration of Compatible Yielding between Soil-Foundation and Superstructure Components. *Journal of Structural Engineering*, *139*(8), 1408–1420. https://doi.org/10.1061/(ASCE)ST.1943-541X.0000637

Ljung, L. (1987). *System identification: Theory for the user*. Pretence Hall, Inc.

Loli, M., Knappett, J. A., Brown, M. J., Anastasopoulos, I., & Gazetas, G. (2014). Centrifuge modeling of rocking-isolated inelastic RC bridge piers. *Earthquake Engineering & Structural Dynamics*, *43*(15), 2341–2359. https://doi.org/10.1002/eqe.2451

Lu, N., Godt, J. W., & Wu, D. T. (2010). A closed-form equation for effective stress in unsaturated soil. *Water Resources Research*, *46*(5). https://doi.org/10.1029/2009WR008646

Lu, N., & Likos, W. J. (2004). *Unsaturated Soil Mechanics*. Wiley.

Masing, G. (1926). *Eigenspannungen und Verfestgung Beim Masing*. Second International Conference of Applied Mechanics.

Mason, H. B., Kutter, B. L., Bray, J. D., Wilson, D. W., & Choy, B. Y. (2010). Earthquake motion selection and calibration for use in a geotechnical centrifuge. *Proceedings of the 7th International Conference on Physical Modeling in Geotechnics*, 361–366.

Massarsch, K. R. (1979). Lateral Earth Pressure in Normally Consolidated Clay. *7th European Conference on Soil Mechanics and Foundation Engineering*, *2*, 245–249.

Menq, F. (2003). *Dynamic Properties of Sandy and Gravelly Soils*. The University of Texas at Austin.

Mirshekari, M., & Ghayoomi, M. (2017). Centrifuge tests to assess seismic site response of partially saturated sand layers. *Soil Dynamics and Earthquake Engineering*, *94*, 254–265. https://doi.org/10.1016/j.soildyn.2017.01.024

Mirshekari, M., Ghayoomi, M., & Borghei, A. (2018). A Review on Soil-Water Retention Scaling in Centrifuge Modeling of Unsaturated Sands. *Geotechnical Testing Journal*, *41*(6), 979–997. https://doi.org/10.1520/GTJ20170120

Mousavi, S. (2020). *Dynamic Performance of Partially Saturated and Unsaturated Soils* [Doctoral Dissertation]. University of New Hampshire, Durham.

Mousavi, S., & Ghayoomi, M. (2021a). Liquefaction Mitigation of Sands with Nonplastic Fines via Microbial-Induced Partial Saturation. *Journal of Geotechnical and Geoenvironmental Engineering*, *147*(2), 04020156. https://doi.org/10.1061/(ASCE)GT.1943-5606.0002444

Mousavi, S., & Ghayoomi, M. (2021b). Seismic Compression of Unsaturated Silty Sands: A Strain-Based Approach. *Journal of Geotechnical and Geoenvironmental Engineering*, *147*(5), 04021023. https://doi.org/10.1061/(ASCE)GT.1943-5606.0002507

Mousavi, S., Ghayoomi, M., & Jones, S. H. (2020). Compositional and geoenvironmental factors in microbially induced partial saturation. *Environmental Geotechnics*, *0*(0), 1–13. https://doi.org/10.1680/jenge.18.00087

NIST. (2016). *Seismic design of steel special moment frames: A guide for practicing engineers, Second Edition* (GCR 16-917-41; NEHRP Seismic Design Technical Brief No. 2). Applied Technology Council and the Consortium of Universities for Research in Earthquake Engineering for the National Institute of Standards and Technology.

Oh, W. T., & Vanapalli, S. K. (2014). Semi-empirical Model for Estimating the Small-Strain Shear Modulus of Unsaturated Non-plastic Sandy Soils. *Geotechnical and Geological Engineering*, *32*(2), 259–271. https://doi.org/10.1007/s10706-013-9708-5

Okamura, M., & Soga, Y. (2006). Effects of Pore Fluid Compressibility on Liquefaction Resistance of Partially Saturated Sand. *Soils and Foundations*, *46*(5), 695–700. https://doi.org/10.3208/sandf.46.695

Oloo, S. Y., Fredlund, D. G., & Gan, J. K.-M. (1997). Bearing capacity of unpaved roads. *Canadian Geotechnical Journal*, *34*(3), 398–407. https://doi.org/10.1139/t96-084

Ortiz, L. A., Scott, R. F., & Lee, J. (1983). Dynamic centrifuge testing of a cantilever retaining wall. *Earthquake Engineering & Structural Dynamics*, *11*(2), 251–268. https://doi.org/10.1002/eqe.4290110207

Oztoprak, S., & Bolton, M. D. (2013). Stiffness of sands through a laboratory test database. *Géotechnique*, *63*(1), 54–70. https://doi.org/10.1680/geot.10.P.078

Pandit, S. M. (1991). *Modal and spectrum analysis*. Wiley.

Paolucci, R. (1997). Simplified Evaluation of Earthquake-Induced Permanent Displacements of Shallow Foundations. *Journal of Earthquake Engineering*, *1*(3), 563–579. https://doi.org/10.1080/13632469708962378

Paolucci, R., & Pecker, A. (1997). Soil inertia effects on the bearing capacity of rectangular foundations on cohesive soils. *Engineering Structures*, *19*(8), 637–643. https://doi.org/10.1016/S0141-0296(96)00141-1

Poulos, H. G., & Davis, E. H. (1974). *Elastic Solutions for Soil and Rock Mechanics*. John Wiley.

Rathje, E. M., Abrahamson, N. A., & Bray, J. D. (1998). Simplified Frequency Content Estimates of Earthquake Ground Motions. *Journal of Geotechnical and Geoenvironmental Engineering*, *124*(2), 150–159. https://doi.org/10.1061/(ASCE)1090-0241(1998)124:2(150)

Rathje, E. M., Kottke, A. R., & Trent, W. L. (2010). Influence of Input Motion and Site Property Variabilities on Seismic Site Response Analysis. *Journal of Geotechnical and Geoenvironmental Engineering*, *136*(4), 607–619. https://doi.org/10.1061/(ASCE)GT.1943-5606.0000255

Richards, R., Elms, D. G., & Budhu, M. (1993). Seismic Bearing Capacity and Settlements of Foundations. *Journal of Geotechnical Engineering*, *119*(4), 662–674. https://doi.org/10.1061/(ASCE)0733-9410(1993)119:4(662)

Roesset, J. M. (1980). *A review of soil-structure interaction* (NUREG/CR-1780 and UCRL 53011; Soil-Structure Interaction: The Status of Current Analysis Methods and Research.). U.S. Nuclear Regulatory Commission.

Şafak, E. (1991). Identification of Linear Structures Using Discrete-Time Filters. *Journal of Structural Engineering*, *117*(10), 3064–3085. https://doi.org/10.1061/(ASCE)0733-9445(1991)117:10(3064)

Schofield, A. N. (1980). Cambridge Geotechnical Centrifuge Operations. *Géotechnique*, *30*(3), 227–268. https://doi.org/10.1680/geot.1980.30.3.227

Seed, H. B., & Idriss, I. M. (1970). *Soil Moduli and Damping Factors for Dynamic Response Analyses* (EERC 70-10). Earthquake Engineering Research Center.

Shin, T.-C., & Teng, T. (2001). An Overview of the 1999 Chi-Chi, Taiwan, Earthquake. *Bulletin of the Seismological Society of America*, *91*(5), 895–913. https://doi.org/10.1785/0120000738

Stewart, J. P., & Fenves, G. L. (1998). System identification for evaluating soil–structure interaction effects in buildings from strong motion recordings. *Earthquake Engineering &*

Structural Dynamics, *27*(8), 869–885. https://doi.org/10.1002/(SICI)1096-9845(199808)27:8<869::AID-EQE762>3.0.CO;2-9

Stewart, J. P., Fenves, G. L., & Seed, R. B. (1999a). Seismic Soil-Structure Interaction in Buildings. I: Analytical Methods. *Journal of Geotechnical and Geoenvironmental Engineering*, *125*(1), 26–37. https://doi.org/10.1061/(ASCE)1090-0241(1999)125:1(26)

Stewart, J. P., Kim, S., Bielak, J., Dobry, R., & Power, M. S. (2003). Revisions to Soil-Structure Interaction Procedures in NEHRP Design Provisions. *Earthquake Spectra*, *19*(3), 677–696. https://doi.org/10.1193/1.1596213

Stewart, J. P., Seed, R. B., & Fenves, G. L. (1999b). Seismic Soil-Structure Interaction in Buildings. II: Empirical Findings. *Journal of Geotechnical and Geoenvironmental Engineering*, *125*(1), 38–48. https://doi.org/10.1061/(ASCE)1090-0241(1999)125:1(38)

Stewart, J. P., Smith, P. M., Whang, D. H., & Bray, J. D. (2004). Seismic Compression of Two Compacted Earth Fills Shaken by the 1994 Northridge Earthquake. *Journal of Geotechnical and Geoenvironmental Engineering*, *130*(5), 461–476. https://doi.org/10.1061/(ASCE)1090-0241(2004)130:5(461)

Stewart, M. A., & McCartney, J. S. (2014). Centrifuge Modeling of Soil-Structure Interaction in Energy Foundations. *Journal of Geotechnical and Geoenvironmental Engineering*, *140*(4), 04013044. https://doi.org/10.1061/(ASCE)GT.1943-5606.0001061

Stinson, E. (2014). *Characterizing Soil-Foundation-Structure Interaction Using Experimental Data From a Test Structure*. Princeton University.

Terzaghi, K. (1943). *Theoretical Soil Mechanics*. Wiley.

Thota, S. K., Cao, T. D., & Vahedifard, F. (2021). Poisson's Ratio Characteristic Curve of Unsaturated Soils. *Journal of Geotechnical and Geoenvironmental Engineering*, *147*(1), 04020149. https://doi.org/10.1061/(ASCE)GT.1943-5606.0002424

Tileylioglu, S. (2008). *Evaluation of Soil-Structure Interaction Effects from Field Performance Data*. University of California Los Angeles.

Tileylioglu, S., Stewart, J. P., & Nigbor, R. L. (2011). Dynamic Stiffness and Damping of a Shallow Foundation from Forced Vibration of a Field Test Structure. *Journal of Geotechnical and Geoenvironmental Engineering*, *137*(4), 344–353. https://doi.org/10.1061/(ASCE)GT.1943-5606.0000430

Travasarou, T., Bray, J. D., & Abrahamson, N. A. (2003). Empirical attenuation relationship for Arias Intensity. *Earthquake Engineering & Structural Dynamics*, *32*(7), 1133–1155. https://doi.org/10.1002/eqe.270

Trifunac, M., Todorovska, M., & Hao, T. V. (2001). *Full-scale experimental studies of soil-structure interaction—A review*. 2nd U.S.-Japan Workshop on Soil-Structure Interaction, Izgradnja, Japan.

Trombetta, N. W., Mason, H. B., Chen, Z., Hutchinson, T. C., Bray, J. D., & Kutter, B. L. (2013). Nonlinear dynamic foundation and frame structure response observed in geotechnical centrifuge experiments. *Soil Dynamics and Earthquake Engineering*, *50*, 117–133. https://doi.org/10.1016/j.soildyn.2013.02.010

Tsai, Y.-B., Yu, T.-M., Chao, H.-L., & Lee, C.-P. (2001). Spatial Distribution and Age Dependence of Human-Fatality Rates from the Chi-Chi, Taiwan, Earthquake of 21 September 1999. *Bulletin of the Seismological Society of America*, *91*(5), 1298–1309. https://doi.org/10.1785/0120000740

Tsatsis, A., & Anastasopoulos, I. (2015). Performance of Rocking Systems on Shallow Improved Sand: Shaking Table Testing. *Frontiers in Built Environment*, *1*, 9. https://doi.org/10.3389/fbuil.2015.00009

Tsukamoto, Y., Ishihara, K., Nakazawa, H., Kamada, K., & Huang, Y. (2002). Resistance of Partly Saturated Sand to Liquefaction with Reference to Longitudinal and Shear Wave Velocities. *Soils and Foundations*, *42*(6), 93–104. https://doi.org/10.3208/sandf.42.6_93

Turner, M. M., Ghayoomi, M., Ueda, K., & Uzuoka, R. (2022a). Centrifuge modeling of a rocking shallow foundation on variably saturated ground. *Proc. 20th Intl. Conference on Soil Mechanics and Geotechnical Engineering*, 1–6.

Turner, M. M., Ghayoomi, M., Ueda, K., & Uzuoka, R. (2022b). Centrifuge Modeling to Evaluate the Seismic Response of Elastic and Inelastic Structures Embedded in Unsaturated Soil. *Geo-Congress 2022*, 284–292. https://doi.org/10.1061/9780784484050.030

Turner, M. M., Ghayoomi, M., Ueda, K., & Uzuoka, R. (2022c). Performance of rocking foundations on unsaturated soil layers with variable groundwater levels. *Géotechnique*, *72*(11), 984–997. https://doi.org/10.1680/jgeot.20.P.221

Turner, M. M., Ghayoomi, M., Ueda, K., & Uzuoka, R. (2022d). Soil-Foundation-Structure Interaction of Inelastic Structural Systems on Unsaturated Soil Layers. *Journal of Geotechnical and Geoenvironmental Engineering*, *148*(7), 04022049. https://doi.org/10.1061/(ASCE)GT.1943-5606.0002819

Turner, M. M., Komolafe, O., Ghayoomi, M., Ueda, K., & Uzuoka, R. (2022). Centrifuge test to assess K0 in unsaturated soil layers with varying groundwater table levels. *Proc. 10th International Conference on Physical Modeling in Geotechnics*, 790–793.

Unno, T., Kazama, M., Uzuoka, R., & Sento, N. (2008). Liquefaction of Unsaturated Sand Considering the Pore Air Pressure and Volume Compressibility of the Soil Particle Skeleton. *Soils and Foundations*, *48*(1), 87–99. https://doi.org/10.3208/sandf.48.87

van Genuchten, M. (1980). A Closed-form Equation for Predicting the Hydraulic Conductivity of Unsaturated Soils. *Soil Science Society of America Journal*, *44*(5), 892–898. https://doi.org/10.2136/sssaj1980.03615995004400050002x

Van Laak, P., Taboada, V. M., Dobry, R., & Elgamal, A. W. (1994). Earthquake Centrifuge Modeling Using a Laminar Box. *Dynamic Geotechnical Testing II, STP 1213*, 370–384.

Vanapalli, S. K., Fredlund, D. G., Pufahl, D. E., & Clifton, A. W. (1996). Model for the prediction of shear strength with respect to soil suction. *Canadian Geotechnical Journal*, *33*(3), 379–392. https://doi.org/10.1139/t96-060

Vanapalli, S. K., & Mohamed, F. M. (2007). Bearing Capacity of Model Footings in Unsaturated Soils. *Experimental Unsaturated Soil Mechanics*, 483–493. https://doi.org/10.1007/3-540-69873-6_48

Veletsos, A. S., & Meek, J. W. (1974). Dynamic behaviour of building-foundation systems. *Earthquake Engineering & Structural Dynamics*, *3*(2), 121–138. https://doi.org/10.1002/eqe.4290030203

Veletsos, A. S., & Nair, V. V. D. (1975). Seismic Interaction of Structures on Hysteretic Foundations. *Journal of the Structural Division*, *101*(1), 109–129. https://doi.org/10.1061/JSDEAG.0003962

Veletsos, A. S., & Verbic, B. (1973). Vibration of viscoelastic foundations. *Earthquake Engineering & Structural Dynamics*, *2*(1), 87–102. https://doi.org/10.1002/eqe.4290020108

Vesic, A. S. (1973). Analysis of Ultimate Loads of Shallow Foundation. *Journal of the Soil Mechanics and Foundations Division*, *99*(1), 45–73.

Vinale, F., D'Onofrio, A., Mancuso, C., Santucci De Magistris, F., & Tatsuoka, F. (2001). *The prefailure behavior of soils as construction material*. International Conference on Pre-failure Deformation Characteristics of Geomaterials, Turin, Italy.

Wolf, J. (1985). *Dynamic soil-structure interaction*. Pretence Hall, Inc.

Xu, J., Ueda, K., & Uzuoka, R. (2022). Evaluation of failure of slopes with shaking-induced cracks in response to rainfall. *Landslides*, *19*(1), 119–136. https://doi.org/10.1007/s10346-021-01734-1

Yee, E., Duku, P. M., & Stewart, J. P. (2014). Cyclic Volumetric Strain Behavior of Sands with Fines of Low Plasticity. *Journal of Geotechnical and Geoenvironmental Engineering*, *140*(4), 04013042. https://doi.org/10.1061/(ASCE)GT.1943-5606.0001041

Yegian, M. K., Eseller-Bayat, E., Alshawabkeh, A., & Ali, S. (2007). Induced-Partial Saturation for Liquefaction Mitigation: Experimental Investigation. *Journal of Geotechnical and Geoenvironmental Engineering*, *133*(4), 372–380. https://doi.org/10.1061/(ASCE)1090-0241(2007)133:4(372)

Yoshimi, Y., Tanaka, K., & Tokimatsu, K. (1989). Liquefaction Resistance of A Partially Saturated Sand. *Soils and Foundations*, *29*(3), 157–162. https://doi.org/10.3208/sandf1972.29.3_157

Zeng, X., & Schofield, A. N. (1996). Design and performance of an equivalent-shear-beam container for earthquake centrifuge modelling. *Géotechnique*, *46*(1), 83–102. https://doi.org/10.1680/geot.1996.46.1.83